THERMOCHEMICAL PRODUCTION OF AMMONIA USING SUNLIGHT, AIR, WATER AND BIOMASS

by

RONALD MICHALSKY

Dipl.-Ing. (FH), University of Applied Sciences Mittelhessen, Giessen, Germany, 2008

AN ABSTRACT OF A DISSERTATION

submitted in partial fulfillment of the requirements for the degree

DOCTOR OF PHILOSOPHY

Department of Chemical Engineering
College of Engineering

KANSAS STATE UNIVERSITY
Manhattan, Kansas

2012

Abstract

Approximately 45% of the global hydrogen production (from fossil fuels such as natural gas or coal totaling 2% of the global energy generation) is absorbed as feedstock in the synthesis of over 130 million metric tons ammonia (NH_3) annually. To achieve food security for a growing world population and to allow for additional uses of the nitrogen-fertilizer for production of bio-energy feedstock or as combustion fuel or H_2 carrier - demand for NH_3 is projected to increase.

This work pursues the synthesis of ammonia at atmospheric pressure and without fossil fuel. Conceptually, concentrated solar radiation is utilized to transfer electrons from the lattice oxygen of a transition metal oxide to the metal ion. This yields a metallic reactant that provides the reducing power for the subsequent six-electron reductive cleavage of N_2 forming a transition metal nitride. In a second reaction, the generated lattice nitrogen is hydrogenated with hydrogen from H_2O to NH_3. This furnishes the transition metal oxide for perpetuated NH_3 synthesis.

Theory and experimentation identified manganese nitride as a promising reactant with fast diffusion characteristics ($8 \pm 4 \times 10^{-9}$ cm^2 s^{-1} apparent nitrogen diffusion constant at 750°C) and efficient liberation of 89 ± 1 mol% nitrogen via hydrolysis at 500°C. Opposed to only 2.9 ± 0.2 mol% NH_3 from manganese nitride, 60 ± 8 mol% of the nitrogen liberated from molybdenum nitride could be recovered as NH_3. Process simulation of a Mo-based NH_3 synthesis at 500-1200°C estimates economically attractive production under fairly conservative process and market conditions. To aid the prospective design of a Mn or Mo-based reactant, correlating the diffusion constants for the hydrolysis of seven nitrides with the average lattice nitrogen charge (9.96-68.83%, relative to an ideal ionic solid) indicates the utility of first-principle calculations for developing an atomic-scale understanding of the reaction mechanism in the future.

THERMOCHEMICAL PRODUCTION OF AMMONIA USING SUNLIGHT, AIR, WATER AND BIOMASS

by

RONALD MICHALSKY

Dipl.-Ing. (FH), University of Applied Sciences Mittelhessen, Giessen, Germany, 2008

A DISSERTATION

submitted in partial fulfillment of the requirements for the degree

DOCTOR OF PHILOSOPHY

Department of Chemical Engineering
College of Engineering

KANSAS STATE UNIVERSITY
Manhattan, Kansas

2012

Approved by:

Major Professor
Peter H. Pfromm

Abstract

Approximately 45% of the global hydrogen production (from fossil fuels such as natural gas or coal totaling 2% of the global energy generation) is absorbed as feedstock in the synthesis of over 130 million metric tons ammonia (NH_3) annually. To achieve food security for a growing world population and to allow for additional uses of the nitrogen-fertilizer for production of bio-energy feedstock or as combustion fuel or H_2 carrier - demand for NH_3 is projected to increase.

This work pursues the synthesis of ammonia at atmospheric pressure and without fossil fuel. Conceptually, concentrated solar radiation is utilized to transfer electrons from the lattice oxygen of a transition metal oxide to the metal ion. This yields a metallic reactant that provides the reducing power for the subsequent six-electron reductive cleavage of N_2 forming a transition metal nitride. In a second reaction, the generated lattice nitrogen is hydrogenated with hydrogen from H_2O to NH_3. This furnishes the transition metal oxide for perpetuated NH_3 synthesis.

Theory and experimentation identified manganese nitride as a promising reactant with fast diffusion characteristics ($8 \pm 4 \times 10^{-9}$ cm^2 s^{-1} apparent nitrogen diffusion constant at 750°C) and efficient liberation of 89 ± 1 mol% nitrogen via hydrolysis at 500°C. Opposed to only 2.9 ± 0.2 mol% NH_3 from manganese nitride, 60 ± 8 mol% of the nitrogen liberated from molybdenum nitride could be recovered as NH_3. Process simulation of a Mo-based NH_3 synthesis at 500-1200°C estimates economically attractive production under fairly conservative process and market conditions. To aid the prospective design of a Mn or Mo-based reactant, correlating the diffusion constants for the hydrolysis of seven nitrides with the average lattice nitrogen charge (9.96-68.83%, relative to an ideal ionic solid) indicates the utility of first-principle calculations for developing an atomic-scale understanding of the reaction mechanism in the future.

Table of Contents

List of Figures

List of Tables

List of Supplemental Files

Parman-Michalsky_NSF-IGERT-poster-competition_final-version (QuickTime Movie): Bryon Parman, Ronald Michalsky, Vincent Amanor-Boadu, Peter H. Pfromm: Sustainable nitrogen fertilizer, NSF IGERT Trainee Online Video & Poster Competition 2012, May 3-6, 2012 (poster and video).

Acknowledgements

I enjoyed my PhD studies at Kansas State University and I am glad and thankful for the experience I have gained. I shared this time with many lovely supportive friends.

Foremost I want to thank my major advisor Dr. Peter Pfromm and Dr. Mary Rezac for their ceaseless motivation and support, their powerful guidance and not at least for providing the graduate student stipend I enjoyed. Throughout, they encouraged me with sound advice and admirable humanity to re-view wordy writing, to re-think fragmentary experiments, to re-structure schedules that may have been cluttered up with energy and time sinks, and to realize chasing bad ideas. For this, and much more, I am infinitely grateful.

The Rezac/Pfromm research group furthered many outstanding individuals and budding engineers. I thank Alexandru Avram, Elizabeth Boyer, Fan Zhang, John Stanford, Leslie Schulte, Mandeep Kular, Matthew Young, Michael Wales, Neha Dhiman, Patrick Bollin, Sebastian Wendel, Dr. Alexander Brix (with particular thanks for his concept and preliminary work towards the construction of a solar furnace), Dr. Devinder Singh, Dr. Juan Cruz Jimenez, Martin Kramer, Dr. Mohammed Hussain, and Volker Bliem for input, reflection, humor, ideas, practical assistance, and wonderful graduate school and hiking experiences.

Much of this dissertation would not have been possible without the precious time of many researchers, students and helping hands at Kansas State University. For their help with assembling, equipping and operating furnaces I thank Dave Threewit, John Linder, James Swanson, Rob Jonson, Nam Nguyen, Kevin Turner, Elliott Meckley, and Brian Peterson. I appreciate the temperature-proof - unfortunately not shatter-proof - and plentiful glass and quartz

ware artfully manufactured by James Hodgson and I am just as well thankful for equally valuable discussions with Jim and ideas that let me think out of the box.

I spent a lot of time in front of X-ray generators, electron microscopes and various ammonia detectors. For their assistance, help with overcoming a plethora of technical challenges, and patience with the many questions I kept asking I like to thank Kent Hampton, Dr. Daniel Boyle, Matthew Lairmore, Lori Fields, Kathy Lowe, Jennifer Aumiller, and Myles Ikenberry. I am grateful to Dr. Keith Hohn, Dr. Vikas Berry, and Dr. Lorena Passarelli for allowing us to use their lab facilities and for instant help with clean and clear water when there was need.

For their assistance with the statistical verification of the free energy plots I am grateful to Dr. Leigh Murray and Dayou Jiang. For many other insights and profound discussions unrelated to mass and energy balances I thank Bryon Parman and Dr. Vincent Amanor-Boadu. They together with all members of the Integrative Graduate Education and Research Training (IGERT) program gave me a new understanding of interdisciplinary work and communication.

I appreciate our administrative specialists and coordinators, particularly Florence Sperman, Karey DeBardeleben, Lauren Muse, Pat Nelson, and Keith Rutlin, for their endless help with paper work and their patience with my semesterly questions on healthcare-related forms. I also thank Dr. Larry Erickson and the faculty of the Department of Chemical Engineering at Kansas State University for sponsoring and awarding the Dr. Larry Erickson Graduate Student Fellowship 2012. Special thanks are to one of the most outstanding teachers I know, Dr. Larry Glasgow who provided me with valuable computational engineering practices and whose prosperous and - obviously - limitless enthusiasm taught me a great deal about didactic initiatives.

Outside of work, I spent my time with my roommates, friends and family. I am thankful for much of the reason and energy - fundamental to this work - that originates from their friendship and support. I am particularly thankful to my parents and sisters, Miguel, Dirk, Jan, Mehrang, Patrick, Marco, Nico, Victoria, Chrischelle, Christina, Celine, Alex, Lisa, Robert, Jay, Sarah, and Dandi.

Finally I thank my PhD committee for guiding my studies, for many stimulating discussions and for coming together and providing constructive comments on my work: Dr. James Steichen (outside chair), Dr. Peter Pfromm, Dr. James Edgar, Dr. Vikas Berry, Dr. Peter Czermak, Dr. Viktor Chikan, and Dr. Vincent Amanor-Boadu.

Lastly, not at least, I am cordially and eternally grateful for Dr. Peter Czermak's first and vital support with offering the possibility of studying abroad and affording high-level and peer-reviewed research activities at Kansas State University during my diploma studies. This and his continuous support have animated my academic ambitions and have thereby facilitated this work.

This material is based upon work supported by National Science Foundation Grant # 0903701: "Integrating the Socioeconomic, Technical, and Agricultural Aspects of Renewable and Sustainable Biorefining Program, awarded to Kansas State University." I thank the Center for Sustainable Energy, Kansas State University kindly for supporting this work and I am grateful for the related Associate Traineeship in Biorefining.

Dedication

In love - to my family

Chapter 1 - Introduction

Chemical synthesis of ammonia from air with the first plant producing the synthetic nitrogen fertilizer at industrial scale in 1913[1] coined the concept "bread from air"[2] and "averted the specter of famine"[2] during World War I. Realized by Fritz Haber's inventive talent (Nobel Prize 1919) and Carl Bosch's engineering skills (Nobel Prize 1931)[1], industrial high-pressure and high-temperature synthesis of ammonia from nitrogen gas (separated from air) and hydrogen gas (produced currently from finite fossil resources such as natural gas, coal, or Naphtha[3, 4]) has been recognized as a major contribution to the "Green Revolution" of the first half of the 20th century[5, 6].

It is perhaps this crucial relation between the industrial production of ammonia on one hand and the global population growth and the availability of infrastructure, technical know-how, and last, but not least, fossil resources on the other hand that Gerhard Ertl hinted at with the statement: "[…] it is quite obvious that our present life would be quite different without the development of the Haber-Bosch process."[1] during his Nobel Lecture in 2007.

The present work explores an alternative synthesis of ammonia from heterogeneous reactions of binary transition metal nitrides with water or water-derived hydrogen sources at ambient pressure. This Chapter reviews (i) the current demand and supply of ammonia, (ii) alternative ammonia synthesis technologies without fossil fuel, outlines (iii) the scope of this work towards a solar thermochemical ammonia synthesis at ambient pressure and without fossil fuel, and (iv) provides background on major experimental techniques that will be utilized in the work presented thereafter.

1.1 Ammonia supply and demand

1.1.1 Current and prospective uses of ammonia

With about 128 million metric tons (t) NH_3 produced world-wide in 2001[6, 7] and a global capacity for NH_3 synthesis (2001/2) at approximately 162 million t per year[8] ammonia is one of the major products of the chemical industry. As comparison, Figure 1.1 shows the top ten most-produced organic and inorganic chemicals in the U.S[9].

Since nitrogen is usually limiting the yield of intensive agriculture[6], the major application of NH_3 is its use as synthetic fertilizer[6, 10, 11]. Between 1975 and 2003 in the U.S., 77-87 wt% of the consumed NH_3 was used as fertilizer[12] (NH_3 or NH_3-derived chemicals: urea, ammonium sulfate or nitrate, etc.)[9]. The remainder is used for the synthesis of plastics and explosives[9].

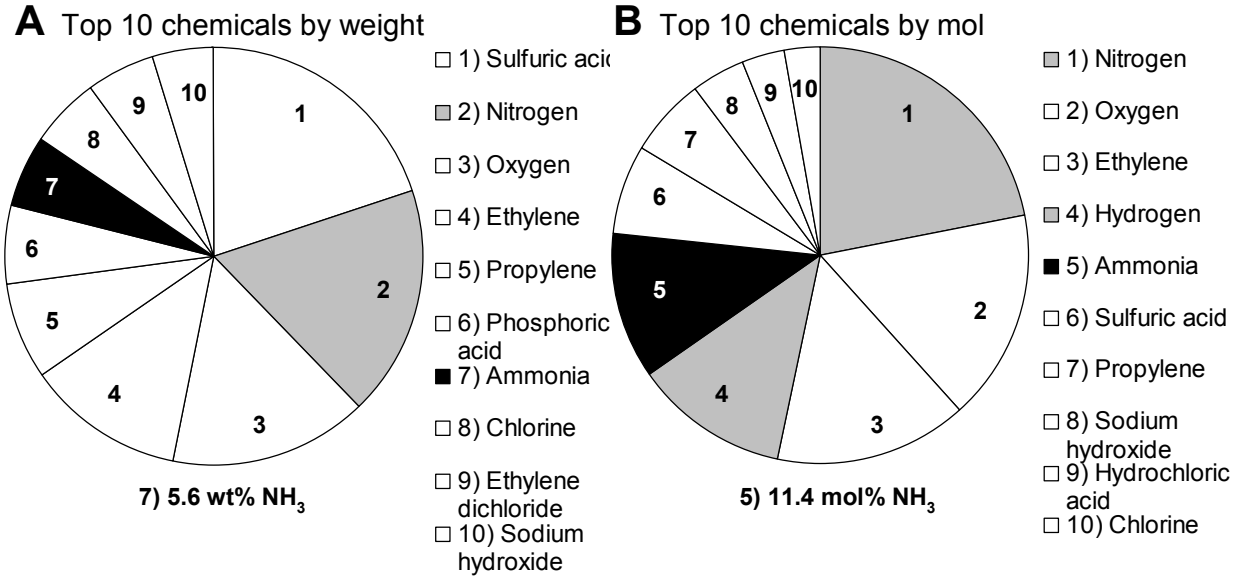

Figure 1.1 Total production of organic and inorganic chemicals (U.S., 2003)[9], A) in wt% of 1.87 x 10^8 t total year^{-1}, B) in mol% of 5.41 x 10^{12} mol year^{-1}. Data are taken in tons per year (all chemicals except N_2, O_2 and H_2) or in cubic meter per year (for N_2, O_2, and H_2)[9].

To achieve food security for an expected world population of 9.1 billion in 2050, global production of food, feed and fiber may have to increase by projected 70%[13]. Achieving this -

particularly in developing countries - is expected to require agricultural intensification[13], that is, a continued and likely increased need for fertilizers. Additionally, due to a global energy demand that has been forecasted to double by 2050[14] prospective competitive uses of NH_3 are:

- Nitrogen-fertilizer to afford an increased demand for agricultural production for biofuels[15-17] (compare, e.g., the expanded renewable fuel standard, RFS2[18])
- "Perfect hydrogen carrier"[19, 20] with an 18 wt% H_2 capacity reaching readily the 9 wt% H_2 capacity U.S. Department of Energy for H_2-based transportation fuels in 2015[21]
- Alternative fuel/fuel-blend in diesel combustion engines[22, 23]

1.1.2 Current industrial ammonia synthesis

Details on the Haber-Bosch process utilized currently for the major fraction of the global NH_3 synthesis will be provided when a comparison of the current technology with a proposed alternative NH_3 production concept is attempted (e.g., Section 2.2 or 7.3.2 respectively). At this point it should suffice to point out the major advantages and disadvantages of the process (Fig. 1.2) and a crucial correlation of the ammonia sales price and the price of natural gas (Fig. 1.3)[4].

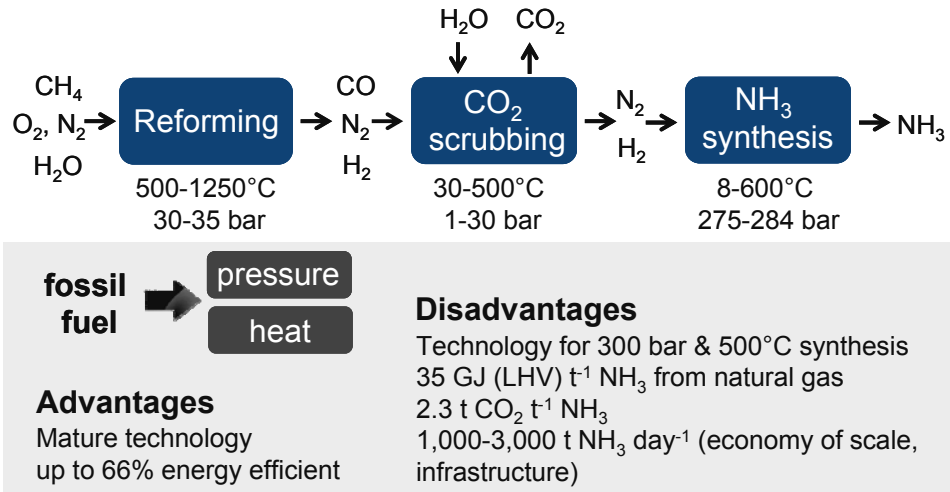

Figure 1.2 First-level overview of the industrial NH_3 synthesis. Temperatures and pressures were simulated with the Aspen Plus (V7.0) Ammonia Model[24], other process specifications were taken from the literature[8].

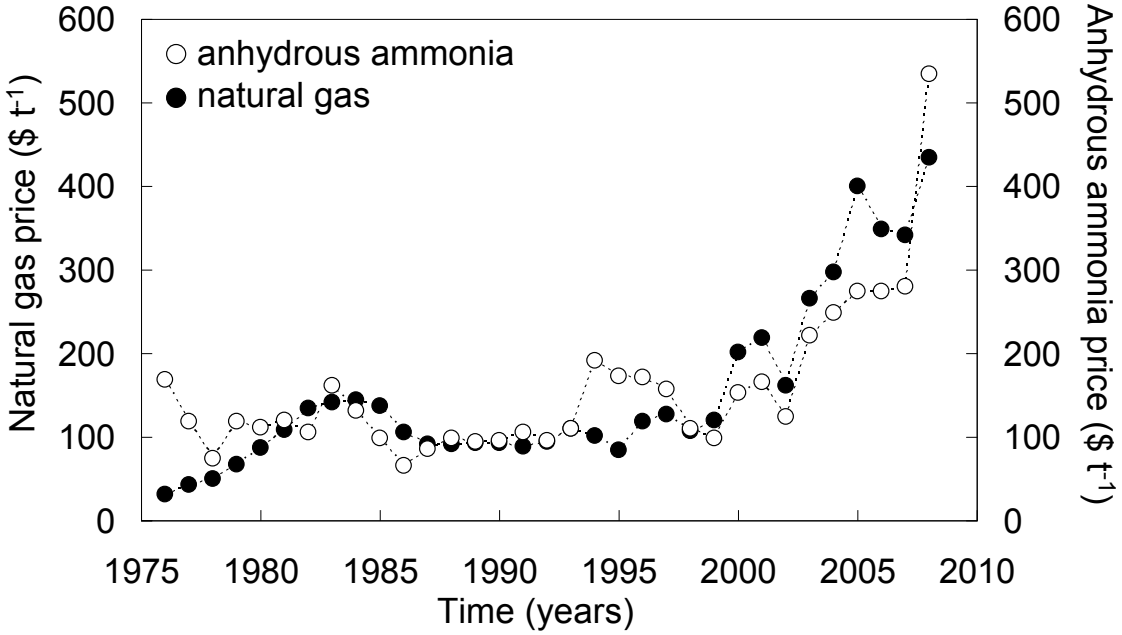

Figure 1.3 Historic prices for natural gas[25] and ammonia[26] in the U.S.

The highly efficient Haber-Bosch process[27] is a milestone of the chemical industry. However, due to consumption of about 1 t natural gas t^{-1} ammonia produced[24], production costs of NH_3 and thereby to some extent food or biofuel prices are tied closely to the volatility of the natural gas price, and also to existing or anticipated carbon dioxide emission regulations[4].

The synthesis of NH_3 at ambient pressure without fossil fuel and without sophisticated high-pressure and high-temperature technology is a long standing goal of the chemical industry[27, 28]. Achieving this may facilitate fertilizer production at smaller scales and in regions with relatively undeveloped infrastructure, e.g., in developing countries with significant population growth. A step into this direction is attempted with this work.

1.2 Ammonia synthesis without fossil fuel

1.2.1 Ammonia production at ambient pressure

Steam reforming with natural gas consumes approximately 84% of the total energy required for industrial NH_3 synthesis via the Haber-Bosch process. Thus, substituting this

reforming step with a sustainable hydrogen production process that employs renewable resources[29-35] is one conceivable route to sustainable NH_3 (see Sections 2.2.1, 2.3.1, and 6.2). Overall this would, however, lead inherently to a multi-step NH_3 production requiring capital-intensive high pressure (the Haber-Bosch process) and high temperature equipment (potentially for H_2 generation and the Haber-Bosch process).

Alternatively, the NH_3 synthesis at ambient pressure investigated by others receives vital current interest[28, 36-39]: Electrochemical nitrogen reduction[37, 40] may be employed for a fuel cell that is converting N_2 and H_2 into NH_3[41, 42] or to produce NH_3 with an ion conducting electrolyte cell that cleaves N_2 and H_2O[36, 37]. Also, substantial yields of NH_3 have been realized by mimicking enzymatic catalysis with transition metal complexes that react N_2 with acids or H_2 in the liquid phase[28, 38, 39, 43].

Although highly promising, these approaches have not yet reached maturity. At present, reliance on electricity generated from the current fossil fuel mix and the required novel electrolyte and electrode materials to increase NH_3 formation rates[36] are drawbacks of the electrochemical NH_3 synthesis. The major obstacle of the biomimetic approach is the external reducing equivalent (mostly a sacrificial alkali metal or pH adjustment) necessary for (re)generating the dinitrogen complex from a high oxidation state halide complex[28, 38, 39].

1.2.2 Solar thermochemical ammonia production

This work pursues an alternative route that is converting air, water, and direct sunlight via a solar thermochemical cycle of inorganic reactions into ammonia[44, 45]. Figure 1.4 contrasts the fundamental process concept with the seminal solar thermochemical H_2 production from H_2O[32-34]. The primary objectives of a solar thermochemical NH_3 production process can be summarized with:

- Air is the essentially inexhaustible nitrogen-feedstock (air separation required).
- Water is the only hydrogen-feedstock (cleaved during the NH_3 formation or separately).
- The reductive cleavage of N_2 is conducted separately from the nitrogen protonation reaction that is yielding NH_3. This allows controlling reaction equlibria via temperature adjustment and reactant (in lieu of a catalyst, see Section 1.3.3) composition.
- The process is conducted near 1 bar and involves at least one endothermic reaction step (e.g., oxide reduction) that is supplying the reducing equivalents of the N_2 and H_2O reductions (at least partly, complemented by a sufficient chemical reducing agent) [46] in form of solar energy concentrated to high-temperature heat[47-50].

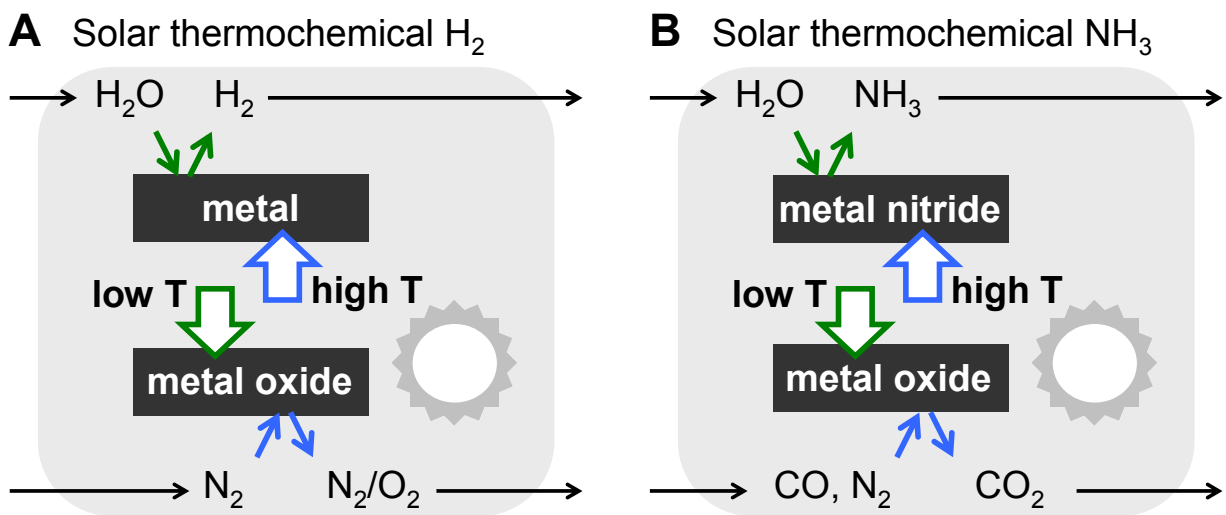

Figure 1.4 Conceptual solar thermochemical (A) H_2 or (B) NH_3 production (T marks temperature). N_2 is a purge gas in the H_2 production cycle and a reactant in the NH_3 production cycle. CO is one possible reducing agent which is required for most metals that are able to reductively cleave N_2 to form a metal nitride.

Relative to photovoltaic/photocatalytic processes (see Section 6.2) solar thermochemical processes utilize solar energy directly in form of heat. Ideally, this avoids energy conversion efficiency losses due to intermediate conversion of solar energy to mechanical/electrical energy - before it is eventually stored in the chemical bonds of the process products[51].

1.3 Scope of the dissertation

1.3.1 Choice of the reactive material

To guide the reactant choice, the fundamental work that started in the 19th century to thermochemically synthesize NH_3, is summarized in Chapter 2, and provides a thermochemical rationale for screening promising reactants. Recently, solar thermochemical synthesis of NH_3 from metal nitrides and steam was demonstrated successfully via an aluminum nitride/oxide reaction cycle[44, 48, 49]. Steam hydrolysis of AlN yielded between 950-1200°C and 5-120 min 68-95 mol% of the lattice nitrogen with 65-88 mol% recovered as NH_3[49]. Substantial carbothermal reduction of Al_2O_3 and formation of AlN[52] was demonstrated in the range of 1750-2000°C[44] using various solid carbon-based reducing agents[48].

Based on this seminal work, this dissertation addresses three major characteristics of the solar thermochemical NH_3 synthesis to potentially increase the technical feasibility and economic viability of this concept. Major aims are:

- ***Low endothermic heat requirement*** - Thermodynamically stable metal oxides require large amounts of heat for their reduction (see Chapter 2 and Section 5.3.1). Supplying this energy requires presumably significant capital investment for building solar concentrators and reactors (see Section 1.4.3 and Chapter 7). Due to the relative low temperature of the exothermic NH_3 formation, possible heat integration is limited, decreasing the net-efficiency of the overall process.
- ***Reaction temperatures below 1500°C*** - Containing temperatures above 1750°C may be difficult in an industrial scale furnace. This is expected to increase materials and maintenance costs[53-55] and likely decreases the overall energy conversion efficiency[53, 56, 57].

- ***Gaseous reducing agent*** - A solid carbonaceous reactant requires solids processing steps such as energy-intensive milling and in-process movement of solids[58, 59].

1.3.2 Hypothesis: Transition metal nitrides for the reactive ammonia synthesis

Based on weaker metal-oxygen and metal-nitrogen bonding, transition metal nitrides, such as those of molybdenum or manganese, can be formed from their oxides at lower temperatures, with less heat and with gaseous reducing agents. The formation of ammonia from transition metal nitrides and water has, however, received little attention (see Chapter 2).

Therefore, the synthesis of ammonia from heterogeneous reactions of binary transition metal nitrides with water or water-derived hydrogen sources is hypothesized and assessed here.

1.3.3 Separate two-step reduction and protonation of N_2 with H_2O to NH_3

To outline the scope of this effort, Figure 1.5 contrasts the NH_3 formation via heterogeneous catalysis[1, 27, 60-62] with the proposed reactive NH_3 synthesis.

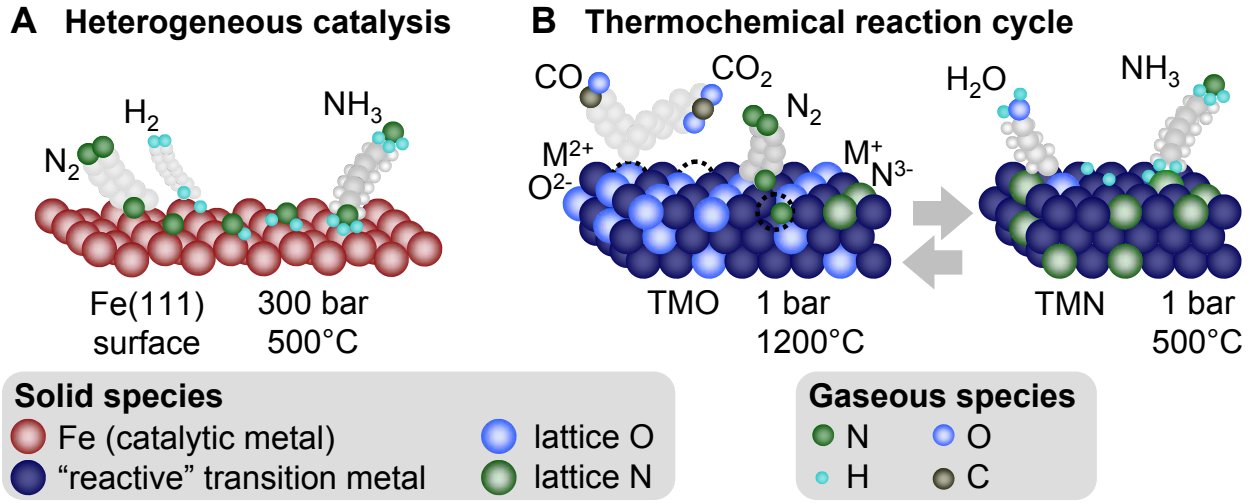

Figure 1.5 Heterogeneous catalysis versus reactive NH_3 synthesis. TMO) transition metal oxide, TMN) transition metal nitride, M) metal, dotted circle) lattice vacancy.

Heterogeneous catalysis forms NH_3 exothermically in equilibrium with its synthesis gas. From a thermodynamic perspective described by the Le Chatelier's principle, this results in

favored NH_3 formation at low temperatures, T, (counteracting the liberated reaction heat) and high pressures, p, (counteracting a decreased number of gas molecules for a given reaction chamber volume). To achieve significant NH_3 yields (e.g., ideally 24 mol% at 284 bar and 400-600°C, Aspen Plus Ammonia Model), the T-p conditions used in practice are a compromise between thermodynamics and kinetics (favoring high T). This demonstrates that the development of an optimized catalyst may moderate T-p requirements[63, 64]. However, the Fe-based catalyst developed by Alwin Mittasch in the first half of the last century is still in use in essentially all industrial plants today[1].

To enable the formation of NH_3 near 1 bar, the proposed reactive NH_3 synthesis separates the dinitrogen cleavage from its protonation to NH_3 into two separate reactions, whereby, the formation of NH_3 from the lattice nitrogen of a reactive transition metal nitride (TMN) and a hydrogen source (e.g., water) is conducted without establishing the equilibrium between NH_3 and its N_2/H_2 decomposition products (i.e., in a reactor open to mass exchange).

With regard to the reactive material: The transition from catalysts, e.g., Fe or Ru[27, 60, 62] to TMN reactants is fairly smooth (see Chapter 2). The reaction rate-determining step of the high-pressure catalysis is the dissociative chemisorption of N_2. The catalyst accomplishes this step via cleavage of the N_2 triple bond with formation of weaker metal-nitrogen bonds on the catalyst surface. These bonds are weak enough to allow formation of NH_3 from chemisorbed N and H species (Figure 1.5) at 400-600°C (providing the remainder of the required activation energy) but too week to form stable metal nitrides at ambient pressure.

Increasing the metal-nitrogen bonding energy leads to possible TMN reactants such as Mo_2N (in fact Mo is also sought as catalyst or catalyst constituent[63-67]) which form nitrides that are thermodynamically stable at 1 bar (and relative broad temperature ranges). The related

transition metal oxides (TMO) formed upon hydrolysis are weak, compared, e.g., to Al_2O_3 (see Section 1.3.1). These materials will be focused on in the present work.

Increasing the metal-nitrogen bonding energy significantly yields mainly ionic bonds between metal cations and N^{3-} (e.g., the nitrides formed by the alkaline earth metals). These materials form highly (ionic) oxides that are difficult to reduce thermochemically and that yield undesirable large amounts of heat during the NH_3 formation (see Sections 1.3.1 and 5.3.1).

1.3.4 Dissertation overview

To assess the hypothesized utility of transition metal nitrides for the reactive synthesis of ammonia from water (or water-derived hydrogen sources) and diatomic nitrogen at ambient pressure, reactant requirements will be defined and a thermochemical rationale intended to aid the choice of the reactant will be presented in Chapter 2. Chapter 3-7 assess the feasibility of a nitride hydrolysis-based ammonia synthesis from a chemical, technical and economical perspective. Attention will be given to trends observed in the reaction chemistry of various metal nitrides. As an outlook, Chapter 8 will assess the possibility of separating the water cleavage from the ammonia formation by studying the reaction of three metal nitrides with hydrogen.

The Chapters are arranged as follows:

Chapter 2

After providing a broad overview of the experimental and computational tools employed, Chapter 2[45] presents a thermochemical rationale for choosing a reactive metal.

Previous work towards a nitride-based reactive NH_3 synthesis will be reviewed along with discussions as to the viability of the proposed concept in comparison to the Haber-Bosch process combined with solar thermochemical H_2 production. Based on a quantified trade-off between the yield of the N_2 reduction and protonation versus the undesirably high

thermodynamic stability of metal oxides, two approaches to select a nitride-reactant will be outlined. TMN reactants may realize a compromise characterized with moderate nitride and NH_3 yields on one hand, and relatively moderate conditions of the oxide reduction on the other hand ("approach one"). For this purpose the utility of metals from the chromium group or manganese respectively will be assessed in the following Chapters. Alternatively ("approach two"), combining[34] a transition metal with a metal that forms mainly ionic metal-nitrogen bonds may be employed to design an optimized reactive material based on the desirable thermochemical properties of two metals.

Chapter 3

Intended as preliminary feasibility studies outlining the potentials and drawbacks of transition metal reactants, converting a TMO with concentrated solar radiation and a gaseous reducing agent below 1500°C into a TMN will be demonstrated experimentally using a Fresnel lens-based solar furnace[50].

The Chapter will outline the central role of the hypothesis guiding this dissertation - NH_3 synthesis via heterogeneous reactions of a TMN and water or water-derived hydrogen sources (see Section 1.3.2). Many TMN do not liberate significant amounts of NH_3 at moderate temperatures, including chromium, as shown here.

Chapter 4

The feasibility of "approach two" (see above) will be assessed experimentally with mixed MgO/TMO (Fe_2O_3 or Cr_2O_3) reactants.

The reduction of N_2 with Mg in reducing environments was unsuccessful (with the employed experimental conditions) although the presence of the transition metal, as hypothesized, appears to aid the reduction of MgO. To make best use of the obtained data, the

Chapter presents the experimental results with focus on the solar thermochemical formation of magnesium chromite and ferrite (the spinel-type materials discussed in Chapter 2) with applications as refractory or catalytic materials. The remainder of the dissertation focuses on "approach one" (see above).

Chapter 5

A reaction mechanism of the nitride hydrolysis is proposed and studied experimentally by steam hydrolysis of the nitrides of Mg, Al, Ca, Cr, Mn, Zn, or Mo at 1 bar and 200-1000°C. To assess the rate-limiting reaction step, the data is described by shrinking-core models and an Arrhenius-type temperature dependence of the rate constants.

Based on the partial nitrogen charge, the nitride ionicity was correlated with the apparent diffusion constants of the nitride hydrolysis suggesting that the reaction kinetics are governed to some extent by the volumetric concentration of active lattice nitrogen or ion vacancies respectively (Figure 1.5). This suggests the utility of the ionicity and first principle computations when developing an atomic-scale understanding of the solid-state reaction mechanism and for controlling the bonding nature of a prospective optimized TMN reactant.

Chapter 6

From the TMN reactants that are studied in Chapter 5, Mo_2N showed relatively promising hydrolysis kinetics and NH_3 yields and the non-stoichiometric nitrides of Mn liberated desirably large quantities of the lattice nitrogen at relatively moderate temperatures. Chapter 6 studies the N_2 reduction with Mo or Mn respectively.

The experimental work presented employs metals (instead of TMO, see Section 6.2 and Appendix E) to simplify the analysis of the fairly complex TMO-TMN conversion (see Figure 1.5). A correlation of the apparent diffusion constants with the interstitial volume of the nitride

lattice will be shown and doping of the TMN with transition metals to possibly control the TMN formation equilibrium will be addressed.

Chapter 7

To complement the preceding feasibility studies of a TMN reactant, a mass and energy balance-based thermodynamic and economic analysis of a solar thermochemical NH_3 production cycle employing Mo as reactant will be provided.

The conditions for this process to compete economically with the current industrial NH_3 synthesis will be summarized. The details of this analysis - conducted in collaboration with the Department of Agricultural Economics at Kansas State University - are presented elsewhere[46].

Chapter 8

To outline one possible alternative to water as hydrogen source, use of an alternative hydrogen source leads to additional processes required to generate the alternative reactant from H_2O. This would undesirably increase the overall process complexity. However, formation of a TMO and the required energy-intensive oxide reduction step would be avoided inherently.

Employing H_2 as the hydrogen source would alleviate the constraint of introducing a highly electronegative reactant (e.g., O or Cl) into the reactant. This avoids the formation of a TMO and thereby the need for a chemical reducing agent. The presented experimental studies employing the nitrides of Mn (and Ca or Sr for comparison) are intended to characterize the reaction kinetics and reaction products and will identify conditions that may enable this concept.

Chapter 9

The findings presented in Chapters 2-8 are summarized in the abstract and conclusion of each Chapter. The conclusion and outlook in Chapter 10 provides a summary of the major findings of this work at an overview-level. Path forward recommendations will be given.

1.4 Major experimental and computational tools

This final section of the introductive chapter presents an overview of the analytical and computational tools that are most fundamental for the generation of the data discussed in this work. A detailed description of these tools would exceed the scope of this section and is available in the cited literature.

1.4.1 Free energy screening of metal nitrides

A simplified theoretical approach based on the computation of free energies of a given reaction or the chemical equilibrium of a selected reaction system is employed throughout this work to guide the materials choice.

Briefly, the free energy of a given reaction as a function of temperature ($\Delta g_{r,T}$ in J mol^{-1}) and the related dimensionless equilibrium constant (K_T) are computed at atmospheric pressure from free energy of formation data ($g_{f,T}$ in J mol^{-1}) available in the literature[68, 69]. With K_T at hand, the equilibrium conversion of a chemical species is then determined with the elemental mol balances of a given reaction system, that are solved at steady-state[70, 71] with MathCad 13.

To demonstrate this approach, the oxidation of CO with the lattice oxygen of Mo(IV) yielding the metal and CO_2 will be considered:

(1.1) $$MoO_2 + 2CO \leftrightarrow Mo + 2CO_2$$

In a closed system at thermochemical equilibrium, $\Delta g_{r,T}$ is given with (compare Section 2.4.1):

(1.2) $$\Delta g_{r,T} = g_{f,T,Mo} + 2g_{f,T,CO_2} - \left(g_{f,T,MoO_2} + 2g_{f,T,CO}\right)$$

Assuming ideal gases and ideal condensed phases yields (compare Section 2.4.2)[70]:

(1.3) $$K_T = \exp\left(\frac{-\Delta g_{r,T}}{RT}\right) = \frac{n_{CO_2}^2}{n_{CO}^2}$$

where n are the moles of the subscript chemical species and R is the gas constant in J mol^{-1} K^{-1}. This relation allows determining the molar system composition by solving the mol balances of Mo, O, and C at steady-state (where 0 marks the reactants present before reaching equilibrium and t represents the course of the reaction, i.e., time):

$$(1.4) \quad \frac{dn_{Mo}}{dt} = n^0_{MoO_2} - \left(n_{MoO_2} + n_{Mo}\right) = 0$$

$$(1.5) \quad \frac{dn_O}{dt} = 2n^0_{MoO_2} + n^0_{CO} - \left(2n_{MoO_2} + n_{CO} + 2n_{CO_2}\right) = 0$$

$$(1.6) \quad \frac{dn_C}{dt} = n^0_{CO} - \left(n_{CO} + n_{CO_2}\right) = 0$$

Algebraic stipulations yield the molar equilibrium composition with:

$$(1.7) \quad n_{CO_2} = \frac{2K_T - 2K_T^{1/2}}{K_T - 1} = 2n_{Mo}$$

$$(1.8) \quad n_{MoO_2} = n^0_{MoO_2} - 1/2(n_{CO_2})$$

$$(1.9) \quad n_{CO} = n^0_{CO} - n_{CO_2}$$

The utility of this approach is limited by the availability of thermochemical data and the choice of the reaction system and may be improved by the use of chemical equilibrium software such as STANJAN or other[44] in the future.

1.4.2 Kinetic Analysis

The diffusion coefficient, D, of reaction participants in the solid state (compare Fig. 1.5) is used throughout the presented work to characterize reaction kinetics and to indicate trends displayed by the tested TMN reactants. In general, D characterizes the correlation of the rate transfer of a diffusing material across a cross-section of the solid reactant and the concentration gradient of the diffusing species in the direction of the diffusion[72, 73]:

$$(1.10) \quad \partial c_{x,t} / \partial t = \nabla^2 \left(D_{c,x} c_{x,t}\right)$$

where the subscripts mark possible dependence on position (x), time (t), or concentration (c) respectively.

As starting point, D will be estimated in this work from kinetic reaction data represented with shrinking core models of spherical solid particles with constant size (Figure 1.6).

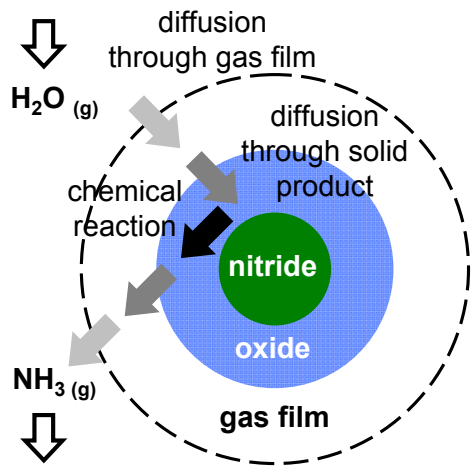

Figure 1.6 Schematic metal nitride particle reacting with water to an oxide and ammonia.

The applied procedure is as follows: The obtained kinetics data (see Section 1.4.4) are used to determine a reaction yield as function of time (X_t), e.g., the yield of NH_3 for the process shown in Figure 1.6. The data are represented with shrinking core models that model a reaction yield Z_t based on a fitted specific rate constant of a reaction process that involves a limiting gas phase diffusion step, solid state diffusion step, or chemical reaction respectively. The derivation of these models is available in the literature[72]. The coefficient of determination (R^2):

$$(1.11)\quad R^2 = 1 - \sum_t (X_t - Z_t)^2 \left(\sum_t (X_t - \overline{X})^2 \right)^{-1}$$

(where $\overline{X}$ is the arithmetic average of the observed data) is used to determine the most appropriate model. Error propagation is employed to estimate the analytical uncertainty of the experimental setup assuming uncorrelated variables.

If the solid-state diffusion model represents the data well (R^2 favorably > 0.9) D is estimated based on the specific rate constants (k_s in s^{-1}) obtained from the kinetic data[72]:

$$(1.12)\quad D = k_s \frac{c_p}{c_g} \frac{d_p^2}{24b}$$

where c_p in mol m^{-3} is the (presumably constant) molar concentration of the solid reactant, c_g in mol m^{-3} is the molar gas concentration at the solid-gas interface, d_p in m is the average particle diameter, and b is the molar ratio of reacted solid per reacted gas.

Obviously, this approach does not observe or proof an actual solid state diffusion process and rather provides "apparent" diffusion constants that evidence such a process step. Usually the diffusion coefficient of a chemical species is followed with isotopic tracer techniques. The presented data will show that such analytical techniques may be valuable tools to assess the nature of the diffusion and to determine the diffusing chemical species in the future.

1.4.3 Solar furnace

Concentration of solar radiation (see Section 1.2.2) was achieved with a Fresnel lens (Figure 1.7). Useful information as to the concentration of solar energy with Fresnel lenses[74-76], light absorption efficiency[53, 56, 77], or heat transfer for solar furnaces[78, 79] is available elsewhere.

Melting experiments with a Ni-alloy, Fe (Figure 1.8) or Cr (no melting observed, melting point 1900°C) powder respectively estimated the maximum temperature achievable with the 7.07 cm^2 large focal point with approximately 1600°C (at an incident energy density of approximately 0.85 kW m^{-2}, see Section 3.3.1). The fused silica flow-through reactor (softening point near 1683°C) was not impacted by heating. To decrease the furnace temperature the reactor was moved perpendicular to the lens slightly out-of-focus. Temperatures below about 1350°C were confirmed with a thermocouple before the experiment.

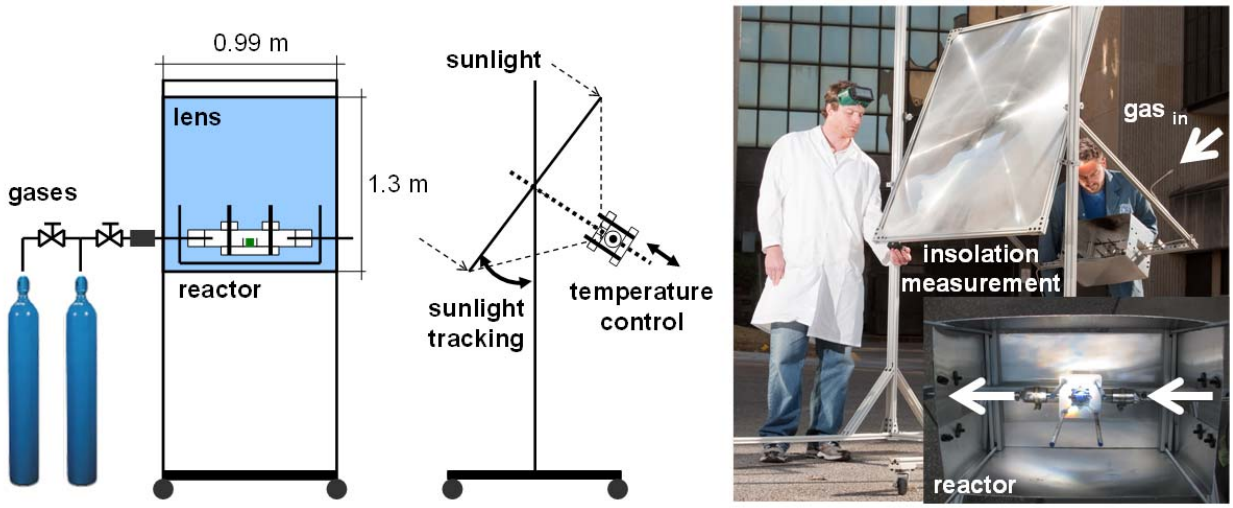

Figure 1.7 Solar furnace setup (the location of the reactant is marked with a green square). Technical information is provided in Section 3.3.1.

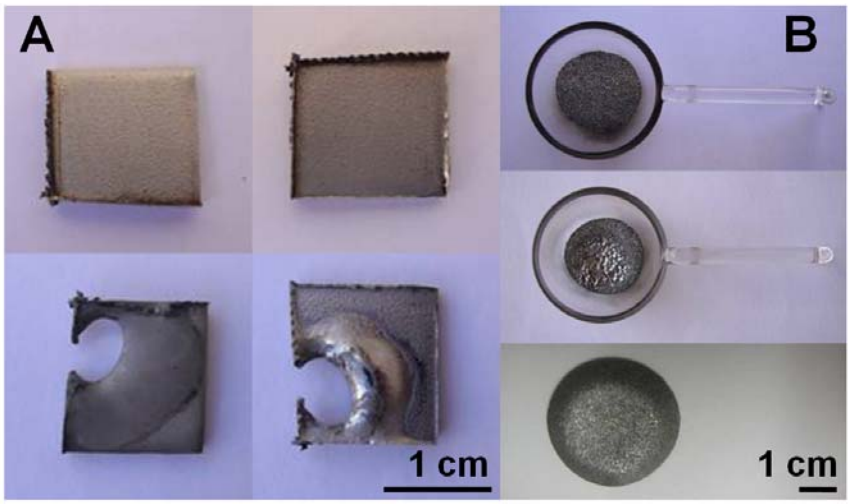

Figure 1.8 Estimation of the maximum furnace temperature: Melting (A) Hastelloy C-276 (melting point, T_m, 1320-1370°C, 10 min), or (B) Fe (99.8 % pure, -325 mesh, 1535°C T_m, 1 min, top row: before heating, middle and bottom: after heating) under He blanket.

1.4.4 Analysis of reaction yields and nitrogen mass balance

1.4.4.1 Lattice nitrogen analysis

X-ray diffraction (XRD)[66, 80-82] and X-ray dispersion (EDS)[83-85] are standard solid-state analytical techniques[86] that are employed in the following for phase identification and to quantify the lattice nitrogen before or after the reaction respectively.

XRD utilizes the constructively interfering X-ray waves that are scattered from the electrons of a solid that is radiated with an X-ray source. The scattered photons are used to generate a crystal lattice-specific diffraction pattern (see Bragg's law). Powder X-ray diffraction is employed in this work for rapid and quantitative phase identification of multi-component samples by comparison of the generated diffraction pattern to a standard (Cambridge Structural Database, CSD). The analysis is non-destructive and does not require large samples (5-10 mm^3)[86] or extensive sample preparation, and has a detection limit of about 0.1-1.0 wt%. Identification of new phases, perhaps ternary nitrides or oxynitrides[87], is complicated by the fact that in powder diffraction studies much information is lost due to the projection of the 3-dimnesional reciprocal lattice space studied by single-crystal XRD onto a 1-dimensional axis. In the present work, powder XRD suffices the purpose and was complemented by EDS to confirm changes in the powder composition semi-qualitatively and to visualize the co-location of nitrogen and a metal(s) at, or a few μm below, the sample surface[86].

Elemental analysis via EDS relies on the material-specific discrete X-ray fluorescence of a material that is irradiated with X-rays. The photons that are emitted from the sample ionize atoms of the detector that is generating a voltage signal proportional to the incident photon energy. The non-destructive analysis has generally a detection limited near 0.1-0.5 wt%[86] and the X-ray beam can be focused on samples > 1-5 μm^2 in size[86]. However, for the analysis of samples containing large fractions of nitrogen and/or oxygen EDS is at best semi-quantitative due to the 133 eV difference between the 392 eV N $K\alpha_1$ and 525 eV O $K\alpha_1$ X-ray emission wavelengths[88], that is, near the ideal 125 eV full width at half maximum resolution of the utilized silicon drift detector[89]. Increased resolution may be obtained by applying alternatively wavelength dispersive X-ray spectroscopy or X-ray photoelectron spectroscopy.

1.4.4.2 Ammonia analysis

The yield of NH_3 was determined with an NH_3 selective electrode with a lower detection limit of 10^{-6} M NH_3 in aqueous solution, an ideal (see manual[90]) reproducibility up to ± 2%, and no interference from ions or dissolved species[90]. Principally, the electrode contains an internal aqueous 0.1 M NH_4Cl filling solution that is separated from the sample by a hydrophobic gas-permeable membrane. If the pH of the sample is adjusted to > 11, essentially all NH_4^+ species are converted to NH_3 gas that diffuses through the membrane to equilibrate the partial pressure of NH_3 on both sides. This results in formation of hydroxyl ions in the filling solution proportional to the NH_3 concentration in the sample. The generated gradient of the hydroxyl ion leads to an electric potential difference (Nernst potential) that is used to quantify NH_3 solute in the sample. A typical calibration curve is given in Appendix B. Complexation of NH_3 with metallic ions may decrease detectable NH_3 concentrations if the metal ions do not form hydroxide complexes (see Pourbaix diagrams) or precipitates. Colored precipitates were observed only when hydrolyzing molybdenum nitride at 1000°C (see Chapter 5). Possibly formed ammonium molybdate decomposes on treatment with alkalis (NaOH during the NH_3 analysis)[91].

1.5 References

1 G. Ertl, Reactions at surfaces: From atoms to complexity (Nobel lecture), Angewandte Chemie-International Edition, 47 (2008) 3524-3535.

2 M. Dunikowska, L. Turko, Fritz Haber: The damned scientist, Angewandte Chemie-International Edition, 50 (2011) 10050-10062.

3 P.L. Louis, Feedstock and energy sources for ammonia production, International Fertilizer Industry Association, with some assistance from CEDIGAZ, France, Available online at: www.fertilizer.org/ifacontent/download/5571/88112/.../1/.../76.pdf (retrieved April 2, 2012).

4 W.-Y. Huang, Impact of rising natural gas prices on U.S. ammonia supply / WRS-0702 / A report from the Economic Research Service, 2007.

[5] V. Smil, Nitrogen and food production: Proteins for human diets, Ambio, 31 (2002) 126-131.

[6] V. Smil, Detonator of the population explosion, Nature, 400 (1999) 415-415.

[7] D.A. Kramer, Nitrogen (fixed) - Ammonia, U.S. Geological Survey, Mineral Commodity Summaries, (2003) 118-119.

[8] I. Rafiqul, C. Weber, B. Lehmann, A. Voss, Energy efficiency improvements in ammonia production - perspectives and uncertainties, Energy, 30 (2005) 2487-2504.

[9] Production: Growth in most regions - Although output increased, rise was probably less than most nations had hoped, Chemical & Engineering News, 83 (2005) 67-76.

[10] W. Steffen, A. Sanderson, P. Tyson, J. Jäger, P. Matson, B. Moore III, F. Oldfield, K. Richardson, J. Schellnhuber, B.L. Turner II, R. Wasson, Global change and the earth system, A planet under pressure, IGBP Secretariat, Royal Swedish Academy of Sciences, ISBN 91-631-5380-7, Available online at: http://www.igbp.net/download/18.1b8ae2051-2db692f2a680007761/IGBP_ExecSummary_eng.pdf (retrieved April 2, 2012).

[11] V. Smil, Enriching the Earth: Fritz Haber, Carl Bosch, and the transformation of world food production, The MIT Press, Boston, MA, 2001.

[12] http://minerals.usgs.gov/ds/2005/140/nitrogen-use.xls (retrieved April 2, 2012).

[13] How to feed the world in 2050, Report of the Food and Agriculture Organization of the United Nations (FAO), Available online at: http://www.fao.org/fileadmin/templates/wsfs-/docs/expert_paper/How_to_Feed_the_World_in_2050.pdf (retrieved April 2, 2012).

[14] R.M. Nault, Basic research needs for solar energy utilization, Report on the Basic Energy Sciences Workshop on Solar Energy Utilization, Argonne National Laboratory, April 18-21, 2005.

[15] C.A. Garcia, A. Fuentes, A. Hennecke, E. Riegelhaupt, F. Manzini, O. Masera, Life-cycle greenhouse gas emissions and energy balances of sugarcane ethanol production in Mexico, Applied Energy, 88 (2011) 2088-2097.

[16] M. Bystricky, T. Knödlseder, G. Weber-Blaschke, M. Faulstich, Comparing environmental impacts of electricity, heat and fuel from energy crops: Evaluating biogas utilization pathways by the basket of benefit methodology, Engineering in Life Sciences, 10 (2010) 570-576.

[17] I. Lewandowski, U. Schmidt, Nitrogen, energy and land use efficiencies of miscanthus, reed canary grass and triticale as determined by the boundary line approach, Agriculture Ecosystems & Environment, 112 (2006) 335-346.

[18] R. Schnepf, B.D. Yacobucci, Renewable Fuel Standard (RFS): Overview and issues, Congressional Research Service, (2010).

[19] C.H. Christensen, T. Johannessen, R.Z. Sørensen, J.K. Nørskov, Towards an ammonia-mediated hydrogen economy?, Catalysis Today, 111 (2006) 140-144.

[20] A.J. Churchard, E. Banach, A. Borgschulte, R. Caputo, J.-C. Chen, D.C. Clary, K.J. Fijalkowski, H. Geerlings, R.V. Genova, W. Grochala, T. Jaroń, J.C. Juanes-Marcos, B. Kasemo, G.-J. Kroes, I. Ljubić, N. Naujoks, J.K. Nørskov, R.A. Olsen, F. Pendolino, A. Remhof, L. Románszki, A. Tekin, T. Vegge, M. Zäch, A. Züttel, A multifaceted approach to hydrogen storage, Physical Chemistry Chemical Physics, 13 (2011) 16955-16972.

[21] P. Wang, X.D. Kang, Hydrogen-rich boron-containing materials for hydrogen storage, Dalton Transactions, (2008) 5400-5413.

[22] A.J. Reiter, S.C. Kong, Combustion and emissions characteristics of compression-ignition engine using dual ammonia-diesel fuel, Fuel, 90 (2011) 87-97.

[23] A.J. Reiter, S.-C. Kong, Demonstration of compression-ignition engine combustion using ammonia in reducing greenhouse gas emissions, Energy & Fuels, 22 (2008) 2963-2971.

[24] Aspen Plus Ammonia Model, Aspen Technology, Inc., Version Number V7.0.

[25] http://www.eia.gov/dnav/ng/hist/n9190us3m.htm (retrieved April 2, 2012).

[26] C.A. DiFrancesco, D.A. Kramer, L.E. Apodaca, Nitrogen (fixed) - Ammonia statistics, U.S. Geological survey, Available online at: http://minerals.usgs.gov/ds/2005/140/ds140-nitro.pdf (retrieved April 2, 2012).

[27] A. Hellman, E.J. Baerends, M. Biczysko, T. Bligaard, C.H. Christensen, D.C. Clary, S. Dahl, R. van Harrevelt, K. Honkala, H. Jonsson, G.J. Kroes, M. Luppi, U. Manthe, J.K. Nørskov, R.A. Olsen, J. Rossmeisl, E. Skúlason, C.S. Tautermann, A.J.C. Varandas, J.K. Vincent, Predicting catalysis: Understanding ammonia synthesis from first-principles calculations, Journal of Physical Chemistry B, 110 (2006) 17719-17735.

[28] M.D. Fryzuk, Side-on end-on bound dinitrogen: An activated bonding mode that facilitates functionalizing molecular nitrogen, Accounts of Chemical Research, 42 (2009) 127-133.

[29] J.J.H. Pijpers, M.T. Winkler, Y. Surendranath, T. Buonassisi, D.G. Nocera, Light-induced water oxidation at silicon electrodes functionalized with a cobalt oxygen-evolving catalyst, Proceedings of the National Academy of Sciences of the United States of America, 108 (2011) 10056-10061.

[30] O. Khaselev, J.A. Turner, A monolithic photovoltaic-photoelectrochemical device for hydrogen production via water splitting, Science, 280 (1998) 425-427.

[31] M. Grätzel, Mesoscopic solar cells for electricity and hydrogen production from sunlight, Chemistry Letters, 34 (2005) 8-13.

[32] J.R. Scheffe, J.H. Li, A.W. Weimer, A spinel ferrite/hercynite water-splitting redox cycle, International Journal of Hydrogen Energy, 35 (2010) 3333-3340.

[33] W.C. Chueh, C. Falter, M. Abbott, D. Scipio, P. Furler, S.M. Haile, A. Steinfeld, High-flux solar-driven thermochemical dissociation of CO_2 and H_2O using nonstoichiometric ceria, Science, 330 (2010) 1797-1801.

[34] J.E. Miller, M.D. Allendorf, R.B. Diver, L.R. Evans, N.P. Siegel, J.N. Stuecker, Metal oxide composites and structures for ultra-high temperature solar thermochemical cycles, Journal of Materials Science, 43 (2008) 4714-4728.

[35] A. Stamatiou, P.G. Loutzenhiser, A. Steinfeld, Solar syngas production from H_2O and CO_2 via two-step thermochemical cycles based on Zn/ZnO and FeO/Fe_3O_4 redox reactions: Kinetic analysis, Energy & Fuels, 24 (2010) 2716-2722.

[36] I.A. Amar, R. Lan, C.T.G. Petit, S. Tao, Solid-state electrochemical synthesis of ammonia: a review, Journal of Solid State Electrochemistry, 15 (2011) 1845-1860.

[37] I. Valov, B. Luerssen, E. Mutoro, L. Gregoratti, R.A. De Souza, T. Bredow, S. Günther, A. Barinov, P. Dudin, M. Martin, J. Janek, Electrochemical activation of molecular nitrogen at the Ir/YSZ interface, Physical Chemistry Chemical Physics, 13 (2011) 3394-3410.

[38] J.D. Gilbertson, N.K. Szymczak, D.R. Tyler, Reduction of N_2 to ammonia and hydrazine utilizing H_2 as the reductant, Journal of the American Chemical Society, 127 (2005) 10184-10185.

[39] D.J. Knobloch, E. Lobkovsky, P.J. Chirik, Dinitrogen cleavage and functionalization by carbon monoxide promoted by a hafnium complex, Nature Chemistry, 2 (2010) 30-35.

[40] D.-K. Lee, C.C. Fischer, I. Valov, J. Reinacher, A. Stork, M. Lerch, J. Janek, An EMF cell with a nitrogen solid electrolyte-on the transference of nitrogen ions in yttria-stabilized zirconia, Physical Chemistry Chemical Physics, 13 (2011) 1239-1242.

[41] M. Lerch, J. Janek, K.D. Becker, S. Berendts, H. Boysen, T. Bredow, R. Dronskowski, S.G. Ebbinghaus, M. Kilo, M.W. Lumey, M. Martin, C. Reimann, E. Schweda, I. Valov, H.D. Wiemhöfer, Oxide nitrides: From oxides to solids with mobile nitrogen ions, Progress in Solid State Chemistry, 37 (2009) 81-131.

[42] V. Kordali, G. Kyriacou, C. Lambrou, Electrochemical synthesis of ammonia at atmospheric pressure and low temperature in a solid polymer electrolyte cell, Chemical Communications, (2000) 1673-1674.

[43] M.M. Rodriguez, E. Bill, W.W. Brennessel, P.L. Holland, N_2 reduction and hydrogenation to ammonia by a molecular iron-potassium complex, Science, 334 (2011) 780-783.

[44] M.E. Gálvez, M. Halmann, A. Steinfeld, Ammonia production via a two-step Al_2O_3/AlN thermochemical cycle. 1. Thermodynamic, environmental, and economic analyses, Industrial & Engineering Chemistry Research, 46 (2007) 2042-2046.

[45] R. Michalsky, P.H. Pfromm, Thermodynamics of metal reactants for ammonia synthesis from steam, nitrogen and biomass at atmospheric pressure, AIChE Journal, http://onlinelibrary.wiley.com/doi/10.1002/aic.13717/pdf, (in press).

[46] R. Michalsky, B.J. Parman, V. Amanor-Boadu, P.H. Pfromm, Solar thermochemical production of ammonia from water, air and sunlight: thermodynamic and economic analyses, Energy 42 (2012) 251-260.

[47] M.E. Gálvez, A. Frei, F. Meier, A. Steinfeld, Production of AlN by carbothermal and methanothermal reduction of Al_2O_3 in a N_2 flow using concentrated thermal radiation, Industrial & Engineering Chemistry Research, 48 (2009) 528-533.

[48] M.E. Gálvez, I. Hischier, A. Frei, A. Steinfeld, Ammonia production via a two-step Al_2O_3/AlN thermochemical cycle. 3. Influence of the carbon reducing agent and cyclability, Industrial & Engineering Chemistry Research, 47 (2008) 2231-2237.

[49] M.E. Gálvez, A. Frei, M. Halmann, A. Steinfeld, Ammonia production via a two-step Al_2O_3/AlN thermochemical cycle. 2. Kinetic analysis, Industrial & Engineering Chemistry Research, 46 (2007) 2047-2053.

[50] R. Michalsky, P.H. Pfromm, Chromium as reactant for solar thermochemical synthesis of ammonia from steam, nitrogen, and biomass at atmospheric pressure, Solar Energy, 85 (2011) 2642-2654.

[51] R. Perret, Solar thermochemical hydrogen production research (STCH), Thermochemical cycle selection and investment priority, Sandia report SAND2011-3622, Sandia National Laboratories, (2011).

[52] J.P. Murray, A. Steinfeld, E.A. Fletcher, Metals, nitrides, and carbides via solar carbothermal reduction of metal-oxides, Energy, 20 (1995) 695-704.

[53] T. Kodama, High-temperature solar chemistry for converting solar heat to chemical fuels, Progress in Energy and Combustion Science, 29 (2003) 567-597.

[54] E.B. Maxted, Ammonia and the nitrides, J. & A. Churchill, London, 1921.

[55] V. Sauchelli, Fertilizer nitrogen its chemistry and technology, Reinhold Publishing Corporation, New York, 1964.

[56] A. Steinfeld, C. Larson, R. Palumbo, M. Foley, Thermodynamic analysis of the co-production of zinc and synthesis gas using solar process heat, Energy, 21 (1996) 205-222.

[57] A. Steinfeld, A.W. Weimer, Thermochemical production of fuels with concentrated solar energy, Optics Express, 18 (2010) A100-A111.

[58] J.P. Murray, E.A. Fletcher, Reaction of steam with cellulose in a fluidized-bed using concentrated sunlight, Energy, 19 (1994) 1083-1098.

[59] J. Lédé, Reaction temperature of solid particles undergoing an endothermal volatilization - Application to the fast pyrolysis of biomass, Biomass & Bioenergy, 7 (1994) 49-60.

[60] J.J. Mortensen, L.B. Hansen, B. Hammer, J.K. Nørskov, Nitrogen adsorption and dissociation on Fe(111), Journal of Catalysis, 182 (1999) 479-488.

[61] F. Bozso, G. Ertl, M. Grunze, M. Weiss, Interaction of nitrogen with iron surfaces .1. Fe(100) and Fe(111), Journal of Catalysis, 49 (1977) 18-41.

[62] G. Ertl, Primary steps in catalytic synthesis of ammonia, Journal of Vacuum Science & Technology a-Vacuum Surfaces and Films, 1 (1983) 1247-1253.

[63] C.J.H. Jacobsen, S. Dahl, B.S. Clausen, S. Bahn, A. Logadottir, J.K. Nørskov, Catalyst design by interpolation in the periodic table: Bimetallic ammonia synthesis catalysts, Journal of the American Chemical Society, 123 (2001) 8404-8405.

[64] C.J.H. Jacobsen, Novel class of ammonia synthesis catalysts, Chemical Communications, (2000) 1057-1058.

[65] D. McKay, J.S.J. Hargreaves, J.L. Rico, J.L. Rivera, X.L. Sun, The influence of phase and morphology of molybdenum nitrides on ammonia synthesis activity and reduction characteristics, Journal of Solid State Chemistry, 181 (2008) 325-333.

[66] A.G. Cairns, J.G. Gallagher, J.S.J. Hargreaves, D. McKay, J.L. Rico, K. Wilson, The effect of low levels of dopants upon the formation and properties of beta-phase molybdenum nitride, Journal of Solid State Chemistry, 183 (2010) 613-619.

[67] L. Volpe, M. Boudart, Ammonia-synthesis on molybdenum nitride, Journal of Physical Chemistry, 90 (1986) 4874-4877.

[68] I. Barin, O. Knacke, Thermochemical properties of inorganic substances, Springer-Verlag, Berlin Heidelberg New York, 1973.

[69] I. Barin, O. Knacke, O. Kubaschewski, Thermochemical properties of inorganic substances, Supplement, Springer-Verlag, Berlin Heidelberg New York, 1977.

[70] H. Scott Fogler, Elements of chemical reaction engineering, Prentice Hall PTR, Upper Saddle River, NJ, 2006.

[71] J.M. Prausnitz, R.N. Lichtenthaler, E. Gomes de Azevedo, Molecular thermodynamics of fluid-phase equilibria, Prentice Hall PTR, Upper Saddle River, NJ, 1999.

[72] O. Levenspiel, Chemical reaction engineering, Third Edition, Chapter 25 Fluid-particle reactions: Kinetics, John Wiley & Sons, New York, 1999.

[73] C.H. Bamford, C.F.H. Tipper, Comprehensive chemical kinetics, Vol. 22, Reactions in the Solid State (page 269), Elsevier Scientific Publishing Company, Amsterdam - Oxford - New York, 1980.

[74] C. Sierra, A.J. Vázquez, High solar energy concentration with a Fresnel lens, Journal of Materials Science, 40 (2005) 1339-1343.

[75] N. Yamada, T. Nishikawa, Evolutionary algorithm for optimization of nonimaging Fresnel lens geometry, Optics Express, 18 (2010) A126-A132.

[76] F. Duerr, Y. Meuret, H. Thienpont, Miniaturization of Fresnel lenses for solar concentration: a quantitative investigation, Applied Optics, 49 (2010) 2339-2346.

[77] A. Steinfeld, Solar thermochemical production of hydrogen - a review, Solar Energy, 78 (2005) 603-615.

[78] R. Müller, W. Lipiński, A. Steinfeld, Transient heat transfer in a directly-irradiated solar chemical reactor for the thermal dissociation of ZnO, Applied Thermal Engineering, 28 (2008) 524-531.

[79] S. Haussener, P. Coray, W. Lipiński, P. Wyss, A. Steinfeld, Tomography-based heat and mass transfer characterization of reticulate porous ceramics for high-temperature processing, Journal of Heat Transfer-Transactions of the ASME, 132 (2010).

[80] H.Q. Yang, H. Al-Brithen, E. Trifan, D.C. Ingram, A.R. Smith, Crystalline phase and orientation control of manganese nitride grown on MgO(001) by molecular beam epitaxy, Journal of Applied Physics, 91 (2002) 1053-1059.

[81] H.L. Cao, C.P. Luo, J.W. Liu, C.L. Wu, G.F. Zou, Formation of a nanostructured CrN layer on nitrided tool steel by low-temperature chromizing, Scripta Materialia, 58 (2008) 786-789.

[82] M. Čekada, M. Maček, D.K. Merl, P. Panjan, Properties of Cr(C,N) hard coatings deposited in Ar-C_2H_2-N_2 plasma, Thin Solid Films, 433 (2003) 174-179.

[83] J.L. Mo, M.H. Zhu, Tribological characterization of chromium nitride coating deposited by filtered cathodic vacuum arc, Applied Surface Science, 255 (2009) 7627-7634.

[84] J. Qi, L.H. Jiang, Q.A. Jiang, S.L. Wang, G.Q. Sun, Theoretical and experimental studies on the relationship between the structures of molybdenum nitrides and their catalytic activities toward the oxygen reduction reaction, Journal of Physical Chemistry C, 114 (2010) 18159-18166.

[85] W.S. Khan, C. Cao, Synthesis, growth mechanism and optical characterization of zinc nitride hollow structures, Journal of Crystal Growth, 312 (2010) 1838-1843.

[86] G. Markl, Minerale und Gesteine, Mineralogie - Petrologie - Geochemie, 2. verbesserte und erweiterte Auflage, Spektrum Akademischer Verlag, Würzburg, Germany, 2008.

[87] D.H. Gregory, Structural families in nitride chemistry, Journal of the Chemical Society-Dalton Transactions, (1999) 259-270.

[88] J.A. Bearden, X-Ray wavelengths, Reviews of Modern Physics, 39 (1967) 78-124.

[89] Oxford Instruments brochure: http://www.oxford-instruments.com/products/x-ray-micro-analysis/Documents/X-Max%20SDD%20brochure.pdf (retrieved April 2, 2012).

[90] Cole-Parmer, Ammonia gas-sensing electrode, Instruction Manual.

[91] P. Patnaik, Handbook of inorganic chemicals, ISBN 0-07-049439-8, McGraw-Hill, New York, 2003.

Chapter 2 - Thermodynamics of metal reactants for ammonia synthesis from steam, nitrogen and biomass at atmospheric pressure

2.1 Abstract

Due to an increasing world population, demand for ammonia as nitrogen fertilizer or energy carrier is expected to increase. The current industrial ammonia synthesis consumes about 5% of the global annual natural gas production causing significant CO_2 emissions. A conceptual solar thermochemical reaction cycle to produce NH_3 at near atmospheric pressure without natural gas is explored here and compared to solar thermochemical steam/air reforming to provide H_2 utilized in the Haber-Bosch process for NH_3 synthesis. Mapping of Gibbs free energy planes quantifies the trade-off between the yield of N_2 reduction via metal nitridation and NH_3 liberation via steam hydrolysis versus the temperatures required for reactant recovery from undesirably stable metal oxides. Equilibrium composition simulations suggest that reactants combining an ionic nitride-forming element (e.g., Mg or Ce) with a transition metal (e.g., $MgCr_2O_4$, $MgFe_2O_4$, or $MgMoO_4$) may enable the concept near 0.1 MPa (at maximum 64 mol% yield of Mg_3N_2 through nitridation of $MgFe_2O_4$ at 1300 K, and 72 mol% of the nitrogen in Mg_3N_2 as NH_3 during hydrolysis at 500 K).

2.2 Introduction

Agriculture is faced with an increasing demand for production due to a growing and developing world population[1]. The global average nitrogen demand for fertilization is about 2.6 to 2.9 kg nitrogen / year / capita and this demand is satisfied mainly by ammonia and ammonia-derived materials such as urea[1]. Additionally, the increasing demand for biofuels is expected to increase the strain on the global ammonia production capacity in the future. For instance, the

expanded Renewable Fuel Standard (RFS2) requires that in the U.S. the annual use of 3.4 x 10^7 m^3 of biofuel (e.g., from corn or cellulosic biomass) in 2008 is to be increased to about 1.4 x 10^8 m^3 in 2022[2].

Ammonia-based fertilizers play a crucial role to satisfy both the demands for food and biofuels. The chemical industry supplies the majority of fertilizers (mainly liquid NH_3, $(NH_2)_2CO$, NH_4NO_3, $(NH_4)_2SO_4$, K_2O, P_2O_5, and various mixtures of these materials) to agriculture. The Haber Bosch process introduced at industrial scale in 1913[1] synthesizes the vast majority of the 1.28 x 10^8 metric tons of the NH_3 produced globally (2001)[3] via catalytic synthesis of NH_3 from a stoichiometric mixture of N_2 and H_2 at 30 MPa and 700-900 K. This requires technologically sophisticated high pressure and high temperature operations that are capital intensive and dictate the need for large facilities producing at above 1000 t NH_3 / day. The process reaches ideally 22.7 mol% conversion of ½ N_2 to NH_3 (estimated via Gibbs free energy minimization, Aspen Plus V7.2). The overall process including H_2 production generates ca. 2.3 t of fossil-derived CO_2 per t of NH_3[4] and expends 2% of the world's energy budget[5] in form of natural gas (about 28-37 GJ/t NH_3 in North America[4, 6]). Steam-reforming of coal instead of using natural gas (a frequent practice in India and China) requires even more energy (about 48-166 GJ/t NH_3[4, 7]). This causes generation of 16.7 t CO_2 per t NH_3 produced[4]. Production costs of NH_3 (and thereby to some extent food or biofuel prices) are tied closely to the volatility of natural gas prices, and also to existing or anticipated CO_2 emission regulations.

Nitrogen fixation remains a challenge. The dependence on natural gas, the technically demanding process conditions, the CO_2 emissions, and the economy of scale all motivate continued interest in NH_3 synthesis. Potential use of NH_3 as a H_2 carrier molecule[8, 9], or as a way to store intermittent solar energy[10-12] could also be cited as motivation.

2.2.1 Alternatives to the current industrial NH_3 synthesis

Investigated as alternatives to the Haber-Bosch process, NH_3 synthesis at mild conditions in the liquid phase via transition metal coordination complexes[13] or electrochemical NH_3 synthesis[14, 15] have not yet reached maturity. Only modest conversions caused by a low conductivity in the working electrode[15] and significant amounts of electrical energy required are concerns for electrochemical NH_3 synthesis. NH_3 production from electrolysis of H_2O as attempted in the 1920s has been reported to consume ca. 90 GJ/t NH_3[16]. This approach would cause a substantial consumption of fossil fuels with the current energy mix to generate electricity (e.g., 49% or 81% of the total electricity in the U.S. or China respectively is generated via combustion of coal[17]). Solar energy for splitting H_2O to generate H_2[11, 12] for subsequent NH_3 synthesis via the Haber-Bosch reaction would alleviate the consumption of natural gas for fertilizer production (84% of the energy required for industrial NH_3 synthesis via the Haber-Bosch process is absorbed in steam reforming with natural gas to produce H_2[4]). The Haber-Bosch process itself and the associated challenges would remain. This approach is further discussed below (see Section 2.3.1).

From the various inorganic routes proposed in the chemical literature for NH_3 synthesis[18-21], few received greater attention than Frank and Caro who commercialized around 1910 a three-step process producing NH_3 via hydrolysis of calcium cyanamide (a salt like compound containing reduced nitrogen in form of CN_2^{2-} ions)[16, 19, 22]. To regenerate calcium cyanamide, calcium carbonate (formed during hydrolysis) is heated to form calcium oxide which is mixed and reacted with coke to yield calcium carbide (ca. 50 mol% at above 2100 K[23]). The carbide reacts at decreased temperatures with N_2 recovering calcium cyanamide. Consumption of coke and the technically demanding process temperatures established with an electric furnace

translated into an energy consumption of ca. 210 GJ/t NH_3[16] which rendered the process economically unattractive.

2.2.2 Thermochemical NH_3 synthesis from a metal nitride / oxide reaction cycle

Based on Serpek's process developed at the beginning of the last century[19-21], reactive NH_3 synthesis was demonstrated successfully via a two-step solar thermochemical cycle of aluminum nitride hydrolysis at around 1300 K and carbothermal reduction and nitridation of aluminum oxide in the range of 2023-2273 K[10, 24-26]. Similar to the calcium cyanamide cycle, this process forms NH_3 near 0.1 MPa without the need of a fossil H_2 source and in absence of a catalyst. High temperatures required for reactant recycling can be provided sustainably by use of abundant solar radiation. Intermittently available solar energy is stored advantageously as NH_3[11, 12], similar to solar thermochemical H_2-production via H_2O-cleavage with a zinc reactant[11]. However, physical containment of these significant reaction temperatures is technically challenging[11, 12] and requires sophisticated construction materials and reactor designs[12, 21].

Focusing on the simpler concept of a nitride-based NH_3 synthesis at near ambient pressure and without natural gas, the work presented here pursues a reactant composition which allows the nitride-based NH_3 synthesis at temperatures where relatively common materials of construction (such as specialty steels and common ceramics) are stable and available as finished objects and machinable stock. The choice of reducing agent (carbonaceous, hydrogen, or none) affecting process economics is discussed briefly.

The following section assesses the viability of a nitride-based NH_3 synthesis process at an overview level. The section concludes with a list of desirable material properties of the reactant that may allow this concept to be competitive with other NH_3 production schemes. Thereafter a thermodynamic rationale is proposed to guide the reactant choice. With regard to the quantified

trade-off between high metal oxide reduction temperatures and high yields of N_2 fixation and NH_3 liberation, a few chemical elements that appear promising for the development of a composite reactant are highlighted. Gibbs free energy computations and simulations of chemical equilibrium compositions focus on magnesium-based reactants to point out possible process limitations and options (such as the possibility of decreasing the oxide reduction temperature by doping the reactant with transition metals). Both, direct conversion of the metal oxide to a metal nitride (dependent on the thermodynamic stability of the nitride at elevated temperatures) or intermediate formation of a metal vapor are considered. To aid the direct oxide-to-nitride route, cerium is discussed as a candidate to increase the stability of the nitride.

2.3 Process concept for solar thermochemical NH_3 synthesis

A solar thermochemical cycle producing NH_3 at atmospheric pressure (Fig. 2.1) by metal nitride hydrolysis and subsequent metal reactant recycling using a carbonaceous reducing agent (e.g., biomass) may be written with generalized stoichiometry as:

$$\text{(2.1)} \quad \frac{a}{bc}M_cO_d + \frac{ad}{bc}C \leftrightarrow \frac{a}{b}M + \frac{ad}{bc}CO$$

$$\text{(2.2)} \quad \frac{a}{b}M + \frac{1}{2}N_2 \leftrightarrow \frac{1}{b}M_aN_b$$

$$\text{(2.3)} \quad \frac{1}{b}M_aN_b + \frac{ad}{bc}H_2O \leftrightarrow \frac{a}{bc}M_cO_d + NH_3 + \left(\frac{ad}{bc} - \frac{3}{2}\right)H_2$$

with M being a metal. Lower case letters indicate stoichiometric coefficients. Carbothermal reduction of M_cO_d (Eq. 2.1) generates a metal capable of breaking the N_2 triple bond via formation of a metal nitride (M_aN_b) (Eq. 2.2). The nitride is then corroded during nitride hydrolysis (Eq. 2.3) forming the metal oxide, the desired NH_3, and possibly H_2. Oxide reduction (Eq. 2.1) may occur concurrently with metal nitridation (Eq. 2.2), see Section 2.6.2. The possibility of hydroxides forming will be addressed below. However, hydroxides are expected to

decompose to the metal oxide and water at the elevated temperature that is required for the reaction generating the reduced metal, and are therefore disregarded in Eq. 2.1-2.3.

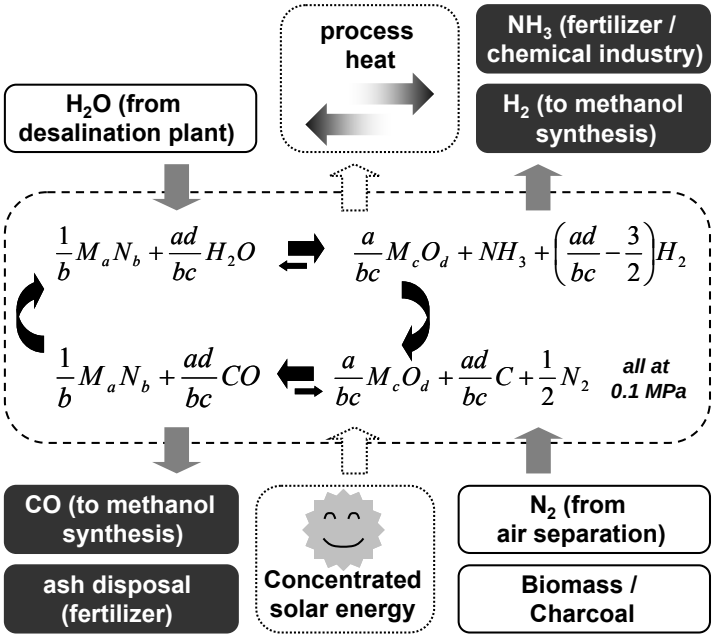

Figure 2.1 Conceptual approach of reactive NH_3 synthesis near 0.1 MPa via a two-step reaction cycle of metal nitride hydrolysis and carbothermal metal oxide nitridation.

2.3.1 Process viability

As a first approximation, Figure 2.2 shows a mass and energy balance-based process analysis for solar thermochemical NH_3 synthesis via an inorganic MgO/Mg_3N_2 cycle (i.e., in Eq. 2.1-2.3, M = Mg, assuming that MgO can be reduced at 1800 K). A similar analysis for solar-driven steam and air reforming to generate H_2 from water and N_2 from air, followed by the conventional Haber-Bosch synthesis is summarized in Figure 2.3. Major conclusions are:

In the nitride-based process ca. 74% of the energy input (absorbed solar heat and charcoal) are recovered in form of chemical energy (45% in NH_3, CO) and electricity (29%). The large fraction of produced electricity is due to the heat released from exothermic reactions at decreased temperatures (label 5 and 10, Fig. 2.2) limiting heat integration. Also, the high reduction temperature of MgO leads to an increased amount of sensible and latent heat in the

gaseous products of the oxide reduction step (label 3) which is converted partly to electricity (label 6). The total energy efficiency of the reforming-based process is estimated analogously at 65% (Fig. 2.3). Comparing these figures to the current industrial NH_3 synthesis (ranging from 12% with coal to 69% with natural gas[4]) or the industrial utilization of absorbed solar thermal energy (e.g., ca. 30% annual average, Andasol power plant, Spain[27]) or coal (35% without CO_2 capture technology[28]) to useful energy in form of electricity, both the solar nitride-based and the solar steam reforming/Haber-Bosch-based approaches to solar thermochemical NH_3 synthesis appear potentially economically competitive.

Solar thermochemical NH_3 synthesis via metal nitride / oxide cycle

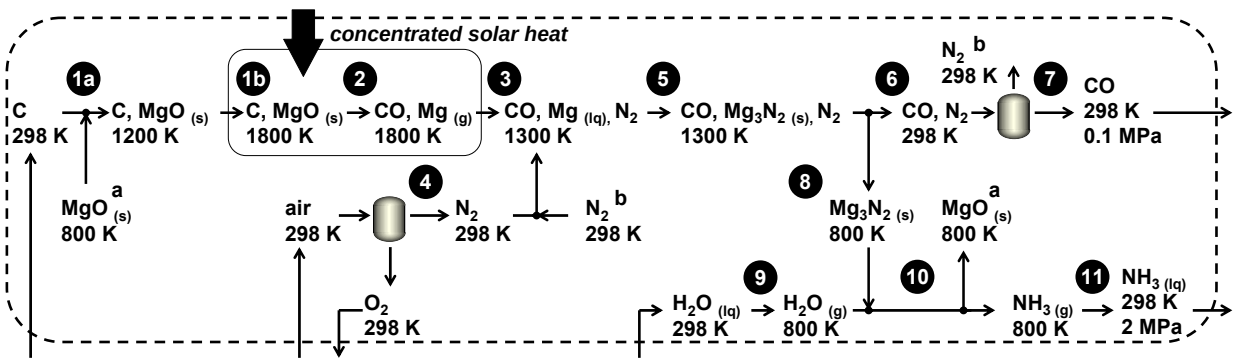

label	process	heat (kJ/mol NH_3)
1a	heat exchange (from process heat)	71.5
1b	heat exchange (from solar heat)	77.1
2	$\Delta_{rxn}H$ for MgO reduction (from solar heat)	917.3
3	heat released to quench gas (N_2)	- 239.2
4	N_2 separation [A]	0.3
5	$\Delta_{rxn}H$ from Mg_3N_2 formation (to steam [B])	- 244.8
6	heat exchange (to steam [B])	- 274.5
7	CO separation [A]	9.7
8	heat exchange (to steam [B])	- 27.8
9	heat exchange (from process heat)	98.2
10	$\Delta_{rxn}H$ from NH_3 formation (to steam [B])	- 352.7
11	heat exchange and compression (net to steam [B])	- 7.1

chemically stored energy, 45.0%
$f_{fuel} = \Delta_{rxn}G_{298K}(NH_3 + 3/4O_2 \rightarrow 1/2N_2 + 3/2H_2O) + \Delta_{rxn}G_{298K}(3/2CO + 3/4O_2 \rightarrow 3/2CO_2) / E_{total,in}^{C}$

energy converted to electricity, 29.2%
f_{elec} = *electricity from steam* [B] / $E_{total,in}^{C}$

total process efficiency, 74.2%
$\eta_{total} = f_{fuel} + f_{elec}$

solar energy integration, 62.7%
f_{solar} = *solar heat*$_{in}$ / $E_{total,in}^{C}$

C-neutral CO generation 1.28 mol/MJ
3/2 mol CO / (η_{total} x $E_{total,in}^{C}$)

Figure 2.2 To assess process viability: All total pressures are 0.1 MPa except if indicated otherwise; critical separation steps are marked with a gray reactor symbol; pumping is disregarded; A, as process steam that is required to generate electricity; B, steam utilized to generate electricity at Carnot efficiency; C, $E_{total,in}$ = (solar heat at (1b) and (2) + lower heating value of the coal utilized), absorption losses not accounted.

Solar thermochemical NH_3 synthesis via steam/air reforming and Haber-Bosch

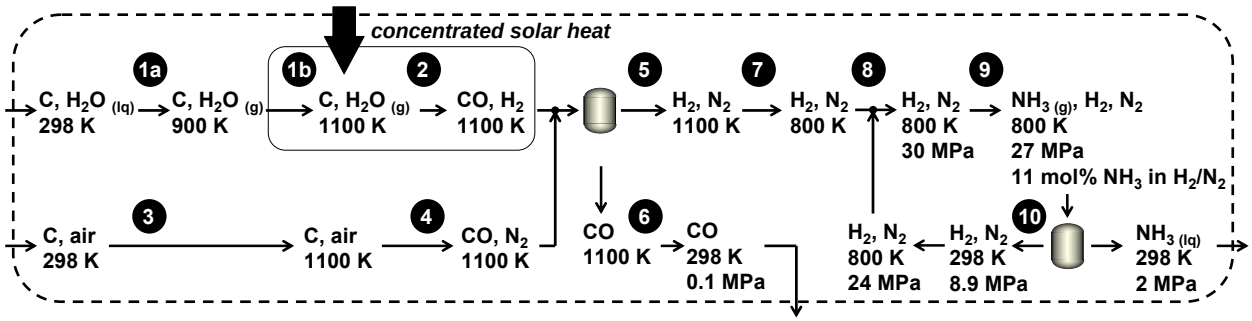

label	process	heat (kJ/mol NH_3)
1a	heat exchange (from process heat)	128.2
1b	heat exchange (from solar heat)	24.8
2	$\Delta_{rxn}H$ for charcoal/steam reforming (from solar heat)	204.9
3	heat exchange (from process heat)	22.6
4	$\Delta_{rxn}H$ from charcoal/air reforming (integrated [A])	- 28.1
5	CO separation [B]	32.5
6	heat exchange (integrated [A])	- 48.1
7	heat exchange (integrated [A])	- 20.4
8	synthesis gas compression [B]	216.8
9	$\Delta_{rxn}H$ from NH_3 formation	- 54.1
10	NH_3 separation loop [B, C]	21.6

total process efficiency, 65.4%
$\eta_{total} = f_{fuel} = \Delta_{rxn}G_{298K}(NH_3 + 3/4O_2 \rightarrow 1/2N_2 + 3/2H_2O) + \Delta_{rxn}G_{298K}(7/4CO + 7/8O_2 \rightarrow 7/4CO_2) / E_{total,in}$

solar energy integration, 19.3%
$f_{solar} = solar\ heat_{in} / E_{total,in}$

C-neutral CO generation 2.25 mol/MJ
7/4 mol CO / (η_{total} x $E_{total,in}$)

fossil CO_2 generation 0.89 mol/MJ
0.69 mol CO_2 / (η_{total} x $E_{total,in}$)

Figure 2.3 To assess process viability (compare to Fig. 2.2): A, assumed as a completely reversible process; B, as lower heating value of coal converted at 35% efficiency to electricity; C, the synthesis loop (label 10) is computed as succession of isochoric operations recovering a total of > 99.5 mol% of the NH_3 formed.

The nitride-based process has three products (NH_3, CO, and electricity) vs. two products with the reforming-based process (NH_3 and CO). This couples both processes to the economics of different products and markets. CO may be utilized for the production of methanol or Fischer-Tropsch chemicals. The dependency on the inherent by-production of these chemicals can be lowered via reactant optimization for the nitride-based process (e.g., aiming at a decreased ratio of *d/b* in Eq. 2.1-2.3 or use of alternative reducing agents such as H_2 if the Gibbs free energy of formation of the metal oxide is sufficiently low) or employment/development of alternative technologies for N_2 separation from air for the reforming-based process. The amount of co-generated electricity in the nitride-based process can be addressed by optimization of the reactive material as well (see previous paragraph).

Assuming biomass as reducing agent, no fossil resources are consumed with the nitride-based process which thereby avoids inherently the emission of fossil CO_2. The mechanical energy required for the reforming-based process (for compressing the synthesis gas to 30 MPa, label 8, and for the synthesis loop, label 10, Fig. 2.3) leads to fossil CO_2 emissions when generating electricity from the current energy mix (see Section 2.2). Avoidance of these emissions would require the generation of electricity from renewable resources in the future.

Another factor favoring the nitride-based process, 63% of the total energy input to the nitride-process is absorbed solar heat (absorption losses due to re-radiation not accounted). The reforming-based process integrates only 19% solar heat. This factor can be increased to 44% if all electricity consumed would be generated (at an efficiency of 30%, see above) from solar heat.

These various facets demonstrate that the assessment of the economic competitiveness depends highly on the current economy (e.g., presence or absence of CO_2 emission regulations, cost of heliostats for concentrating solar energy, etc.). An economic analysis (e.g., a net present value analysis) exceeds the scope of this Chapter and will be presented in Chapter 7. Concerning the nitride-based process, the sensitivity of process efficiency to the reactant choice offers the possibility to optimize via reactant composition as shown below.

2.3.2 Desirable material properties of the reactant

Major criteria for selecting a reactant constituent (*M* in Eq. 2.1-2.3) are:

(1) moderate to high nitridation yields of the metal with acceptable kinetics

(2) moderate to high yield of NH_3 from the metal nitride with acceptable kinetics

(3) metal oxide reduction temperature which can be contained in an industrial-scale, solar-heated reactor[12, 29] and that is near the optimal temperature of the reactor receiving solar radiation[11], see Section 2.5.1

(4) reactant regeneration using a sustainable reducing agent (preferably a gas[30]) in economically attractive quantities[12, 25], see Section 2.3.1

(5) absence of melting and boiling of the reactant to avoid pipe blocking, decreased reactant porosity, or cumbersome gas phase separations[31, 32] (for possible benefits of gaseous reaction *products* see Section 2.6.2)

(6) low to moderate amount of heat liberated by exothermic reactions at temperatures significantly below the temperature of the metal oxide reduction (which absorbs this heat as solar radiation at high temperatures dependent on the metal oxide stability), see Section 2.3.1

(7) acceptable cost and availability of the reactive material[10] and absence of toxicity to humans or the environment[30] (in particular when biomass is used as reducing agent leading to the need for ash disposal, see Fig. 2.1)

(8) low number of chemical reactions to reduce complexity[30]

(9) low number of separation steps due to an otherwise increased energy demand[30] (except for gas-liquid or gas-solid separations, see Fig. 2.2 and 2.3)

(10) high ratio of solar energy utilized as process energy

2.4 Theory and modeling

A rationale to guide the reactant choice for nitride-based solar thermochemical NH_3 synthesis is proposed here. The simplified theoretical approach is based on the analysis of the Gibbs free energy of Eq. 2.1-2.3 for various elements and the computation of chemical equilibrium compositions.

2.4.1 Gibbs free energy analysis

Molar Gibbs free energy of formation data (g_f) for various nitride/oxide pairs in the literature[23, 33] and used previously for similar computations[32] were used here to perform a thermodynamic analysis computing the Gibbs free energy of reaction ($\Delta_{rxn}G$):

$$(2.4) \quad \Delta_{rxn}G = \sum_{i=products} n_i g_{f,i} - \sum_{j=reactants} n_j g_{f,j}$$

where n are the mols of reactants j or products i, and $\Delta_{rxn}G$ in kJ/mol is negative if the reaction is thermodynamically favored at equilibrium in a closed system, i.e., the reaction yield exceeds a half-stoichiometric conversion of reactants. The behavior in an open (flow-through) system may differ substantially from thermodynamic predictions due to non-equilibrium situations including mass transfer. However, thermodynamics is used here as a starting point. The absolute error of g_f was estimated previously with ± 3 kJ[32] and was taken as 2% of the value in kJ/mol. Error propagation was used to estimate the error of $\Delta_{rxn}G$ values computed.

2.4.2 Computation of equilibrium compositions

Assuming ideal gases and ideal condensed phases yields[34]:

$$(2.5) \quad K_T = \exp\left\{\frac{-\Delta_{rxn}G}{RT}\right\} = \prod_{i=products} n_i^{Si} \prod_{j=reactants} n_j^{-Sj} \left(\frac{p}{n}\right)^{Si-Sj}$$

where K_T is the dimensionless equilibrium constant of a given reaction as a function of temperature (T) in K. R is the gas constant in kJ/mol/K, S_i and S_j are reaction stoichiometric coefficients, p is the total pressure in MPa, and n in mol is the total number of chemical species in the system, for simplicity taken as the arithmetic mean of the number of reactants and the number of products at complete conversion. Eq. 2.4 and 2.5 together with the elemental mol balances of a given reaction system were solved (MathCad 13, see also Section 1.4.1) to yield the equilibrium composition as a function of T at 0.1 MPa (carbide formation disregarded). It is

indicated below when $\Delta_{rxn}G$ calculations were extrapolated using a linear fit (R^2 generally > 0.999) (see other chemical equilibrium software such as STANJAN). Generally, g_f values were extrapolated for $Mg_3N_{2(s)}$ > 1300 K, for $Mg_{(g)}$ > 2000 K and for N_2 and CO > 2500 K.

2.5 Thermochemical trends of metal nitride / oxide formation

The following provides a thermodynamic analysis of 35 candidate nitride/oxide pairs (Li_3N/Li_2O, Be_3N_2/BeO, BN/B_2O_3, Mg_3N_2/MgO, AlN/Al_2O_3, Si_3N_4/SiO_2, Ca_3N_2/CaO, ScN/Sc_2O_3, TiN/TiO_2, VN/V_2O_5, $VN_{0.465}/V_2O_5$, CrN/Cr_2O_3, Cr_2N/Cr_2O_3, Mn_5N_2/MnO, Mn_4N/MnO, Fe_2N/Fe_2O_3, Fe_4N/Fe_2O_3, Co_3N/Co_3O_4, Zn_3N_2/ZnO, GaN/Ga_2O_3, Sr_3N_2/SrO, YN/Y_2O_3, ZrN/ZrO_2, NbN/Nb_2O_5, Nb_2N/Nb_2O_5, Mo_2N/MoO_2, InN/In_2O_3, Ba_3N_2/BaO, CeN/CeO_2, HfN/HfO_2, TaN/Ta_2O_5, Ta_2N/Ta_2O_5, Th_3N_4/ThO_2, ThN/ThO_2, and UN/UO_2) to guide the material selection for the reactive NH_3 synthesis. Focusing on a single element of this selection will furthermore require consideration of boiling points (see, e.g., Mg in Section 2.5.3), kinetics (see Section 2.5.2) and different oxidation states of the metal (see, e.g., Mn(IV) to Mn(II), Section 2.6.2).

The analysis quantifies a correlation between thermodynamically favorable metal nitridation and NH_3 liberation via hydrolysis and undesirable strong metal-oxide bonds formed during hydrolysis. Nitride-based NH_3 synthesis may be realized with elements representing a trade-off (the gray region in Fig. 2.4 and 2.5) of these conflictive, thermochemical properties. However, these elements may cause only moderate NH_3 yields above 298 K (e.g., Mo[35], Fig. 2.5) or require activation of the N_2 prior to fixation (e.g., Zn[36], Fig. 2.4, see Section 2.5.4).

An alternative approach, combining elements far outside this trade-off region to manufacture a mixed material incorporating two desired reactive properties is conceivable. This will be explored selecting Mg or Ce for their high expected yields of fixed nitrogen and liberated

NH_3 on one hand (Fig. 2.4 and 2.5) and Cr, Mn, Fe or Mo for their tendency to form less stable metal oxides on the other hand (Fig. 2.4).

2.5.1 Gibbs free energy mapping of chemical elements

Figure 2.4 shows $\Delta_{rxn}G$ of the nitridation reaction ($\Delta_{nit}G$) at 0.1 MPa and 298 K as a function of $\Delta_{rxn}G$ of the carbothermal metal oxide reduction ($\Delta_{red}G$) at 0.1 MPa and 1400 K (reduction of Co_3O_4 was computed at 1000 K due to availability of data). The classification of nitrides was taken from the literature[37]. Uncertainties of $\Delta_{rxn}G$ follow a normal distribution with on average ± 4.01% of $\Delta_{nit}G$ or ± 20.66% of $\Delta_{red}G$, respectively. Monte Carlo simulation yields the dimensionless slope of a linear regression with -0.40 ± 0.01 (Fig. 2.4).

This trend suggests a necessary trade-off: the stability of the oxide increases with the increasing tendency of a metal to form nitrides. Recovering the metal from stable oxides unfortunately requires high reduction temperatures aided by carbon as a chemical reducing agent.

Nitridation computed at 1000 K (except Co_3N at 600 K, Zn_3N_2 at 700 K, and AlN, Ca_3N_2, Cr_2N, CrN, Mn_4N, Mn_5N_2, and Mo_2N at 800 K) is represented by a linear fit (dashed line, individual data points omitted for clarity, details see Appendix A). Increasing the nitridation temperature to a kinetically reasonable value[37, 38] positions some elements that are attractive due to their low metal-oxygen bond energy, at a region with positive $\Delta_{nit}G$, i.e., nitride formation is not favored (Fig. 2.4). Formation of these nitrides requires elevated N_2 pressure and/or nitrogen activation (e.g., plasma dissociation or other activated N sources)[39] if the nitride is only stable at low temperatures. Low temperatures do not allow useful nitride formation from N_2 due to decreased reaction kinetics.

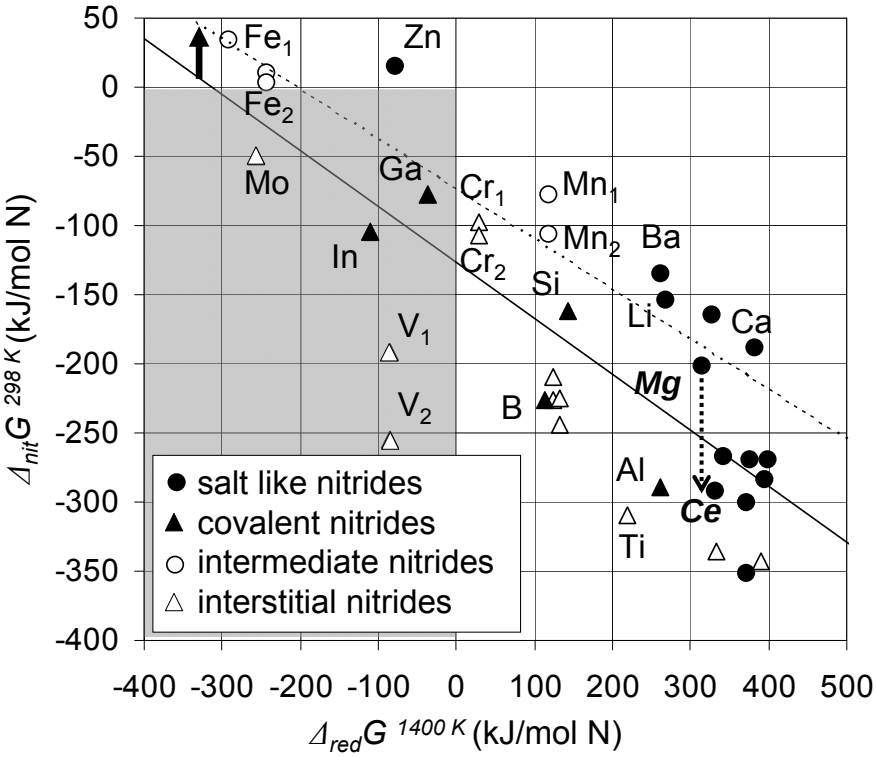

Figure 2.4 Utility of various elements for reactive NH_3 synthesis at atmospheric pressure: $\Delta_{rxn}G$ of metal nitridation (Eq. 2.2) vs. $\Delta_{rxn}G$ of carbothermal metal oxide reduction (Eq. 2.1)[23, 33]. Selected nitride/oxide pairs (see Section 2.5) are represented with the chemical symbol of the metallic constituent (subscript "2" marks lower nitrides, e.g., Fe_4N/Fe_2O_3 marked with Fe_2, Fe_2N/Fe_2O_3, marked with Fe_1). A complete description of the diagram is provided in Appendix A. The trade-off region of negative $\Delta_{rxn}G$ for nitride formation *and* oxide reduction is the gray rectangular area. A linear fit is marked with a solid line. The computation is repeated for nitridation at 1000 K (or lower, limited by available data), represented by a linear fit (dashed line, no individual data points shown).

Plotting $\Delta_{rxn}G$ for hydrolysis ($\Delta_{hyd}G$, ± 19.43% average uncertainty) at 0.1 MPa and 298 K vs. $\Delta_{red}G$ yields the dimensionless slope of a linear regression with -0.45 ± 0.03 kJ (Fig. 2.5). A correlation similar to that in Figure 2.4 is observed: Elements forming an undesirably strong bond with oxygen tend to liberate NH_3 upon nitride hydrolysis. Increasing the hydrolysis temperature[37, 38] decreases the tendency for formation of NH_3 and favors undesirable N_2 formation (computed at 800 K, except Co_3N at 600 K, and Zn_3N_2 at 700 K).

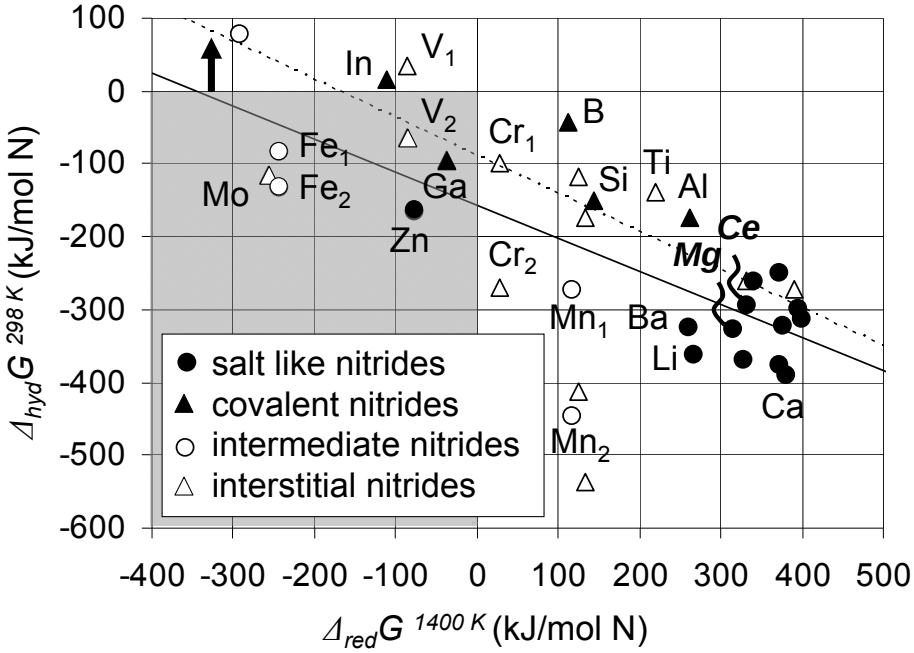

Figure 2.5 Utility of various elements for reactive NH_3 synthesis at atmospheric pressure: $\Delta_{rxn}G$ of metal nitride hydrolysis (Eq. 2.3) vs. $\Delta_{rxn}G$ of carbothermal metal oxide reduction (Eq. 2.1)[23, 33]. Selected nitride/oxide pairs are abbreviated such as in Figure 2.4. A complete description of the diagram is given in Appendix A. The trade-off region of negative $\Delta_{rxn}G$ for NH_3 formation *and* oxide reduction is marked (gray rectangle). A linear fit is marked with a solid line. The computation is repeated for corrosion at 800 K (or lower, limited by available data), represented by a linear fit (dashed line, no individual data points shown).

2.5.2 Trade-off elements

Metals that are - at the computed temperatures - elements of both trade-off regions (Fig. 2.4 and 2.5), V, Ga, and Mo are only of limited attractiveness for the investigated reaction cycle due to physical material properties and reaction kinetics. Carbothermal reduction of V_2O_5 would require precise temperature control to conduct the initial reduction of V(V) to V(IV) at below 943 K, the melting point of V_2O_5. More importantly, V reduces N_2 only slowly (20-25 hours at red glow[20]) and hydrolysis of the vanadium nitrides will results in low NH_3 yields (Fig. 2.5). Nitridation kinetics of Ga and Mo dictate N_2 reduction at above or near the decomposition temperature of the nitrides (ca. 919 K for GaN or 1115 K for Mo_2N[23]) leading commonly (see

Chapter 6) to the use of increased partial N_2 pressures (reportedly 6 MPa for Mo[20] and on the order of GPa for Ga[36, 40]).

2.5.3 Promising elements for the nitride formation and NH_3 liberation step

Elements with high $\Delta_{red}G$ (and relatively low $\Delta_{nit}G$ and $\Delta_{hyd}G$) values (Fig. 2.4 and 2.5) such as the highly electropositive Li, Mg, Ca, Ba and Ce form salt like nitrides (criteria 1, Section 2.3.2). These nitrides are composed mainly of metal cations and N^{3-} anions[20, 37]. Hydrolysis of these materials forms NH_3 readily and rapidly[37, 38] (criteria 2) but also highly stable oxides (violating criteria 3 and 6).

Regenerating Li_3N from LiOH formed during hydrolysis[20] is further complicated by the low melting point of LiOH at 744 K which would likely result in undesirable vapor formation of reactants and products at atmospheric pressure during the oxide reduction[23] (violating criteria 5).

MgO is a solid and abundant material (criteria 5 and 7). Due to increased entropy values when forming gases, the reaction equilibrium for carbothermal reduction of MgO favors Mg vapor formation at above ca. 2100 K[23]. In an open (non-equilibrium) system carbothermal reduction of MgO at a molar ratio of MgO/C of 1/2 was demonstrated successfully yielding 50 mol% Mg after 30 min at 1823 K when using wood-derived charcoal as reducing agent[41]. Similar to MgO, reduction of CaO, BaO and CeO_2 forming nitrides requires carbon and relatively high temperatures (Fig. 2.4). Carbothermal reduction of CaO and BaO in presence of N_2 suppresses the nitride formation completely and has been reported to yield cyanide-like compounds[20] (violating criteria 8). This difficulty to form the nitride directly can be expected for Mg-based reactants as well and is focused below (see Section 2.6.2 and Chapter 4).

The utility of Al for the nitride-based NH_3 synthesis has been demonstrated successfully (see Section 2.2)[10, 24-26]. Intermittent operation and containment of temperatures above 2000 K

required for Al_2O_3 reduction in a large-scale, non-equilibrium reactor will likely require refractory construction materials that constitute a crucial capital cost and construction feasibility factor[12, 20, 21]. Also, liberation of NH_3 from the highly corrosion-resistant AlN requires high temperatures and thus rapid quenching of the NH_3 liberated to prevent decomposition. The utility of Ti can be expected to be comparable to that of Al. The carbothermal reduction of TiO_2 may proceed at slightly lower temperatures than those required for the reduction of Al_2O_3 (Fig. 2.4 and 2.5). However, hydrolysis of TiN requires high temperatures and appears to yield less NH_3[36] than the hydrolysis of AlN (Fig. 2.5).

2.5.4 Promising elements for the NH_3 liberation and oxide reduction step

Oxides of elements with low $\Delta_{red}G$ (and relatively low $\Delta_{hyd}G$) values, e.g., Fe, Zn and Mo, can be reduced at below 2200 K without carbon[23] (criteria 4) or at significantly lower temperatures with carbon or H_2 as reducing agent (criteria 3 and 6).

Metals of this group tend not to react with 0.1 MPa N_2 (e.g., Fe[20] and Zn[19, 20]) or show low nitridation yields (e.g., Mo[38]) (violating criteria 1). NH_3 synthesis utilizing Zn_3N_2 has been proposed previously[42]. The high ratio of ionic bonding in Zn_3N_2[37] and the thoroughly studied thermal dissociation of ZnO via solar radiation[11] are attractive. However, N_2 fugacities in equilibrium with Zn_3N_2 and Zn metal are (dependent on temperature) on the order of TPa[36, 43] leading to the need for prohibitively high pressurization of N_2 gas when forming Zn_3N_2 from its elements.

Doping a reactant from the first group (e.g., Mg) with an element from this group (e.g., Fe) may aid in decreasing the oxide reduction temperature of a composite material[31, 44-48]. Whether this decreases the stability of the ternary nitride[49] relative to the nitride of the first group metal deserves attention when manufacturing a selected material.

2.5.5 Promising elements for the nitride formation and oxide reduction step

Among the remaining elements with intermediate values of $\Delta_{red}G$ (see Section 2.5.2), B, Si, V, Ga, and In have undesirably low melting points or form undesirable volatile oxides or hydroxides[23] (violating criteria 5). Perhaps determined by the ionization potential of the metal and the degree of incompleteness of the d-electron orbitals (with respect to the transition metals) the nitrides of this group are reported to yield only traces of NH_3 upon hydrolysis[19, 20, 37, 50].

The presence of Cr[50] or Mn in a reactant from the first group might be used to aid the oxide reduction of this element. Whether this affects the ability of the composite reactant to liberate nitrogen in form of NH_3 deserves attention when selecting a dopant from this group.

2.6 Mixed reactants for thermochemical NH_3 synthesis

The properties of elemental nitrogen[39] appear to result in a trade-off in the chemistry of reactive NH_3 synthesis. The high triple bond energy of the N_2 molecule yields small values of Gibbs free energy for a metal nitride relative to Gibbs free energy values for the corresponding metal oxide. Therefore, high metal nitridation yields correlate with formation of highly stable metal oxides formed during hydrolysis of the nitride for NH_3 formation. Analogously, due to the low electron affinity of nitrogen only the most electropositive elements show a high ratio of ionic bonding[49] correlating with desirable high yields of NH_3 formation and undesirable stable metal-oxygen bonding.

The resulting quandary of obtaining reasonable process conditions with a single chemical element may be resolved by intimately combining two elements with different desired reactant properties in close contact. This has been applied successfully for reactants for solar thermochemical H_2O or CO_2 splitting[31, 44, 48], catalysts for NH_3 synthesis[45, 46], and Li-air batteries[47] and is explored here for Mg-based reactants. From the discussed elements Mg was

chosen due to its high potential of reducing N_2 to $2N^{3-}$ and due to the high stability of the formed nitride relative to those formed by Li or Ba for instance (Fig. 2.4). To fix nitrogen in the solid state (in form of a salt like nitride) at the temperatures required for the oxide reduction step, Ce is proposed as alternative to Mg. Conclusions are summarized in Table 2.1.

Reactant component for N_2 fixation and NH_3 liberation	
Mg	**Advantages** • Mg breaks the N_2 triple bond and forms reactive N^{3-} ions (Mg_3N_2) • Mg_3N_2 liberates NH_3 quickly via hydrolysis at 0.1 MPa and < 373 K • abundant, cheap and non-toxic, decreased reactant make-up costs **Disadvantages, risks and unknowns** • MgO requires carbothermal reduction at ca. 2130 K (closed system) • Mg_3N_2 decomposes at temperatures required for MgO reduction; alternative separate formation of Mg metal vapor requires quenching
Ce [A]	**Advantages** • CeN directly from CeO_2, C, and N_2 at ca. 2150 K (closed system) **Disadvantages, risks and unknowns** • Decreased contribution of ionic bonding in CeN • Uncertain NH_3 liberation kinetics • Increased costs for Ce reactant-make up
Reactant component to aid metal oxide reduction	
Fe	**Advantages** • Increased Mg_3N_2 yield (decreased MgO reduction temperatures) • abundant, cheap and low toxicity **Disadvantages, risks and unknowns** • Catalyses NH_3 decomposition • May reduce the concentration of N^{3-} in the reactant • Increased amount of reducing agent required
Cr, Mn, Mo [B]	**Advantages** • Contribute to N_2 fixation (Cr, Mn) and NH_3 liberation (Mo) • Decreased catalytic NH_3 decomposition activity **Disadvantages, risks and unknowns** • Decreased abundance (increased reactant make-up costs) • Increased oxide stability (decreased yield of Mg_3N_2) (Cr, Mn) • Increased oxide volatility (Mo)
Zn [B]	**Advantages** • Mg/Zn vapor formation may aid two-step nitridation of Mg at decreased temperatures **Disadvantages, risks and unknowns** • Rapid quenching of reaction products required

Table 2.1 Overview of thermochemical concepts to produce NH_3 from H_2O and N_2 at near atmospheric pressure (A, relative to Mg; B, relative to Fe).

2.6.1 Step one: Reduction of MgM_nO_4 (M_n = Cr_2, Fe_2, Mo) reactants

$Mg(OH)_2$ formed during hydrolysis of Mg_3N_2 decomposes at elevated temperatures into highly stable MgO. Reduction of MgO in a closed system requires carbon as reducing agent and technically unsuitable high temperatures of ca. 2130 K (Fig. 2.6). Carbothermal reduction of Cr_2O_3 on the other hand is favored thermodynamically at above ca. 1500 K (Fig. 2.6). Also, Cr_2O_3 can be reduced with a gaseous reducing agent (criteria 4) and solar radiation[50]. A material such as $MgCr_2O_4$ (i.e., $MgO*Cr_2O_3$) may be reduced at temperatures significantly below 2130 K[31, 44, 48] (Fig. 2.6).

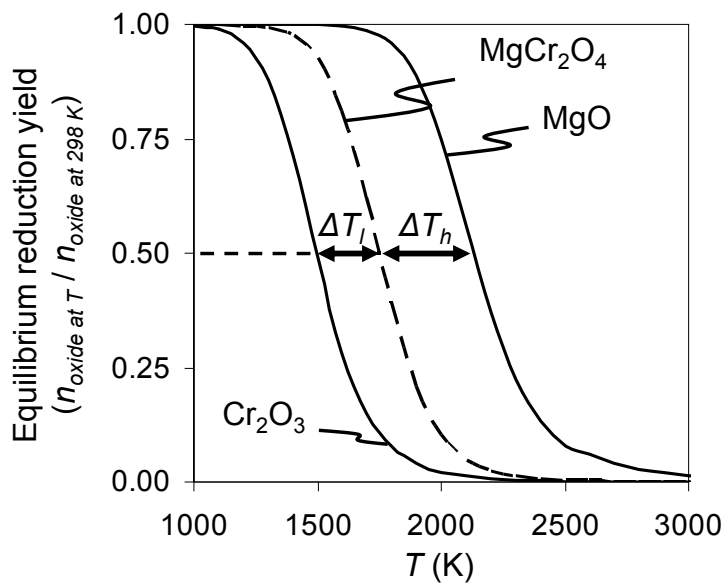

Figure 2.6 Carbothermal reduction of Cr_2O_3 (extrapolated above 1800 K), MgO, and $MgCr_2O_4$ (extrapolated above 2000 K) to the metal.

Computations are based on g_f values for oxides of the spinel group. These stable compounds[51] have increased values of g_f[23], relative to the pure metal oxides. Therefore the presence of a transition metal may allow the reduction of MgO at decreased temperatures due to an increased amount of oxidized reducing agent formed or due to reduction at the solid-solid MgO/transition metal oxide particle boundary. Possible formation of carbides (which tend to

convert to oxides during the hydrolysis step) is disregarded at this point. Replacing Cr_2O_3 with Fe_2O_3 or MoO_3 (not shown, see Section 2.5) respectively yields $\Delta T_l/\Delta T_h$ values (Fig. 2.6) for the three mixed materials in the range of 0.49 to 0.98. If such a decrease in the oxide reduction temperature could be realized even partially, then the costs for reactor construction materials required to physically contain the reaction temperature could be decreased significantly.

2.6.2 Step two: Formation of Mg_3N_2

Mg_3N_2 decomposes (Fig. 2.7B) below the temperature required for carbothermal reduction of MgO (Fig. 2.7A) causing low yields of the nitride when formed directly from the oxide at equilibrium (Fig. 2.8).

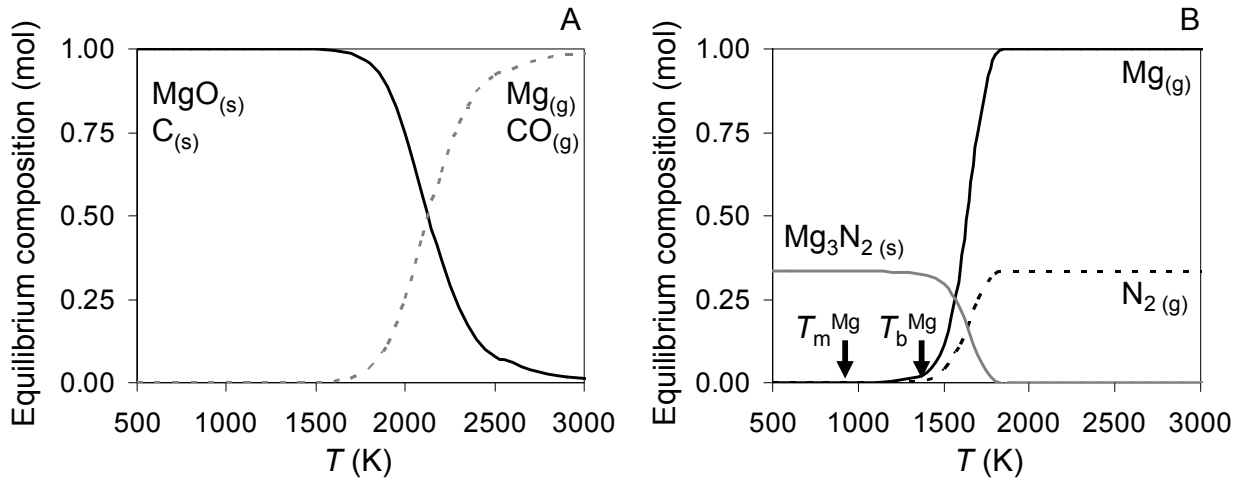

Figure 2.7 Chemical equilibrium composition of two-step MgO to Mg_3N_2 conversion (endothermic MgO reduction at high temperatures and exothermic nitridation of the condensed metal at decreased temperatures). Melting (T_m) and boiling (T_b) points of Mg are marked.

This offers the possibility of conducting the NH_3 synthesis cycle in three steps (criteria 1 but violating criteria 8). These are (Fig. 2.2): Carbothermal reduction of $MgO_{(s)}$ forming $Mg_{(g)}$ (Fig. 2.7A), nitridation of a fine $Mg_{(s)}$ powder at decreased temperatures yielding $Mg_3N_{2(s)}$ (Fig 2.7B), and hydrolysis of $Mg_3N_{2(s)}$ recycling $MgO_{(s)}$ and yielding NH_3 (see Section 2.6.3). To

avoid product recombination during the oxide reduction step this three-step process requires rapid quenching of the Mg/CO vapor[11, 30]. A transition metal oxide forming a metal vapor during its reduction (e.g., ZnO) may possibly serve to lower the reduction temperature of the Mg-based reactant (Table 2.1).

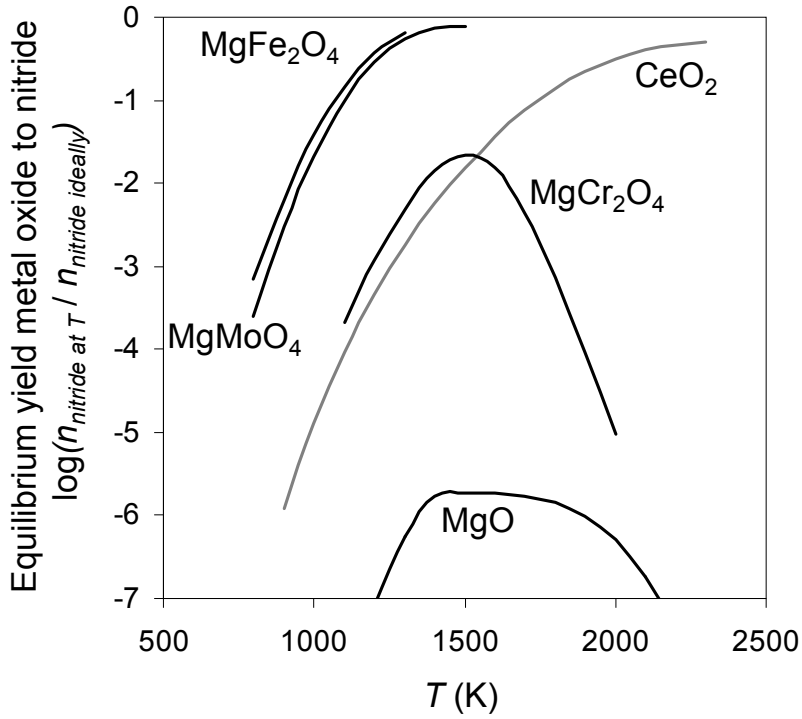

Figure 2.8 Yield of Mg_3N_2 or CeN respectively from the indicated oxides (the yield of CeN is extrapolated above 2000 K). Maximum yields are due to favorable oxide reduction at high temperatures and favorable nitride formation at lower temperatures. Conducting both reactions separately, at different temperatures, may allow for increased nitride yields.

To form the nitride directly from the oxide (criteria 8) one may attempt either to decrease the temperature required for the oxide reduction step or to increase the stability of the nitride at elevated temperature. The first approach (utilizing reactant doping with transition metals) is demonstrated in the previous section. The theoretical maximum yield of Mg_3N_2 via carbothermal reduction in the presence of N_2 and when introducing various transition metals into the magnesium oxide is shown in Fig. 2.8. Addition of Fe_2O_3 for instance yields at least theoretically

at 1300 K ca. 64.21 mol% Mg in form of solid Mg_3N_2, 1.02 mol% Mg in form of liquid Mg and the balance solid $MgFe_2O_4$ (see Appendix A). Formation of carbides and transition metal nitrides (as expected for Cr and Mo) is for simplicity disregarded. The increased yield of Mg_3N_2 using Fe or Mo as a component for Mg-based reactants has to be weighed against the low vapor pressure of MoO_3[23] (criteria 5), the costs for Mo make-up (criteria 7), and the undesirable catalytic properties of Fe in NH_3 formation and decomposition (criteria 2).

Alternatively, an approach to stabilizing the metal nitride is shown in Fig. 2.4, indicating (dotted arrow) a significant decrease in $\Delta_{nit}G$ by -91.3 kJ/mol N when substituting Mg with Ce. This modification does only slightly increase $\Delta_{red}G$ (+15.9 kJ/mol N) and $\Delta_{hyd}G$ (+32.5 kJ/mol N) (Fig. 2.4 and 2.5) (criteria 1, 2, and 8). The increased stability of CeN will likely increase the yield of nitrogen in the solid state during the high-temperature oxide reduction step circumventing the intermediate formation of a metal phase (Fig. 2.8). The nitride possesses a significant degree of ionic bonding and is expected to liberate sufficient quantities of NH_3 when hydrolyzed[20].

The temperature required for the direct conversion of CeO_2 to CeN (50 mol% conversion in a closed system at ca. 2150 K) might be decreased in a similar way as discussed above for Mg. Due to a limited amount of data for ternary Ce compounds Figure 2.9 shows an Ellingham diagram of Ce and Mn oxides using carbon or H_2 as reducing agent. The diagram illustrates the possible presence of various oxidation states of Ce and Mn compounds. H_2 may be used to generate lower metallic oxidation states (criteria 4). Metals in lower oxidation states may aid the reduction of metals in higher oxidation states, i.e., leading to oxygen transfer from Ce to Mn atoms. However, the reduction of Ce(III) to the metal (Fig. 2.9) or its conversion to CeN (Fig. 2.8) requires high temperatures and a solid, carbonaceous reducing agent such as biomass or

charcoal causing ash formation and thus the need of some reactant make-up. Technical advantages of Ce for the overall cycle studied here have to be weighed against criteria 4 and 7.

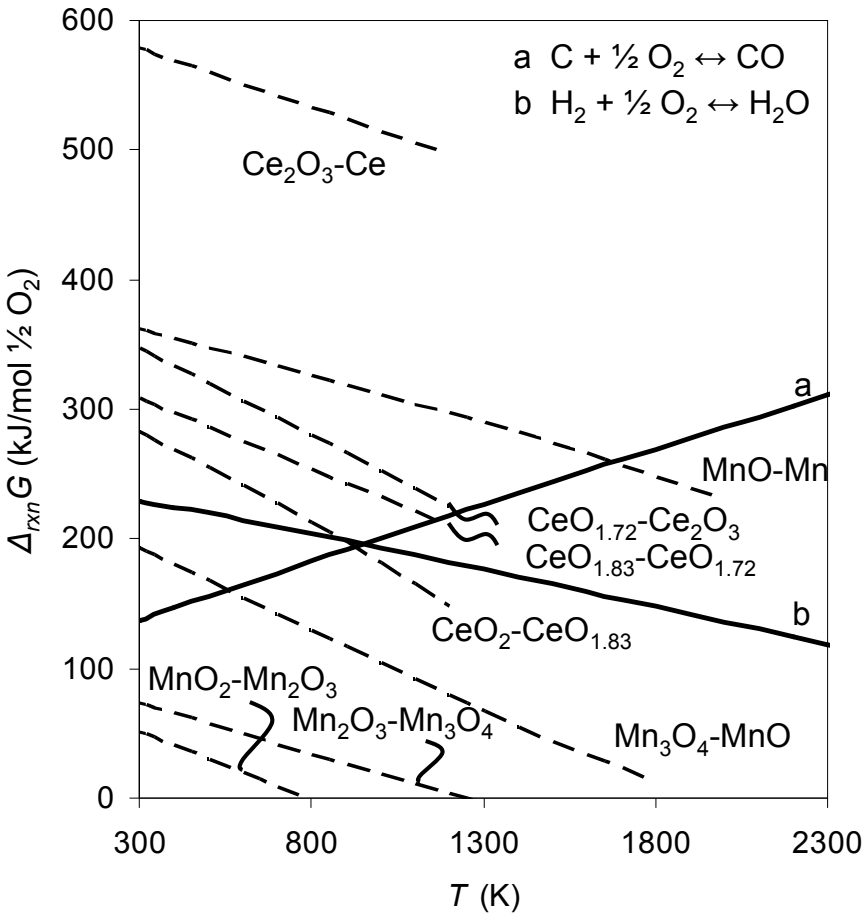

Figure 2.9 Ellingham diagram for the reduction of oxides of Ce or Mn respectively. Removal of 1 atom O from an oxide to form a lower oxidation state (e.g., MnO-Mn abbreviating the equilibrium between MnO and Mn + 1/2 O_2) occurs spontaneously if its $\Delta_{rxn}G$ reaches 0, or if its $\Delta_{rxn}G \leq \Delta_{rxn}G$ of an oxygen absorbing reaction such as combustion of C or H_2 (a or b).

2.6.3 Step three: Hydrolysis of Mg_3N_2 yielding NH_3

To close the cycle, Mg_3N_2 hydrolyzed at 368 K yields NH_3 quickly[22]. Formation of NH_3 at this temperature and at 0.1 MPa total pressure would avoid the need for gas compression since

NH_3 is thermodynamically stable at these conditions. The exothermic heat of reaction liberated at near this temperature would be of low value (see criteria 6).

Gibbs free energy analysis shows that hydrolysis of Mg_3N_2 (Fig. 2.10A) forming $Mg(OH)_2$, N_2 and H_2 is favored at equilibrium over NH_3 formation at above 400-500 K (Fig. 2.10B). To account for this formation of N_2, the amount of NH_3 liberated from the nitride is estimated here based on the ratio of the equilibrium constants for NH_3 formation relative to N_2 formation decreasing the yield of NH_3 when increasing the hydrolysis temperature (Fig. 2.10A). This illustrates that NH_3 formation via nitride hydrolysis is most promising if nitrides are employed which liberate NH_3 at intermediate temperatures and in a system open to mass exchange (to thus avoid the decomposition shown in Figure 2.10B). Maximized NH_3 yields might be promoted by reducing opportunities for surface diffusion of NH_3 and by carefully minimizing any resistance to the mass transfer of NH_3 away from the metal reactant.

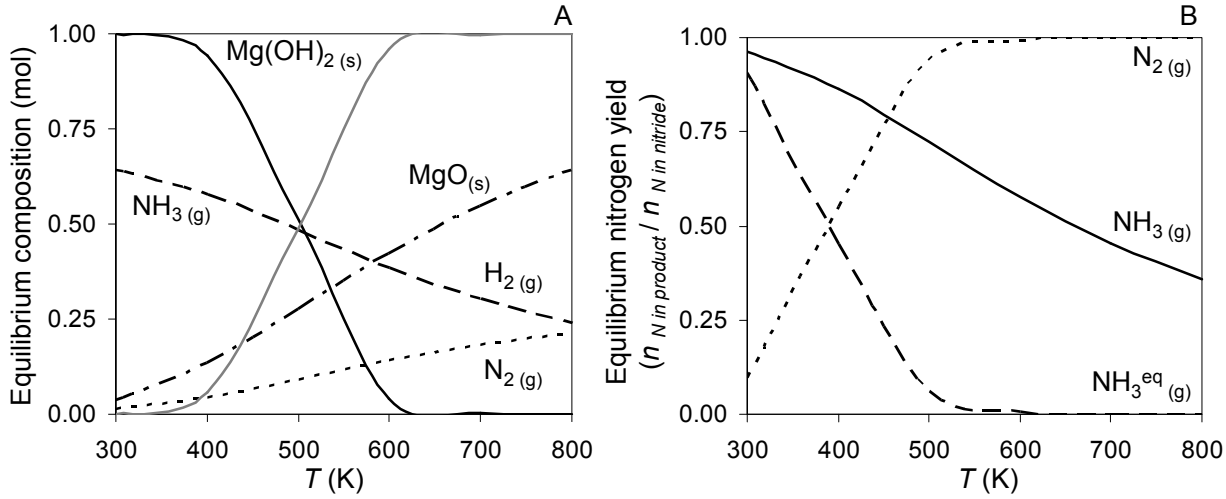

Figure 2.10 Formation of NH_3 at 0.1 MPa via hydrolysis of Mg_3N_2 ($Mg(OH)_2$ extrapolated above 500 K) (A) and equilibrium yield of N in the gas phase during the hydrolysis if NH_3 is not withdrawn (NH_3^{eq}) from the system and quenched (B).

The presence of transition metals in the reactant may reduce the ratio of ionic bonding within the nitride and may thus decrease the yield of NH_3. Bonding in ternary nitrides is however

not well understood[49]. Future research quantifying the bonding nature in mixed or ternary nitrides and assessing the catalytic contribution of nitride components to the decomposition of the NH_3 formed[20, 45, 46] will further the development of a composite reactant for the solar thermochemical NH_3 synthesis at near ambient pressure.

2.7 Conclusions

The thermodynamic equilibrium of the Haber-Bosch reaction - conducted catalytically at 700-900 K - dictates the need for high partial pressures of the reactants, i.e., ca. 22.5 MPa H_2 and 7.5 MPa N_2. Separating the N_2 reduction step from the nitrogen protonation step offers the possibility of conducting both steps at different temperatures and thereby favorable equilibrium positions at 0.1 MPa. This may avoid the need for sophisticated high pressure utilities and decrease the reliance on fossil fuels for electricity generation of the conventional NH_3 synthesis.

Utilizing water as the source of hydrogen and solar radiation for process heat leads to a process (Eq. 2.1-2.3) that converts solar energy to chemical energy, stored in NH_3, CO, and electricity. The dependency on the inherent by-production of electricity may be addressed by control of the reactant composition: The higher the heat of reaction that is absorbed in the endothermic metal oxide reduction step at high temperature (from solar radiation) the higher the heat of reaction of the exothermic NH_3 formation at low temperature (to electric energy byproduct). The present thermochemical analysis quantifies furthermore a rule of thumb: the higher the Gibbs free energy of the metal oxide reduction (need for high reduction temperatures) is, the lower the Gibbs free energy of the NH_3 liberation becomes (high NH_3 yields) (Fig. 2.5).

Given the unfavorable kinetics of the N_2 reduction step of single elements representing a trade-off of these conflicting properties (V, Ga and Mo) and given the quick formation of NH_3 via hydrolysis of salt-like nitrides (e.g., Li, Mg, Ba and Ce), nitrides with high ionic contribution

to the metal-nitrogen bond have been focused here. From this group, Mg and Ce have been selected due to the inferior thermodynamic stability of Li and Ba nitrides (Fig. 2.4) and presumably complicated processing of Li-based reactants (highly volatile oxides and a hydroxide with a low melting point). A qualitative summary of these thermochemical properties is given in Fig. 2.11.

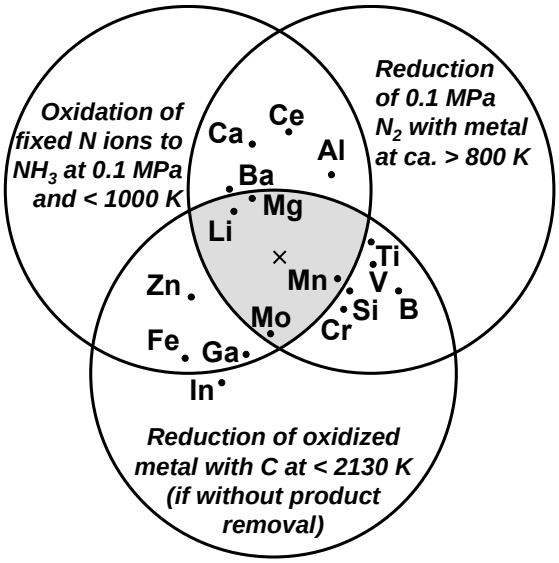

Figure 2.11 Primary demands of the solar thermochemical NH_3 synthesis on the reactive materials and qualitative summary (see kinetic effects and limited thermochemical data at elevated temperatures above) of the related thermochemical properties for single elements. The metal oxide reduction temperature was chosen for guidance only. Increasing this temperature or removing reaction products will allow the reduction of all oxides shown. The ideal combination of thermochemical properties is marked with "x".

In principle, MgO may be reduced carbothermally to a metal vapor formed at near 1800 K in a system open to mass exchange. The condensed metal could thereafter be used as electron donor for the N_2 reduction step. However, the conceivable direct conversion of MgO to Mg_3N_2 at decreased temperatures (required due to the decomposition of the nitride at elevated temperatures) is more attractive from a practical perspective since this would greatly simplify processing (rapid quenching to suppress the oxidation of Mg by CO, handling a metal vapor,

reactor materials and design for high temperatures). The potential of decreasing the reduction temperature of the metal oxide by doping with transition metals has been employed for solar thermochemical H_2O or CO_2 cleavage and has been explored here for the Mg-based (i.e., $MgCr_2O_4$, $MgFe_2O_4$, or $MgMoO_4$) solar thermochemical NH_3 synthesis. Future work needs to experimentally verify this concept (nitride formation near 1500 K) and the possibility of increasing the nitride stability at higher temperatures by using Ce-based reactants.

2.8 Associated content in Appendix A

Supporting Information: Detailed versions of Figure 2.4 and 2.5 and a computation of the Mg vapor expectedly formed during carbothermal nitridation of $MgFe_2O_4$.

2.9 References

1 V. Smil, Population growth and nitrogen: An exploration of a critical existential link, Population and Development Review, 17 (1991) 569-601.

2 R. Schnepf, B.D. Yacobucci, Renewable Fuel Standard (RFS): Overview and issues, Congressional Research Service, (2010).

3 D.A. Kramer, Nitrogen (fixed) - Ammonia, U.S. Geological Survey, Mineral Commodity Summaries, (2003) 118-119.

4 I. Rafiqul, C. Weber, B. Lehmann, A. Voss, Energy efficiency improvements in ammonia production - perspectives and uncertainties, Energy, 30 (2005) 2487-2504.

5 S.K. Ritter, The Haber-Bosch reaction: An early chemical impact on sustainability, Chemical & Engineering News, 86 (2008) 53.

6 Z. Kirova-Yordanova, Exergy analysis of industrial ammonia synthesis, Energy, 29 (2004) 2373-2384.

7 G. Thomas, G. Parks, Potential roles of ammonia in a hydrogen economy, a study of issues related to the use ammonia for on-board vehicular hydrogen storage, U.S. Department of Energy (2006), Available online at: http://www.hydrogen.energy.gov/-pdfs/nh3_paper.pdf (retrieved December, 2011).

8 C.H. Christensen, T. Johannessen, R.Z. Sørensen, J.K. Nørskov, Towards an ammonia-mediated hydrogen economy?, Catalysis Today, 111 (2006) 140-144.

[9] A.J. Reiter, S.C. Kong, Combustion and emissions characteristics of compression-ignition engine using dual ammonia-diesel fuel, Fuel, 90 (2011) 87-97.

[10] M.E. Gálvez, M. Halmann, A. Steinfeld, Ammonia production via a two-step Al_2O_3/AlN thermochemical cycle. 1. Thermodynamic, environmental, and economic analyses, Industrial & Engineering Chemistry Research, 46 (2007) 2042-2046.

[11] A. Steinfeld, A.W. Weimer, Thermochemical production of fuels with concentrated solar energy, Optics Express, 18 (2010) A100-A111.

[12] T. Kodama, High-temperature solar chemistry for converting solar heat to chemical fuels, Progress in Energy and Combustion Science, 29 (2003) 567-597.

[13] J.A. Pool, E. Lobkovsky, P.J. Chirik, Hydrogenation and cleavage of dinitrogen to ammonia with a zirconium complex, Nature, 427 (2004) 527-530.

[14] M. Lerch, J. Janek, K.D. Becker, S. Berendts, H. Boysen, T. Bredow, R. Dronskowski, S.G. Ebbinghaus, M. Kilo, M.W. Lumey, M. Martin, C. Reimann, E. Schweda, I. Valov, H.D. Wiemhöfer, Oxide nitrides: From oxides to solids with mobile nitrogen ions, Progress in Solid State Chemistry, 37 (2009) 81-131.

[15] A. Skodra, M. Stoukides, Electrocatalytic synthesis of ammonia from steam and nitrogen at atmospheric pressure, Solid State Ionics, 180 (2009) 1332-1336.

[16] G. Kongshaug, Energy consumption and greenhouse gas emissions in fertilizer production, International Fertilizer Industry Association, Technical Conference, Marrakech, Morocco, 28 September-1 October 1998.

[17] http://www.worldcoal.org/resources/coal-statistics/ (retrieved December, 2009)

[18] F. Haber, G. van Oordt, Über die Bildung von Ammoniak aus den Elementen, Zeitschrift für anorganische Chemie, 44 (1905) 341-378.

[19] G. Lunge, Coal-tar and ammonia, Gurney and Jackson, London, 1916.

[20] E.B. Maxted, Ammonia and the nitrides, J. & A. Churchill, London, 1921.

[21] V. Sauchelli, Fertilizer nitrogen its chemistry and technology, Reinhold Publishing Corporation, New York, 1964.

[22] D.R. Glasson, S.A.A. Jayaweera, Formation and reactivity of nitrides .2. Calcium and magnesium nitrides and calcium cyanamide, Journal of Applied Chemistry of the USSR, 18 (1968) 77-83.

[23] I. Barin, O. Knacke, Thermochemical properties of inorganic substances, Springer-Verlag, Berlin Heidelberg New York, 1973.

[24] M.E. Gálvez, A. Frei, F. Meier, A. Steinfeld, Production of AlN by carbothermal and methanothermal reduction of Al_2O_3 in a N_2 flow using concentrated thermal radiation, Industrial & Engineering Chemistry Research, 48 (2009) 528-533.

[25] M.E. Gálvez, I. Hischier, A. Frei, A. Steinfeld, Ammonia production via a two-step Al_2O_3/AlN thermochemical cycle. 3. Influence of the carbon reducing agent and cyclability, Industrial & Engineering Chemistry Research, 47 (2008) 2231-2237.

[26] M.E. Gálvez, A. Frei, M. Halmann, A. Steinfeld, Ammonia production via a two-step Al_2O_3/AlN thermochemical cycle. 2. Kinetic analysis, Industrial & Engineering Chemistry Research, 46 (2007) 2047-2053.

[27] S.M. AG, The parabolic trough power plants Andasol 1 to 3, http://www.solarmillennium.de/upload/Download/Technologie/eng/Andasol1-3engl.pdf (retrieved November 25, 2011).

[28] M. Ramezan, T.J. Skone, N. Nsakala, G.N. Liljedahl, Carbon dioxide capture from existing coal-fired power plants, National Energy Technology Laboratory, Final Report (Original Issue Date, December 2006), DOE/NETL-401/110907 (2007).

[29] J.P. Murray, A. Steinfeld, E.A. Fletcher, Metals, nitrides, and carbides via solar carbothermal reduction of metal-oxides, Energy, 20 (1995) 695-704.

[30] R. Perret, Solar thermochemical hydrogen production research (STCH), Thermochemical cycle selection and investment priority, Sandia report SAND2011-3622, Sandia National Laboratories (2011).

[31] J.E. Miller, M.D. Allendorf, R.B. Diver, L.R. Evans, N.P. Siegel, J.N. Stuecker, Metal oxide composites and structures for ultra-high temperature solar thermochemical cycles, Journal of Materials Science, 43 (2008) 4714-4728.

[32] M. Lundberg, Model-calculations on some feasible 2-step water splitting processes, International Journal of Hydrogen Energy, 18 (1993) 369-376.

[33] I. Barin, O. Knacke, O. Kubaschewski, Thermochemical properties of inorganic substances, Supplement, Springer-Verlag, Berlin Heidelberg New York, 1977.

[34] H. Scott Fogler, Elements of chemical reaction engineering, Prentice Hall PTR, Upper Saddle River, NJ, 2006.

[35] G.V. Samsonov, Handbook of the physicochemical properties of the elements, Oldbourne Book Co., London, 1968.

[36] R. Juza, Über die Nitride der Metalle der ersten großen Periode, Angewandte Chemie, 58 (1945) 25-30.

[37] H.O. Pierson, Handbook of refractory carbides and nitrides, Noyes Publications, Westwood, New Jersey, 1996.

[38] D.R. Glasson, S.A.A. Jayaweer, Formation and reactivity of nitrides .I. Review and introduction, Journal of Applied Chemistry of the USSR, 18 (1968) 65-77.

[39] F.J. DiSalvo, New ternary nitrides, Nitrides and Oxynitrides, Proceedings of the Second International Symposium on Nitrides, 325-326 (2000) 3-9.

[40] T. Yamada, H. Yamane, T. Ohta, T. Goto, T. Yao, Preparation of GaN crystals by heating a Li_3N-added Ga melt in Na vapor and their photoluminescence, Crystal Research and Technology, 42 (2007) 13-17.

[41] M.E. Gálvez, A. Frei, G. Albisetti, G. Lunardi, A. Steinfeld, Solar hydrogen production via a two-step thermochemical process based on MgO/Mg redox reactions - Thermodynamic and kinetic analyses, International Journal of Hydrogen Energy, 33 (2008) 2880-2890.

[42] K. Kaiser, Verf. zur Gewinnung von Zinknitrid und Ammoniak, Zeitschrift für angewandte Chemie, 27 (1914) 481.

[43] H.A. Wriedt, The N-Zn (nitrogen-zinc) system, Bulletin of Alloy Phase Diagrams, 9 (1988) 247-251.

[44] M. Roeb, H. Müller-Steinhagen, Concentrating on solar electricity and fuels, Science, 329 (2010) 773-774.

[45] C.J.H. Jacobsen, Novel class of ammonia synthesis catalysts, Chemical Communications, (2000) 1057-1058.

[46] C.J.H. Jacobsen, S. Dahl, B.S. Clausen, S. Bahn, A. Logadottir, J.K. Nørskov, Catalyst design by interpolation in the periodic table: Bimetallic ammonia synthesis catalysts, Journal of the American Chemical Society, 123 (2001) 8404-8405.

[47] M. Jacoby, Rechargeable metal-air batteries, Chemical and Engineering News, 88 (2010) 29-31.

[48] J.R. Scheffe, J.H. Li, A.W. Weimer, A spinel ferrite/hercynite water-splitting redox cycle, International Journal of Hydrogen Energy, 35 (2010) 3333-3340.

[49] D.H. Gregory, Structural families in nitride chemistry, Journal of the Chemical Society-Dalton Transactions, (1999) 259-270.

[50] R. Michalsky, P.H. Pfromm, Chromium as reactant for solar thermochemical synthesis of ammonia from steam, nitrogen, and biomass at atmospheric pressure, Solar Energy, 85 (2011) 2642-2654.

[51] G.A. El-Shobaky, A.A. Mostafa, Solid-solid interactions in Fe_2O_3/MgO system doped with aluminium and zinc oxides, Thermochimica Acta, 408 (2003) 75-84.

Chapter 3 - Chromium as reactant for solar thermochemical synthesis of ammonia from steam, nitrogen, and biomass at atmospheric pressure

3.1 Abstract

Essentially half of the nitrogen required for the global agricultural production is supplied as artificial nitrogen fertilizer, mainly in form of ammonia or ammonia-derived chemicals. Ammonia is an important commodity chemical, and it can serve as a fuel for combustion engines or as a carrier molecule for hydrogen. Global NH_3 production of over 100 million metric tons per year relies almost entirely on natural gas for energy and hydrogen. About 2% of the world's energy budget is spent to produce NH_3. Experiments towards a solar thermochemical cycle for NH_3 synthesis at near atmospheric pressure using a transition metal reactant and a Fresnel-lens solar furnace are reported here: reacting Cr metal powder with gaseous N_2 to Cr nitride, hydrolyzing Cr nitride powder with steam to NH_3 and Cr_2O_3, and finally reducing Cr_2O_3 powder back to Cr with mixtures of H_2, CO, and N_2. At about 1000 °C it was found that Cr readily fixes N_2 from the gas phase as Cr nitride (4.13×10^{-2} mol N_2 / mol Cr / min, 85 ± 4 mol% of hexagonal Cr_2N after 5.6 min). Cr_2N converts over time to a cubic CrN phase. Corrosion of Cr nitride with steam at 1000 °C and about 1 bar forms Cr_2O_3 and CrO while liberating 53 ± 11 mol% of the nitrogen contained in the solid Cr nitride in 60 min. Of the N liberated, 0.28 ± 0.07 mol% forms the desired NH_3. This results in a yield of 0.15 ± 0.02 mol% NH_3 relative to the N in the nitride (1.07×10^{-4} mol NH_3 / mol Cr / min). Addition of $CaO/Ca(OH)_2$ powder or quartz wool to provide more reactive sites and promote protonation of N increased the yield of NH_3 only slightly (0.24 ± 0.01 or 0.39 ± 0.03 mol% NH_3 relative to the N in the nitride respectively).

The thermochemical cycle is closed by heating Cr_2O_3 to 1200-1600 °C with a reduction yield near the surface of the particles of approximately 82.85 mol% (40 min at 1600 °C) in a gas stream of H_2 and CO (2.7 x 10^{-3} mol Cr / mol Cr_2O_3 / min). An unreacted core model was applied to estimate the activation energy of Cr_2O_3 reduction with 128 ± 4 kJ/mol. Cr appears promising to promote nitridation and oxide reduction as a basis for a future custom-designed reactant with high specific surface area enabling sustainable and more scalable NH_3 production from N_2 and H_2O at ambient pressure without natural gas consumption.

3.2 Introduction

Ammonia is irreplaceable as a base chemical for fertilization of crops that supply growing global demand for food and bio-energy[1]. In the USA in 2007, 58 wt% of all fertilizer consumed (mainly liquid NH_3, $(NH_2)_2CO$, K_2O and P_2O_5) was NH_3-based[2]. The U.S. produces about 9% (1.18 x 10^7 metric tons of NH_3 in 2001) of the NH_3 produced globally (1.28 x 10^8 metric tons of NH_3 in 2001)[3].

Ammonia could also be used as a hydrogen carrier or directly as a liquid fuel. The U.S. Department of Energy has set a 2015 target of 9 wt% H_2 capacity for H_2-based transportation fuels[4] which is reached by liquified NH_3 (18 wt% H_2). NH_3 is easily liquefied at 25 °C above 10 bar and contains by volume approximately 130-fold more H_2 as H_2 itself at the same conditions. NH_3 might be useful blended into diesel or as a stand-alone chemical fuel enabling solar-derived H_2 storage for a H_2 economy[5, 6]. Modified diesel engines can combust NH_3 releasing mainly H_2O and N_2 as combustion products[7]. H_2 can also be recovered catalytically on board a vehicle from NH_3 for subsequent combustion[5].

Fixation of atmospheric N_2 in form of NH_3 is challenging due to the strong N-N triple bond, a high ionization potential, and the nonpolarity of N_2[8]. A milestone of chemical

engineering (Nobel Prizes to F. Haber, 1918, C. Bosch, 1931, and G. Ertl, 2007), the classic Haber-Bosch process synthesizes NH_3 industrially from N_2 and H_2. The reaction equilibrium is shifted at about 300 bar towards formation of ideally 22.7 mol% NH_3 (via Gibbs free energy, $\Delta_{rxn}G$, minimization, Aspen Plus V7.2) at increased temperatures (400-600 °C) and in presence of a catalyst[9, 10]. The process imposes the need for large facilities that produce on the order of 1000 tons of NH_3 per day to alleviate the capital intensity of technologically sophisticated high pressure and high temperature operations. A significant natural gas supply is needed within reasonable distance for situating Haber-Bosch facilities.

The Haber-Bosch process including hydrogen production from natural gas consumes 28-37 GJ/t NH_3 (North America)[10, 11] which translates to about 1-2% of the world's annual energy production[12]. Approximately 84% of the energy required for industrial NH_3 synthesis is consumed in the H_2 production step (in form of synthesis gas, mixed with N_2) via natural gas reforming[11]. About 16% is used for compression work[11]. Per ton of NH_3 produced, approximately 2.3 t of fossil-derived CO_2 are generated[11]. The hydrogen and energy from natural gas to perform the Haber-Bosch closely ties the cost of NH_3 to somewhat volatile natural gas prices and current or future CO_2 emission charges[13, 14].

Alternatives to the Haber-Bosch-based process have been the subject of research for decades. Substantial research efforts have pursued the adaptation of the biological mechanism of fixing N_2 enzymatically via nitrogenase breaking the N_2 bond near room temperature in the aqueous phase. N_2 is reduced catalytically by coordination of molecular N_2 to transition metal complexes and formation of NH_3 by subsequent protonation in the aqueous phase[8, 15]. Electrochemical NH_3 synthesis on the basis of reduction of N_2 in high temperature N_2/H_2 fuel cells[16] has also been investigated. Both approaches have not reached maturity. Electrochemical

NH_3 synthesis for instance yields relatively modest conversions due to low conductivity in the working electrode[17] and requires significant amounts of electrical energy to move 3 electrons per molecule NH_3 formed from the anode that is splitting H_2O to the cathode for reducing and protonating N_2 to form NH_3.

Inorganic routes for the fixation of N_2 are outlined in the literature[18-21]. Recently the reactive synthesis of NH_3 at atmospheric pressure without the need of a fossil hydrogen source was demonstrated successfully via a two-step solar thermochemical cycle. This was based on hydrolysis of aluminum nitride, subsequent carbothermal reduction, and finally nitridation of aluminum oxide to close the cycle[22-25]. Similar to solar H_2 production, the overall products of the cycle (NH_3 and syngas) store the intermittently available solar energy and constitute valuable chemical fuels and raw materials with potential uses as sustainable fertilizer and chemical feedstock[26-30].

Substantial carbothermal reduction of Al_2O_3 and formation of AlN[31] was demonstrated in the range of 1750-2000 °C[23, 25]. The need for absorption of concentrated solar energy at this significant temperature and for physical containment of this temperature is not trivial[27, 29, 30]. The refractory construction materials required to contain this temperature in a large-scale reactor are often not resistant to severe thermal shocks as expected under intermittent concentrated solar radiation and constitute a crucial capital cost and construction feasibility factor[19, 20, 30]. Also, solid carbon as reducing agent requires solids processing steps such as energy-intensive milling to decrease the particle size and the often cumbersome movement and mixing of substantial amounts of solids[32, 33]. A decrease in the reaction temperature to levels where specialty steels and common ceramics can be used and avoidance of solids handling appears beneficial and is pursued here.

Manufacturing a reactive composite material which combines two desired properties due to the presence of two different elements has been applied in the development of, e.g., catalysts for NH_3 synthesis[34, 35], reactants for solar thermochemical H_2O or CO_2 splitting[36-38], and Li-air batteries[39]. Replacing, e.g., some Fe in Fe_2O_3 with Mn, Co, Ni, or Zn was reported to decrease the reduction temperature of the oxide that was selected for its high H_2 yield during H_2O splitting[36, 37]. Similarly, a reactant for solar thermochemical NH_3 synthesis might conceivably be assembled combining reactive sites facilitating nitrogen fixation and NH_3 liberation (e.g., Al) with reactive sites aiding oxide reduction and possibly nitrogen fixation (e.g., Cr or Mn). The work shown here is a first step in identifying desirable properties of the element Cr for such a composite reagent.

The presence of transition elements such as Cr might aid a prospective composite reactant enabling the reduction of a stable metal oxide (e.g., Al_2O_3 or oxides of the alkaline earth metals) at decreased temperatures[36, 37]. It is shown here that Cr_2O_3 can be reduced with a gaseous reducing agent at below 1500 °C (Rxn. 3.1 and 3.2). The metal then fixes N_2 readily in form of a metal nitride (Rxn. 3.3):

$$\text{(3.1)} \quad \begin{aligned} & Cr_2O_{3\,(s)} + 3CO_{(g)} \leftrightarrow 2Cr_{(s)} + 3CO_{2\,(g)} \\ & \Delta_{rxn}H_{1527°C} \approx 278.6\ kJ/mol\ N \end{aligned}$$

$$\text{(3.2)} \quad \begin{aligned} & Cr_2O_{3\,(s)} + 3H_{2\,(g)} \leftrightarrow 2Cr_{(s)} + 3H_2O_{(g)} \\ & \Delta_{rxn}H_{1527°C} \approx 360.0\ kJ/mol\ N \end{aligned}$$

$$\text{(3.3)} \quad \begin{aligned} & 2Cr_{(s)} + 1/2N_{2\,(g)} \leftrightarrow Cr_2N_{(s)} \\ & \Delta_{rxn}H_{527°C} \approx -122.2\ kJ/mol\ N \end{aligned}$$

Solar energy concentrated using a Fresnel lens[40] to at maximum of about 1600 °C and simulated gasified biomass are used in the experiments reported here to form chromium nitride from Cr_2O_3. $\Delta_{rxn}G$ computations[41] indicate that the reduction of Cr_2O_3 (Rxn. 3.1 and 3.2) with

CO[42] or H_2[43, 44] may involve intermediate reactions, e.g., carbon or chromium carbide formation[43, 45, 46] discussed below. Fractions of the N liberated from Cr nitride during hydrolysis of the prospective composite reactant form NH_3 (Rxn. 3.4):

$$(3.4)\quad \begin{aligned} &Cr_2N_{(s)} + 3H_2O_{(g)} \leftrightarrow Cr_2O_{3\,(s)} + NH_{3\,(g)} + 3/2H_{2\,(g)} \\ &\Delta_{rxn}H_{527°C} \approx -312.1\, kJ/mol\ N \end{aligned}$$

Due to the mainly metallic bonding nature of nitrogen with transition metals the step of efficient NH_3 formation from the fixed nitrogen remains a challenge. This will be tackled in future work by introducing a second element like Al or an alkaline earth metal. The solid compounds involved in the proposed cycle do not have melting or boiling points within the temperature range required for conducting the thermochemical cycle. Vapor pressures of chromium hydroxides are low (10^{-5} to 10^{-9} bar)[47, 48]. This prevents the need to handle vapors.

The overall reaction cycle (Fig. 3.1):

$$(3.5)\quad 1/2N_2 + 3H_2O + 3CO \rightarrow NH_3 + 3/2H_2 + 3CO_2$$

$$(3.6)\quad 1/2N_2 + 3/2H_2 \rightarrow NH_3$$

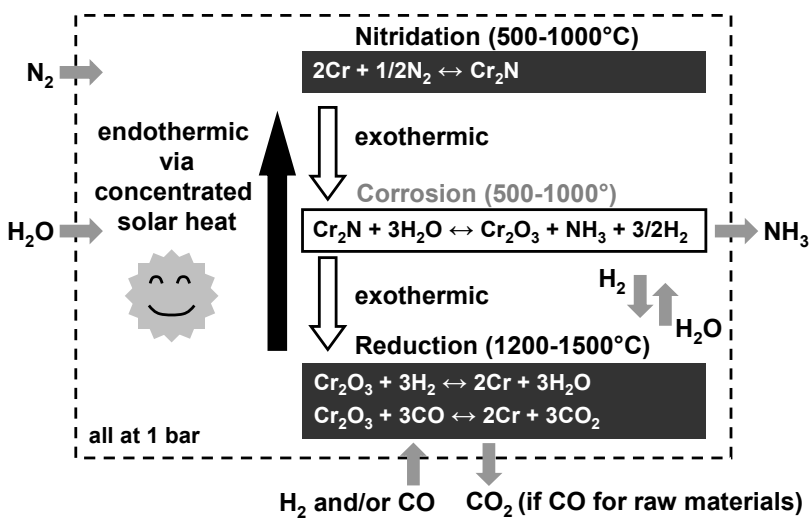

Figure 3.1 Overall approach of N_2 fixation via three-step solar thermochemical NH_3 synthesis at atmospheric pressure. Cr is investigated here for its potential to aid metal oxide reduction and nitridation.

synthesizes NH_3 from water if CO is utilized as reducing agent (Eq. 3.5) or yields an alternative to conduct the Haber-Bosch reaction at near atmospheric pressure if H_2 is used as reducing agent (Eq. 3.6). Although the cycle (Eq. 3.5 or 3.6) is exergonic, a supply of energy is required since the endothermic reactions 3.1 and 3.2 absorb energy at temperatures above where reaction 3.3 and 3.4 release energy.

In summary, the thermochemical properties of chromium in a thermochemical cycle to produce ammonia at near ambient pressure are investigated here as a step towards a sustainable NH_3 production without fossil fuels.

- Opposed to combustion of a fossil fuel to provide compression work for conducting the Haber-Bosch reaction in industrial practice at about 300 bar and 500 °C[9, 10], concentrated solar energy is a sustainable energy source that provides the heat of an endothermic oxide reduction at atmospheric pressure and high temperatures[27, 29].
- Solar thermochemical NH_3 synthesis has the potential of producing NH_3 in scalable plants and at lower temperatures (e.g., if an alkaline earth metal is used for liberating NH_3) without the cumbersome pressurization of the synthesis gas to several 100 bar.
- The reducing agent (syngas or H_2) can be regenerated via endothermic biomass gasification[30, 32] or water dissociation[27], both demonstrated previously via solar processing.
- Cost efficient membrane technology can be used for nitrogen recovery from air since traces of O_2 introduced into the reactor will be removed from the reactant during the oxide reduction step.

3.3 Materials and Methods

3.3.1 Solar furnace

Solar radiation was concentrated (tubular flow-through reactor, 27 mm ID, 30 mm OD, 200 mm length, fused quartz, Technical Glass Products) using a Fresnel lens (0.93 x 1.24 m, 0.7 mm thickness, 1.03 m focal length, UV filtering acrylic, geometrical concentration ratio ~ 2440[49], Mitsubishi TV) mounted in a mobile scaffold (Skarda Equipment Company). Tracking was manual. Pressurized gas cylinders were connected to the reactor via a tubing system equipped with a gas flow meter (0.04-0.50 l/min as air, Omega Engineering) and a flashback arrestor (8491-F, Linweld).

A solar meter (SP1065, 300-1100 nm wavelength detection range, EDTM Glass, Window & Film Test Equipment) was used to determine the incident solar power density before concentration in front of the lens (P_s). A thermocouple (High Temperature Flexible Ceramic Fiber-Insulated Probe, Type K; IR-Pro Infrared Thermometer, 1371 °C maximum temperature (T_{max}), both ThermoWorks) was used to determine the furnace temperature before the experiment.

Melting experiments with Si, Fe, and Cr metal powders under a He blanket atmosphere determined T_{max} in the focal point ~ 1600 °C at P_s ~ 0.85 ± 0.03 kW/m^2. To decrease the temperature the reactor was moved perpendicular to the lens slightly out-of-focus. The furnace temperature, T_f in °C, as a function of the focal spot diameter, D_{int} in mm (the bright spot of concentrated solar radiation intersecting the reactor), was empirically estimated as $T_f = (4.8736 - D_{int})/0.0018$, $R^2 = 0.997$).

3.3.2 Nitridation of chromium metal

To study the reaction kinetics of N_2 gas at 1 bar with Cr metal, 1 g Cr powder was placed into a quartz boat (Table 3.1) and exposed for times ranging from 5.6 to 360 ± 0.5 min to 0.4 ± 0.1 $l_{(STP)}$/min N_2 while being held at 983 ± 40 °C[50-52] by concentrated solar radiation (P_s ~ 0.93 ± 0.09 kW/m^2) (Fig. 3.2). After the reaction, the reactor was allowed to cool down to ambient temperature within about 15 min under 1.6 ± 0.1 $l_{(STP)}$/min N_2. All solid samples were subsequently stored under N_2 at 4 °C.

Powder characterization	Cr	Cr_2N/CrN	Cr_2O_3
Maximum particle size [A] (μm)	45	150	45
BET surface area [A] (m^2/g)	0.69	0.40	1.5
Powder bed thickness [B] (mm)	1.3	0.30 (0.10 [E])	4.7
Powder bed surface [C] (cm^2)	2.4	2.4 (33 [E])	2.4
Void fraction [D] (m^3/m^3)	0.57	0.55	0.83

Table 3.1 Characterization of solid powder beds: A, see Sections 3.2.5 and 3.2.7; B, ± 14.03 %; C, ± 9.44 %; D, ± 5.98 % (all via error propagation); E, electric furnace experiments.

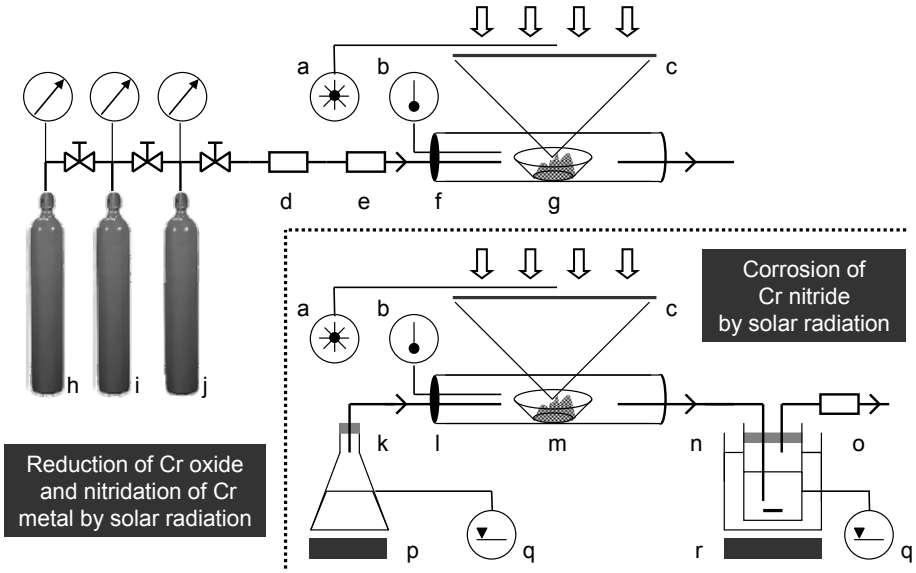

Figure 3.2 Experimental setups (a, solar meter; b, thermocouple; c, Fresnel-lens; d, flashback arrestor; e, flow meter; f, tubular reactor; g, quartz boat; h, N_2; i, 0.695 mol H_2 / mol CO, j, 0.698 mol H_2 / mol CO, diluted in 55 mol% N_2; k, H_2O; l, tubular reactor or electric furnace; m, quartz boat; n, 0.01 mol/l HCl solution chilled with ice-cold H_2O; o, NH_3 gas detection tube; p, heating plate; q, liquid level control; r, magnetic stirrer).

3.3.3 Corrosion of chromium nitride by steam to chromium oxide to liberate ammonia

To assess corrosion of Cr nitride in presence of steam using solar radiation the solar furnace setup was equipped with a heating plate (540 °C T_{max}, Cimarec, Barnstead-Thermolyne) to evaporate H_2O. Steam (average of 1.1 ± 0.1 $ml_{(STP)}$/min) was conducted to a tubular flow-through reactor (48.5 mm ID, 53.5 mm OD, 190 mm length, borosilicate glass). Cr nitride (0.219 g, Table 3.1) was exposed directly for 1 h to 500, 640, 1000 or 1600 ± 100 °C (P_s ~ 0.83 ± 0.03 kW/m^2).

To assess the change in composition of the solid reactant during corrosion using heat only and to further quantify yield and kinetics of NH_3 liberation, an electric resistance furnace (60 mm ID, 1 m length, quartz, model HTF55347C, temperature controller model CC58434C, Lindberg/Blue) was equipped with a heating plate to evaporate H_2O (Fig. 3.2). The steam was conducted to the reactor and condensed and quantified at the furnace outlet in ice water. To remove residual O_2 the furnace was purged for 5 min with 1.9 ± 0.1 $l_{(STP)}$/min N_2 before each experiment.

Cr nitride as purchased (1 g, Table 3.1) or mixed with ground CaO (1 g) was heated to 500, 640, or 1000 ± 1 °C[43, 53, 54]. To test whether the reaction yields were possibly limited by the powder surface available for reaction, at 1000 °C a dispersion of 0.16 g Cr nitride or 0.21 g Cr nitride mixed with 0.21 g CaO was supported by quartz wool (0.9 g or 1.5 g respectively) and placed into a tubular quartz support. Samples were introduced into the furnace at 200-300 °C and heated (~ 47-121 °C/min at 0-3 min, 2-9 °C/min during the last 3 min). Temperatures were held for 60 min and steam was supplied at 0.9 ± 0.2 $ml_{(STP)}$/min. The gas phase leaving the furnace was routed through a liquid absorbent (25 ± 5 ml H_2O). After 60 min the furnace was opened and cooled (~ -210 to -520 °C/min at 0-1 min, -37 to -66 °C/min at 1-3 min).

Reaction kinetics for corrosion of pure Cr nitride powder were determined at 500 and 1000 °C using 0.01 mol/l HCl solutions as liquid absorbent. Samples (5 ml) were taken at 0, 5, 10, and 30 ± 0.5 min after the reaction temperature was reached. All solid samples were stored in air at 4 °C.

3.3.4 Reduction of chromium oxide

To study the reduction of Cr_2O_3 under solar radiation and a reducing gas at 1 bar, 1 g Cr_2O_3 powder (Table 3.1) was exposed for 30 ± 0.5 min to an alternating gas flow of 5 min each of 0.695 mol H_2 / mol CO and H_2/CO/N_2 (0.698 mol H_2 / mol CO, diluted in 55 mol% N_2) and heated directly to 800, 1000, 1200 or 1600 ± 100 °C by concentrated solar radiation (P_s ~ 0.96 ± 0.04 kW/m^2) (Fig. 3.2). Gas compositions were chosen to simulate gasified biomass compositions estimated using $\Delta_{rxn}G$ for the reaction of cellulose with CO_2 at 1 bar and 900 °C (Aspen Plus V7.2).

The furnace was cooled down every 10 min to detect the weight change of the reactant. Experiments at 1600 ± 100 °C were repeated using either H_2/CO or N_2 gas flows for 60 min. Gas flows were turned off at the end of the experiments and the reactor was allowed to cool down to ambient temperature. All solid samples were stored in N_2 at 4 °C. All gas flows were 1.7 ± 0.1 $l_{(STP)}$/min.

3.3.5 Solid state analysis

Powder X-ray diffraction (XRD) patterns were taken with a Miniflex II diffractometer (Cu-target X-ray tube, 30 kV / 15 mA output, diffracted beam monochromator, Rigaku) with a 5-80 °2θ range, °2θ/min scan speed, and 0.02 data points/°2θ, continuous mode for quantitative solid phase identification (PDXL Software Version 1.6.0.0). The relative error of XRD analysis was estimated as ± 7.5 wt%. Energy-dispersive X-ray spectroscopy (EDS) was employed using

the S-3500N scanning electron microscope (20 keV, Hitachi), the Link Pentafet 7021 X-ray detector, and the Inca Energy X-ray analysis software (both Oxford Instruments). All weights were determined using an AE260 DeltaRange balance (± 0.1 mg, Mettler). The specific BET surface area was analyzed by NanoScale Inc., Manhattan, KS.

3.3.6 Liquid phase and gas phase ammonia detection

NH_3 absorbed by the liquid absorbent was quantified with an NH_3 Ion Selective Electrode (ISE) and a pH/ISE Controller (model 270) (both Denver Instrument), combined with the liquid level change in the absorption vessel (error estimated at ± 5 ml). Liquid samples were analyzed in triplicate to estimate the concentration of dissolved NH_3 with zeroing for the signal from pure water (for a representative calibration curve see Appendix B). The uncertainty of NH_3 concentrations was estimated using one standard deviation. To estimate the amount of residual NH_3 contained in the exhaust gas after routing through the absorbent, the outlet of the absorption vessel was equipped with a Dräger tube (range 0.25-3 ppm NH_3, Dräger).

3.3.7 Chemicals

All gases (N_2, He, and Ar) or gas mixtures (41 mol% H_2 in CO, and 18.5 mol% H_2 plus 26.5 mol% CO in N_2) were UHP Zero grade (Linweld).

Solid chemicals were Fe metal (99.9 % pure, -325 mesh), Cr metal (99.86 % pure, -325 mesh), and Cr_2O_3 (99.7% pure, -325 mesh), all from Noah Technologies; Si metal (99.9% pure, -100 mesh) and Cr nitride (98% pure, -100 mesh; XRD analysis 84.6 ± 0.7 wt% Cr_2N, 10.1 ± 0.9 wt% CrN, and 5 ± 1 wt% Cr), both purchased from Prochem; NaOH (99.6%, certified ACS pellets, Fisher Scientific); NH_4Cl (99.5%, extra pure, Acros Organics); and CaO (97.3 % pure, XRD analysis 75 ± 1 wt% CaO and 25 ± 1 wt% $Ca(OH)_2$, Mississippi Lime). Quartz wool (fine,

Leco) was purchased from Fisher Scientific. Glassware was cleaned with acetone (certified ACS, Fisher Scientific).

H_2O was deionized (Direct-Q 3 UV, Millipore) and degassed with He or Ar. Hydrochloric acid (certified ACS Plus) was purchased from Fisher Scientific.

3.4 Results and Discussion

The discussion below follows the overall process scheme (Fig. 3.1). The results of the processes described below are generally reported as a fractional yield X_{rxn}:

$$(3.7) \qquad X_{rxn,t}^{EI,PI} = \frac{n_t^{EI,PI}}{n_0^{EI}} = \frac{s^{EI} \sum_{all\ PI} z_t^{PI} m_t^{PI} / MW^{PI}}{\sum_{all\ EI} z_0^{EI} m_0^{EI} / MW^{EI}}$$

where n_0^{EI} is the number of moles of the element of interest (abbreviated *EI*) in the reactant(s), $n_t^{EI,PI}$ is the number of moles of the *EI* contained in the product(s) of interest (abbreviated *PI*) at a given time, and s^{EI} is a factor accounting for the number of *EI* stoichiometrically contained in *PI*. The distinction between *EI* and *PI* is demonstrated in Figure 3.3.

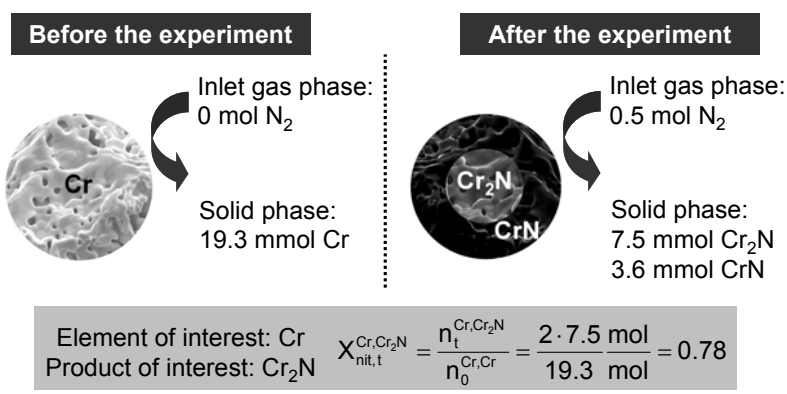

Figure 3.3 Analytical results are reported in this work as fractional yields X_{rxn} here demonstrated for the nitridation of Cr metal powder.

Generally X_{rxn} of Cr metal nitridation (X_{nit}), Cr nitride hydrolysis (X_{hyd}), and Cr oxide reduction (X_{red}) were calculated utilizing XRD to determine solid mass fractions (z), direct weight (m) analysis or the product of liquid volume and concentration measurements using an ISE when

determining the mass of NH_3 liberated during hydrolysis, and the molar weight of the compounds regarded (*MW*). Due to analytical errors (tracked via error propagation) X_{rxn} may be reported within a range extending beyond unity.

Unreacted-core models have been applied successfully to describe gas-solid reactions limited by the diffusion of a reactant through a spherical product shell covering a solid particle[55]. Commonly used to describe gas-solid reactions limited by diffusion[24, 55], Jander's rate law:

$$(3.8) \quad (1-(1-X_{rxn})^{1/3})^2 = k_J t$$

where t is the reaction time, can be derived from the unreacted-core model[55] and is employed in this study for kinetic analyses. The reaction constant k_J is proportional to the diffusion constant of the diffusing reactant and the inverse square of the particle radius. A tangent constructed at the first data point X_{rxn} is used to estimate the initial reaction rate (r_0) given in Table 3.2.

Nitridation of Cr metal powder

experimental conditions	Chemical product	time range (min)	k_J (1/min)	R^2	r_0 (mol N_2 / mol Cr / min)
N_2 flow, 1000 °C	Cr_2N	0 - 11.3	4.18×10^{-2}	0.997	$(4.1 \pm 0.5) \times 10^{-2}$
”	CrN	0 - 11.3	2.73×10^{-6}	0.484	$(5 \pm 4) \times 10^{-4}$
”	Cr_2N	11.3 - 360	2.41×10^{-4}	0.948	$-(3.7 \pm 0.9) \times 10^{-3}$
”	CrN	11.3 - 360	2.03×10^{-4}	0.942	$(7.4 \pm 0.7) \times 10^{-3}$

Liberation of NH_3 from CrN/Cr_2N powder

experimental conditions	Chemical product	time range (min)	k_J (1/min)	R^2	r_0 (mol NH_3 / mol Cr / min)
steam flow, 500 °C	NH_3	0 - 30	1.52×10^{-10}	0.832	$(9 \pm 2) \times 10^{-6}$
steam flow, 1000 °C	NH_3	0 - 30	2.33×10^{-8}	0.999	$(1.1 \pm 0.2) \times 10^{-4}$

Reduction of Cr_2O_3 powder

experimental conditions	Chemical product	time range (min)	k_J (1/min)	R^2	r_0 (mol Cr / mol Cr_2O_3 / min)
$CO/H_2/N_2$ flow, 800 °C	Cr	0 - 10	3.34×10^{-9}	0.964	$(1 \pm 1) \times 10^{-4}$
$CO/H_2/N_2$ flow, 1000 °C	Cr	0 - 10	7.01×10^{-8}	0.844	$(7 \pm 1) \times 10^{-4}$
$CO/H_2/N_2$ flow, 1200 °C	Cr	0 - 30	5.49×10^{-7}	0.948	$(1.6 \pm 0.2) \times 10^{-3}$
$CO/H_2/N_2$ flow, 1600 °C	Cr	0 - 30	2.82×10^{-6}	0.982	$(2.8 \pm 0.2) \times 10^{-3}$
N_2 flow, 1600 °C	Cr	0 - 60	1.39×10^{-7}	0.885	$(8 \pm 1) \times 10^{-4}$
CO/H_2 flow, 1600 °C	Cr	0 - 50	3.82×10^{-6}	0.930	$(2.7 \pm 0.2) \times 10^{-3}$

Table 3.2 Reaction kinetics of the solar thermochemical NH_3 production cycle. Errors indicated were derived via error propagation.

3.4.1 Nitrogen fixation: Nitridation of chromium metal with N_2 gas

Cr metal powder was nitridated (Rxn. 3.3) at 1000 °C in a flow of N_2 under concentrated solar radiation. As expected[47, 50-52, 56, 57] Cr converted quickly and essentially quantitatively to hexagonal Cr_2N (94 ± 2 mol% X_{nit} after 11.3 min) (Fig. 3.4A) which converted subsequently into cubic CrN (68 ± 2 mol% X_{nit} after 360 min) (Fig. 3.4B).

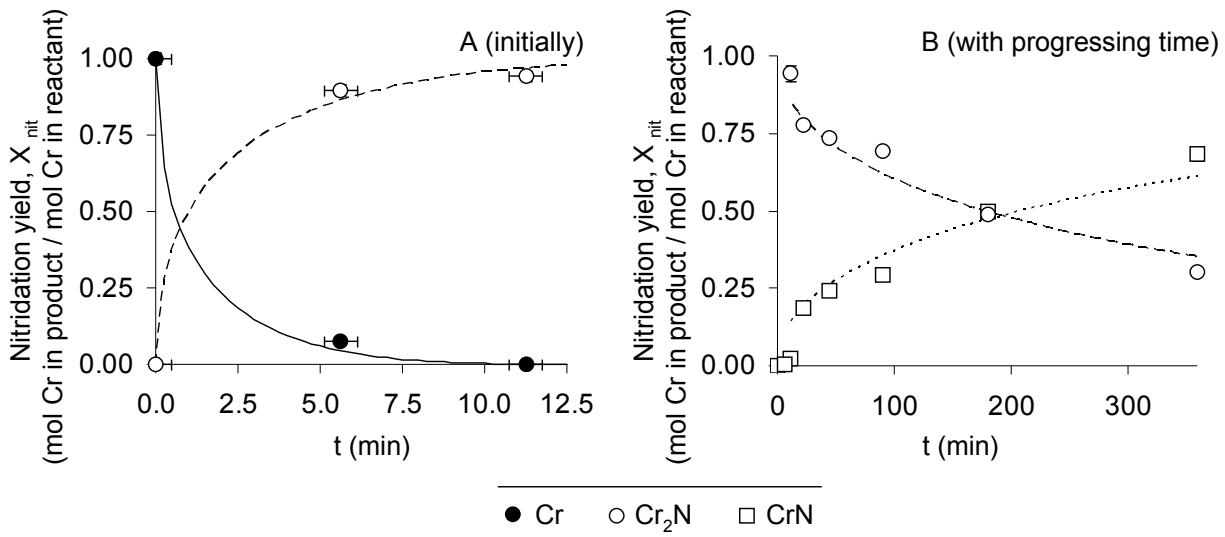

Figure 3.4 N_2 fixation using Cr metal and concentrated sunlight. Jander's unreacted core model is fitted to the data. Analytical uncertainty was ± 7.89 % (error propagation). The uncertainty on the abscissa is estimated as 0.5 min.

EDS confirmed qualitatively the fixation of N (see Appendix B). Slow conversion to CrN is expected[58, 59] due to the required diffusion of N_2 into the solid bed and diffusion of N through the solid nitride shell formed initially around the remaining metal towards the center of the particle (Fig. 3.3). Decreasing N-diffusivity with increasing N-concentration in Cr nitride has been reported previously[59]. Accounting for diffusion-limited mass transfer in the solid state, results are well described by an unreacted core model as shown in Fig. 3.3 and Table 3.2. O_2 as a contaminant in N_2 gas has been reported to form a Cr_2O_3 layer on the surface of CrN at 600-1000 °C[50]. Only insignificant amounts of Cr_2O_3 were detected in the experiments described here (2.3 wt% after 11.3 min). Formation of CrN detected after consumption of Cr to below the detection

limit of XRD (Fig. 3.4B) is evidence for indirect formation of CrN from an intermediate Cr_2N phase[56, 58].

In summary, fixation of N from N_2 gas using Cr powder in a solar furnace at atmospheric pressure was confirmed quantitatively and modeled successfully. The relatively fast kinetics for Cr_2N formation are promising for practical application.

3.4.2 Ammonia formation: Corrosion of chromium nitride with steam

Significant formation of NH_3 (Rxn. 3.4) is not expected during hydrolysis of Cr nitrides. Steam hydrolysis of Cr nitride resulting in NH_3 formation[43, 60, 61] reported previously has not been quantified before. Cr nitride is well known in applications for protective coatings of tools and machine parts[53, 54, 58, 62] due in part to its high corrosion resistance. The high Cr-N bond energy of 64 or 123 kJ/mol Cr in Cr_2N or CrN respectively[41] inhibits desorption of N[63]. At temperatures below 178 °C[41] steam corrosion of Cr nitride favors formation of NH_3 over the formation of N_2 if the N released is protonated. At this temperature slow reaction kinetics unfortunately prohibit approaching the reaction equilibrium in a practical process.

3.4.2.1 Nitride corrosion kinetics limiting NH_3 formation

Heating at 500 or 640 °C in the electrical furnace liberated 2-10 mol% of N from Cr_2N and CrN (Fig. 3.5A) and formed Cr_2O_3 (Fig. 3.6A). Only 0.01-0.03 mol% of the N liberated is recovered as NH_3 (Fig. 3.5B). At 1000 °C an increased loss of N from the solid is found with increased concentration of Cr_2O_3 and CrN, and increased recovery of N in form of NH_3 (Fig. 3.5, Fig. 3.6A). Other than NH_3, only N_2 is assumed to be formed from the N liberated due to thermal nitride decomposition[64-66]. As opposed to a shrinking core model fit[24], data were represented well with an unreacted core model (Table 3.2) accounting for mass transfer limitations due to diffusion of reactive species through a layer of solid Cr_2O_3 formed on the surface of the nitride

(Eq. 3.8). Thus, NH_3 formation while favored thermodynamically at lower temperatures appears to be increased at higher temperatures (Fig. 3.5B) due to accelerated solid state diffusion (decreased mass transfer limitations) and thus accelerated apparent corrosion kinetics are found at higher temperatures (Fig. 3.5A, Fig. 3.6A).

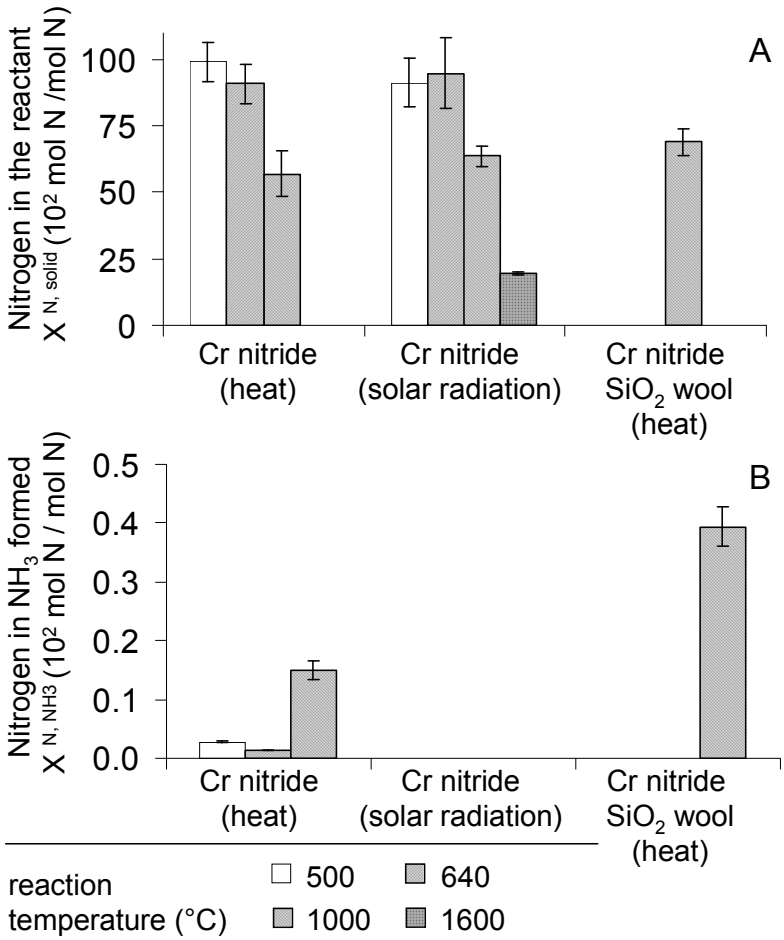

Figure 3.5 Liberation of NH_3 due to hydrolysis of Cr nitride: solid phase composition (A), NH_3 absorbed into a liquid absorbent (B). Error bars are via error propagation.

The poor NH_3 recovery illustrates the necessity of complementing a reactant for reactive NH_3 synthesis with reactive sites of another element liberating sufficient quantities of NH_3 in situations far from thermodynamic equilibrium.

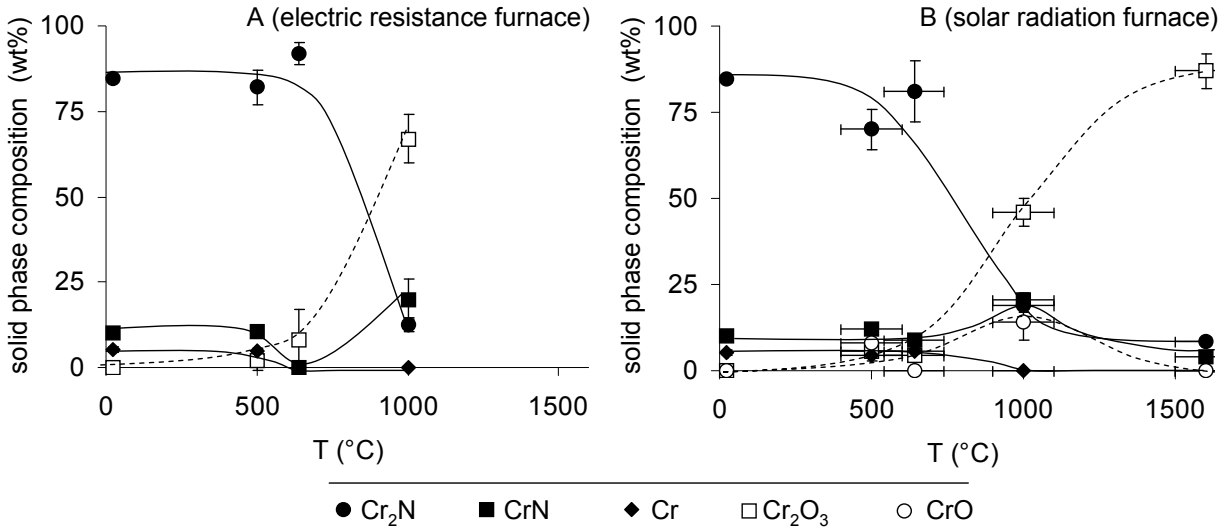

Figure 3.6 Composition change of the solid reactant during Cr nitride corrosion. Lines are added to guide the eye. Uncertainties of data shown on the ordinate are given by X-ray diffraction. Uncertainties on the abscissa are estimated at ± 1 °C (A) and ± 100 °C (B).

3.4.2.2 Investigating CaO/Ca(OH)$_2$-assisted protonation of nitrogen to ammonia

The presence of CaO/Ca(OH)$_2$ during corrosion of Cr nitride[19, 43] may increase the concentration of Lewis acid centers (unsaturated Ca^{2+} cations) on the reactant surface thereby assisting protonation of N[67]. Hydrolyzing Cr nitride mixed with equal masses of CaO confirmed (see Appendix B) trends of N liberated from the nitride forming more NH_3. NH_3 yield increased 1.56 fold (0.24 ± 0.01 mol% NH_3 relative to mol lattice nitrogen) when hydrolyzing Cr nitride with steam at 1000 °C in the presence of CaO/Ca(OH)$_2$ vs. no CaO/Ca(OH)$_2$. This slight improvement is evidence for surface limitations or low N^{3-} concentrations in the nitride limiting the formation of NH_3[64]. Excess electrons after formation of Cr_2O_3 may rather react with protons originating from splitting H_2O, such that N atoms are able to form N_2 molecules. Substantial formation of NH_3 may be further promoted by the presence of a more ionic reactant than Cr_2N/CrN.

3.4.2.3 Surface limitations

To test if reaction yields are limited by the powder surface available for reaction, Cr nitride dispersed on high-surface quartz wool (SiO_2) was heated in steam at 1000 °C. Although this modification did not significantly change the yield of N liberated (Fig. 3.5A) recovery of N in form of NH_3 increased 2.61 fold (0.39 ± 0.03 mol% NH_3 relative to mol N in the nitride) relative to hydrolysis in absence of the SiO_2 wool (Fig. 3.5B). Mass transfer resistance due to diffusion of NH_3 from a solid powder bed into the gas phase is reduced or eliminated in this experiment. Results are evidence for an increased yield of NH_3 due to an increased availability of effective reactive surface sites forming NH_3 that is removed quickly before N_2 formation. Given the reaction of surface nitrides forming NH_3 via corrosion[60, 61] an essentially constant yield of N liberated (Fig. 3.5A) can be explained by conversion of the nitride below the particle surface into Cr_2O_3 and N_2 via outward diffusion of Cr ions through the oxide layer formed and formation of N_2 molecules from insufficiently charged N atoms[53, 60].

3.4.2.4 Beneficial effects of concentrated solar radiation vs. high temperature only

Heating in a solar furnace that allows radiation to enter the reactor has benefits over a setup where only high temperature is used, such as in a conventional oven or a "closed" solar reactor. Formation of CrO and Cr_2O_3 during nitride hydrolysis via solar radiation (Fig. 3.6B) was compared to the formation of Cr_2O_3 only in a conventional furnace (Fig. 3.6A). CrO is beneficial for the recovery of Cr from its oxide due to the lower O to Cr ratio compared to Cr_2O_3. This will result in proportionally less reducing agent needed per mol of Cr recovered.

3.4.3 Reactant recycling: Reduction of Cr_2O_3 to Cr with simulated syngas

Recovery of Cr metal from Cr oxide is necessary to close the thermochemical cycle (Fig. 3.1). Cr_2O_3 was reduced carbothermally at above 1000 °C using solid graphite powder[43, 45, 68].

Using a reducing gas instead of a solid avoids cumbersome handling and mixing of two solids. This would be especially challenging on a technical scale. It will be demonstrated that the gas-solid route (Rxn. 3.1 and 3.2) is promising as the final synthesis step if a high specific reactant surface area is maintained.

3.4.3.1 Suggested reaction mechanism

Reduction starts quickly when exposing Cr_2O_3 to a reducing gas composition (H_2/CO or H_2/CO/N_2). Higher temperatures lead to accelerated conversion (Fig. 3.7A). A maximum apparent reduction yield of 3.64 ± 0.06 mol% (1.15 ± 0.02 wt% weight loss) was obtained if Cr_2O_3 powder was exposed for 40 min to a flow of 1.7 ± 0.1 $l_{(STP)}$ H_2/CO (0.695 mol/mol) / min and solar radiation at 1600 °C (Fig. 3.7B).

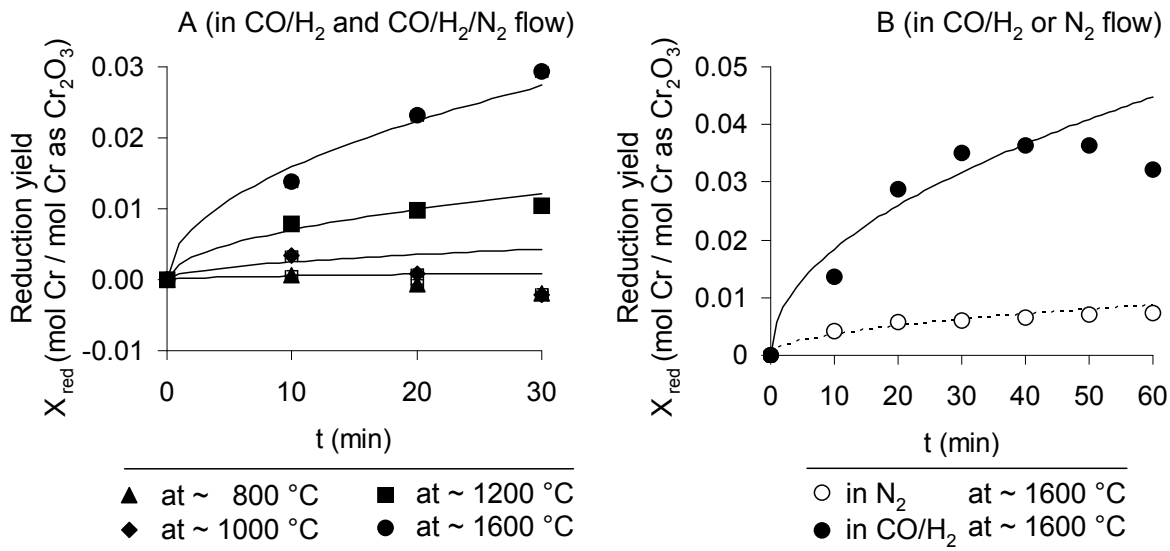

Figure 3.7 Yield of Cr_2O_3 reduction (A, alternate gas flows of 5 min 0.695 mol H_2 / mol CO and 5 min 0.698 mol H_2 / mol CO, diluted in 55 mol% N_2; B, 0.695 mol H_2 / mol CO or N_2). Jander's unreacted core model (lines) is fit to the data. Analytical uncertainty was ± 10.32 % (error propagation). The uncertainty on the abscissa is estimated at 0.5 min.

Jander's rate law yields a reasonable fit (Fig. 3.7, Table 3.2) except for a mass increase when Cr_2O_3 powder was heated with a chemical reducing agent for > 10 min at 800 °C or 1000

°C, or > 50 min at 1600 °C respectively. The underlying assumption that all weight loss is due to oxygen-removal will be verified below. Simply heating Cr_2O_3 at 1600 °C in a flow of N_2 resulted in an apparent reduction yield of only 0.73 ± 0.06 mol% (Fig. 3.7B). This can be attributed to the evaporation of minor components such as 0.73 mol% H_2O, Al, and Ca (certificate of analysis, Noah Technologies). Rationalizing the unexpected weight gain (Fig. 3.7) accompanied by visual black discoloration through deposition of amorphous carbon on the solid offers the possibility of carbothermal Cr_2O_3 reduction[43, 45, 68]. Although reduction of Cr_2O_3 by H_2[43, 44] or CO[42] in systems open to mass exchange has been reported, oxidation of C is favored thermodynamically over oxidation of CO or H_2[41]. This is proposed in this work as the initial step of Cr_2O_3 reduction: carbon supplied from the gas phase (CO) is disproportionated via the Boudouard reaction (at equilibrium < 710 °C[41]) and deposited in form of amorphous C on the solid reactant surface.

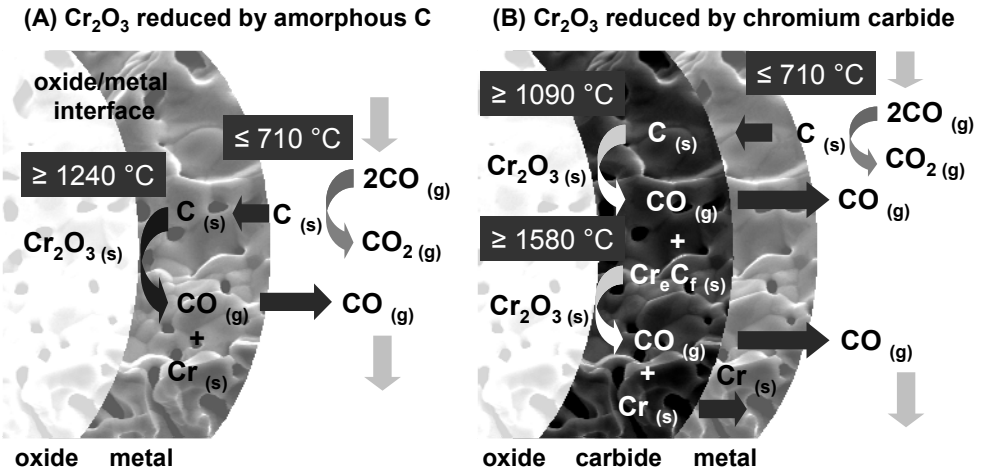

Figure 3.8 Cr_2O_3 reduction scenarios: oxide reduction at the oxide-metal interface (A), or oxide reduction at the oxide-carbide (Cr_eO_f) interface (B).

Accelerated by increased temperatures, varying in the solar furnace, C atoms diffuse after deposition on the particles through a solid layer of Cr metal and reduce Cr_2O_3 (reaction equilibrium at approximately 1240 °C[41]) at the oxide-metal interface (Fig. 3.8A). Alternatively, reduction of Cr_2O_3 by carbon may proceed with formation of chromium carbides (such as Cr_4C,

Cr_7C_3, or Cr_3C_2)[45, 46], commencing at lower temperatures (above 1090°C[41]). Cr would then be formed at the carbide-oxide interface (above 1580 °C[41]) due to reaction of Cr oxide with Cr carbide[68] (Fig. 3.8B). The Cr carbide phase involved in this reduction mechanism may be transient if it is consumed in the metal formation.

Experiments were performed to test the hypothesis that Cr_2O_3 particles are reduced by carbon at the oxide-metal interface. As-purchased Cr_2O_3 powder or samples of the surface of Cr_2O_3 samples after 60 min exposure to solar radiation at 1600 °C and a flow of N_2 or H_2/CO respectively were analyzed using EDS and XRD (Fig. 3.9). The atomic ratio, R_a = mol O or C / mol Cr, obtained shows a significantly decreased concentration of O in Cr_2O_3 in agreement with the hypothesized oxide reduction. XRD indicated the appearance of the expected and desired cubic Cr metal phase. EDS shows a significantly increased concentration of C in the surface of Cr_2O_3 samples heated in a chemically reducing atmosphere (detection of C in unprocessed Cr_2O_3 samples and in samples heated in N_2 flow arise likely from organic contamination). The presence of a stable Cr carbide (or nitride) phase could however not be detected using XRD.

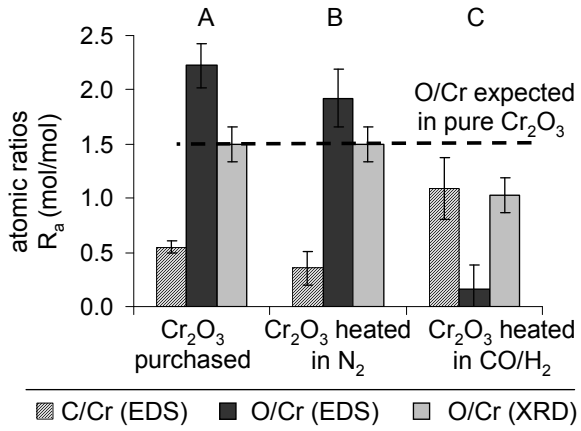

Figure 3.9 Cr_2O_3 powder as purchased (A) or heated for 60 min at 1600 °C by concentrated solar radiation in N_2 (B) or 0.695 mol H_2 / mol CO (C) was analyzed determining the atomic ratio C or O / Cr (R_a) by EDS (at best semi-quantitative, see Section 1.4.4.1) and XRD. Error bars are by error propagation.

The experimental results support direct reduction of Cr_2O_3 particles by amorous carbon (Fig. 3.8A) which accumulates on the particles when reduction of the near-surface oxide is approaching completion (Fig. 3.7B). This can be avoided by terminating the reduction process appropriately. Appendix B provides a supportive EDS analysis of the oxygen and content of the solids versus the reaction temperature.

3.4.3.2 Mass transfer limitations of Cr_2O_3 reduction via the gas-solid route

Leveling and decreased apparent reduction yields (Fig. 3.7) arising from amorphous carbon deposited on the particle surface (Fig. 3.9 and Section 3.4.3.1) imply that the mass transport below the surface of the particle is the rate limiting reduction step. Low apparent reduction yields of Cr_2O_3 can be rationalized when accounting for a large mass of bulk material not available in the experimental setup for reduction on the surface or even at marginal distance from the surface of Cr_2O_3 particles.

Using the slope of a linear regression (R^2 = 0.969) of four kinetic constants (Eq. 3.8, Table 3.2) plotted versus the inverse temperature yields the activation energy of Cr_2O_3 reduction with ~ 128 ± 4 kJ/mol (0.012 1/min, constant factor of the Arrhenius equation utilized, see Appendix B). Activation energies for carbothermal Cr_2O_3 reduction reported in the range of 72-182 kJ/mol[69] support the hypothesis of reduction of Cr_2O_3 by C. The magnitude of the activation energy implies diffusion-controlled Cr_2O_3 reduction[69]. Thus, the delayed weight gain (i.e., carbon deposition on the metal surface) when heating at higher temperatures (Fig. 3.7) can be rationalized with an increased diffusion constant at increased temperature enhancing the consumption of C and formation of Cr. Heating Cr_2O_3 for 60 min at 1600 °C in a flow of H_2 and CO resulted in formation of an approximately 10 μm thick layer of sponge-like Cr[43] with visually metallic appearance, similar to "sponge iron" (Fig. 3.10). When heated in an inert

atmosphere Cr_2O_3 particles crystallized[43] (Fig. 3.10), without formation of the metal. Assuming removal of oxygen in a 10 µm thick shell only (Fig. 3.10) of a spherical Cr_2O_3 particle (Table 3.1) correlates to a reduction yield of 82.85 mol% when exposing Cr_2O_3 for 40 min to a flow of H_2/CO and solar radiation at 1600 °C (Fig. 3.7B).

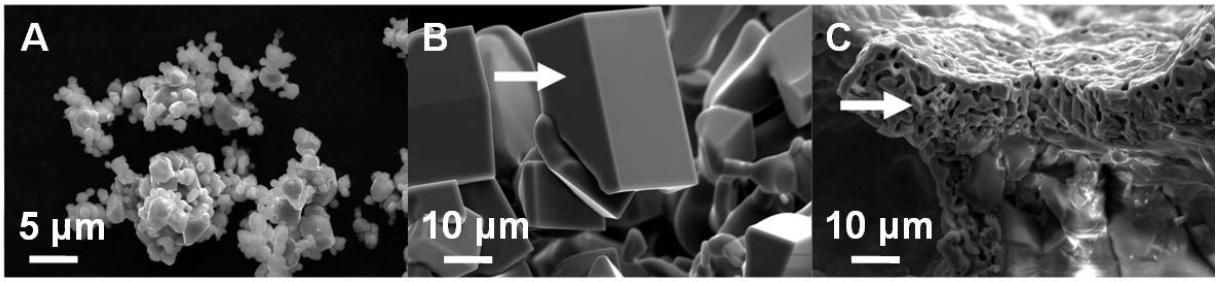

Figure 3.10 Scanning electron micrographs of Cr_2O_3: as-purchased (A), heated for 60 min at 1600 °C by concentrated solar radiation in N_2 (B) or in 0.695 mol H_2 / mol CO (C).

In summary, a fast surface reaction (Fig. 3.7, Table 3.2) reduces Cr_2O_3 initially and produces amorphous carbon due to temperatures varying locally on the reactant surface and due to the use of a gas flow shifting the chemical equilibrium by product removal[70]. With longer reaction times the reaction slows down due to the required diffusion of C and CO through the solid Cr phase formed. This implies that diffusion below the particle surface is dominating the mass transfer rather than diffusion of gaseous reactants and products between the gas phase and the solid phase. Due to fast reaction kinetics and high yields of Cr_2O_3 reduction using a gaseous reducing agent and relatively low temperatures Cr appears to be a promising reactant constituent for solar thermochemical NH_3 production.

3.5 Conclusions

A prospective material allowing sustainable NH_3 synthesis from N_2 and H_2O through a solar thermochemical reaction cycle may make use of more than one chemical element. This will

facilitate a trade-off between the technical difficulties of N_2 fixation and NH_3 liberation on one hand and oxide reduction on the other hand.

Cr was found to be a good material for N_2 fixation. Cr readily breaks the N_2 triple bond forming Cr_2N from its elements via solar heating at 1000 °C. The reaction equilibrium is approached at approximately 5 min.

In the presence of solar radiation, hydrolysis of Cr nitride at 1 bar and at 1000 °C formed both CrO and Cr_2O_3 as opposed to only Cr_2O_3 in a conventional furnace. Application of solar radiation therefore decreases the need for a chemical reducing agent (i.e., operational costs). Liberation of only traces of NH_3 during hydrolysis of Cr nitride is evidence for corrosion kinetically limiting NH_3 liberation from Cr nitride. The presence of CaO particles in the solid reactant was not sufficient to promote the formation of NH_3 since N atoms bonded with Cr atoms would need to diffuse to neighboring CaO particles. The presence of an alkaline earth metal nitride or aluminum nitride on the surface of a prospective composite reactant may enable adequate formation of NH_3 from reactive nitrogen liberated.

Reactive Cr sites on the surface of such a reactant may decrease required reduction temperatures during reactant recycling and may thus facilitate the challenging and costly construction of solar furnaces. Solar thermochemical reduction of Cr_2O_3 using simulated gasified biomass as gaseous reducing agent to avoid handling and mixing of two solids shows an initially fast and presumably reaction-controlled surface reaction forming Cr metal between 1200 and 1600 °C and producing carbon due to CO disproportionation. The layer of Cr metal formed decreases the apparent reduction kinetics due to required diffusion of C and CO through the metal phase formed. The availability of reactive atoms of two types on the surface and in close

proximity deserves utmost attention when designing a solid reactant for solar thermochemical NH_3 synthesis.

In summary, chromium shows some of the characteristics needed for a realistic solar thermochemical ammonia synthesis process operating at atmospheric pressure and without natural gas as hydrogen or energy source. The challenge of nitrogen fixation and subsequent metal recovery should be addressed via composite reactants with a well-designed surface distribution of two elements where one easily reduces nitrogen to N^{3-} and liberates the reduced nitrogen in form of NH_3 via hydrolysis, while the other assists in metal oxide reduction.

3.6 Associated content in Appendix B

Supporting Information: Representative calibration curve of the NH_3 analysis in the liquid phase using an ISE, EDS data confirming qualitatively the N_2 reducing with Cr and the Cr_2O_3 reduction with CO/N_2, NH_3 formation via steam hydrolysis of chromium nitride mixed with calcium oxide/hydroxide (completed Fig. 3.5), and the Arrhenius plot to estimate the activation energy of the Cr_2O_3 reduction.

3.7 References

1 V. Smil, Population growth and nitrogen: An exploration of a critical existential link, Population and Development Review, 17 (1991) 569-601.

2 http://www.ers.usda.gov/Data/FertilizerUse (retrieved March, 2011)

3 D.A. Kramer, Nitrogen (fixed) - Ammonia, U.S. Geological Survey, Mineral Commodity Summaries (2003) 118-119.

4 P. Wang, X.D. Kang, Hydrogen-rich boron-containing materials for hydrogen storage, Dalton Transactions, (2008) 5400-5413.

5 T. Lipman, N. Shah, Ammonia as an alternative energy storage medium for hydrogen fuel cells: Scientific and technical review for near-term stationary power demonstration projects (Final Research Report, UCB-ITS-TSRC-RR-2007-5), Institute of Transportation Studies UC Berkeley Transportation Sustainability Research Center (University of California, Berkeley), 2007.

[6] C.H. Christensen, T. Johannessen, R.Z. Sørensen, J.K. Nørskov, Towards an ammonia-mediated hydrogen economy?, Catalysis Today, 111 (2006) 140-144.

[7] A.J. Reiter, S.C. Kong, Combustion and emissions characteristics of compression-ignition engine using dual ammonia-diesel fuel, Fuel, 90 (2011) 87-97.

[8] J.A. Pool, E. Lobkovsky, P.J. Chirik, Hydrogenation and cleavage of dinitrogen to ammonia with a zirconium complex, Nature, 427 (2004) 527-530.

[9] A.V. Slack, G. Russell James, Ammonia Marcel Dekker, Inc., New York, 1977.

[10] Z. Kirova-Yordanova, Exergy analysis of industrial ammonia synthesis, Energy, 29 (2004) 2373-2384.

[11] I. Rafiqul, C. Weber, B. Lehmann, A. Voss, Energy efficiency improvements in ammonia production - perspectives and uncertainties, Energy, 30 (2005) 2487-2504.

[12] S.K. Ritter, The Haber-Bosch reaction: An early chemical impact on sustainability, Chemical & Engineering News, 86 (2008) 53.

[13] W.-Y. Huang, Impact of rising natural gas prices on U.S. ammonia supply / WRS-0702 / A report from the Economic Research Service, www.ers.usda.gov (retrieved September, 2010)

[14] L.C. Skinner, H.R. Batchelder, S. Katell, Comparative cost study of ammonia plants - using either natural gas or coal gasification as a source of synthesis gas, Industrial and Engineering Chemistry, 44 (1952) 2381-2385.

[15] D.V. Yandulov, R.R. Schrock, Catalytic reduction of dinitrogen to ammonia at a single molybdenum center, Science, 301 (2003) 76-78.

[16] M. Lerch, J. Janek, K.D. Becker, S. Berendts, H. Boysen, T. Bredow, R. Dronskowski, S.G. Ebbinghaus, M. Kilo, M.W. Lumey, M. Martin, C. Reimann, E. Schweda, I. Valov, H.D. Wiemhöfer, Oxide nitrides: From oxides to solids with mobile nitrogen ions, Progress in Solid State Chemistry, 37 (2009) 81-131.

[17] A. Skodra, M. Stoukides, Electrocatalytic synthesis of ammonia from steam and nitrogen at atmospheric pressure, Solid State Ionics, 180 (2009) 1332-1336.

[18] F. Haber, G. van Oordt, Über die Bildung von Ammoniak aus den Elementen, Zeitschrift für anorganische Chemie, 44 (1905) 341-378.

[19] E.B. Maxted, Ammonia and the nitrides, J. & A. Churchill, London, 1921.

[20] V. Sauchelli, Fertilizer nitrogen its chemistry and technology, Reinhold Publishing Corporation, New York, 1964.

[21] G. Lunge, Coal-tar and ammonia, Gurney and Jackson, London, 1916.

[22] M.E. Gálvez, A. Frei, F. Meier, A. Steinfeld, Production of AlN by Carbothermal and Methanothermal Reduction of Al_2O_3 in a N_2 Flow Using Concentrated Thermal Radiation, Industrial & Engineering Chemistry Research, 48 (2009) 528-533.

[23] M.E. Gálvez, I. Hischier, A. Frei, A. Steinfeld, Ammonia production via a two-step Al_2O_3/AlN thermochemical cycle. 3. influence of the carbon reducing agent and cyclability, Industrial & Engineering Chemistry Research, 47 (2008) 2231-2237.

[24] M.E. Gálvez, A. Frei, M. Halmann, A. Steinfeld, Ammonia production via a two-step Al_2O_3/AlN thermochemical cycle. 2. Kinetic analysis, Industrial & Engineering Chemistry Research, 46 (2007) 2047-2053.

[25] M.E. Gálvez, M. Halmann, A. Steinfeld, Ammonia production via a two-step Al_2O_3/AlN thermochemical cycle. 1. Thermodynamic, environmental, and economic analyses, Industrial & Engineering Chemistry Research, 46 (2007) 2042-2046.

[26] D. Suresh, P.K. Rohatgi, J.P. Coutures, Use of solar furnaces .1. Materials research, Solar Energy, 26 (1981) 377-390.

[27] A. Steinfeld, A.W. Weimer, Thermochemical production of fuels with concentrated solar energy, Optics Express, 18 (2010) A100-A111.

[28] R. Palumbo, J. Lédé, O. Boutin, E.E. Ricart, A. Steinfeld, S. Möller, A. Weidenkaff, E.A. Fletcher, J. Bielicki, The production of Zn from ZnO in a high-temperature solar decomposition quench process - I. The scientific framework for the process, Chemical Engineering Science, 53 (1998) 2503-2517.

[29] A. Steinfeld, C. Larson, R. Palumbo, M. Foley, Thermodynamic analysis of the co-production of zinc and synthesis gas using solar process heat, Energy, 21 (1996) 205-222.

[30] T. Kodama, High-temperature solar chemistry for converting solar heat to chemical fuels, Progress in Energy and Combustion Science, 29 (2003) 567-597.

[31] J.P. Murray, A. Steinfeld, E.A. Fletcher, Metals, nitrides, and carbides via solar carbothermal reduction of metal-oxides, Energy, 20 (1995) 695-704.

[32] J.P. Murray, E.A. Fletcher, Reaction of steam with cellulose in a fluidized-bed using concentrated sunlight, Energy, 19 (1994) 1083-1098.

[33] J. Lédé, Reaction temperature of solid particles undergoing an endothermal volatilization - Application to the fast pyrolysis of biomass, Biomass & Bioenergy, 7 (1994) 49-60.

[34] C.J.H. Jacobsen, S. Dahl, B.S. Clausen, S. Bahn, A. Logadottir, J.K. Nørskov, Catalyst design by interpolation in the periodic table: Bimetallic ammonia synthesis catalysts, Journal of the American Chemical Society, 123 (2001) 8404-8405.

[35] G. Ertl, S.B. Lee, M. Weiss, Kinetics of nitrogen adsorption on Fe(111), Surface Science, 114 (1982) 515-526.

[36] J.E. Miller, M.D. Allendorf, R.B. Diver, L.R. Evans, N.P. Siegel, J.N. Stuecker, Metal oxide composites and structures for ultra-high temperature solar thermochemical cycles, Journal of Materials Science, 43 (2008) 4714-4728.

[37] M. Roeb, H. Müller-Steinhagen, Concentrating on solar electricity and fuels, Science, 329 (2010) 773-774.

[38] A.G. Cairns, J.G. Gallagher, J.S.J. Hargreaves, D. McKay, E. Morrison, J.L. Rico, K. Wilson, The influence of precursor source and thermal parameters upon the formation of beta-phase molybdenum nitride, Journal of Alloys and Compounds, 479 (2009) 851-854.

[39] M. Jacoby, Rechargeable metal-air batteries, Chemical and Engineering News, 88 (2010) 29-31.

[40] C. Sierra, A.J. Vázquez, High solar energy concentration with a Fresnel lens, Journal of Materials Science, 40 (2005) 1339-1343.

[41] I. Barin, O. Knacke, Thermochemical properties of inorganic substances, Springer-Verlag, Berlin Heidelberg New York, 1973.

[42] T. Hashizume, K. Terayama, T. Shimazaki, H. Ito, Carbothermic reduction mechanism of Cr_2O_3, Journal of High Temperature Society, 27 (2001) 299-305.

[43] R.J. Meyer, E.H.E. Pietsch, A. Kotowski, Gmelins Handbuch der Anorganischen Chemie, Verlag Chemie GmbH, Weinheim/Bergstrasse, 1962.

[44] F. Trombe, M. Foëx, Essai de métallurgie du chrome par l'hydrogène au four solaire, Revje de Metallurgie, XLVIII (1951) 359-362.

[45] L.M. Berger, S. Stolle, W. Gruner, K. Wetzig, Investigation of the carbothermal reduction process of chromium oxide by micro- and lab-scale methods, International Journal of Refractory Metals & Hard Materials, 19 (2001) 109-121.

[46] X.G. Zheng, D.J. Young, High-temperature corrosion of Cr_2O_3-forming alloys in CO-CO_2-N_2 atmospheres, Oxidation of Metals, 42 (1994) 163-190.

[47] P. Biedenkopf, T. Karwath, D. Kobertz, M. Rane, E. Wessel, K. Hilpert, L. Singheiser, Vaporization and corrosion of refractories in the presence of pressurized pulverized coal combustion slag, Journal of the American Ceramic Society, 84 (2001) 1445-1452.

[48] D.J. Young, B.A. Pint, Chromium volatilization rates from Cr_2O_3 scales into flowing gases containing water vapor, Oxidation of Metals, 66 (2006) 137-153.

[49] F. Duerr, Y. Meuret, H. Thienpont, Miniaturization of Fresnel lenses for solar concentration: a quantitative investigation, Applied Optics, 49 (2010) 2339-2346.

[50] Y.S. Ho, F.S. Huang, F.H. Lu, Influences of oxygen impurity contained in nitrogen gas on the reactions of chromium with nitrogen, Journal of Materials Research, 20 (2005) 2745-2753.

[51] G. Mangamma, T.N. Sairam, S. Dash, M. Rajalakshmi, M. Kamruddin, V.K. Mittal, S.V. Narasimhan, A.K. Arora, C.S. Sundar, A.K. Tyagi, B. Raj, Spectroscopic characterization of nanocrystalline chromium nitride (CrN), Journal of Nanoscience and Nanotechnology, 7 (2007) 970-976.

[52] Y.G. Li, L. Gao, G.G. Li, D.S. Yan, Synthesis of nanocrystalline chromium nitride powders by direct nitridation of chromium oxide, Journal of the American Ceramic Society, 85 (2002) 1294-1296.

[53] I. Milošev, J.M. Abels, H.H. Strehblow, B. Navinšek, M. Metikoš-Huković, High temperature oxidation of thin CrN coatings deposited on steel, Journal of Vacuum Science & Technology A - Vacuum Surfaces and Films, 14 (1996) 2527-2534.

[54] F.H. Lu, H.Y. Chen, C.H. Hung, Degradation of CrN films at high temperature under controlled atmosphere, Journal of Vacuum Science & Technology A, 21 (2003) 671-675.

[55] A. Shimizu, Y.J. Hao, Influence of particle contact on the estimation of powder reaction kinetics of binary mixtures, Journal of the American Ceramic Society, 80 (1997) 557-568.

[56] H.Y. Lee, S.H. Lee, J.H. Kim, M.C. Kim, D.M. Wee, Formation behavior of Cr-nitride by thermal nitridation in two-phase Cu-Cr alloy for application in metallic separators in PEMFCs, Journal of the Korean Institute of Metals and Materials, 45 (2007) 602-608.

[57] P.H. Mayrhofer, F. Rovere, M. Moser, C. Strondl, R. Tietema, Thermally induced transitions of CrN thin films, Scripta Materialia, 57 (2007) 249-252.

[58] C. Real, M.A. Roldán, M.D. Alcalá, A. Ortega, Synthesis of nanocrystalline chromium nitride powder by mechanical processing, Journal of the American Ceramic Society, 90 (2007) 3085-3090.

[59] W. Mayr, W. Lengauer, P. Ettmayer, D. Rafaja, J. Bauer, M. Bohn, Phase equilibria and multiphase reaction diffusion in the Cr-C and Cr-N systems, Journal of Phase Equilibria, 20 (1999) 35-44.

[60] P.R. Levey, A. van Bennekom, The involvement of alloyed nitrogen in the corrosion of stainless steels, Journal of the South African Institute of Mining and Metallurgy, 95 (1995) 337-346.

[61] P.R. Levey, A. van Bennekom, A mechanistic study of the effects of nitrogen on the corrosion properties of stainless-steels, Corrosion, 51 (1995) 911-921.

[62] J.L. Mo, M.H. Zhu, Tribological characterization of chromium nitride coating deposited by filtered cathodic vacuum arc, Applied Surface Science, 255 (2009) 7627-7634.

[63] J.C. Ganley, F.S. Thomas, E.G. Seebauer, R.I. Masel, A priori catalytic activity correlations: the difficult case of hydrogen production from ammonia, Catalysis Letters, 96 (2004) 117-122.

[64] H.O. Pierson, Handbook of refractory carbides and nitrides, Noyes Publications, Westwood, New Jersey, 1996.

[65] K.H. Linke, K. Schrödter, Contributions to chemistry of hydrazine and its derivatives .47. Partial reduction of nitrogen molecule to N_2^{4-}-ion by means of barium, Zeitschrift für Anorganische und Allgemeine Chemie, 413 (1975) 165-170.

[66] J. Gaudé, J. Lang, Presence of hydrazine among products of strontium nitride hydrolysis, Comptes Rendus Hebdomadaires Des Seances De L Academie Des Sciences Serie C, 271 (1970) 510-512.

[67] A.M. Heyns, L.C. Prinsloo, K.J. Range, M. Stassen, The vibrational spectra and decomposition of alpha-calcium nitride (alpha-Ca_3N_2) and magnesium nitride (Mg_3N_2), Journal of Solid State Chemistry, 137 (1998) 33-41.

[68] T. Mori, J. Yang, M. Kuwabara, Mechanism of carbothermic reduction of chromium oxide, ISIJ International, 47 (2007) 1387-1393.

[69] M.B.C. Tsomondo, D.J. Simbi, Kinetics of chromite ore reduction from MgO-CaO-SiO_2-FeO-Cr_2O_3-Al_2O_3 slag system by carbon dissolved in high carbon ferrochromium alloy bath, Ironmaking & Steelmaking, 29 (2002) 22-28.

[70] E.A. Fletcher, Solar thermochemical and electrochemical research - How they can help reduce the carbon dioxide burden, Energy, 21 (1996) 739-745.

Chapter 4 - Formation of magnesium chromite or magnesium ferrite with solar radiation in reducing environments

4.1 Abstract

Based on a novel solid-state synthesis of high-temperature magnesium ceramics with renewable energy, MgM_2O_4 (M = Cr, Fe) spinels were produced from inexpensive oxide feedstock with concentrated solar radiation. In reducing environments, 17 ± 2 mol% $MgFe_2O_4$ or 8.6 ± 0.9 mol% $MgCr_2O_4$ were produced rapidly after 30 min at 1200°C. The nanocrystalline refractories were purified and structurally characterized by X-ray analysis and BET gas adsorption (9.7-11.9 m^2 g^{-1} specific surface, apparent macroporous structure). The promoting effect of solar radiation in the synthesis of the ferrite (42 ± 5 μmol $MgFe_2O_4$ per mol Fe_2O_3 s^{-1} versus 26 ± 3 μmol mol^{-1} s^{-1} in the absence of solar radiation, atomic ratio of graphite/Fe^{3+} of 3.99 ± 0.01) is correlated with the difference in the free energy of the spinel formation. The kinetic data are described with a model of spherical particles where the diffusion of O^{2-} and metal ions across the spinel lattice limits the reaction.

4.2 Introduction

Spinels are cubic double oxides with the general formula AB_2O_4 (A = divalent metal ion, e.g., Mg^{2+}, B = trivalent metal ion, e.g., Fe^{3+} or Cr^{3+}). Their unique chemical properties (such as high-temperature stability and flexible order[1, 2] and exchange capacity for cations of various sizes[3]) have been explored or employed for industrially important refractory[4, 5] catalytic[6-9] or high-temperature reactive materials[10-14].

Magnesium chromite ($MgCr_2O_4$, normal spinel ion ordering[15], p-type semiconductor[5, 16]) and magnesium ferrite ($MgFe_2O_4$, inverse spinel ion ordering[1, 15], n-type semiconductor[16, 17]) are

chemically stable ceramic refractories[4, 5] resistant to slag attack[18]. $MgCr_2O_4$ has been used as highly selective oxidation catalyst (e.g., as efficient complete combustion catalyst for the oxidation of propane and propene)[6, 7]. The magnetic properties of $MgFe_2O_4$ have been utilized for various electronic, catalytic[9, 17] or medical applications (e.g., for achieving local hyperthermia[19], that is localized heating of tumors[20, 21]). The interest in these materials increases permanently due their utility under extreme conditions[22].

Conventionally, these oxides are produced by solid-state reaction of MgO and transition metal oxide (TMO, i.e., Cr_2O_3 or Fe_2O_3 respectively) particles[1, 2] near 1200°C[6, 15, 23]. To increase the specific surface and catalytic activity[6] a number of alternative synthesis techniques at lower temperatures have been developed, including[9] sol-gel methods[9] with calcination in the range of 500-1100°C[6, 8, 17, 24], co-precipitation in reverse microemulsion[9, 25] with calcination around 600°C[6], mechanical activation[9, 22], or high-pressure hydrothermal methods[9]. However, these techniques are energy-intensive[9], consume complex chemicals such as solvents, surfactants, and complexing or precipitating agents[6, 9], and require occasionally catalysts[9].

Given these technological and environmental/economical challenges simple and energy-efficient production and processing routes of nanocrystalline high-temperature ceramics are sought[9, 22, 26]. Among the many types of production techniques the solid-state reaction-based methods utilize inexpensive and available raw materials[22] and may synthesize their products rapidly and at large scale. Solar radiation has been used at industrial scale as environmentally benign source of elevated temperatures and process heat[27, 28]. Solar energy is essentially unlimited and can be concentrated, theoretically, up to the surface temperature of the sun (practically limited only by unavoidable energy losses from the solar furnace). Based on the seminal solar thermochemical production of binary metal carbides and nitrides[29-33], a novel

method producing magnesium chromite or ferrite from inexpensive oxide feedstock via rapid solid-state synthesis at 1200°C with concentrated solar radiation is presented here.

Section 4.4.1 assesses the chemical composition of the solids formed during the reaction of MgO and TMO particles in presence of graphite and N_2. The experimental data do not support the previously proposed utility of MgM_2O_4 (M = Cr, Fe) materials for the thermochemical reduction of nitrogen (see Section 2.6). Given the strong relation between the properties of spinel ceramics and their preparation conditions[17, 22], Section 4.4.2 characterizes the morphology of the synthesized nanocrystalline ceramics. Specific surface areas are comparable to those reported for chromites and ferrites synthesized at lower temperatures or via sol-gel methods.

Understanding the effect of reducing environments in the formation of magnesium-containing chromite or ferrite is important when studying the natural formation of these minerals in carbonaceous sediments or in presence of coal depositions/feedstock[34]. The resistance to reducing environments becomes relevant in the industrial production of ferrochrome or stainless steel[35] or when fabricating refractories for applications in high-temperature and chemically reducing processes such as, e.g., the carbothermal production of aluminum or silicon with concentrated solar radiation[36, 37]. Here the formation of MgM_2O_4 (M = Cr, Fe) in presence of graphite (atomic ratio of graphite to transition metal of 1.99-5.00) with concentrated solar energy is studied (see Section 4.4.3). Section 4.4.4 compares the yield of magnesium chromite or ferrite employing either concentrated solar radiation or conventional electric resistance heat.

4.3 Experimental

4.3.1 Solar radiation experiments

To study the formation of MgM_2O_4 (M = Cr, Fe) under solar radiation and in reducing environments powder mixtures were prepared from the starting materials characterized in Table

4.1. The materials were mixed at molar ratios of MgO:M_2O_3:C of 1:1:4, 1:1:8, 2:1:5, or 2:1:10, that is an equimolar ratio of MgO:M_2O_3[7, 22] or excess MgO as suggested previously[1, 2] and a 1:1 or 2:1 ratio of graphite to lattice oxygen. The mixtures were placed into a quartz boat (0.37 ± 0.05 g) and were heated under a 30 ± 2 $ml_{(STP)}$ s^{-1} N_2 flow at 1200 ± 100 °C[6, 14, 15, 23] (Fig. 4.1) by concentrated solar radiation (0.82 ± 0.02 kW m^{-2} normal insolation, SP1065, 300-1100 nm wavelength detection range, EDTM Glass, Window & Film Test Equipment).

Characterization of solid reactants

reactant	MgO	Cr_2O_3	α-Fe_2O_3	graphite
space group	$Fm\bar{3}m$	$R\bar{3}c$	$R\bar{3}c$	$P6_3/mmc$
d_p [a] (μm)	4 ± 4	6 ± 4	17 ± 11	24 ± 15
A_{BET} [b] (m^2 g^{-1})	20.5 ± 0.2	1.45 ± 0.02	8.0 ± 0.1	12.4 ± 0.2
Φ [c] (m^3 m^{-3})	0.882 ± 0.004	0.81 ± 0.01	0.87 ± 0.01	0.839 ± 0.006

Table 4.1 Solid reactants: *a*) average particle diameter, *b*) BET surface area, *c*) void space fraction $\Phi = 1 - \rho_{bulk}/\rho_p$, ρ_i is the density in kg m^{-3}, powder bed surface: 2.4 ± 0.2 or 33 ± 2 cm^2 for solar or electric experiments respectively, powder bed thickness < 1 mm.

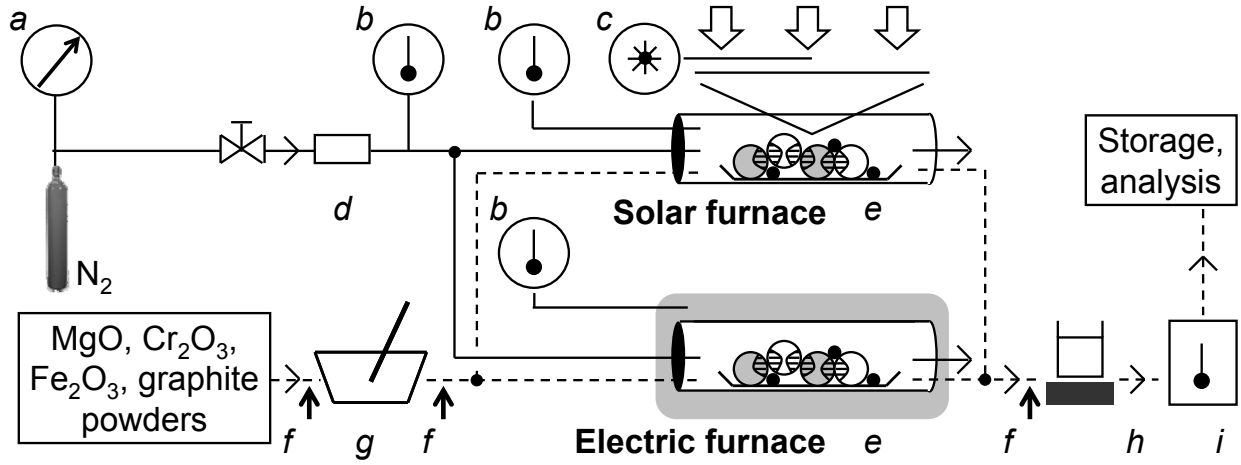

Figure 4.1 MgM_2O_4 (M = Cr, Fe) synthesis: *a*) N_2 gas and barometer, *b*) thermometer, *c*) Fresnel-lens and solar meter, *d*) flow meter, *e*) powder mixture (white, MgO particles; gray, TMO particles; black, dashed area, particle contact and MgO/TMO diffusion zone, see Section 4.3.4), *f*) solid state analysis (see Section 4.3.3), *g*) powder mixing, *h*) magnetic separation and/or washing with H_2O and acetone, *i*) drying.

The radiation was concentrated with a Fresnel lens-based solar furnace (tubular flow-through reactor, fused quartz, Technical Glass Products) that has been described previously[38] (see Sections 1.4.3 and 3.3.1). A thermocouple (High Temperature Flexible Ceramic Fiber-Insulated Probe, Type K; IR-Pro Infrared Thermometer, 1371°C maximum temperature, both ThermoWorks) was used to determine the furnace temperature before the experiment. After the reaction the furnace was moved out-of-focus to cool the reactor down to ambient temperature within about 15 min. All solid samples were stored subsequently under air at 4°C.

4.3.2 Electric resistance heat experiments

To study the spinel formation in absence of solar radiation 0.36 ± 0.01 g MgO:M_2O_3:C mixtures (1:1:8 molar ratio) or 0.16 ± 0.03 g 1:8 mol/mol MgO:C as reference respectively were placed into a quartz boat and were heated for 30, 60, or 120 min respectively under a 31 ± 2 $ml_{(STP)}$ s^{-1} N_2 gas flow at 1200 ± 1 °C (Fig. 4.1) using an electric resistance furnace (flow-through quartz reactor, model HTF55347C, temperature controller model CC58434C, Lindberg/Blue). Samples were introduced into the furnace at about 305 ± 45 °C, heated at a rate of 0.79 ± 0.03 °C s^{-1} to 1200°C, and cooled at -4 ± 1 °C s^{-1} (initial cooling rate) to below 210°C after 10 min. All solids were removed from the furnace at ambient temperature and were stored under air at 4°C.

4.3.3 Solid state analysis

Powder X-ray diffraction (XRD) patterns were taken with a Miniflex II diffractometer (Cu-target X-ray tube, 30 kV / 15 mA output, diffracted beam monochromator, Rigaku) with a 5-80 °2θ range, °2θ/min scan speed, and 0.02 data points/°2θ, continuous mode for quantitative solid phase identification (PDXL Software Version 1.6.0.0). All powder mixtures were analyzed gravimetrically before and after the experiment (AE260 DeltaRange balance, ± 0.1 mg, Mettler).

The average particle diameter (Table 4.1) was determined using scanning electron microscopy (SEM, S-3500N Scanning Electron Microscope, Hitachi, 20 kV). The specific BET surface area (6-multi point analysis) was analyzed by NanoScale Inc., Manhattan, KS (Table 4.1). To characterize the spinel morphology selected powders (Section 4.4.2) were mixed consecutively with 5-10 ml water and acetone, separated from the liquid phase via sedimentation ($MgCr_2O_4$) or by a magnetic field ($MgFe_2O_4$, using a neodymium disc magnet, 13,200 Gauss residual induction, 42 MegaGauss-Oersteds maximum energy product, K&J Magnetics, Inc.) and dried for 24 hrs at 60°C. The washed samples were analyzed via energy-dispersive X-ray spectroscopy (EDS, Nova NanoSEM 430, FEI Company, 5-15 kV, beam deceleration, high stability Schottky field emission gun, and Oxford X-Max Large Area Analytical silicon drift detector).

4.3.4 Chemicals

All metal oxide powers (99.95% pure MgO, 99% pure Cr_2O_3, and 99.2% pure Fe_2O_3) were -325 mesh and purchased from Noah Technologies. Graphite powder (crystalline, 99% pure, -300 mesh) was from Alfa Aesar. BET surface and SEM analysis indicate relative comparable morphological powder characteristics (Table 4.1). Acetone and water were HPLC grade (Fisher Scientific). N_2 gas was UHP Zero grade (Linweld).

4.4 Results and Discussion

4.4.1 Chemical composition

Heating the MgO/TMO/graphite powder mixtures under N_2 flow for 30 min with concentrated solar radiation at 1200°C yielded MgM_2O_4 (M = Cr, Fe) in all eight experiments. Figure 4.2 shows a representative XRD spectrum of an $MgO/Cr_2O_3/C$ powder mixture after heating. The incomplete conversion[7, 39, 40] of the metal oxides is expected due to the short reaction time (see Section 4.4.4)[1, 2, 15]. The remaining peaks in the diffraction patter can be

identified with Cr_3C_2, Cr_7C_3[18, 41], and Cr_2N. Besides the MgO, Fe_2O_3, and graphite reactants Fe, FeO, Fe_3O_4 (i.e., $FeO*Fe_2O_3$) and $MgFe_2O_4$ were identified in the $MgO/Fe_2O_3/C$ system (see Appendix C). This confirms the expected reduction of the transition metal.

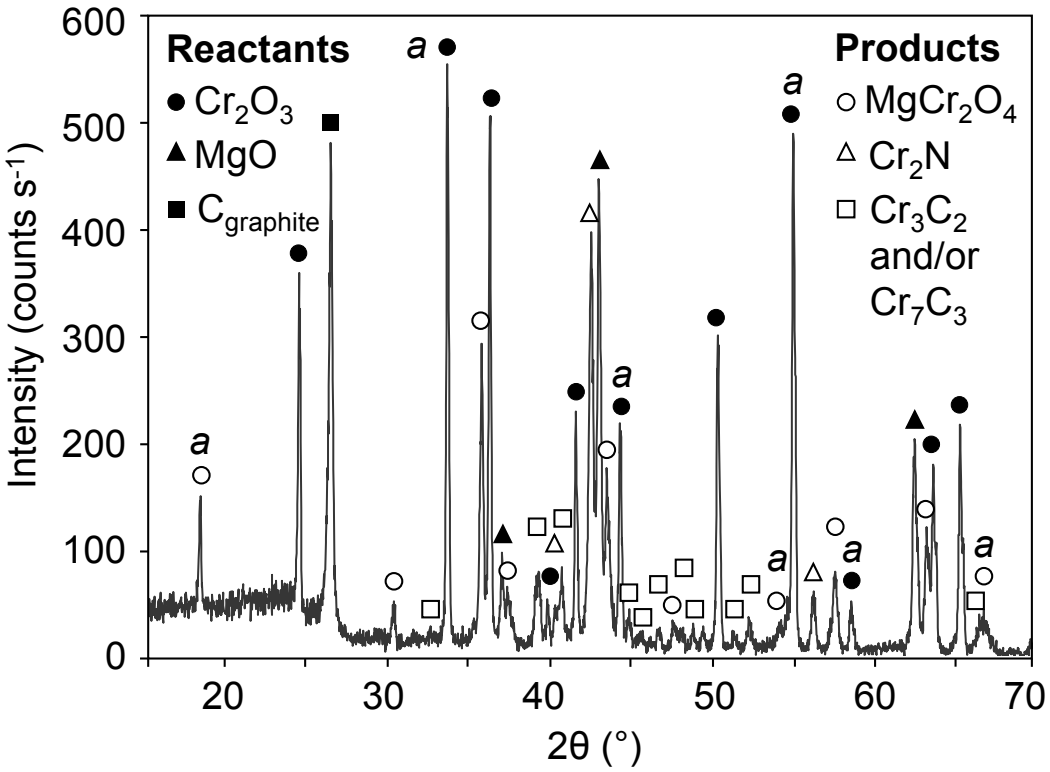

Figure 4.2 Representative XRD spectrum of a $MgO:Cr_2O_3:C$ powder mixture (molar ratio 1:1:4) after heating in a N_2 flow for 30 min at 1200°C with concentrated solar radiation. Marked with *a*) $MgCN_2$ is the only compound of Mg and N that is matching the spectrum.

The diffraction pattern of magnesium cyanamide ($MgCN_2$) matches the XRD data of some powder samples (Fig. 4.2). However, the compound is not identified due to a figure of merit computation by the XRD software inferior to that of the identified phases (e.g., Cr_2O_3 and $MgCr_2O_3$ in Figure 4.2). EDS analysis (see 4.4.2) did not confirm unambiguously the presence of lattice nitrogen. The reduction of nitrogen by magnesium[14] cannot be concluded unerringly.

However, a mass balance of Mg atoms contained in the solid before or after the experiment indicates a recovery of only 57 ± 34 at% Mg (the average of eight experiments with

an atomic ratio of carbon to O^{2-} in the range of 0.99-2.00). As a reference, 99.5 ± 1.6 at% Mg were recovered when heating an MgO/graphite powder mixture (atomic ratio of C/O^{2-} = 2.03) in N_2 gas flow for 240 min at 1200°C. Thus, the presence of the transition metal appears to aid the reduction[10, 13, 14 42] of Mg^{2+} and leads likely to formation of Mg metal vapor exiting the reactor with the N_2 gas flow. Ascertaining whether Cr is actually affecting the interfacial bonding state of Mg^{2+} [43] requires certainly further studies.

4.4.2 Morphological characterization

To characterize the materials produced with concentrated solar radiation two samples (2:1:5 molar ratio of MgO:TMO:C reactants) were washed and separated gravimetrically or magnetically respectively and analyzed by BET adsorption, EDS and SEM.

The specific surface area (A_{BET}) of the powder after the reaction and washing is approximately 47-58% of the A_{BET} determined for the MgO starting material and by a factor of 1.2-8.2 higher than that of the TMO reactant (Table 4.2).

Characterization of reaction products

spinel	$MgCr_2O_4$ [a]	$MgFe_2O_4$ [a]	$MgCr_2O_4$ [b]	$MgFe_2O_4$ [b]
space group	$Fd\bar{3}m$	$Fd\bar{3}m$		
d_c [c] (nm)	11-53	7-53		
A_{BET} [d] ($m^2\ g^{-1}$)	8.07 ± 0.06	7.67 ± 0.07	11.9 ± 0.2	9.7 ± 0.3
d_{BET} [e] (nm)	171 ± 3	174 ± 3	116 ± 3	137 ± 8

Table 4.2 Solid products: *a*) before washing, *b*) after washing, *c*) crystallite size, *d*) BET surface area, *e*) particle size assuming spherical particles, error propagation within a 95% confidence interval.

If the magnetic separation of the Fe-containing sample removed the major traces of unconverted MgO and graphite than 9.7 $m^2\ g^{-1}$ A_{BET} can be assumed to not relate to the non-magnetic reactants. That is the $MgFe_2O_4$ formed appears to have a specific surface area slightly higher than the Fe_2O_3 staring material leading to an A_{BET} of the iron oxide/spinel mixture about

21% above the A_{BET} of the pure Fe_2O_3. Comparing $MgCr_2O_4$ produced with various alternative methods, the A_{BET} of the materials prepared with solar radiation is higher than 1.8 m^2 g^{-1} (via reaction of MgO and Cr_2O_3 at 1200°C for 24 hrs), lower than 83.8 m^2 g^{-1} (co-precipitation in reverse microemulsion) and comparable to 9.0 m^2 g^{-1} (sol-gel-based synthesis)[6].

The crystallite size of the formed spinel was determined using Scherrer's equation ($d_c = 0.89\lambda/(\beta\cos\theta)$, where λ in nm is the X-ray radiation wavelength, β in radians is the line broadening at half the maximum intensity, and θ in degree is the diffraction angle)[9, 17, 22]. Table 4.2 shows that the spinel produced with solar radiation is nanocrystalline[22], comparable to, e.g., 15-24 nm for $MgFe_2O_4$ prepared from metal nitrate solution and calcined at 500-800°C[44], or $MgCr_2O_4$ with 52.4 nm using a sol-gel synthesis and calcination at 850°C (versus 77.8 nm via reaction of the oxides at 1200°C)[6].

The particle size determined from the BET measurement[6, 24] ($d_{BET} = 6/(A_{BET}\rho)$, based on a spherical particle model where ρ is the spinel density, i.e., 4.348 g cm^{-3} for $MgCr_2O_4$[4-6] or 4.502 g cm^{-3} for $MgFe_2O_4$[24]) is in average about 11.7 times that corresponding to the crystallite size (Table 4.2). This indicates the presence of porous structure[6]. To confirm this hypothesis the spinel was identified via EDS (Fig. 4.3).

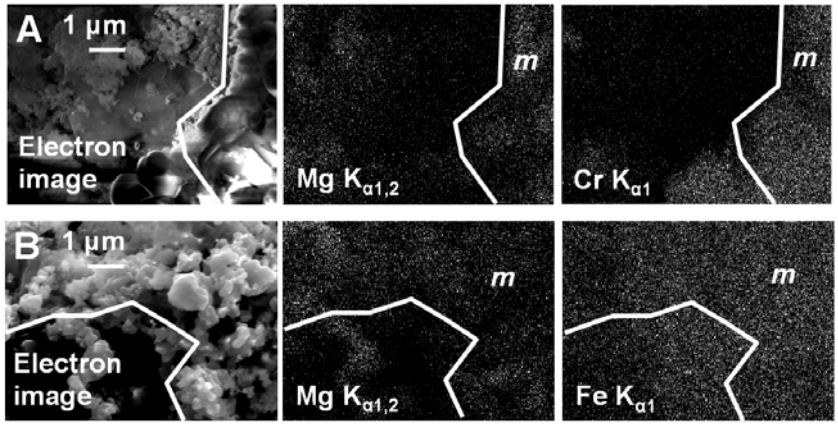

Figure 4.3 EDS analysis of MgO:M_2O_3:C (molar ratio 2:1:5) after heating for 30 min in N_2 at 1200°C. A) *M* = Cr, B) *M* = Fe, *m*) larger areas with Mg and *M* specific X-ray emission.

The analysis confirms the formation of both spinels evidenced by XRD (Fig. 4.2) and allows visualizing the spinel surface (Fig. 4.4). Figure 4.4 shows particles or particle agglomerates with diameters ranging from approximately 3-20 or 6-38 µm for Cr- or Fe-containing powders respectively (panel A and C). The surface of both samples appears macroporous (panel B and D)[6].

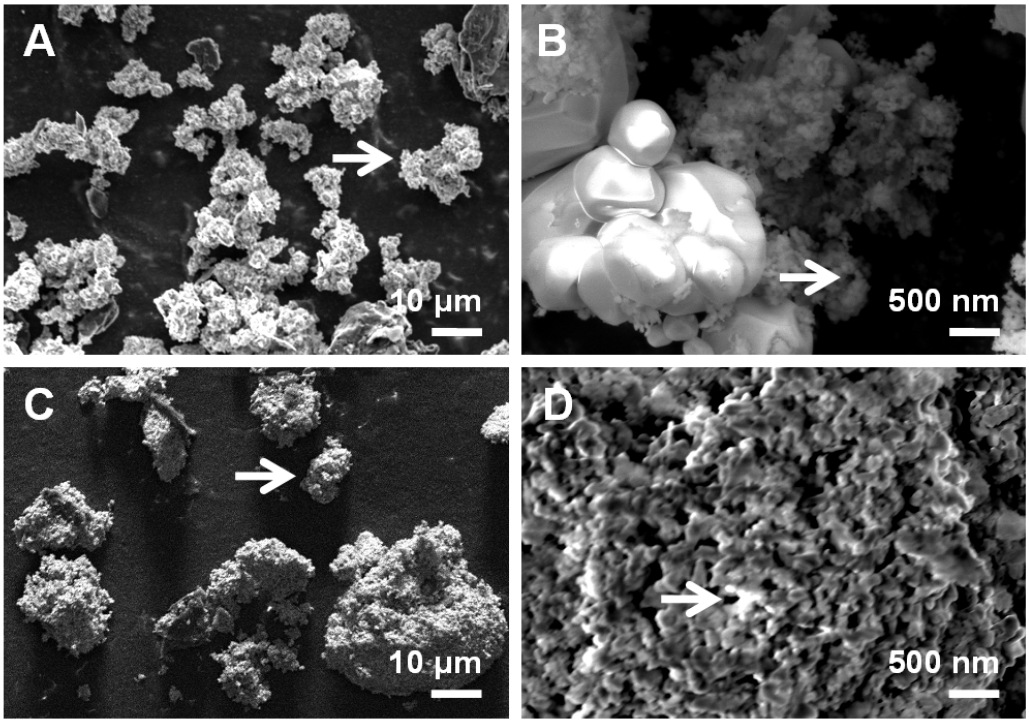

Figure 4.4 SEM analysis of MgO:M_2O_3:C powder mixtures (molar ratio 2:1:5) after heating for 30 min in N_2 with concentrated solar radiation at 1200°C. A and B) *M* = Cr, C and D) *M* = Fe. Arrows see Section 4.4.2.

4.4.3 Effect of reducing environments

Studies of the magnesium chromite or ferrite formation in reducing environments are scarce[18, 35, 45]. The resistance of these refractories to reducing environments, however, plays an important role in various industrial situations, such as, for example in conventional smelting processes[35] or prospective solar thermochemical high-temperature reaction cycles[14, 36-38, 46]. The following assess the reaction yield of the spinels when heating powder mixtures of MgO and

Cr_2O_3 or Fe_2O_3 respectively in the presence of graphite and solar radiation. The yield of $MgCr_2O_4$ or $MgFe_2O_4$, X_{spinel}, is here defined as the molar ratio (n in mol) of the spinel to the limiting reactant (LR), i.e., MgO, Cr_2O_3 or Fe_2O_3 respectively:

$$(4.1) \quad X_{spinel} = \frac{n_{spinel}}{n_{LR}} = \frac{m_t}{m_0} \frac{x_{spinel}}{x_{LR}} \frac{M_{LR}}{M_{spinel}}$$

where m in g is the weight of the solid before the reaction (subscript 0) or at a time t, x_i in g g^{-1} is the weight fraction of a chemical species i, and M_i in g mol^{-1} is the molar mass.

A plot of the spinel yield vs. the atomic ratio of graphite to the transition metal ion (Fig. 4.5) yields a semi-quantitative linear correlation.

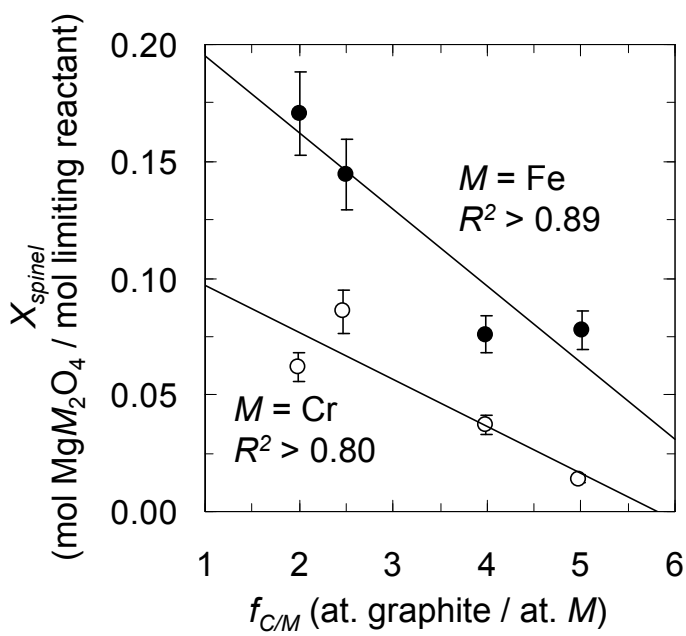

Figure 4.5 Yield of magnesium chromite (empty circles) or ferrite (filled circles) respectively using concentrated solar radiation (after 30 min at 1200°C) vs. the atomic ratio of graphite to Cr or Fe ($f_{C/M}$). Liner fits are to guide the eye. Error bars are via error propagation within a 95% confidence interval in average about ± 10.5%.

Doubling the ratio of graphite to Cr^{3+} or Fe^{3+} from about 2.00 to 3.99 decreases the spinel yield by about 40 ± 6 % ($MgCr_2O_4$) or 56 ± 8 % ($MgFe_2O_4$) respectively. Even a highly reducing

environment did not suppress the spinel formation entirely (e.g., 1.4 ± 0.1 mol% $MgCr_2O_4$ or 7.8 ± 0.8 mol% $MgFe_2O_4$ after 30 min at 1200°C and $f_{C/M}$ = 4.99 ± 0.01). From a chemical perspective, this makes the studied materials promising refractories for applications dealing with high temperatures, solar radiation and reducing reaction chemistry[14, 36-38, 46].

4.4.4 Effect of solar radiation

To assess the effect of concentrated solar radiation on the formation of magnesium chromite or ferrite Figure 4.6 shows the spinel yield versus the heating time for powder mixtures (MgO:TMO:C = 1:1:8, i.e., $f_{C/M}$ = 4, compare Figure 4.5) heated in an electric resistance furnace. After 30 min, the yield of $MgCr_2O_4$ reaches 10.3 ± 1.1 mol% (about 2.8 times the value in presence of solar radiation), the yield of $MgFe_2O_4$ is 4.7 ± 0.5 mol% (about 62% of the value in presence of solar radiation).

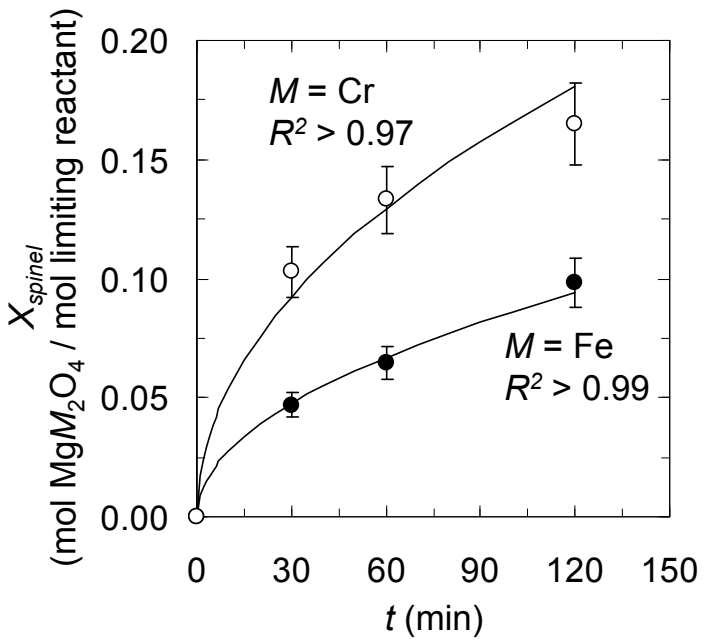

Figure 4.6 Yield of magnesium chromite (empty circles) or ferrite (filled circles) using electric resistance heat vs. the reaction time (molar ratio MgO:TMO:C = 1:1:8, i.e., $f_{C/M}$ = 4, see Fig. 4.5). Lines are solid-state diffusion-limited shrinking core models[47] and error bars are via error propagation within a 95% confidence interval in average about ± 10.5%.

The data is well described (Fig. 4.6) with a kinetic model of spherical particles where the diffusion of O^{2-} and metal ions across a growing layer of solid product limits the reaction[40]:

$$(4.2) \quad 1-\frac{2}{3}X_{spinel}-(1-X_{spinel})^{2/3}=\frac{8D_{cation}c_0t}{c_{spinel}d_p^{\ 2}}$$

where D_{cation} in m s^{-1} is the apparent diffusion coefficient of the participating metal cations[39, 40], c_0 in mol m^{-3} is the concentration of the diffusing species at the outer shell of the reacting particle, and c_{spinel} in mol m^{-3} is the concentration of the diffusing species in the spinel product.

Taking the spinel yield at the intercept of Figure 4.5 (i.e., $f_{C/M} = 0$) and describing it with a diffusion-limited formation mechanism (Eq. 4.2)[7, 40] allows to estimate a spinel yield > 95 mol% (heating with solar radiation in absence of graphite) after approximately 72 hrs for $MgCr_2O_4$ or 18 hrs for $MgFe_2O_4$ respectively. This demonstrates slow formation of $MgCr_2O_4$ and fast formation of $MgFe_2O_4$ in presence of solar radiation, relative to, e.g., the reported preparation of either spinel by heating MgO and the TMO for 24 hrs at 1200°C[6, 15] or formation of $MgFe_2O_4$ by heating for 120-240 hrs at 900-1000°C[1, 2].

Comparing Figure 4.5 and Figure 4.6 shows that the magnesium chromite is favorably formed in the electric resistance furnace opposing the increased formation of magnesium ferrite in the solar furnace. Given the temperature fluctuations in the solar furnace (meteorological conditions, incrementally adjusted alignment of the focal point and the reactor, etc.) thermodynamic or kinetic explanations are conceivable. The reaction of 1 mol MgO and 1 mol M_2O_3 forming 1 mol MgM_2O_4 is thermodynamically favorable at high temperatures if M = Cr (a free energy of about -59.6 kJ/mol $MgCr_2O_4$ at 1200°C, decreasing with increasing temperatures). On the other hand, the formation of $MgFe_2O_4$ is favored thermodynamically only at temperatures below approximately 900°C (a slightly positive free energy of 12.4 kJ/mol $MgFe_2O_4$ at 1200°C, increasing with increasing temperatures). If the average temperature in the solar furnace is below

1200°C (adjusted before to the experiment with a thermocouple, see Section 4.3.1) than the different reaction equilibria in both furnaces may explain the decreased yield of chromite and increased yield of ferrite in the solar furnace.

Alternatively, the apparent diffusion coefficients, D_{cation}, can be estimated (Eq. 4.2) assuming counter current diffusion of Mg^{2+} and Cr^{3+} or Fe^{3+} respectively is limiting the spinel formation[7, 23, 40]. The computation yields D_{cation} in the range of 2.5-7.3 x 10^{-15} or 1.1-3.4 x 10^{-14} cm^2 s^{-1} (the lower end of the stated range represents diffusion of Mg^{2+}) for the formation of chromite or ferrite respectively using the electric resistance furnace. This is assuming MgO as the host lattice dissoluting Cr^{3+} and forming $MgCr_2O_4$ and Fe_2O_3 as host lattice for the formation of $MgFe_2O_4$[39, 40]. In the solar system D_{cation} decreases to 0.40-1.2 x 10^{-15} cm^2 s^{-1} during the formation of $MgCr_2O_4$ and increases to 2.9-8.8 x 10^{-14} cm^2 s^{-1} during the formation of $MgFe_2O_4$.

Assuming an increasing diffusion coefficient with increasing temperature, this may hint towards increased temperatures (the maximum temperature in the employed solar furnace was estimated previously with about 1600°C[38]) accelerating the ferrite formation. However, increased temperatures do not explain the decreased formation kinetics of $MgCr_2O_4$. This reinforces the above hypothesized decreased temperatures causing the change in the yield of the chromite and ferrite on thermodynamic ground.

In summary, the proposed solar thermochemical synthesis yields significant amounts of magnesium chromite or ferrite respectively. The relative fast synthesis of $MgFe_2O_4$ may facilitate a rapid large-scale production of the high-temperature ceramic if unconverted reactants are separated from the ferrite product.

4.5 Conclusions

Synthesis of magnesium chromite or ferrite from inexpensive oxide feedstock via solid-state synthesis at 1200°C with concentrated solar radiation was presented.

In a reducing environment, the presence of Cr or Fe appears to aid the reduction of Mg^{2+} leading to the removal of in average 43 ± 26 at% Mg likely in form of a metal vapor. Nitrogen (and carbon) was reduced only by Cr. Unambiguous evidence for formation of Mg-N bonds was not found.

Even in presence of 62.40 ± 0.04 mol% graphite in the reactant powder mixture, 9 ± 7 mol% $MgCr_2O_4$ or 14 ± 7 mol% $MgFe_2O_4$ with a specific surface area of 11.9 ± 0.2 or 9.7 ± 0.3 $m^2\ g^{-1}$ were formed respectively after heating with solar radiation for 30 min. The spinels are nanocrystalline with an apparent macroporous surface structure. The yield of the reaction product decreases with increasing graphite concentration (1.4 ± 0.1 mol% $MgCr_2O_4$ or 7.8 ± 0.8 mol% $MgFe_2O_4$ respectively at 76.91 ± 0.01 mol% graphite). These are promising features of a refractory material for applications dealing with high temperatures, solar radiation and reducing reaction chemistry.

The accelerated formation of the ferrite in presence of solar radiation (42 ± 5 μmol $MgFe_2O_4$ per mol Fe_2O_3 s^{-1} versus 26 ± 3 μmol mol^{-1} s^{-1} in the absence of solar radiation, both at an atomic ratio of graphite/Fe^{3+} of 3.99 ± 0.01) may be useful for a rapid large scale production of the ceramic from an inexpensive oxide feedstock and a sustainable energy source if the spinel product is separated from unconverted reactants.

4.6 Associated content in Appendix C

Supporting Information: To complement the formation of carbide and nitride in the $MgO/Cr_2O_3/C$ system (Fig. 4.2), XRD data showing Fe^{3+} reduction in the $MgO/Fe_2O_3/C$ system.

4.7 References

[1] S.M. Antao, I. Hassan, J.B. Parise, Cation ordering in magnesioferrite, $MgFe_2O_4$ to 982°C using in situ synchrotron X-ray powder diffraction, American Mineralogist, 90 (2005) 219-228.

[2] D. Levy, V. Diella, M. Dapiaggi, A. Sani, M. Gemmi, A. Pavese, Equation of state, structural behaviour and phase diagram of synthetic $MgFe_2O_4$, as a function of pressure and temperature, Physics and Chemistry of Minerals, 31 (2004) 122-129.

[3] G. Markl, Minerale und Gesteine, Mineralogie - Petrologie - Geochemie, 2. verbesserte und erweiterte Auflage, Spektrum Akademischer Verlag, Würzburg, Germany, 2008.

[4] N. Yoshida, Y. Takano, M. Yoshinaka, K. Hirota, O. Yamaguchi, Formation, powder characterization and sintering of $MgCr_2O_4$ by the hydrazine method, Journal of the American Ceramic Society, 81 (1998) 2213-2215.

[5] L.V. Morozova, V.P. Popov, Synthesis and investigation of magnesium chromium spinel, Glass Physics and Chemistry, 36 (2010) 86-91.

[6] K. Rida, A. Benabbas, F. Bouremmad, M.A. Pena, A. Martínez-Arias, Influence of the synthesis method on structural properties and catalytic activity for oxidation of CO and C3H6 of pirochromite $MgCr_2O_4$, Applied Catalysis a-General, 375 (2010) 101-106.

[7] H. Nayak, D. Bhatta, Catalytic effects of magnesium chromite spinel on the decomposition of lanthanum oxalate, Thermochimica Acta, 389 (2002) 109-119.

[8] M. Stefanescu, M. Barbu, T. Vlase, P. Barvinschi, L. Barbu-Tudoran, M. Stoia, Novel low temperature synthesis method for nanocrystalline zinc and magnesium chromites, Thermochimica Acta, 526 (2011) 130-136.

[9] M.A. Willard, L.K. Kurihara, E.E. Carpenter, S. Calvin, V.G. Harris, Chemically prepared magnetic nanoparticles, International Materials Reviews, 49 (2004) 125-170.

[10] J.R. Scheffe, J.H. Li, A.W. Weimer, A spinel ferrite/hercynite water-splitting redox cycle, International Journal of Hydrogen Energy, 35 (2010) 3333-3340.

[11] J.R. Scheffe, M.D. Allendorf, E.N. Coker, B.W. Jacobs, A.H. McDaniel, A.W. Weimer, Hydrogen Production via Chemical Looping Redox Cycles Using Atomic Layer Deposition-Synthesized Iron Oxide and Cobalt Ferrites, Chemistry of Materials, 23 (2011) 2030-2038.

[12] A. Stamatiou, P.G. Loutzenhiser, A. Steinfeld, Solar Syngas Production from H_2O and CO_2 via Two-Step Thermochemical Cycles Based on Zn/ZnO and FeO/Fe_3O_4 Redox Reactions: Kinetic Analysis, Energy & Fuels, 24 (2010) 2716-2722.

[13] J.E. Miller, M.D. Allendorf, R.B. Diver, L.R. Evans, N.P. Siegel, J.N. Stuecker, Metal oxide composites and structures for ultra-high temperature solar thermochemical cycles, Journal of Materials Science, 43 (2008) 4714-4728.

[14] R. Michalsky, P.H. Pfromm, Thermodynamics of metal reactants for ammonia synthesis from steam, nitrogen and biomass at atmospheric pressure, AIChE Journal, http://onlinelibrary.wiley.com/doi/10.1002/aic.13717/pdf, (in press).

[15] D. Lenaz, H. Skogby, F. Princivalle, U. Halenius, The $MgCr_2O_4$-$MgFe_2O_4$ solid solution series: effects of octahedrally coordinated Fe^{3+} on T-O bond lengths, Physics and Chemistry of Minerals, 33 (2006) 465-474.

[16] R.J. Willey, P. Noirclerc, G. Busca, Preparation and characterization of magnesium chromite and magnesium ferrite aerogels, Chemical Engineering Communications, 123 (1993) 1-16.

[17] S. Reddy, B.E.K. Swamy, U. Chandra, K.R. Mahathesha, T.V. Sathisha, H. Jayadevappa, Synthesis of $MgFe_2O_4$ nanoparticles and $MgFe_2O_4$ nanoparticles/CPE for electrochemical investigation of dopamine, Analytical Methods, 3 (2011) 2792-2796.

[18] A. Yamaguchi, T. Okamura, Sintering and compounds in the $MgCr_2O_4$-TiO_x system, Ceramics International, 15 (1989) 147-153.

[19] T. Maehara, K. Konishi, T. Kamimori, H. Aono, T. Naohara, H. Kikkawa, Y. Watanabe, K. Kawachi, Heating of ferrite powder by an AC magnetic field for local hyperthermia, Japanese Journal of Applied Physics Part 1-Regular Papers Short Notes & Review Papers, 41 (2002) 1620-1621.

[20] S. Balivada, R.S. Rachakatla, H. Wang, T.N. Samarakoon, R.K. Dani, M. Pyle, F.O. Kroh, B. Walker, X. Leaym, O.B. Koper, M. Tamura, V. Chikan, S.H. Bossmann, D.L. Troyer, A/C magnetic hyperthermia of melanoma mediated by iron(0)/iron oxide core/shell magnetic nanoparticles: a mouse study, BMC Cancer, 10 (2010).

[21] R.S. Rachakatla, S. Balivada, G.-M. Seo, C.B. Myers, H. Wang, T.N. Samarakoon, R. Dani, M. Pyle, F.O. Kroh, B. Walker, X. Leaym, O.B. Koper, V. Chikan, S.H. Bossmann, M. Tamura, D.L. Troyer, Attenuation of mouse melanoma by A/C magnetic field after delivery of bi-magnetic nanoparticles by neural progenitor cells, ACS Nano, 4 (2010) 7093-7104.

[22] M. Pavlović, Č. Jovalekić, A.S. Nikolić, D. Manojlović, N. Šojić, Mechanochemical synthesis of stoichiometric $MgFe_2O_4$ spinel, Journal of Materials Science-Materials in Electronics, 20 (2009) 782-787.

[23] S.S. Apoyan, V.S. Bakunov, P.Y. Popilskii, Diffusion processes during synthesis of chromium -magnesia spinel, Glass and Ceramics, 34 (1977) 308-310.

[24] R.A. Candeia, M.A.F. Souza, M.I.B. Bernardi, S.C. Maestrelli, I.M.G. Santos, A.G. Souza, E. Longo, $MgFe_2O_4$ pigment obtained at low temperature, Materials Research Bulletin, 41 (2006) 183-190.

[25] C. Liu, B.S. Zou, A.J. Rondinone, J. Zhang, Chemical control of superparamagnetic properties of magnesium and cobalt spinel ferrite nanoparticles through atomic level magnetic couplings, Journal of the American Chemical Society, 122 (2000) 6263-6267.

[26] S. Verma, P.A. Joy, Y.B. Khollam, H.S. Potdar, S.B. Deshpande, Synthesis of nanosized $MgFe_2O_4$ powders by microwave hydrothermal method, Materials Letters, 58 (2004) 1092-1095.

[27] M. Roeb, H. Müller-Steinhagen, Concentrating on solar electricity and fuels, Science, 329 (2010) 773-774.

[28] W.C. Chueh, C. Falter, M. Abbott, D. Scipio, P. Furler, S.M. Haile, A. Steinfeld, High-flux solar-driven thermochemical dissociation of CO_2 and H_2O using nonstoichiometric ceria, Science, 330 (2010) 1797-1801.

[29] J.P. Murray, A. Steinfeld, E.A. Fletcher, Metals, nitrides, and carbides via solar carbothermal reduction of metal-oxides, Energy, 20 (1995) 695-704.

[30] M.E. Gálvez, A. Frei, F. Meier, A. Steinfeld, Production of AlN by carbothermal and methanothermal reduction of Al_2O_3 in a N_2 flow using concentrated thermal radiation, Industrial & Engineering Chemistry Research, 48 (2009) 528-533.

[31] J.C. Fernandes, L.G. Rosa, D. Martínez, J. Rodríguez, N. Shohoji, Influence of gas environment on synthesis of silicon carbide through reaction between silicon and amorphous carbon in a solar furnace at PSA (Plataforma Solar de Almeria), Journal of the Ceramic Society of Japan, 106 (1998) 839-841.

[32] N. Shohoji, P.M. Amaral, J.C. Fernandes, L.G. Rosa, D. Martínez, J. Rodríguez, Catalytic graphitisation of amorphous carbon during solar carbide synthesis of VIa group metals (Cr, Mo and W), Materials Transactions JIM, 41 (2000) 246-249.

[33] L.G. Rosa, J.C. Fernandes, P.M. Amaral, D. Martínez, J. Rodríguez, N. Shohoji, Photochemically promoted formation of higher carbide of molybdenum through reaction between metallic molybdenum powders and graphite powders in a solar furnace, International Journal of Refractory Metals & Hard Materials, 17 (1999) 351-356.

[34] Magnesioferrite, (c) 2001-2005 Mineral Data Publishing, version 1, Available online at: http://rruff.geo.arizona.edu/doclib/hom/magnesioferrite.pdf (retrieved April 4, 2012).

[35] Y. Xiao, Y. Yang, L. Holappa, R. Boom, Microstructure changes of chromite reduced with CO gas, Proceedings of the XI International Conference on Innovation in Ferro Alloys Industry, Available online at: http://www.pyrometallurgy.co.za/InfaconXI/013.pdf (retrieved April 4, 2012), (2007).

[36] M. Kruesi, M.E. Gálvez, M. Halmann, A. Steinfeld, Solar aluminum production by vacuum carbothermal reduction of alumina-thermodynamic and experimental analyses, Metallurgical and Materials Transactions B-Process Metallurgy and Materials Processing Science, 42 (2011) 254-260.

[37] P.G. Loutzenhiser, O. Tuerk, A. Steinfeld, Production of Si by vacuum carbothermal reduction of SiO_2 using concentrated solar energy, JOM, 62 (2010) 49-54.

[38] R. Michalsky, P.H. Pfromm, Chromium as reactant for solar thermochemical synthesis of ammonia from steam, nitrogen, and biomass at atmospheric pressure, Solar Energy, 85 (2011) 2642-2654.

[39] C.H. Bamford, C.F.H. Tipper, Comprehensive Chemical Kinetics Vol. 2, The Theory of Kinetics (page 422), Elsevier Publishing Company, Amsterdam, 1969.

[40] C.H. Bamford, C.F.H. Tipper, Comprehensive chemical kinetics, Vol. 22, Reactions in the Solid State (page 269), Elsevier Scientific Publishing Company, Amsterdam - Oxford - New York, 1980.

[41] L.M. Berger, S. Stolle, W. Gruner, K. Wetzig, Investigation of the carbothermal reduction process of chromium oxide by micro- and lab-scale methods, International Journal of Refractory Metals & Hard Materials, 19 (2001) 109-121.

[42] Y. Tamaura, M. Kojima, N. Hasegawa, M. Tsuji, K. Ehrensberger, A. Steinfeld, Solar energy conversion into H_2 energy using ferrites, Journal De Physique IV, 7 (1997) 673-674.

[43] E. Pippel, J. Woltersdorf, J. Gegner, R. Kirchheim, Evidence of oxygen segregation at Ag/MgO interfaces, Acta Materialia, 48 (2000) 2571-2578.

[44] S. Maensiri, M. Sangmanee, A. Wiengmoon, Magnesium ferrite ($MgFe_2O_4$) nanostructures fabricated by electrospinning, Nanoscale Research Letters, 4 (2009) 221-228.

[45] S. Klemme, H.S. O'Neill, The reaction $MgCr_2O_4 + SiO_2 = Cr_2O_3 + MgSiO_3$ and the free energy of formation of magnesiochromite ($MgCr_2O_4$), Contributions to Mineralogy and Petrology, 130 (1997) 59-65.

[46] M.E. Gálvez, M. Halmann, A. Steinfeld, Ammonia production via a two-step Al_2O_3/AlN thermochemical cycle. 1. Thermodynamic, environmental, and economic analyses, Industrial & Engineering Chemistry Research, 46 (2007) 2042-2046.

[47] O. Levenspiel, Chemical reaction engineering, Third Edition, Chapter 25 Fluid-particle reactions: Kinetics, John Wiley & Sons, New York, 1999.

Chapter 5 - Solar fuel production via decoupled dinitrogen reduction and protonation of mobile nitrogen ions to ammonia

5.1 Abstract

Currently produced from fossil resources and near 30 MPa and 500°C, ammonia is an important fertilizer and a convenient hydrogen carrier. This work studies a solar thermochemical reaction cycle that separates the reductive N_2 cleavage from the hydrogenation of nitrogen to yield N^{3-} and finally NH_3 without using electricity or fossil fuel. The hydrolysis of binary metal nitrides of magnesium, aluminum, calcium, chromium, manganese, zinc, or molybdenum at 0.1 MPa and 200-1000°C yielded 0-100 mol% of the lattice nitrogen with 0-69.9 mol% as NH_3 liberated at rates ranging at 500°C from 1.45 x 10^{-7} (interstitial and covalent nitrides at the lower end) to 1.45 x 10^{-3} (ionic nitrides) mol NH_3 mol^{-1} metal s^{-1}. To assess the rate-limiting step the data is described by shrinking-core models and an Arrhenius-type temperature dependence of the rate constants. Based on the theoretical partial nitrogen charge, the nitride ionicity (9.96-68.83% relative to an ideal ionic solid) was found to correlate with the diffusion constants (6.56 x 10^{-14} to 4.05 x 10^{-7} cm^2 s^{-1}) suggesting that the corrosion kinetics of AlN, Cr_2N/CrN, Mn_4N/Mn_2N, Zn_3N_2, or Mo_2N are governed by the volumetric concentration of active lattice nitrogen or ion vacancies respectively. The ionicity appears useful when developing an atomic-scale understanding of the solid-state reaction mechanism and for controlling the bonding nature of a prospective optimized ternary nitride reactant.

5.2 Introduction

Energy, water, and food have been cited by Nobel laureate R. Smalley in order of priority as the top three problems that mankind will face in the next decades[1]. Solar energy is essentially

inexhaustible and environmentally benign. Employing solar energy for solutions to society's most demanding challenges, however, requires harvesting of a relatively dilute, intermittent, and geographically non-homogeneous energy source[2].

Man-made ammonia has been recognized as to some extent responsible for the "green revolution" of the first half of the 20th century. In other words, it provides the basis of survival of a large portion of the human population on earth. Global production of ammonia (NH_3) is currently about 130 million metric tons (t) annually[3]. Ammonia is produced industrially via heterogeneous catalysis that cleaves N_2 and hydrogenates nitrogen to NH_3 in a single step conducted at up to 30 MPa and 500°C[4]. The compression work required for the technically sophisticated synthesis accounts for about 16% of the 28-37 GJ t^{-1} NH_3 consumed by the process[5]. Approximately 45% of the global H_2 production is absorbed as feedstock in the synthesis of NH_3[6]. The H_2 feedstock is generated on-site from fossil resources (mainly natural gas), leading to significant fossil-based CO_2 emissions[4] and production of NH_3 in a few hundred large-scale centralized facilities world-wide[7]. Given the increasing global population[8] and recognizing the potential of NH_3 as a "perfect hydrogen carrier"[9, 10] and as a convenient alternative fuel in diesel combustion engines[11, 12], direct synthesis of NH_3 from N_2, H_2O and sunlight may contribute to a sustainable solution to two of our most demanding challenges, energy and food.

Substantial research efforts have pursued the synthesis of NH_3 at ambient pressure[7]. NH_3 has been synthesized electrochemically or electrocatalytically[13-19], e.g., at the cathode of an ion conducting electrolyte cell that is cleaving N_2[15] and H_2O to generate O^{2-} which is oxidized at the anode to O_2[14]. Alternatively, homogeneous catalysis via N_2 reduction with transition metal complexes that give substantial yields of NH_3 when reacted with acid or with H_2 has attempted to

mimic the enzymatic catalysis of N_2 fixation in the liquid phase[20-24]. Albeit promising, both approaches have not yet reached maturity. Electrochemical synthesis relies on electricity and requires novel electrolyte and electrode materials to increase NH_3 formation rates[14]. A major obstacle of the biomimetic approach[23] is the external reducing equivalent (mostly a sacrificial alkali metal or pH adjustment) that is required for generating the dinitrogen complex from a high oxidation state halide complex[21-23].

This work pursues an alternative strategy that separates the N_2 cleavage from the nitrogen protonation (Fig. 5.1).

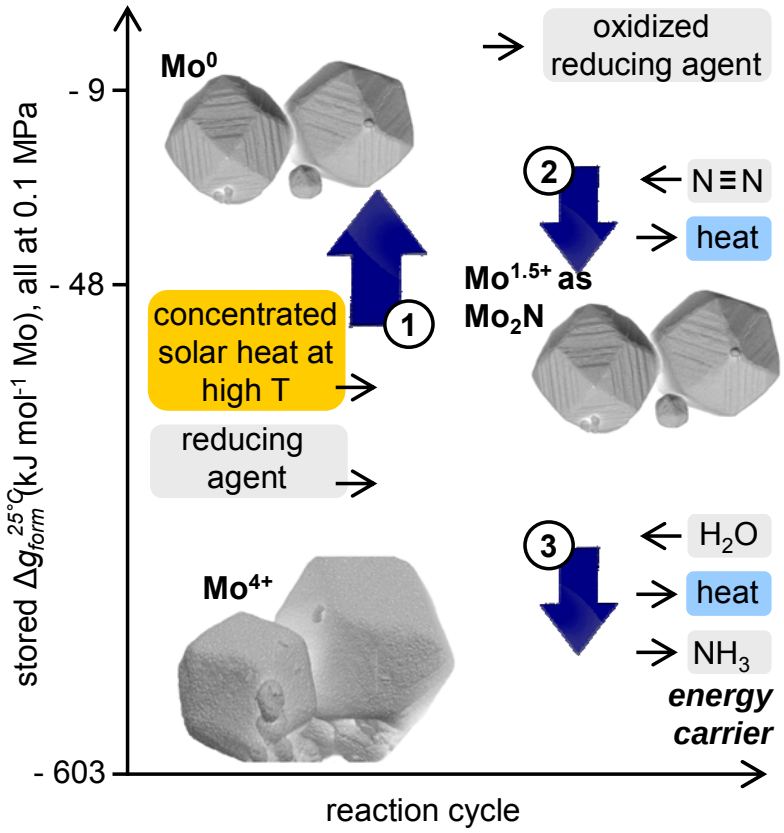

Figure 5.1 Two-step reactive NH_3 synthesis from N_2, H_2O and solar heat. The (1) endothermic reduction of an oxidized material (e.g., Mo^{4+}) and the (2) exothermic reduction of N_2 may be conducted in one step. This generates reduced N^{3-} in the solid state that can be (3) protonated with H_2O.

Conceptually (with generalized stoichiometry), an oxidized inorganic material (M_cO_d) can be reduced with a suitable reducing agent (R) at elevated temperatures:

$$(5.1) \quad \frac{a}{bc}M_cO_d + \frac{ad}{bc}R \leftrightarrow \frac{a}{b}M + \frac{ad}{bc}RO$$

with M being a metal and lower case letters indicating stoichiometric coefficients. The reaction accomplishes storage of the O 2p electrons in the metal. This can be achieved with concentrated solar radiation[2], that is, harvesting photons from the entire insolation spectrum as reducing equivalents[25-28]. Dependent on the free energy of formation of the metal, the remaining reducing equivalents required for the thermochemical charge transfer are supplied by a relative week reducing agent[23, 29]. This may be H_2 or perhaps biomass allowing for a syngas byproduct[30-33].

The generated reactant can thereafter be utilized to provide the reducing power for the six-electron reductive cleavage of N_2 (forming N^{3-} ions in the solid state) and splitting of H_2O (yielding the metal oxide, the desired NH_3, and possibly H_2) without electricity or a fossil fuel:

$$(5.2) \quad \frac{a}{b}M + \frac{1}{2}N_2 \leftrightarrow \frac{1}{b}M_aN_b$$

$$(5.3) \quad \frac{1}{b}M_aN_b + \frac{ad}{bc}H_2O \leftrightarrow \frac{a}{bc}M_cO_d + NH_3 + \left(\frac{ad}{bc} - \frac{3}{2}\right)H_2$$

This separation of N_2 cleavage[34] and protonation allows optimizing the equilibrium positions and kinetics of each reaction conducted at favorable temperatures near 0.1 MPa.

Previous studies have outlined the economic competiveness of this concept[31, 33, 35] (see Chapter 2 and 7). Realization of the reaction cycle, however, requires research for a reactive material that balances conflicting thermochemical properties and technical requirements[33] (see Chapter 2). These are in particular: (i) acceptable yields and kinetics of the N_2 reduction and protonation of the lattice nitrogen near 0.1 MPa, (ii) reduction of the oxidized reactant (recycling) at temperatures that can be contained physically in an industrial-scale solar furnace,

(iii) use of moderate quantities of a sustainable reducing agent, and (iv) significant energy conversion efficiencies. The "degree of freedom" to control the reduction temperature and the quantities of reducing agent and byproducts by adjusting the reactant composition is illustrated with supporting material in Appendix D. Here the hydrolysis yield and kinetics and the impact of this step on the overall process efficiency are the main subjects.

5.3 Thermochemical theory and reaction mechanism

5.3.1 Materials composition determining energy conversion efficiencies

Figure 5.2A maps the ratios of heat released during the N_2 reduction or NH_3 formation relative to the energy absorbed in the oxide reduction for various binary nitride/oxide pairs[33,36,37].

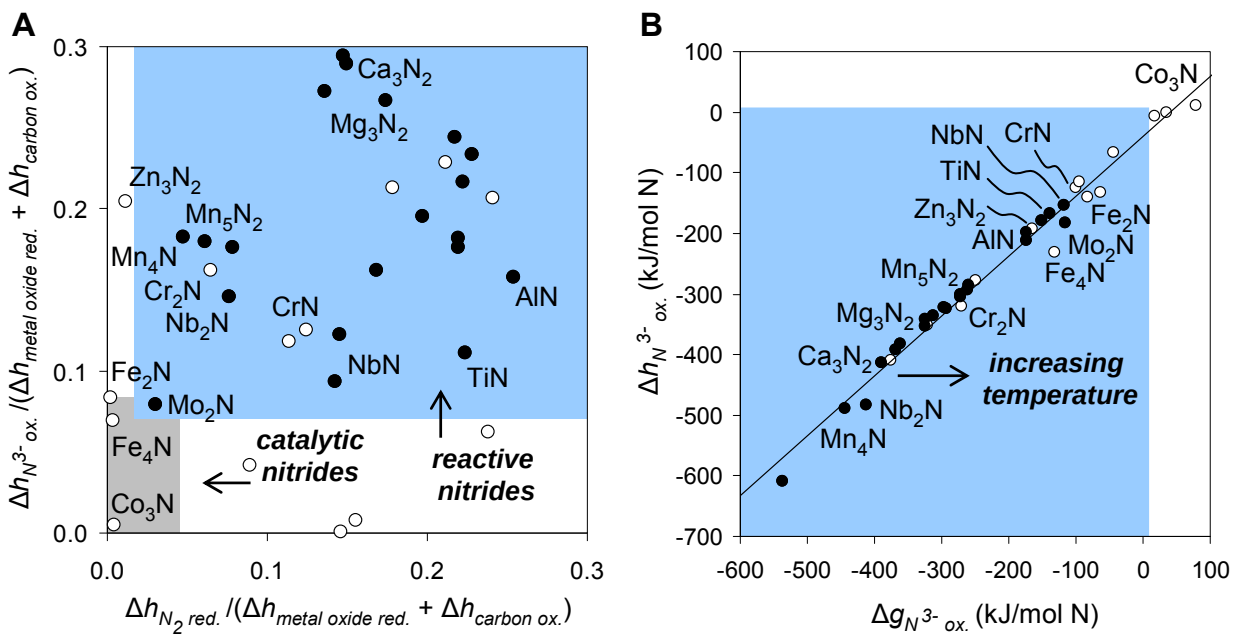

Figure 5.2 Rationale for the choice of metals: (A) Enthalpy mapping of the exothermic heat liberated during the N^{3-} oxidation ($\Delta h_{N3-\,ox.}$, Eq. 5.3) versus N_2 reduction ($\Delta h_{N2\,red.}$, Eq. 5.2), both relative to the energy supplied during the solar-thermal metal oxide reduction (red.) step (Eq. 5.1). Empty circles mark materials that do not fix 0.1 MPa N_2, do not liberate NH_3 effectively, or are radioactive (see Appendix D). (B) Correlation of $\Delta h_{N3-\,ox.}$ with Gibbs free energy of the reaction ($\Delta g_{N3-\,ox.}$). All computations are at 25°C and 0.1 MPa.

The calculation indicates high theoretical ratios of the heating value of the generated solar fuel[38] (NH_3 and syngas) to the supplied solar and chemical energy of about 52 to 85%. This is assuming no in-process heat recovery (worst case), separate metal reduction and nitridation, and use of (non-radioactive) nitrides that are expected to conform to criterion (i) above, good yields and kinetics. As well, the favorably high ratio of energy supplied in form of solar radiation to chemical energy supplied with the reducing agent ranges from 0.29 to 1.33 and can be controlled by the choice of the reactive material.

Predominantly ionic nitrides (e.g., Mg_3N_2 or Ca_3N_2) liberate large quantities of heat during their hydrolysis at lower temperatures (Fig.5.1A). This limits their attractiveness for the proposed concept since this energy can not be integrated at the higher temperatures required for the endothermic oxide reduction step. On the other hand, binary transition metal nitrides with relatively high NH_3 equilibrium yields (e.g., Mn_4N or Nb_2N, Fig.5.1B) will require large quantities of chemical reducing agent due to unfavorable stoichiometric compositions (e.g., 4 mol C per mol NH_3 for a Mn_4N/MnO reactive material relative to 3/2 mol C per mol NH_3 for a Mg_3N_2/MgO reactant). Furthermore, although well-studied for their wear resistance and refractory properties[39, 40] hydrolysis of binary nitrides and NH_3 formation kinetics are rarely reported[32, 41-44]. Similarly, bonding (and thereby reactivity) of metal nitrides appears not well understood[45, 46].

Determining an optimum reactant composition is a complex task of balancing contradictory requirements. Finding trends in the chemical reactivity and reaction kinetics is an essential first step in understanding material properties and in rational materials design[47]. With regard to the electronic structure of metal nitrides the electronegativity of the metallic constituent correlates only qualitatively with the free energy of the NH_3 formation (see Appendix D). On the

other hand, Figure 5.3 shows that higher number of d electrons correlates with reduced stability of the metal nitride. This has been attributed to the higher number of electrons in nonbonding orbitals or weakening of the metal-nitrogen bond[47, 48]. Recognizing that this bond has to be stable enough to reduce 0.1 MPa N_2 but weak enough[33] to avoid excessive liberation of heat during hydrolysis illustrates the importance of understanding the electronic structure[7, 48, 49] of the metal-nitrogen bond. This will be inevitable for the design of a novel, perhaps ternary[50, 51], optimized reactant for the solar thermochemical NH_3 synthesis.

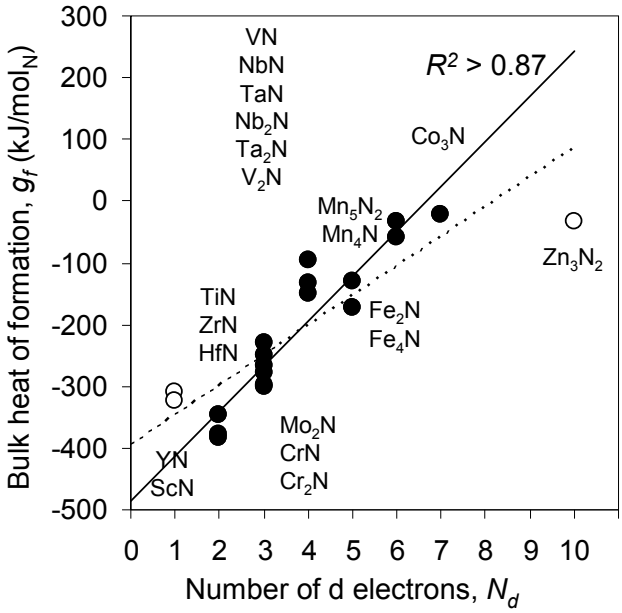

Figure 5.3 Correlation between the bulk heat of formation for transition metal nitrides, g_f, in kJ mol^{-1} lattice nitrogen versus the number of d electrons, N_d. A nearly quantitative linear correlation (solid line) is obtained when excluding elements with nominally only one d electron or with a completely occupied 3d^{10} orbital (empty circles, dashed line).

5.3.2 Possible reaction mechanism

In lieu of a complete quantitative description of the overall NH_3 formation mechanism and the derivation of a rate law from the electronic structure of the metal-nitrogen bond, which exceed the scope of this work, a schematic of the hypothetical reaction mechanism is given in

Figure 5.4. With regard on an ideal ionic solid the overall process converting N^{3-} ions and H_2O to O^{2-} ions and NH_3 is envisioned as succession of serial steps involving the diffusion of lattice nitrogen through the condensed phase. The present study provides evidence for the presence of this diffusion step and attempts to characterize its effect on the NH_3 formation kinetics.

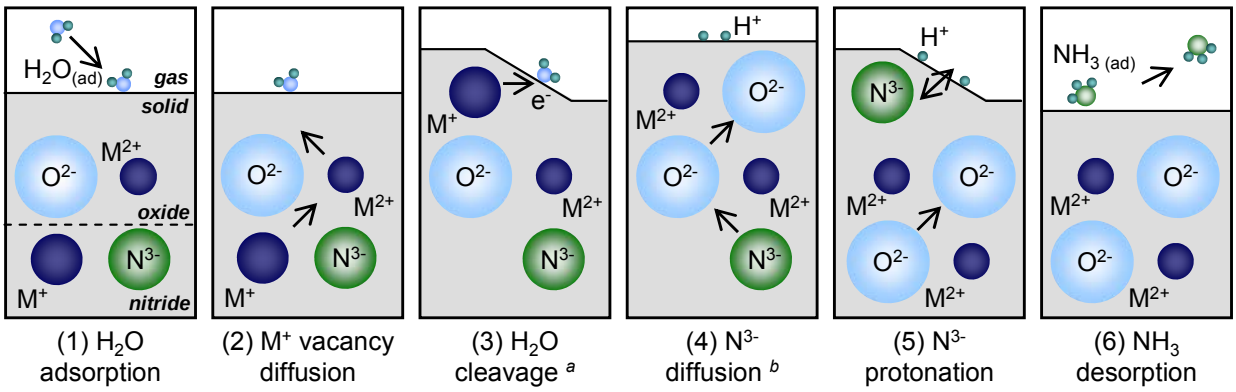

Figure 5.4 Schematic protonation of reduced nitrogen. M^{n+} is a metal in a low (e.g., n = 1, nitride) or high oxidation state (e.g., n = 2, oxide). *a*, dependent on reaction stoichiometry and the oxidation state of the metal. *b*, N^{3-} may diffuse via vacancy diffusion through the oxide or via grain boundary diffusion respectively.

Following an initially interface-controlled reaction, H_2O is adsorbed by a vacant surface site on the metal oxide. This is followed by metal vacancies diffusion through the oxidized phase to accomplish the cleavage of H_2O to H^+, OH^- and oxidized metal cations. The formed hydroxide may be transient and decompose to the oxide at elevated temperatures. Thereafter the lattice nitrogen diffuses through the oxide layer and is protonated to NH_3. The succession of these two steps may be reversed leading to possible (boundary or interstitial) diffusion of NH_3 species to the surface. Finally, the formed NH_3 is desorbed from the oxide surface indicating the importance of the Brønsted acidity of some metal cations leading to possible formation of ammonium[43], catalytic properties of the reactant, and the material geometry and surface morphology[47] determining the resistance to the mass transfer of NH_3 away from the reactant.

As a starting point, the kinetics of the H_2O cleavage and NH_3 formation employing binary metal nitrides at ambient pressure are assessed here. After describing the metal nitrides chosen for their mix of bonding properties in Section 5.5.1, experimental data for the hydrolysis of seven binary nitrides at various temperatures are summarized in Section 5.5.2 to 5.5.6. To determine the nature of kinetic limitations, characteristic kinetic parameters were determined by applying three shrinking core models discussed in Section 5.5.3. Sections 5.5.5 and 5.5.6 introduce the concept of nitride ionicity as a parameter to predict trends in the NH_3 liberation kinetics. Correlating the average electric charge of the lattice nitrogen to the reaction characteristics of the bulk material will be shown to help developing an atomic-scale understanding of the reaction mechanisms and activation barriers in the future.

5.4 Experimental

5.4.1 Metal nitridation

The nitrides of Ca, Mn and Mo were prepared (Fig. 5.5) from ca. 2 g of metal powder heated from 400°C to 700°C (Mn[52]) or 750°C (Ca[53], Mo[54]) in a quartz boat inside of a tube furnace (60 mm ID, 1 m length, quartz, model HTF55347C, temperature controller model CC58434C, Lindberg/Blue). Mn and Mo were pre-treated at 60°C for 10 min to remove water. The heating rate r_H was not constant and can be represented as $r_H = At + B$, where t is the heating time in min, A = -9.29°C min^{-2}, and B = 82.1°C min^{-1} ($R^2 > 0.90$).

N_2 was always supplied at 0.1 MPa, i.e., 1.83 ± 0.02 $l_{(STP)}N_2$ min^{-1} (Ca, Mn), or diluted with H_2, i.e., 1.09 ± 0.01 $l_{(STP)}N_2$ min^{-1} mixed with 0.364 ± 0.003 $l_{(STP)}H_2$ min^{-1} (Mo). The nitridation temperature was held for 120 (Mn), 180 (Mo) or 240 min (Ca) respectively and cooling was at about -4.87°C s^{-1} at ≤ 1 min, -50.6°C min^{-1} at ≤ 10 min, and -3.63°C min^{-1} at > 10

min. The α-Ca_3N_2/Ca_2N product was milled with pestle and mortar. All Ca-containing chemicals were handled and stored under Ar. All solids were stored under Ar or N_2 at 4°C.

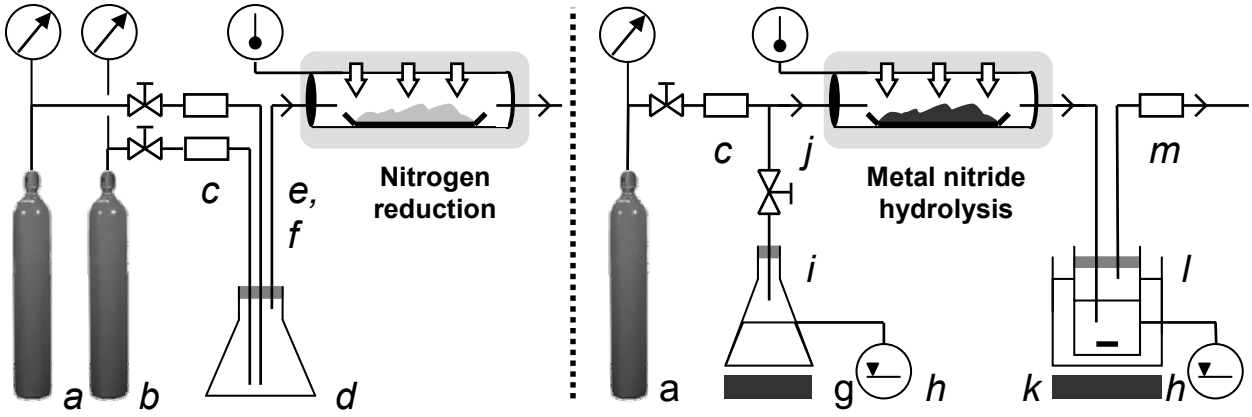

Figure 5.5 Experimental setups (*a*, N_2 gas; *b*, H_2 gas, *c*, flow meter; *d*, gas mixing; *e*, tubular flow-through furnace; *f*, metal powder in quartz boat; *g*, heating plate; *h*, liquid level control; *i*, liquid H_2O; *j*, metal nitride powder in quartz boat; *k*, magnetic stirrer; *l*, 10 mM HCl chilled with ice-cold H_2O; *m*, NH_3 gas detection tube).

5.4.2 Metal nitride hydrolysis

To describe the reaction kinetics of the lattice nitrogen seven metal nitrides (Table 5.1) with varying bonding character were reacted at different temperatures with steam (Fig. 5.5).

nitride	Mg_3N_2	w-AlN	α-Ca_3N_2 (Ca_2N)	Cr_2N (CrN)	Mn_4N ($Mn_6N_{2.58}$)	Zn_3N_2	β-Mo_2N
space group [a]	$Ia\bar{3}$	$P6_3mc$	$Ia\bar{3}$ ($R\bar{3}m$)	$P\bar{3}1m$ ($Fm\bar{3}m$)	$Pm\bar{3}m$ ($P6_322$)	$Ia\bar{3}$	$I4_1/amd$
solid phase concentration [a] (wt%)	100 ± 1	100 ± 1	86 ± 5 (14 ± 5)	85 ± 1 (10.1 ± 0.3)	70 ± 5 (28 ± 3)	100 ± 1	24.9 ± 0.4
average particle diameter (μm)	27 ± 11	16 ± 6	105 ± 25	43 ± 14	46 ± 19	21 ± 7	13 ± 6
BET surface area (m^2 kg^{-1})	8800 ± 300	4900 ± 100	672 ± 3	402 ± 5	270 ± 3	3750 ± 30	426 ± 3
powder bed surface [b] (cm^2)	42	42	42	33	33	42	33
void space fraction [c] (m^3 m^{-3})	0.68	0.69	0.55	0.55	0.65	0.73	0.73
partial nitrogen charge [d]	-2.06 ± 0.19	-0.36 ± 0.05	-1.91 ± 0.29	-0.30 ± 0.03	-0.47 ± 0.18	-0.64 ± 0.00	-0.53 ± 0.10

Table 5.1 Characterization of the metal nitride powder beds. *a*, X-ray diffraction data; *b*, ± 5.24 %, powder bed thickness generally < 1 mm; *c*, ± 5.15 % (both via error propagation); *d*, based on the literature (see Section 5.5.1).

To remove residual O_2 the furnace was purged for ca. 10 min with 0.5-0.9 $l_{(STP)}N_2$ min^{-1} before each experiment. Nitride powder was placed into a quartz boat (0.5 g, except 1 g Cr_2N,

i.e., 5.82 x 10^{-1} to 1.23 x 10^{1} mmol total lattice nitrogen), introduced at 100°C into the furnace, and heated to 200-1000°C. Heating rates can be estimated (R^2 = 0.75-0.83) with A = -6.85°C min^{-2}, and B = 50.2°C min^{-1} (at 200-300°C), A = -4.23°C min^{-2}, and B = 61.4°C min^{-1} (500-600°C), or A = -3.59°C min^{-2}, and B = 82.8°C min^{-1} (1000°C) respectively. Final temperatures were held for 60 min and steam was supplied at 0.8 ± 0.1 $ml_{(STP)}H_2O$ min^{-1}.

The gas leaving the furnace was routed through a liquid absorbent (25 ± 5 $ml_{(STP)}$ aqueous HCl, 10 mM HCl, chilled with ice-cold H_2O). To estimate the yield of absorbed NH_4^+ in the liquid phase, 5 ml samples were taken at 0, 1, 5, 10 and 60 ± 0.5 min (Mg_3N_2, AlN, Ca_3N_2, and Zn_3N_2) or 0 (this includes the heating phase), 5, 10, 30 and 60 ± 0.5 min (Cr_2N, Mn_4N, and Mo_2N) after the reaction temperature was reached. After 60 min the furnace was opened and cooled (at -0.90 to -8.7 °C s^{-1} within the first minute, -8.8 to -82 °C min^{-1} at < 10 min, and -1.1 to -18°C min^{-1} at > 10 min) to below 100°C. All solids were stored under Ar (Mg_3N_2, Ca_3N_2) or air at 4°C. All liquids were stored at room temperature.

5.4.3 Solid state analysis

Powder X-ray diffraction (XRD) patterns were taken with a Miniflex II diffractometer (Cu-target X-ray tube, 30 kV / 15 mA output, diffracted beam monochromator, Rigaku) with a 5-80 °2θ range, 1 or 10 °2θ/min scan speed, and 0.02 data points/°2θ, continuous mode for quantitative solid phase identification (PDXL Software Version 1.6.0.0). To confirm metal nitridation energy-dispersive X-ray spectroscopy (EDS) was employed using scanning electron microscopy (SEM) (20 keV, S-3500N, Hitachi; Link Pentafet 7021 X-ray detector and Inca Energy X-ray analysis software, both Oxford Instruments). Nitride particles were imaged by SEM. All weights were determined using an AE260 DeltaRange balance (± 0.1 mg, Mettler). The specific BET surface area was analyzed by NanoScale Inc., Manhattan, KS.

5.4.4 Liquid and gas phase analysis

NH_3 absorbed by the liquid absorbent was quantified with an NH_3 Ion Selective Electrode and a pH/ISE Controller (model 270) (both Denver Instrument), combined with the liquid level in the absorption vessel (error ca. ± 5 ml). Liquid samples were analyzed in triplicate to estimate the concentration of dissolved NH_3 with zeroing for the signal from pure water. The uncertainty of NH_3 concentrations was estimated as the average of one standard deviation of about 65 liquid samples analyzed in triplicate. The outlet of the absorption vessel was equipped with an NH_3 gas detection tube (0.25-3 or 5-70 ppm NH_3 detection range, Dräger).

5.4.5 Chemicals

Solid chemicals were AlN (99.8% pure, -325 mesh), Mn metal (99.9% pure, -325 mesh), Zn_3N_2 (99.9% pure, -200 mesh), and Mo metal (99.95% pure, -325 mesh) all from Noah Technologies; Ca metal (99% pure, granular) and NH_4Cl (99.5%, extra pure) both from Acros Organics; Mg_3N_2 (99.6% pure, -325 mesh, AlfaAesar); Cr_2N (98% pure, -100 mesh, Prochem); and NaOH (99.6%, certified ACS pellets, Fisher Scientific). Glassware was cleaned with acetone (certified ACS, Fisher Scientific). All gases (H_2, N_2, and Ar) were UHP Zero grade (Linweld). H_2O was deionized (Direct-Q 3 UV, Millipore) and degassed with Ar. HCl (12.1 N, certified ACS Plus) was from Fisher Scientific.

5.5 Results and Discussion

5.5.1 Characterization of the binary metal nitrides

Only a few elements of the Periodic System show significant ionic bonding with nitrogen (i.e., charge transfer and formation of the N^{3-} ion). Nitrogen is reluctant to accept electrons due to the negative electron affinity caused by the N $2p^3$ configuration[34, 46, 55]. The contribution of the ionic character to the metal-nitrogen bond is relatively large (salt-like nitrides) if the metal

constituent is strongly electropositive and has a low ionization potential (e.g., alkali or alkaline earth metals), or if the metal has a highly occupied d-band (e.g., Zn). Alternatively, covalent metal-nitrogen bonds (with most p-block elements, incl. Al) are formed if electrons are not transferred entirely to the N atom. This increases the corrosion resistance of the nitride[55]. Interstitial crystal structures are found if the N atom neither accepts nor shares electrons. In this case a relative large fraction of the nitrogen occupies the interstices in the metal lattice as N atoms. This leads to chemically stable (e.g., with metals from the Ti, V, and Cr group) or unstable compounds (intermediate nitrides, e.g., with Mn or Fe).

Table 5.1 characterizes the metal nitrides tested in this work. Values of the partial electronic charge of the lattice nitrogen, q_N (in units of the absolute elementary charge e), are given as arithmetic average within one standard deviation based on the estimates of 4-12 (if not stated otherwise) first principle computations. The estimation of q_N is generally based on density functional theory (DFT) and Mulliken population analysis[56-63].

The partial nitrogen charge for AlN is given as the average of two computations[59, 60]. Given the available data, the contribution of the Ca_2N sub-nitride[46] to the partial nitrogen charge of the α-Ca_3N_2/Ca_2N mixture was neglected. The value provided for the Cr_2N/CrN mixture was based on literature employing DFT[61], a complete-active-space self-consistent-field approach[64] and the modified neglect of diatomic overlap method[65]. One value for q_N of CrN[65] that is significantly higher than the remaining values[61, 64, 65] was neglected. The partial nitrogen charge for manganese nitride was based on two estimates for Mn_4N and MnN using electron diffraction[66] and DFT[61]. The q_N value for the relatively unstudied Zn_3N_2[67] was taken as estimated near ambient pressure[58]. The partial nitrogen charge of Mo_2N was based on 12 computational values[62, 63] with a deviation of less than 50% from their arithmetic average. If possible the data

range was narrowed to large clusters ($Mo_{2n}N_n$ clusters with $n \geq 4$)[62]. The partial charge of nitrogen in NH_3 has been reported as -0.246[68] which is below all solid-state nitrogen values selected and estimated here (Table 1). This confirms qualitatively that the solid state data is at least not in gross error.

X-ray diffraction identified the nitridated Ca as a mixture of α-Ca_3N_2 and a minor fraction Ca_2N[46]. The synthesized manganese nitride consists of a cubic ε-Mn_4N and a hexagonal $Mn_6N_{2.58}$ phase. Given the broad non-stoichiometry range for transition metal nitrides[46], $Mn_6N_{2.58}$ may be identified as ζ-phase Mn_2N (or Mn_5N_2 respectively)[52]. The calculations below (see Section 5.5.2), however, are based on a $Mn_6N_{2.58}$ composition as-identified. Nitridation of Mo yielded a tetragonal β-phase Mo_2N[69] which was assumed for Section 5.5.2. Possible reasons for the relative low yield of Mo_2N (confirmed with EDS)[54] include convective cooling of the metal surface by the gas flow and diffusion of N through Mo_2N[54].

The BET specific surface area (Table 5.1) of the materials is consistent with nitrides studied for catalytic or reactive NH_3 formation[42, 54]. The surface area of the nitrides that have been prepared from their elements is of the same order of magnitude as for purchased Cr_2N and about one order of magnitude below the specific surface area of Mg_3N_2, AlN and Zn_3N_2. Whether this may affect NH_3 yields is addressed in Section 5.5.3.

5.5.2 Data and data processing

To determine the reaction kinetics for the hydrolysis of seven binary metal nitrides varying in their partial nitrogen charge, Mg_3N_2, AlN, Ca_3N_2, Cr_2N, Mn_4N, Zn_3N_2, and Mo_2N powders were exposed to steam at about 0.1 MPa and at temperatures ranging from 200-1000°C. The yield of NH_3 from these reactions, X_{NH3}, is reported as molar ratio of NH_3 captured by the

acidic absorbent (n in mol) at a given time, t, relative to the lattice nitrogen of the reactant before the reaction:

$$(5.4) \quad X_{NH_3} = \frac{n_{absorbed\ NH_3,t}}{n_N} = \frac{\sum_{t=0-60\,\mathrm{min}} \left(c_{NH_3,t} - c^*_{NH_3}\right) V_t}{m_r \sum_{i=all\ nitrides} b_i x_i M_i^{-1}}$$

where c_{NH3} in mol L^{-1} is the concentration of NH_3 detected in the absorbent, the asterisk marks pure water used as a reference, V in L is the sample volume, m_r in g is the mass of metal nitride powder reacted, b is a stoichiometric coefficient (see Eq. 5.3), x in g g^{-1} is the nitride weight fraction (Table 5.1), and M in g mol^{-1} is the molar mass. The initial reaction rate, r_0, is calculated analogously from a tangent to the data point collected at Δt = 5 min.

The rate-determining step of a heterogeneous reaction will depend on either diffusion or the making and breaking of chemical bonds, k_r, where k marks a specific rate constant and diffusion of the reaction participants occurs in the gas phase, k_g, or in the condensed phase, k_s. To determine the rate-limiting step three shrinking-core models for spherical particles of unchanging size[70] were applied:

$$(5.5) \quad k_g t = X_{NH_3}$$

$$(5.6) \quad k_s t = 1 - 3 \times (1 - X_{NH_3})^{2/3} + 2 \times (1 - X_{NH_3})$$

$$(5.7) \quad k_r t = 1 - (1 - X_{NH_3})^{1/3}$$

The kinetic data and the specific rate constants fitted[28, 41] in the time interval Δt_{fit} with a maximum R^2 are summarized in Table 5.2. Representative graphs of the NH_3 yield versus the reaction time (at the temperature that resulted in the maximum X_{NH3}) are given in Figure 5.6. As an aside, the yield of NH_3 after 60 min is below the value that would be predicted by the applied models and is in most cases even below the yield determined after 10 or 30 min respectively

presumably due to unwanted stripping of the absorbent by the steam routed through the liquid. An atomic nitrogen balance is attempted below.

metal as nitride	T_{hyd} (°C)	r_0 (mol_{NH3} mol_{metal}^{-1} s^{-1})	model	k (s^{-1})	R^2 >	Δt_{fit} (min)
ionic nitrides						
Mg	200	$1.0 \pm 0.2 \times 10^{-4}$	g	6.2×10^{-4}	0.80	10
	300	$2.3 \pm 0.4 \times 10^{-5}$	g	9.7×10^{-5}	0.99	60
	500	$1.1 \pm 0.2 \times 10^{-3}$	g [b]	1.2×10^{-3}	0.90	10
Ca	200	$1.4 \pm 0.2 \times 10^{-5}$	g [b]	7.7×10^{-5}	0.99	60
	300	$4.3 \pm 0.6 \times 10^{-6}$	g [b]	4.4×10^{-5}	0.90	60
	500	$1.6 \pm 0.2 \times 10^{-5}$	g [b]	2.9×10^{-4}	0.75	60
Zn [c]	300	$8 \pm 1 \times 10^{-7}$	s	3.3×10^{-10}	0.87	10
	500	$3.3 \pm 0.6 \times 10^{-4}$	g	8.9×10^{-4}	0.91	10
	1000	$2.9 \pm 0.4 \times 10^{-4}$	s	2.8×10^{-5}	0.72	5
covalent nitrides						
Al	300	$9 \pm 2 \times 10^{-8}$	s	6.3×10^{-13}	0.96	10
	500	$8 \pm 1 \times 10^{-6}$	s	6.9×10^{-9}	0.92	60
	1000	$4.9 \pm 0.8 \times 10^{-5}$	s	1.4×10^{-7}	0.88	60
interstitial and intermediate nitrides						
Cr	500	$1.5 \pm 0.3 \times 10^{-7}$	s	7.6×10^{-12}	0.80	30
	600	$1.0 \pm 0.2 \times 10^{-7}$	s	3.3×10^{-12}	0.95	10
	1000	$1.8 \pm 0.3 \times 10^{-6}$	s	1.2×10^{-9}	0.99	30
Mn	300	$8 \pm 1 \times 10^{-8}$	r [b]	8.2×10^{-8}	0.98	30
	500	$9.7 \pm 0.9 \times 10^{-6}$	s	6.9×10^{-8}	0.93	60
	1000	$5.3 \pm 0.7 \times 10^{-6}$	s	3.6×10^{-8}	0.96	30
Mo [c]	500	$3.2 \pm 0.3 \times 10^{-5}$	s	6.4×10^{-6}	0.82	30
	600	$4.9 \pm 0.7 \times 10^{-6}$	s	1.5×10^{-7}	0.88	30
	1000	$7 \pm 1 \times 10^{-6}$	s	4.0×10^{-7}	0.85	30

Table 5.2 Kinetic data and modeling. Applying shrinking core models (controlled by: s, diffusion through the solid reaction product; r, reaction; g, diffusion through the gas film) in the time range Δt_{fit}. *b*, r or g respectively show an only slightly (< 0.05) lower R^2 value. *c*, gray rectangles mark data that deviate somewhat from the data obtained for other nitrides in the same chemical category (ionic, etc.).

The solid reaction products were mixtures of the reacted metals and nitrides and their oxides or hydroxides, i.e., $Mg(OH)_2/MgO$, $Al(OH)_3/Al_2O_3$, $Ca(OH)_2/CaO$, Cr_2O_3, MnO/Mn_3O_4, ZnO, and MoO_3/MoO_2. For a given metal the presence of the second compound in the solid

listed above increased with increasing temperature. Significant removal of metal atoms from the solid phase and condensation of a solid product at the furnace outlet is unlikely and was only observed (about 43.6 mol%) for the hydrolysis of Mo_2N at 1000°C yielding MoO_3 vapor.

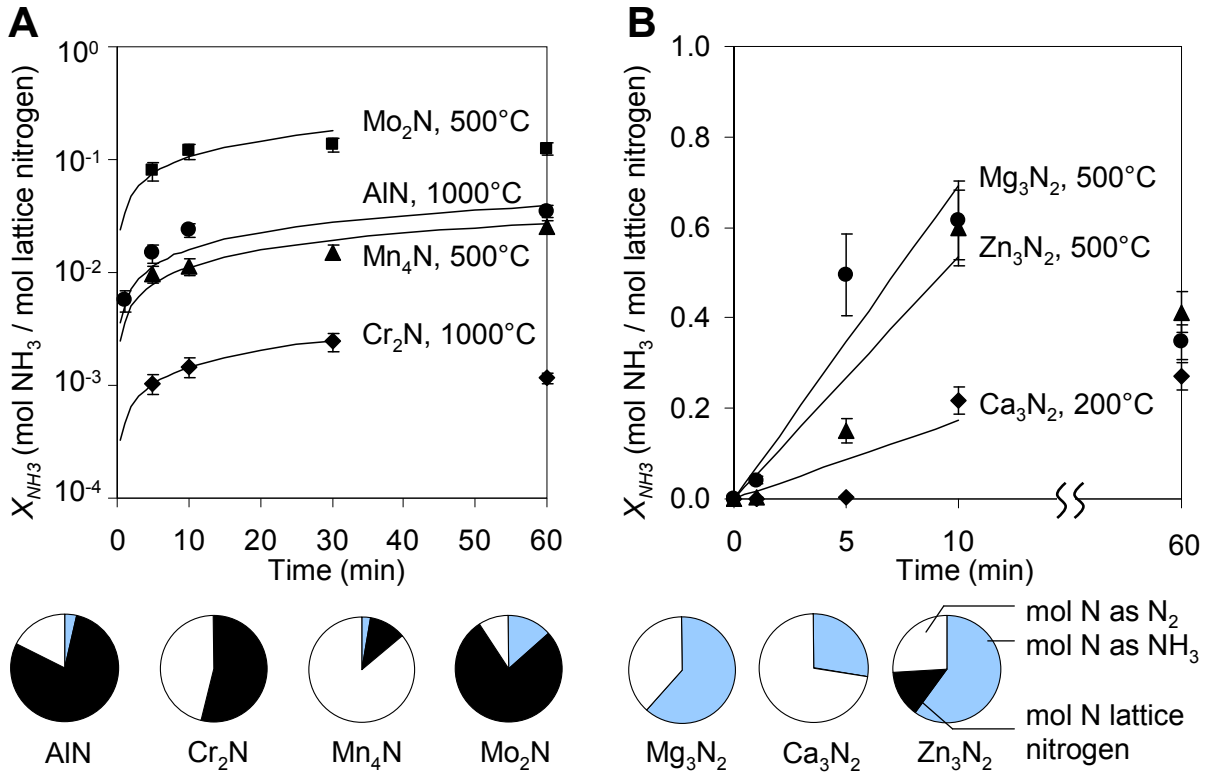

Figure 5.6 Representative results (for a complete version see Appendix D) for steam hydrolysis of various metal nitride powders illustrating the kinetic fitting with maximized R^2 (see Table 5.2): (A) solid-state diffusion-governed NH_3 formation from Al (circle), Cr (diamond), Mn (triangle), and Mo (square) nitrides and (B) the supply of H_2O from the gas phase controlling NH_3 formation from Mg (circle), Ca (diamond) and Zn (triangle) nitrides. Error bars indicated are via error propagation.

5.5.3 Kinetics of the NH_3 liberation

The hydrolysis of AlN and all tested transition metal nitrides except Mo_2N shows increasing initial reaction rates r_0 with increasing temperature with AlN and Zn_3N_2 most responsive to temperature. Based on minimizing the residual sum of squares between the

experimental data and the employed shrinking core models Eq. 5.5-5.7 a solid-state diffusion limitation (Eq. 5.6, Fig. 5.4) describes the formation of NH_3 from the tested p- and d-block nitrides (with few exceptions, see Table 5.2) best.

Solid-state diffusion limited NH_3 formation is in agreement with the low yield of NH_3 via corrosion of chromium nitrides or stainless steel with dissolved nitrogen[32, 40]. The NH_3 formation from Mn_4N, Zn_3N_2 and Mo_2N appears to follow a diffusion limited mechanism over a relative broad range of the tested reaction temperatures and times. Some factors that may contribute to this mixed behavior are addressed below (this section and Section 5.5.4). The hydrolysis of the refractory AlN[71] has been shown previously to depend significantly on the steam temperature and pressure, and the AlN particle size[39, 41, 44]. Hot pressed AlN particles have been found to yield only 0.3% Al_2O_3 after steam hydrolysis for 30 hrs at 1000°C[39]. Also, a 2 mol% oxidation of fine AlN powder has been reported when hydrolyzing the nitride for 60 min at 900°C[41]. On the other hand, NH_3 from AlN and H_2O at below 100°C has been reported[44]. Up to 70 mol% conversion via hydrolysis for 60 min at 1000°C has been reported as well[41]. The relative comparisons of nitrides shown here are still meaningful while the literature and our experiments may not be amenable to a consistent rationale at this point.

The hydrolysis of Mg_3N_2 or Ca_3N_2 respectively appears to follow a mechanism that is limited by the diffusion in the gas phase (Eq. 5.5). Analogously, the minimum initial reaction rates for these nitrides at 300°C may originate from the opposing effects of high reactant concentrations at low temperatures (i.e., about 25, 21, or 16 mol H_2O m^{-3} at 200, 300, or 500°C respectively, assuming an ideal gas) and short residence times of the meta-stable NH_3 product at high temperatures (about 13, 11, or 8 s at 200, 300, or 500°C respectively, assuming NH_3 in the gas phase). Furthermore, accounting for the difference in the average particle diameter, d_p, (k_g ~

d_p^{-1} [70]) between Mg_3N_2 and Ca_3N_2 particles (Table 5.1) yields a "corrected" specific rate constant k_g for Ca_3N_2 in the range of 0.47-1.72 times k_g for Mg_3N_2. Thus, the delayed NH_3 formation observed during the hydrolysis of Ca_3N_2 can be explained to a large part with the difference in specific surface area available for the reaction. Previous studies of the Mg_3N_2 decomposition described the formation of $Mg(OH)_2$ as a diffusion limited process with specific rate constants on the same order as those reported here. In agreement with the data reported here, the formation of the chemisorbed NH_4^+ could not be fitted to a solid-state diffusion controlled model[43] and appears limited either by gas-phase diffusion or reaction kinetics.

NH_3 formation without solid-state diffusion control for Mg_3N_2 or Ca_3N_2 respectively is supported by a correlation between the specific rate constant and the specific volumes of nitrides, oxides and hydroxides (Fig. 5.7) leading to crevice formation during the hydrolysis of Mg_3N_2, Ca_3N_2 (Fig. 5.7) or Zn_3N_2 (see Appendix D) respectively.

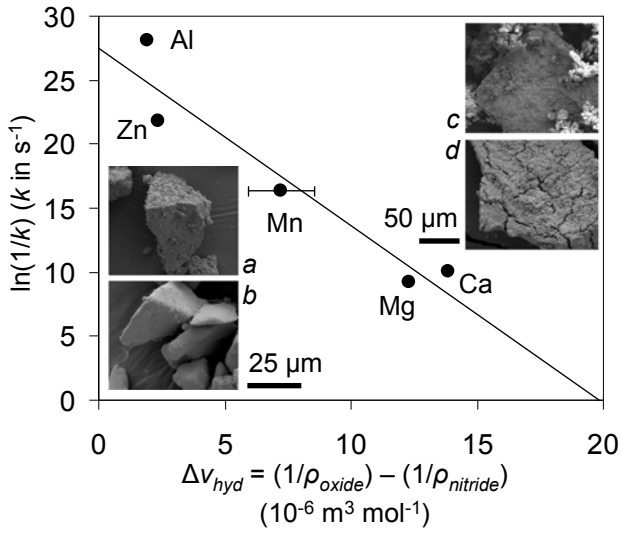

Figure 5.7 The specific rate constant *k* (maximum R^2) vs. the specific volume change (Δv_{hyd}) when oxidizing the nitrides at 300°C (ρ_i is the density in mol m^{-3} of substance i). Error bars are three standard deviations; R^2 for the fit (line) is > 0.91. SEM images are representative nitrides of (*a*) or (*b*) Mn, and (*c*) or (*d*) Ca before or after the hydrolysis respectively.

Analogously, by 88.9 or 56.7 % decreased Mg_3N_2 or Ca_3N_2 particle sizes respectively after hydrolysis can be explained with physical disintegration of the particles due to specific volumes differences.

5.5.4 Nitrogen mass balance

The nitrogen mass balance (Fig. 5.6) neglects the relatively small amount of NH_3 detected in the vented gas phase (about 3.4-4.6 µmol NH_3 after 60 min via hydrolysis of Mg_3N_2 or Ca_3N_2 respectively). No formation of chemical compounds containing nitrogen other than NH_3 and N_2 is assumed. Figure 5.6 shows that all ionic nitrides are nearly completely oxidized after 60 min under steam. At 500°C 27-70 mol% of the removed N^{3-} is recovered as NH_3. All other nitrides except Mn_4N liberated less than 50 mol% of the lattice nitrogen with 0-17 mol% recovered as NH_3, except 41 ± 3 mol% NH_3 from 0.80 ± 0.01 mol% nitrogen liberated by AlN at 300°C or 60 ± 5 mol% NH_3 from 23 ± 2 mol% nitrogen liberated by Mo_2N at 500°C.

Regarding Mn_4N, significant nitrogen conversion to N_2H_4 was suspected[22, 72] but back titration of the liquid absorbent did not confirm this. Therefore the large amount of lattice nitrogen liberated from Mn_4N either does not form NH_3 effectively or NH_3 is formed but not removed quickly enough from the material surface, e.g., due to Lewis or Brønsted acid-base interactions between Mn^{2+}, Mn^{3+}, NH_4^+ and NH_3.

Projecting the nitride unit cells on the BET surface area of the bulk material estimates the lattice yield of a pure surface reaction (independent on the orientation of the crystal facets) with 0.07-0.80 mol% N from Mn_4N, CrN, Cr_2N, $Mn_6N_{2.58}$, Mo_2N, AlN or 2.34 mol% N from Zn_3N_2 respectively. This evidences the continuous formation of NH_3 from these materials (Fig. 5.6) involves the transport of lattice nitrogen from the bulk material (approximately 13-490 nm below the particle surface) to the solid/gas interface (compare Figure 5.4).

5.5.5 Nitride ionicity controlling the solid-state diffusion

The metal nitride hydrolysis yielding NH_3 is in a thermodynamic sense an essentially spontaneous process (Fig. 5.2B), impaired at elevated temperatures only by thermal decomposition of the solid forming N_2 or the decomposition of NH_3 to N_2 and H_2. The reaction characteristics reported here are presumably of kinetic nature. Ionic materials such as Mg_3N_2 yield NH_3 quickly, opposed, e.g., to the interstitial Cr_2N liberating NH_3 only at elevated temperatures.

Ionicity[73], i_N, here defined as the partial nitrogen charge (see Section 5.5.1) relative to a theoretical -3 oxidation state of the lattice nitrogen, $i_N = q_N /(-3)$, can be correlated with the specific rate constant k_s (Fig. 5.8).

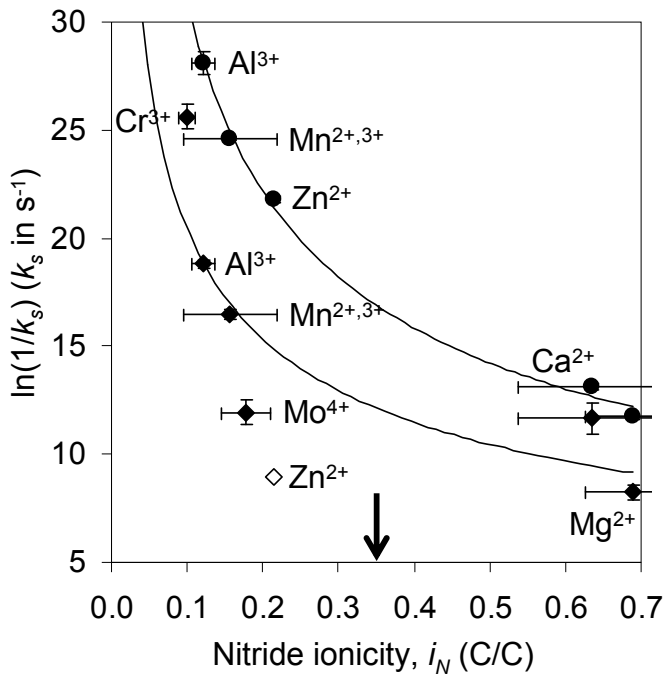

Figure 5.8 The specific rate constant k_s at 300°C (circles, solid line fit with R^2 > 0.99) or 500°C (diamonds, fit excluding Zn^{2+} with R^2 > 0.76) versus nitride ionicity (arrow see Section 5.5.5). Metal cations indicated mark the oxides/hydroxides detected after hydrolysis. Error propagation using three standard deviations yields in average ca. ± 2.22% (300°C) or ± 3.23% (500°C).

Assuming that the solid state diffusion is controlling the NH_3 formation kinetics Figure 5.8 indicates a promotion of the reaction kinetics by the partial electric charge of the lattice nitrogen, leveling off at about 35% ionicity (arrow, Fig. 5.8). As reported for the diffusion of nitrogen or carbon in other solid state processes[74, 75], the effective diffusion coefficient appears dependent on the lattice nitrogen activity.

Limiting the focus on the p- and d-block nitrides, the effective chemical diffusion coefficient, D in $m^2\ s^{-1}$, is given with[70]:

$$(5.8) \qquad D = \frac{ad}{24c}\frac{\rho_{nitride} k_s d_p^2}{\rho_{steam}} \approx 8.54\times10^{-23}\exp\left(1.24\times10^2\times i_N\right)$$

where a, c, and d are stoichiometric coefficients (see Eq. 5.3) and $\rho_{nitride}$ and ρ_{steam} are the molar densities of the solid and gaseous reactants at 500°C in mol m^{-3} respectively. Figure 5.9 shows a plot of the diffusion coefficient versus the nominal radius of a single metal ion[6, 76] (Fig. 5.9A) or the nitride ionicity respectively (Fig. 5.9B).

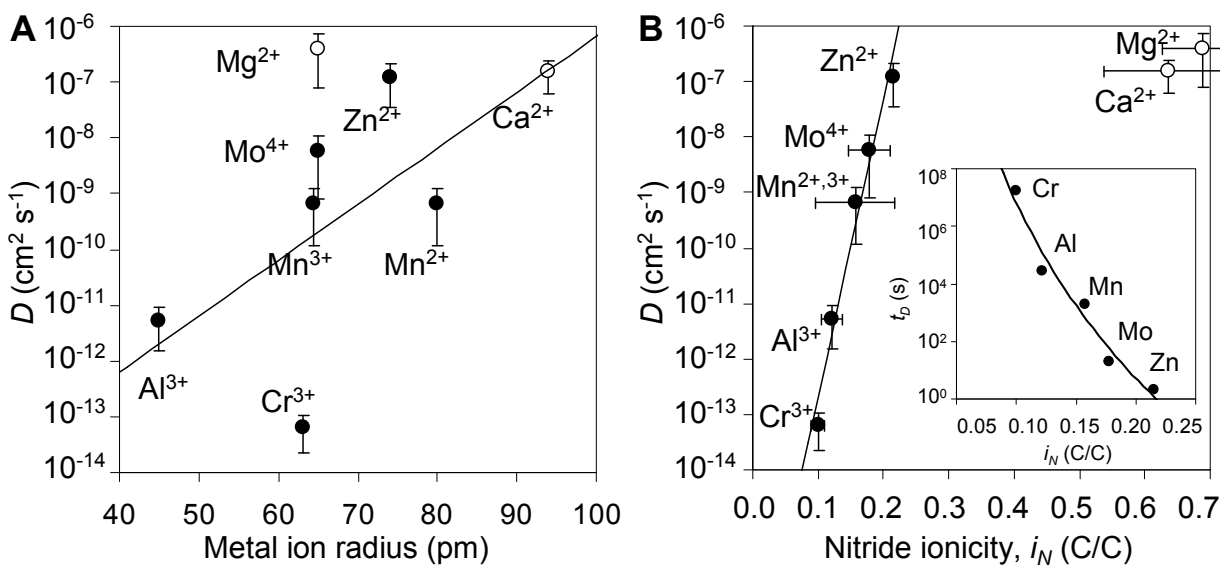

Figure 5.9 The diffusion coefficient *D* at 500°C plotted against (A) the nominal radius of a single metal ion with $R^2 > 0.28$ or (B) the nitride ionicity with $R^2 > 0.97$. The inlet shows the characteristic time for the diffusion process with $R^2 > 0.96$. R^2 computations are based on the data set without Mg^{2+} and Ca^{2+}. Error bars on the ordinate are via error propagation.

Apparently, D as estimated for the bulk material does not correlate with the nominal radius of a single metal ion but yields a nearly quantitative correlation ($R^2 > 0.97$) with the nitride ionicity. This supports the inferred link between solid-state diffusion-controlled NH_3 formation and the partial charge of the nitrogen atom.

For comparison, assuming a diffusion length equal to half the particle diameter yields the characteristic time for a diffusion-limited process, t_D, with approximately[77] $d_p^2/(16D)$. The characteristic diffusion times (Fig. 5.9B) for Cr_2N, AlN, or Mn_4N are about 206 days, 7.9 hrs, or 33.7 min respectively. This is by orders of magnitude larger than, e.g., the 0.1-2 ms range estimated for a solar thermochemical H_2 production cycle that had been assessed as not limited by oxygen vacancies diffusion in a ceria lattice[77]. The characteristic times for the NH_3 liberation from Mo_2N or Zn_3N_2, 19.7 or 2.16 s respectively, fall in between these two time ranges. This again confirms the deviation of Zn_3N_2 from the ionic nitrides of the s-block and of Mo_2N from the interstitial d-block nitrides evidenced above (Table 5.2, Fig. 5.7). Nevertheless, the formation of NH_3 from Mo_2N ceases before the reactive lattice nitrogen is consumed (Fig. 5.6) probably due to the formation of a thick oxide layer (confirmed via SEM, see Appendix D). Formation of NH_3 from Zn_3N_2 nears completion presumably due to the observed crevice formation (see Section 5.5.3).

The diffusion coefficient is increasing with increasing ionicity (and thereby theoretically increasing size of the nitrogen ion vacancy) suggesting that the size of hypothetical N^0, N^{1-}, N^{2-}, and N^{3-} ions[66, 71] is not the determining factor for the NH_3 liberation kinetics. The nitride ionicity and its relation to the diffusion coefficient may be rather understood in terms of ambipolar diffusion that is the coupled migration of nitrogen ion vacancies and electrons under a nitrogen chemical potential gradient[77]. Increasing the nitride ionicity increases the volumetric

concentration of reactive lattice nitrogen or ion vacancies respectively. This increases the ambipolar diffusion coefficient assuming generally a higher mobility of electrons in the conduction band[45, 46] compared to the mobility of the nitrogen ion vacancies.

5.5.6 Ionicity guiding the design of an optimized nitride reactant

Determination of the actual diffusing nitrogen species resulting of formation of NH_3 from the studied transition metal nitrides requires further studies. With regard to the hypothesizes ammonia formation mechanism (Fig. 5.4) the nitride ionicity appears useful when developing an atomic-scale understanding of the solid-state reaction mechanism and for controlling the bonding nature of a prospective optimized ternary nitride reactant.

The experimental data presented here are evidence for a rate limiting solid-state diffusion step that correlates to the nitride ionicity. The activation energies for the nitride hydrolysis determined from Arrhenius plots of the specific rate constants[28] given in Table 5.2 are approximately 92, 106, or 63 kJ mol^{-1} for Cr_2N, AlN, or Mn_4N respectively (with ±50.3% relative standard deviation). The literature reports activation energies of about 60 kJ mol^{-1} for the diffusion of Mn^{2+}, Mn^{3+}, or Mn^{4+} vacancies during the oxidation of Mn_3O_4[78] and about 135 kJ mol^{-1} (about 1.4 eV in average for a particle grain size ≥ 1 μm) for conduction in α-Al_2O_3[79]. From the ionic nitrides, Zn_3N_2 shows high activation energy of approximately 96 kJ mol^{-1}. That is, the hydrolysis of only the most ionic nitrides, i.e., Mg_3N_2 and Ca_3N_2 or with activation energy in the range of 9-14 kJ mol^{-1}, is likely not limited by diffusion in the solid state.

However, whether it is the lattice nitrogen or nitrogen ion vacancies respectively or a molecular species[80] that is diffusing to the surface cannot be inferred unerringly. Whether the oxides conduct the basic N^{3-} ion requires validation.

5.6 Conclusions

This study was motivated by the desire to find new pathways to produce ammonia from air and water without the use of natural gas. Metal nitrides were investigated experimentally. The reaction yields and kinetics of the NH_3 formation via protonation of the lattice nitrogen of seven binary metal nitrides were determined. The data are evidence for a rate limiting solid-state diffusion step during the hydrolysis of AlN, Cr_2N/CrN, Mn_4N/Mn_2N, Zn_3N_2, or Mo_2N powders respectively. A correlation between the nitride ionicity and the effective diffusion coefficient suggests a reaction mechanism governed by the volumetric concentration of active nitrogen ions or their vacancies respectively. Whether the oxides formed on the nitride particles conduct N^{3-} ions requires, however, validation.

It can be anticipated that the nitride ionicity may prove useful as a modeling parameter controlling the bonding nature and reaction kinetics of a prospective ternary nitride reactant. Based on NH_3 liberation kinetics, the nitrogen mass balance and the minimum quantity of heat liberated during the hydrolysis step Mo_2N may be a promising major constituent of reactant for the solar thermochemical NH_3 synthesis.

5.7 Associated content in Appendix D

Supporting Information: An Ellingham diagram for the reduction of MgO, Al_2O_3, CaO, Cr_2O_3, Mn_2O_3, MnO, ZnO, MoO_2 and the oxidation of various reducing agents vs. temperature, the dependence of the free energy stored in the reaction cycle products (NH_3, H_2, or CO) on the stoichimetric composition of the nitride/oxide reactant, a detailed version of Fig. 5.2A, a plot of the free energy of the N^{3-} oxidation reaction vs. the electronegativity of the metal constituent of the nitride, a complete version of Fig. 5.6 providing kinetic NH_3 formation data and the nitrogen mass balance, SEM micrographs of the Zn_3N_2 and Mo_2N hydrolysis, and plots correlating the

maximum NH_3 yield via hydrolysis of the tested nitrides at 300 and 500 °C to the average charge of the nitrogen ion in the solid state.

5.8 References

[1] M. Grätzel, Mesoscopic solar cells for electricity and hydrogen production from sunlight, Chemistry Letters, 34 (2005) 8-13.

[2] M. Roeb, H. Müller-Steinhagen, Concentrating on solar electricity and fuels, Science, 329 (2010) 773-774.

[3] V. Smil, Detonator of the population explosion, Nature, 400 (1999) 415-415.

[4] Z. Kirova-Yordanova, Exergy analysis of industrial ammonia synthesis, Energy, 29 (2004) 2373-2384.

[5] I. Rafiqul, C. Weber, B. Lehmann, A. Voss, Energy efficiency improvements in ammonia production - perspectives and uncertainties, Energy, 30 (2005) 2487-2504.

[6] H.P. Latscha, M. Mutz, Chemie der Elemente, Chemie-Basiswissen IV, Springer, Heidelberg, 2011, ISBN 978-3-642-16914-4.

[7] A. Hellman, E.J. Baerends, M. Biczysko, T. Bligaard, C.H. Christensen, D.C. Clary, S. Dahl, R. van Harrevelt, K. Honkala, H. Jonsson, G.J. Kroes, M. Luppi, U. Manthe, J.K. Nørskov, R.A. Olsen, J. Rossmeisl, E. Skúlason, C.S. Tautermann, A.J.C. Varandas, J.K. Vincent, Predicting catalysis: Understanding ammonia synthesis from first-principles calculations, Journal of Physical Chemistry B, 110 (2006) 17719-17735.

[8] V. Smil, How many billions to go?, Nature, 401 (1999) 429-429.

[9] C.H. Christensen, T. Johannessen, R.Z. Sørensen, J.K. Nørskov, Towards an ammonia-mediated hydrogen economy?, Catalysis Today, 111 (2006) 140-144.

[10] A.J. Churchard, E. Banach, A. Borgschulte, R. Caputo, J.-C. Chen, D.C. Clary, K.J. Fijalkowski, H. Geerlings, R.V. Genova, W. Grochala, T. Jaroń, J.C. Juanes-Marcos, B. Kasemo, G.-J. Kroes, I. Ljubić, N. Naujoks, J.K. Nørskov, R.A. Olsen, F. Pendolino, A. Remhof, L. Románszki, A. Tekin, T. Vegge, M. Zäch, A. Züttel, A multifaceted approach to hydrogen storage, Physical Chemistry Chemical Physics, 13 (2011) 16955-16972.

[11] A.J. Reiter, S.-C. Kong, Demonstration of compression-ignition engine combustion using ammonia in reducing greenhouse gas emissions, Energy & Fuels, 22 (2008) 2963-2971.

[12] A.J. Reiter, S.C. Kong, Combustion and emissions characteristics of compression-ignition engine using dual ammonia-diesel fuel, Fuel, 90 (2011) 87-97.

[13] G. Marnellos, M. Stoukides, Ammonia synthesis at atmospheric pressure, Science, 282 (1998) 98-100.

[14] I.A. Amar, R. Lan, C.T.G. Petit, S. Tao, Solid-state electrochemical synthesis of ammonia: a review, Journal of Solid State Electrochemistry, 15 (2011) 1845-1860.

[15] I. Valov, B. Luerssen, E. Mutoro, L. Gregoratti, R.A. De Souza, T. Bredow, S. Günther, A. Barinov, P. Dudin, M. Martin, J. Janek, Electrochemical activation of molecular nitrogen at the Ir/YSZ interface, Physical Chemistry Chemical Physics, 13 (2011) 3394-3410.

[16] M. Lerch, J. Janek, K.D. Becker, S. Berendts, H. Boysen, T. Bredow, R. Dronskowski, S.G. Ebbinghaus, M. Kilo, M.W. Lumey, M. Martin, C. Reimann, E. Schweda, I. Valov, H.D. Wiemhöfer, Oxide nitrides: From oxides to solids with mobile nitrogen ions, Progress in Solid State Chemistry, 37 (2009) 81-131.

[17] D.-K. Lee, C.C. Fischer, I. Valov, J. Reinacher, A. Stork, M. Lerch, J. Janek, An EMF cell with a nitrogen solid electrolyte-on the transference of nitrogen ions in yttria-stabilized zirconia, Physical Chemistry Chemical Physics, 13 (2011) 1239-1242.

[18] V. Kordali, G. Kyriacou, C. Lambrou, Electrochemical synthesis of ammonia at atmospheric pressure and low temperature in a solid polymer electrolyte cell, Chemical Communications, (2000) 1673-1674.

[19] E. Skúlason, T. Bligaard, S. Gudmundsdóttir, F. Studt, J. Rossmeisl, F. Abild-Pedersen, T. Vegge, H. Jónsson, J.K. Nørskov, A theoretical evaluation of possible transition metal electro-catalysts for N_2 reduction, Physical Chemistry Chemical Physics, 14 (2012) 1235-1245.

[20] M.M. Rodriguez, E. Bill, W.W. Brennessel, P.L. Holland, N_2 reduction and hydrogenation to ammonia by a molecular iron-potassium complex, Science, 334 (2011) 780-783.

[21] D.J. Knobloch, E. Lobkovsky, P.J. Chirik, Dinitrogen cleavage and functionalization by carbon monoxide promoted by a hafnium complex, Nature Chemistry, 2 (2010) 30-35.

[22] J.D. Gilbertson, N.K. Szymczak, D.R. Tyler, Reduction of N_2 to ammonia and hydrazine utilizing H_2 as the reductant, Journal of the American Chemical Society, 127 (2005) 10184-10185.

[23] M.D. Fryzuk, Side-on end-on bound dinitrogen: An activated bonding mode that facilitates functionalizing molecular nitrogen, Accounts of Chemical Research, 42 (2009) 127-133.

[24] R.B. Yelle, J.L. Crossland, N.K. Szymczak, D.R. Tyler, Theoretical studies of N_2 reduction to ammonia in $Fe(dmpe)_2N_2$, Inorganic Chemistry, 48 (2009) 861-871.

[25] J.R. Scheffe, J.H. Li, A.W. Weimer, A spinel ferrite/hercynite water-splitting redox cycle, International Journal of Hydrogen Energy, 35 (2010) 3333-3340.

[26] W.C. Chueh, C. Falter, M. Abbott, D. Scipio, P. Furler, S.M. Haile, A. Steinfeld, High-flux solar-driven thermochemical dissociation of CO_2 and H_2O using nonstoichiometric ceria, Science, 330 (2010) 1797-1801.

[27] J.E. Miller, M.D. Allendorf, R.B. Diver, L.R. Evans, N.P. Siegel, J.N. Stuecker, Metal oxide composites and structures for ultra-high temperature solar thermochemical cycles, Journal of Materials Science, 43 (2008) 4714-4728.

[28] A. Stamatiou, P.G. Loutzenhiser, A. Steinfeld, Solar Syngas Production from H_2O and CO_2 via Two-Step Thermochemical Cycles Based on Zn/ZnO and FeO/Fe_3O_4 Redox Reactions: Kinetic Analysis, Energy & Fuels, 24 (2010) 2716-2722.

[29] S. Licht, B. Wang, H. Wu, STEP-A solar chemical process to end anthropogenic global warming. II: Experimental results, Journal of Physical Chemistry C, 115 (2011) 11803-11821.

[30] M.E. Gálvez, I. Hischier, A. Frei, A. Steinfeld, Ammonia production via a two-step Al_2O_3/AlN thermochemical cycle. 3. Influence of the carbon reducing agent and cyclability, Industrial & Engineering Chemistry Research, 47 (2008) 2231-2237.

[31] M.E. Gálvez, M. Halmann, A. Steinfeld, Ammonia production via a two-step Al_2O_3/AlN thermochemical cycle. 1. Thermodynamic, environmental, and economic analyses, Industrial & Engineering Chemistry Research, 46 (2007) 2042-2046.

[32] R. Michalsky, P.H. Pfromm, Chromium as reactant for solar thermochemical synthesis of ammonia from steam, nitrogen, and biomass at atmospheric pressure, Solar Energy, 85 (2011) 2642-2654.

[33] R. Michalsky, P.H. Pfromm, Thermodynamics of metal reactants for ammonia synthesis from steam, nitrogen and biomass at atmospheric pressure, AIChE Journal, http://onlinelibrary.wiley.com/doi/10.1002/aic.13717/pdf, (in press).

[34] F.J. DiSalvo, New ternary nitrides, Nitrides and Oxynitrides, Proceedings of the Second International Symposium on Nitrides, 325-326 (2000) 3-9.

[35] R. Michalsky, B.J. Parman, V. Amanor-Boadu, P.H. Pfromm, Solar thermochemical production of ammonia from water, air and sunlight: thermodynamic and economic analyses, Energy 42 (2012) 251-260.

[36] I. Barin, O. Knacke, Thermochemical properties of inorganic substances, Springer-Verlag, Berlin Heidelberg New York, 1973.

[37] I. Barin, O. Knacke, O. Kubaschewski, Thermochemical properties of inorganic substances, Supplement, Springer-Verlag, Berlin Heidelberg New York, 1977.

[38] J.W. Warner, R.S. Berry, On the thermodynamics of fuel synthesis, Journal of Physical Chemistry, 91 (1987) 2216-2226.

[39] P.T.B. Shaffer, Plenum Press Handbooks of High-Temperature materials, No.1 Materials Index, Plenum Press, New York, 1964.

[40] H. Baba, Y. Katada, Effect of nitrogen on crevice corrosion in austenitic stainless steel, Corrosion Science, 48 (2006) 2510-2524.

[41] M.E. Gálvez, A. Frei, M. Halmann, A. Steinfeld, Ammonia production via a two-step Al_2O_3/AlN thermochemical cycle. 2. Kinetic analysis, Industrial & Engineering Chemistry Research, 46 (2007) 2047-2053.

[42] D.R. Glasson, S.A.A. Jayaweera, Formation and reactivity of nitrides .2. Calcium and magnesium nitrides and calcium cyanamide, Journal of Applied Chemistry of the USSR, 18 (1968) 77-83.

[43] A.M. Heyns, L.C. Prinsloo, K.J. Range, M. Stassen, The vibrational spectra and decomposition of alpha-calcium nitride (alpha-Ca_3N_2) and magnesium nitride (Mg_3N_2), Journal of Solid State Chemistry, 137 (1998) 33-41.

[44] S. Fukumoto, T. Hookabe, H. Tsubakino, Hydrolysis behavior of aluminum nitride in various solutions, Journal of Materials Science, 35 (2000) 2743-2748.

[45] G.A. Landrum, R. Dronskowski, R. Niewa, F.J. DiSalvo, Electronic structure and bonding in cerium (nitride) compounds: Trivalent versus tetravalent cerium, Chemistry-A European Journal, 5 (1999) 515-522.

[46] D.H. Gregory, Structural families in nitride chemistry, Journal of the Chemical Society-Dalton Transactions, (1999) 259-270.

[47] D.J. Mowbray, J.I. Martínez, F. Calle-Vallejo, J. Rossmeisl, K.S. Thygesen, K.W. Jacobsen, J.K. Nørskov, Trends in metal oxide stability for nanorods, nanotubes, and surfaces, Journal of Physical Chemistry C, 115 (2011) 2244-2252.

[48] T. Bligaard, J.K. Nørskov, Ligand effects in heterogeneous catalysis and electrochemistry, Electrochimica Acta, 52 (2007) 5512-5516.

[49] J. Rossmeisl, J.K. Nørskov, C.D. Taylor, M.J. Janik, M. Neurock, Calculated phase diagrams for the electrochemical oxidation and reduction of water over Pt(111), Journal of Physical Chemistry B, 110 (2006) 21833-21839.

[50] C.J.H. Jacobsen, Novel class of ammonia synthesis catalysts, Chemical Communications, (2000) 1057-1058.

[51] C.J.H. Jacobsen, S. Dahl, B.S. Clausen, S. Bahn, A. Logadottir, J.K. Nørskov, Catalyst design by interpolation in the periodic table: Bimetallic ammonia synthesis catalysts, Journal of the American Chemical Society, 123 (2001) 8404-8405.

[52] F. Lihl, P. Ettmayer, A. Kutzelnigg, Beitrag zum System Mangan-Stickstoff, Zeitschrift für Metallkunde, 53 (1962) 715-719.

[53] P. Höhn, S. Hoffmann, J. Hunger, S. Leoni, F. Nitsche, W. Schnelle, R. Kniep, beta-Ca_3N_2, a metastable nitride in the system Ca-N, Chemistry-a European Journal, 15 (2009) 3419-3425.

[54] A.G. Cairns, J.G. Gallagher, J.S.J. Hargreaves, D. McKay, J.L. Rico, K. Wilson, The effect of low levels of dopants upon the formation and properties of beta-phase molybdenum nitride, Journal of Solid State Chemistry, 183 (2010) 613-619.

[55] H.O. Pierson, Handbook of refractory carbides and nitrides, Noyes Publications, Westwood, New Jersey, 1996.

[56] Y.H. Chen, L. Kang, C.R. Zhang, Y.C. Luo, Z.M. Wu, M.L. Zhang, Density functional theory study on the structures and properties of $(Mg_3N_2)_n$ (n=1 similar to 4) clusters, Chinese Journal of Inorganic Chemistry, 24 (2008) 1029-1034.

[57] Y.-H. Chen, L. Kang, C.-R. Zhang, Y.-C. Luo, L.-H. Yuan, Y.-L. Li, Density functional theory study on the structures and properties of $(Ca_3N_2)_n$ (n=1-4) clusters, Acta Physica Sinica, 57 (2008) 6265-6270.

[58] Z. Li, P. Wang, H. Chen, X. Cheng, Structural, electronic and thermodynamic properties of cubic Zn_3N_2 under high pressure from first-principles calculations, Physica B-Condensed Matter, 406 (2011) 1182-1186.

[59] H. Sharma, I. Garg, K. Dharamvir, V.K. Jindal, Ab initio study of structural and electronic properties of Al_nN (n=1-22) clusters, Journal of Computational and Theoretical Nanoscience, 7 (2010) 2297-2307.

[60] Q. Bai, B. Song, J. Hou, P. He, First principles study of structural and electronic properties of Al_nN (n=1-19) clusters, Physics Letters A, 372 (2008) 4545-4552.

[61] A. Chaudhari, S.-L. Lee, Theoretical study of 3d-metal mononitrides using DFT method, International Journal of Quantum Chemistry, 107 (2007) 212-218.

[62] H. Chen, X.L. Lei, L.R. Liu, Z.F. Liu, H.J. Zhu, Structures and electronic properties of $Mo_{2n}N_n$ (n=1-5): a density functional study, Chinese Physics B, 19 (2010).

[63] J. Qi, L.H. Jiang, Q.A. Jiang, S.L. Wang, G.Q. Sun, Theoretical and experimental studies on the relationship between the structures of molybdenum nitrides and their catalytic activities toward the oxygen reduction reaction, Journal of Physical Chemistry C, 114 (2010) 18159-18166.

[64] M.R.A. Blomberg, P.E.M. Siegbahn, A comparison between multireference CI and effective medium theories for diatomic FeN, Theoretica Chimica Acta, 81 (1992) 365-374.

[65] E.E. Mola, E. Coronel, Y. Joly, J.L. Vicente, Bonding studies of chromium-nitrogen molecules, Langmuir, 4 (1988) 917-920.

[66] S. Nagakura, N. Ōtsuka, Electron state of Mn_4N studied by electron-diffraction, Journal of the Physical Society of Japan, 39 (1975) 1047-1052.

[67] N. Pereira, L.C. Klein, G.G. Amatucci, The electrochemistry of Zn_3N_2 and LiZnN - A lithium reaction mechanism for metal nitride electrodes, Journal of the Electrochemical Society, 149 (2002) A262-A271.

[68] M.J.S. Dewar, W. Thiel, Ground-states of molecules .39. MNDO results for molecules containing hydrogen, carbon, nitrogen, and oxygen, Journal of the American Chemical Society, 99 (1977) 4907-4917.

[69] P. Ettmayer, System molybdenum - nitrogen, Monatshefte für Chemie, 101 (1970) 127-140.

[70] O. Levenspiel, Chemical reaction engineering, Third Edition, Chapter 25 Fluid-particle reactions: Kinetics, John Wiley & Sons, New York, 1999.

[71] D.R. Glasson, S.A.A. Jayaweer, Formation and reactivity of nitrides .I. Review and introduction, Journal of Applied Chemistry of the USSR, 18 (1968) 65-77.

[72] K.H. Linke, K. Schrödter, Contributions to chemistry of hydrazine and its derivatives .47. Partial reduction of nitrogen molecule to N_2^{4-}-ion by means of barium, Zeitschrift für Anorganische und Allgemeine Chemie, 413 (1975) 165-170.

[73] A. García, M.L. Cohen, 1st-principles ionicity scales .1. Charge asymmetry in the solid-state, Physical Review B, 47 (1993) 4215-4221.

[74] T. Christiansen, K.V. Dahl, M.A.J. Somers, Nitrogen diffusion and nitrogen depth profiles in expanded austenite: experimental assessment, numerical simulation and role of stress, Materials Science and Technology, 24 (2008) 159-167.

[75] T.L. Christiansen, M.A.J. Somers, Determination of the concentration dependent diffusion coefficient of nitrogen in expanded austenite, International Journal of Materials Research, 99 (2008) 999-1005.

[76] R.D. Shannon, P.S. Gumerman, J. Chenavas, Effect of octahedral distortion on mean Mn^{3+}-O distances, American Mineralogist, 60 (1975) 714-716.

[77] W.C. Chueh, S.M. Haile, A thermochemical study of ceria: exploiting an old material for new modes of energy conversion and CO_2 mitigation, Philosophical Transactions of the Royal Society a-Mathematical Physical and Engineering Sciences, 368 (2010) 3269-3294.

[78] B. Gillot, M. El Guendouzi, M. Laarj, Particle size effects on the oxidation-reduction behavior of Mn_3O_4 hausmannite, Materials Chemistry and Physics, 70 (2001) 54-60.

[79] J. Öijerholm, Ionic transport in metal oxides studied in situ by impedance spectroscopy and cyclic voltammetry, Doctoral thesis, ISBN 978-91-7178-587-9, Division of Corrosion Science, Department of Chemistry, School of Chemical Science and Engineering, Royal Institute of Technology, Stockholm, 2007.

[80] T. Duong, A.M. Limarga, D.R. Clarke, Diffusion of water species in yttria-stabilized zirconia, Journal of the American Ceramic Society, 92 (2009) 2731-2737.

Chapter 6 - Dinitrogen reduction near ambient pressure using solar energy and molybdenum or manganese nitride-based redox reactions

6.1 Abstract

Facing an increased demand for agricultural production for food and biofuels in the future is expected to increase the demand for ammonia, an essential nitrogen fertilizer, combustion fuel and a promising hydrogen carrier. As an alternative to the fossil fuel-intensive high-pressure Haber-Bosch process, NH_3 may be synthesized directly from air, water, and concentrated solar radiation at 500-1200°C near 0.1 MPa using transition metal nitride reactants. This may optimize the NH_3 formation by controlling separately the temperature of the N_2 cleavage and the nitrogen hydrogenation step. Focusing on the N_2 fixation, lattice nitrogen diffusion ($3 \pm 2 \times 10^{-11}$ cm^2 s^{-1} apparent diffusion constant at 750°C) appears to limit approaching the reaction equilibrium (21 ± 3 mol%, i.e., about 49% of the equilibrium yield) in Mo_2N. In contrast, the formation of Mn_4N (75-85 mol% after 10-30 min) is quick and likely not limited by solid-state diffusion controlling the relative quick subsequent conversion to $Mn_6N_{2.58}$ ($8 \pm 4 \times 10^{-9}$ cm^2 s^{-1}). The diffusion constants determined for nitrides of chromium, manganese and molybdenum correlate nearly quantitatively with the interstitial volume of the nitride lattice, i.e., the atomic or ionic radii respectively. Doping the reactants with a weak nitride former (Fe, i.e., -34.0 kJ mol^{-1} Fe_2N free energy of formation) appears to catalyze the nitride decomposition. Whether doping with a strong nitride former (Cr, -136.2 kJ mol^{-1} Cr_2N) shifts the equilibrium towards nitrogen fixation requires further studies.

6.2 Introduction

Hydrogen generated from essentially inexhaustible resources such as solar radiation and water is one of the most promising non-fossil transportation fuels and an environmentally benign feedstock of the chemical industry. However, due to its low volumetric energy-density H_2 storage and transport is energy-intensive (e.g., liquefaction requires about 30% of the fuel's energy)[1, 2]. One approach to store H_2 economically[2, 3], ammonia (or ammine salts such as $Mg(NH_3)_6Cl_2$) has been assessed previously as perfect hydrogen carrier (17.6 wt% hydrogen capacity, energy-efficient production, existing infrastructure for distribution, etc.)[1, 4]. NH_3 can be combusted directly, e.g., when blended into a diesel fuel (up to 95% energy replacement in only slightly modified diesel engines)[5, 6]. In addition, availability of NH_3 fertilizer will play a key role in a future society facing an increased demand for agricultural production for food[7, 8] and biofuels[9-11].

Currently, NH_3 is produced industrially in a few hundred centralized plants world-wide via heterogeneous catalysis[12, 13] that is cleaving and hydrogenating N_2 to NH_3 in a single step at up to 30 MPa and 500°C[14]. The compression work required for the technically sophisticated synthesis accounts alone for about 16% of the 28-37 GJ/t NH_3 consumed totally by the process[15]. The required H_2 feedstock is generated on-site from fossil resources such as natural gas or coal with significant fossil-based CO_2 emissions[14].

Employing the Haber-Bosch process with a solar-derived H_2 feedstock represents one route[16-22] to sustainable NH_3. Wavelength-specific photons may be harvested and stored in H_2 via photocatalytic[16, 17] or photovoltaic/electrolytic[18] H_2O cleavage. The seminal research in these areas has led to conversion efficiencies of incident solar energy to chemical energy stored in H_2 as high as 7-16%[17, 18]. Major obstacles include the corrosion of the expensive semiconductor, lack of efficient light absorption, and the difficulty of matching the semiconductor band-edge

energies with the H_2 and O_2 evolution reactions[17]. Alternatively, concentrated solar energy may be utilized in form of high-temperature heat to cleave H_2O thermochemically[19-22]. This concept has high theoretical energy conversion efficiencies since photons from the entire insolation spectrum are harvested[23, 24]. However, overall this would lead inherently to a multi-step NH_3 production process requiring capital-intensive and technically sophisticated high pressure (the Haber-Bosch process) and high temperature equipment (both, H_2 generation and the Haber-Bosch process).

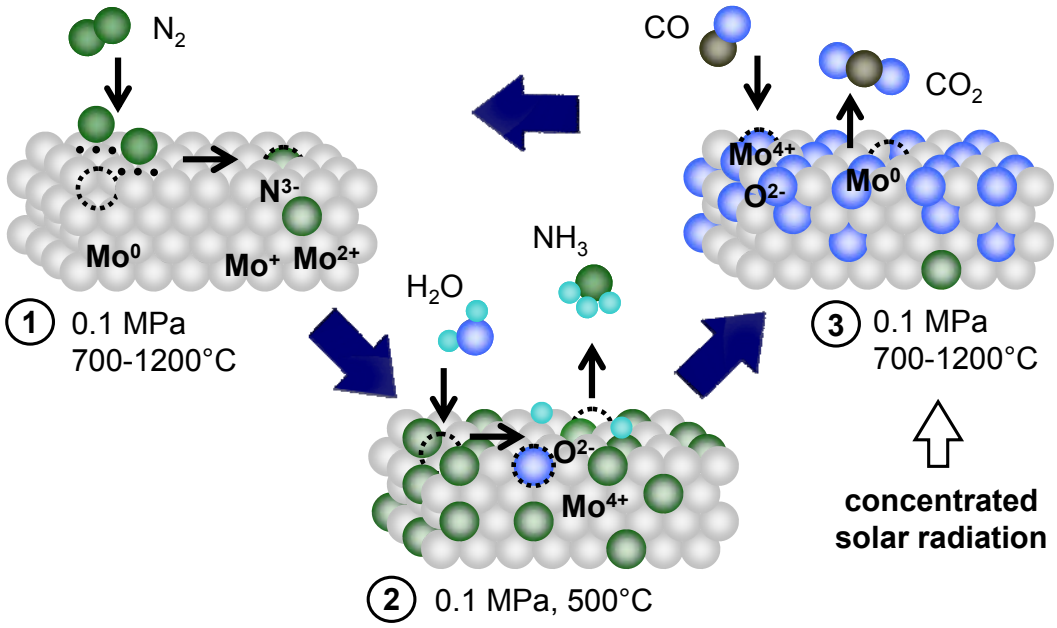

Figure 6.1 Reactive ammonia synthesis from atmospheric nitrogen, water and solar radiation. In practice, the N_2 fixation may be realized concurrently with the oxide reduction (see Figure 6.2)[34, 35]. Dashed lines mark lattice vacancies.

Alternatively[25-33], NH_3 may be synthesized directly in a two-step solar thermochemical redox reaction cycle at ambient pressure (Fig. 6.1)[34, 35]. Conceptually, N_2 is cleaved and reduced thermochemically at elevated temperature by a metallic reactant. Due to the relative small free energy of formation of metal nitrides[36] the nitridated material can be further oxidized with H_2O at decreased temperatures. This second reaction step forms NH_3 at an optimized equilibrium

position at 0.1 MPa (Fig. 6.2). To close the reaction cycle the metallic constituent of the reactant can be reduced with concentrated solar radiation[19, 20, 22, 37] and a relative week reducing agent[33, 37] such as CO or H_2 respectively (i.e., gasified biomass)[35, 38, 39]. The related charge transfer provides the reducing-equivalents for repetitive N_2 reduction.

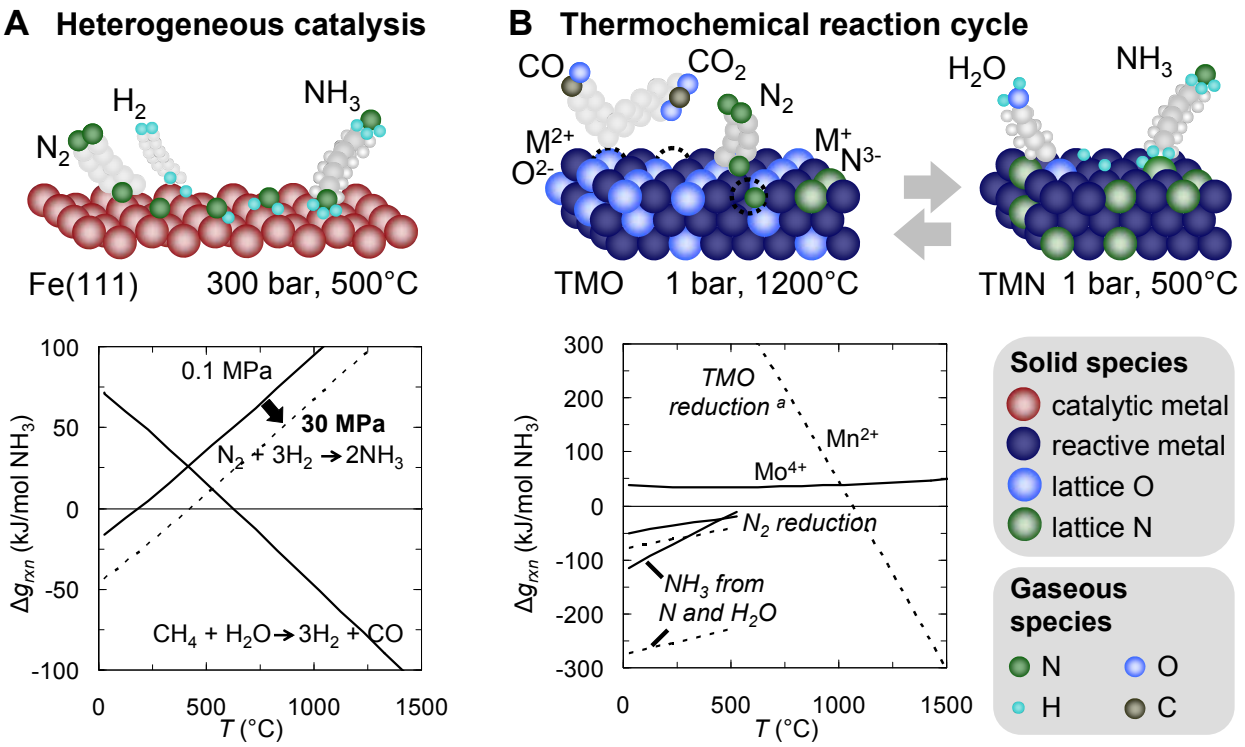

Figure 6.2 Heterogeneous catalysis at the Fe(111) surface versus reactive NH_3 synthesis with a transition metal oxide (TMO) / transition metal nitride (TMN) reactant. M marks a metal. The dotted circles mark lattice vacancies. Free energy of the major reactions (above half-stoichiometric conversion if $\Delta g_{rxn} \leq 0$) involved in (A) the current industrial NH_3 synthesis, or (B) the proposed solar thermochemical NH_3 production cycle at 0.1 MPa. *a*, efficient reduction of MoO_2 to Mo via oxidation of 2CO (e.g., gasified biomass) to $2CO_2$ requires the continuous removal of CO_2. Alternatively, reduction of MnO with CH_4 near 1000°C yields H_2. CH_4 can be recycled from H_2 and CO (methanation). The equilibrium yield of the oxide reductions is given in Appendix E.

The concept has been demonstrated successfully with an Al-based reactant[35, 40] and the thermochemical demands on the reactive material[35, 41] and the economic feasibility of Al- or Mo-

based reactants[34, 39] have been outlined. Opposing the technically rather difficult reduction of Al_2O_3 with solid carbon at above 1700°C[35, 40, 42], the nitrides of Mo and Mn can be formed from their oxides with less solar energy and gaseous reducing agents at below 1200°C[38, 41]. Transition metal-based reactive synthesis of NH_3[35, 41] is, however, not well studied. Thus, the present work focuses on the N_2 reduction kinetics with Mo- or Mn-based reactants and address reactant doping with Fe or Cr respectively.

The reported formation kinetics of non-stoichiometric nitrides such as those formed by Mn do mostly not distinguish between the various phases formed[43, 44] and the nitrogen diffusion coefficients for transition metal nitrides vary greatly (e.g., about 10^{-9} to 10^{-14} cm^2 s^{-1} for Mo_2N near 750°C[45, 46]). Given the economic importance of the nitride formation kinetics and stoichiometry (e.g., up to 50% more reducing agent required to recycle MnO formed when hydrolyzing Mn_4N compared to Mn_2N), Sections 6.4.1 and 6.4.3 characterize the formation of the nitrides of Mo, Mn, and Cr (see below). Furthermore, the interstitial nitrogen diffusion (Fig. 6.3) in the nitrides of less electropositive metals is relative high[45, 47], e.g., up to 5 x 10^{-7} cm^2 s^{-1} near 750°C for Mn[43, 44]. That is relative to the N^{3-} vacancy diffusion (Fig. 6.3), e.g., near 2 x 10^{-11} cm^2 s^{-1} at 700°C in good anion conductors such as nitrogen-doped yttria-stabilised zirconia (YSZ)[48-50]. A correlation between the interstitial crystal space and the beneficially high diffusion coefficients in some transition metal nitrides is discussed in Section 6.4.4.

To address the thermodynamic aspect of the N_2 reduction, Mo_2N contains at equilibrium at 750°C (see Section 6.4.1) only about 17.9 at% N, relative to 50.0 at% N in AlN[51]. Doping nitrides with other metals affects reportedly the charge transfer between the metal and the nitrogen[52] and may, thus, shift the equilibrium position of the nitride and increase the nitrogen capacity[53, 54]. Doping with Cr or Fe respectively is assessed in Sections 6.4.2 and 6.4.3.

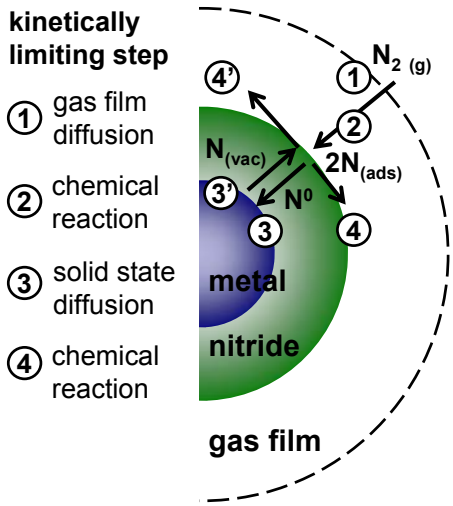

Figure 6.3 Schematic of the nitrogen reduction with transition metals: (1) diffusion of N_2 through the gas film, (2) chemisorption and cleavage of N_2 on two surface sites, (3) interstitial N^0 diffusion, and (4) saturation of the lattice and nucleation of nitride phases. Alternatively, (3') diffusion of N^{3-} vacancies enabling (4') the partial reduction of N^0 to N^{3-}.

6.3 Experimental

6.3.1 Nitrogen reduction

A characterization of the studied materials is given in Table 6.1. To determine the temperature that results in a minimum formation of surface oxides during the nitridation of Mo with N_2 was studied at various temperatures. Mo metal powder (998 ± 3 mg in a quartz boat was pretreated for 10 min at 60°C to remove water. The reactant was thereafter introduced into an electric resistance furnace (60 mm ID, 1 m length, quartz, model HTF55347C, temperature controller model CC58434C, Lindberg/Blue, purged for 10 min with 0.5-0.9 $l_{(STP)}N_2$ min^{-1} before each experiment) at 400°C and heated to T_{red} = 450, 500, 550, 600, 650, 700, 750, 1000 or 1200°C respectively (Fig. 6.4). The heating rate, r_H, was about $r_H = At + B$, where t is the heating time in min, A ranges from -9.36 to -2.82 °C min^{-2} (1200-450°C T_{red}), and B ranges from 65.9 to 67.9 °C min^{-1} (450-1200°C T_{red}). H_2 was supplied at 0.47 ± 0.05 $l_{(STP)}H_2$ min^{-1}. When T_{red} was reached the gas was switched to 1.86 ± 0.05 $l_{(STP)}N_2$ min^{-1}. After holding T_{red} for 2 hrs the

furnace was cooled (at -13.5 to -2.73 °C s^{-1} within the first 60 s, -3.85 to 0.767 °C s^{-1} at 60 to 180 s and > -0.767 °C s^{-1} at > 180 s) to below 75°C. Solids were removed and stored under air at 4°C.

metal	Mo	Cr	Fe	Mn	nitride	β-Mo_2N	Cr_2N (CrN)	ε-Mn_4N (ζ-$Mn_6N_{2.58}$)
space group [a]	$Im\bar{3}m$	$Im\bar{3}m$	$Im\bar{3}m$	$I\bar{4}3m$		$I4_1/amd$	$P\bar{3}1m$ ($Fm\bar{3}m$)	$Pm\bar{3}m$ ($P6_322$)
d_p [b] (μm)	6 ± 4	18 ± 13	29 ± 21	43 ± 22		7 ± 4	17 ± 11	46 ± 19
A_{BET} [c] (m^2 kg^{-1})	429 ± 3	692 ± 8	281 ± 5	269 ± 2		426 ± 3	654 ± 9	270 ± 3
Φ [d] (m^3 m^{-3})	0.75	0.57	0.66	0.62		-	-	-

Table 6.1 Characterization of the metal and binary metal nitride powder beds: *a*, via X-ray diffraction; *b*, average particle diameter; *c*, BET surface area; *d*, void space fraction $\Phi = 1 - \rho_{bulk}/\rho_{particle}$, where ρ_i is the density in kg m^{-3}, relative error via error propagation ± 5.98 %; generally, powder bed surface = 33 ± 2 cm^2, powder bed thickness < 1 mm.

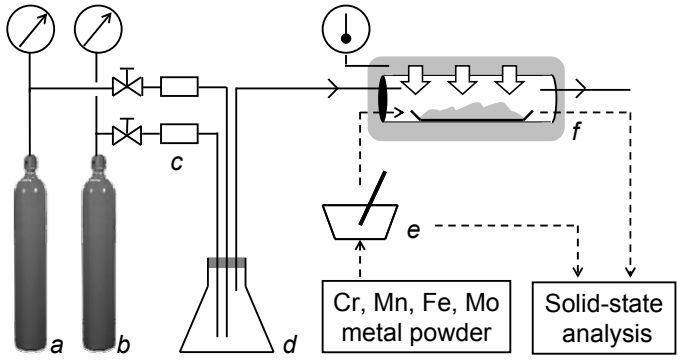

Figure 6.4 Experimental setup: *a*, N_2 gas; *b*, H_2 gas; *c*, flow meter; *d*, gas mixing; *e*, metal powder mixing; *f*, tubular flow-through furnace.

The effect of doping a Mo- or Mn-based reactant with Cr or Fe was studied by reacting N_2 gas with about 0.75-2.00 g Cr, Mn, Fe, Mo, or equimolar mixtures of Mo and Cr or Fe, or Mn and Fe respectively (Fig. 6.4). Using the procedure described above the metal powder was heated for 0.5, 5, 10, 30, or 120 min (all samples) and 60, 90 or 240 min (Mn reactants) at 750°C (with A = -6.91 °C min^{-2} and B = 77.4 °C min^{-1}, see above).

To assess the presence of surface oxides impacting the nitrogen reduction kinetics all experiments with Cr, Fe, Mo, or their mixtures were repeated using a gas flow of 1.86 ± 0.05 $l_{(STP)}N_2$ min^{-1} diluted with 0.47 ± 0.05 $l_{(STP)}H_2$ min^{-1}. To eliminate the possibility of rapid

quenching affecting the yield of Mo_2N the nitridation of Mo with N_2 for 120 min at 450 or 750 °C respectively was repeated with a cooling rate of about -6.05 to -1.80 °C min^{-1}.

6.3.2 Solid state analysis

Powder X-ray diffraction (XRD) patterns were taken with a Miniflex II diffractometer (Cu-target X-ray tube, 30 kV / 15 mA output, diffracted beam monochromator, Rigaku) with a 5-80 °2θ range, °2θ/min scan speed, and 0.02 data points/°2θ, continuous mode for quantitative solid phase identification (PDXL Software Version 1.6.0.0). Scanning electron microscopy (SEM) was employed (S-3500N Scanning Electron Microscope, Hitachi, 20 kV) to visualize the reactant surface and to determine the average particle diameter of the tested materials. To locate the distribution of metal dopant and nitrogen on the materials surface samples were analyzed via energy-dispersive X-ray spectroscopy (EDS, Nova NanoSEM 430, FEI Company, 5-15 kV, beam deceleration, high stability Schottky field emission gun, and Oxford X-Max Large Area Analytical silicon drift detector). The reactants were analyzed gravimetrically before and after the experiment (AE260 DeltaRange balance, ± 0.1 mg, Mettler). The specific BET surface area was analyzed by NanoScale Inc., Manhattan, KS.

6.3.3 Chemicals

All metal powders (99.8% pure Cr, 99.9% Mn, 99.9% Fe, and 99.95% Mo) were -325 mesh and from Noah Technologies. BET surface and SEM analysis indicate comparable specific surface areas (Table 6.1). All glassware was cleaned with acetone (certified ACS, Fisher Scientific). The N_2 or H_2 gas respectively was UHP Zero grade (Linweld).

6.4 Results and Discussion

To reduce N_2 near 100 kPa the formation of binary transition metal nitrides at elevated temperature and the effect of nitride doping is assessed. The yield, X_i, of product i (a nitride or

oxide respectively) is reported as molar ratio of the detected product (n_i in mol) relative to the theoretical amount of this compound formed at stoichiometric conversion (n_i^* in mol):

$$(6.1) \quad X_i = \frac{n_i}{n_i^*} = \frac{\Delta m_t x_i M_{metal}}{\Delta m_0 x_{metal} M_i a_i}$$

where Δm in g is the weight difference between the solid reactant and the quartz boat at time-point t or before the reaction (subscript 0), x in g g^{-1} is the nitride or metal weight fraction, M in g mol^{-1} is the molar mass, and a is a coefficient accounting for the stoichiometric amount of metal atoms contained in the reaction product.

To assess the contribution of the solid-state diffusion to the resistance to fix N_2 (Fig. 6.3) a diffusion-limited shrinking-core model for particles with constant size[55] (equating the rate of N_2 consumption at steady-state with Fick's law of diffusion[56]) was applied[22, 40, 41]:

$$(6.2) \quad k_s t = 1 - 3(1 - X_i)^{2/3} + 2(1 - X_i)$$

where k_s is a specific rate constant.

6.4.1 Formation of Mo_2N, Cr_2N, and CrN from their elements

To assess the formation of MoO_2 that had been reported previously during nitridation experiments of Mo at 400°C[56] Mo metal powder and N_2 gas were heated at temperatures, T_{red}, ranging from 400-1200°C (Fig. 6.5). As expected, 1.5-1.6 mol% MoO_2 (monoclinic $P2_1/c$, not the volatile MoO_3 phase[56]) is formed at 400-450°C (likely due to minor traces O_2 in the reacting gas and/or H_2O on the metal surface). At this temperature the yield of Mo_2N remains below 1.3 mol%. This supports the understanding of MoO_2 acting a barrier to the nitrogen diffusion[56]. Increasing T_{red} decreases the formation of MoO_2 and increases the formation of Mo_2N yielding at 750°C (7 ± 2) x 10^{-3} mol% MoO_2 and 3.3 ± 0.3 mol% Mo_2N. In agreement with the expected decomposition of Mo_2N at elevated temperatures[51, 57] Mo_2N was not detected at 1000 or 1200°C.

A mass balance of Mo shows recovery of the metal within ± 1.6% (see Appendix E). Formation of volatile Mo compounds can not be inferred. To minimize the formation of MoO_2 and to ensure comparability of the experimental data in this study all kinetic experiments were conducted at 750°C (arrow, Fig. 6.5).

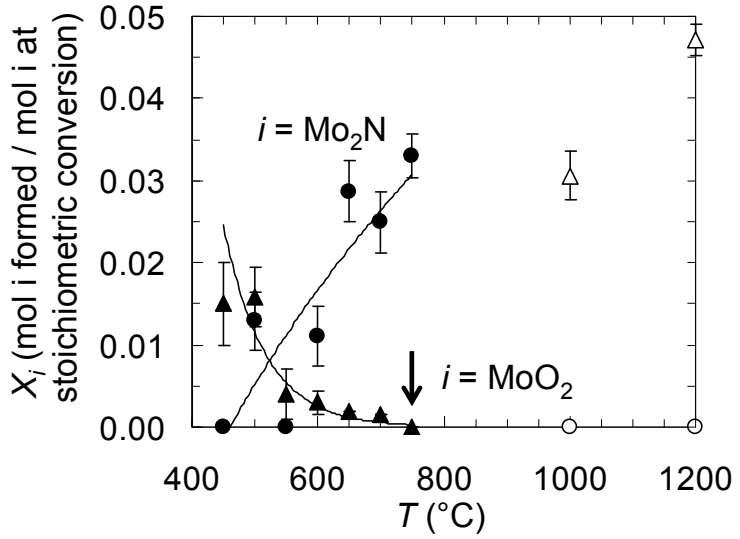

Figure 6.5 Yield of Mo_2N (circles) or MoO_2 (triangles, arrow see Section 6.4.1) from the metal at 100 kPa N_2 vs. temperature. Lines fitting filled symbols are a guide only. Error bars are via error propagation within a 95% confidence interval in average ± 22.86%.

The nitridation of Mo at 750°C reaches a 1.2 mol% yield after 30 s increasing thereafter with diminished kinetics to a maximum of 3.3 mol% after 120 min (Fig. 6.6A). XRD identified the nitride as a tetragonal β-Mo_2N with a homogeneity range of 28.7 to 34.5 mol% N[57]. Quantitative calculations in this work assume a stoichiometric Mo_2N as-indicated. Computing the equilibrium yield of the reaction 2 Mo + ½ N_2 → Mo_2N at 750°C (disregarding temperature fluctuations due to the liberated -62.9 kJ mol^{-1} N heat of reaction or due to cooling with the synthesis gas flow, see also Section 6.4.3, and extrapolating data for Mo_2N at > 527°C, R^2 > 0.999)[51, 58] indicates that the yield of Mo_2N is far below the equilibrium yield of about 43.5 mol%. Reducing the cooling rate after the reaction did not affect the Mo_2N yield.

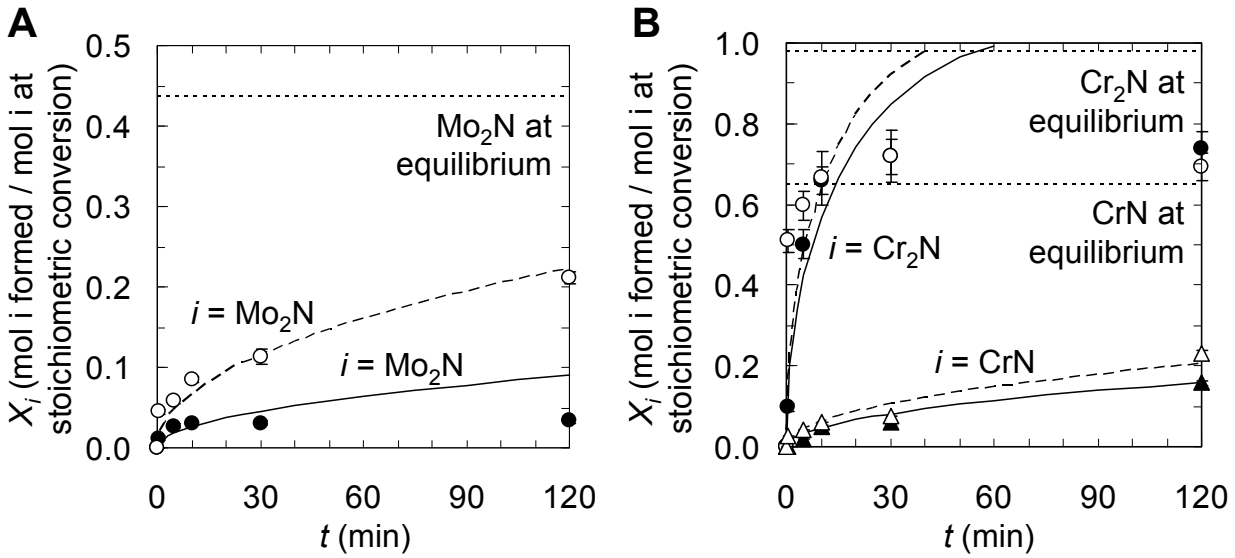

Figure 6.6 Kinetics of the dinitrogen reduction at 750°C with (A) Mo forming Mo_2N (circles), or (B) Cr forming Cr_2N (circles) and CrN (triangles). Solid and dashed lines represent shrinking-core models controlled by diffusion in the solid state. Filled symbols and solid lines are at 100 kPa N_2, empty symbols and dashed lines are at 80.1 kPa N_2 and 19.9 kPa H_2. Error propagation within a 95% confidence (error bars) yields in average ± 8.84%. Computations of the equilibrium yield (dotted lines) are based on[51, 60].

Figure 6.6B shows in comparison Cr converts quickly and nearly completely to Cr_2N (66 ± 3 mol% after 10 min). A solid-state diffusion limited formation mechanism can not be fitted to the data conclusively (see Section 6.4.4). The reaction equilibrium is not reached due to the concurrent conversion of Cr_2N to CrN (15.8 ± 0.5 mol% after 120 min). The formation of CrN is slow and fits a diffusion-limited mechanism well ($R^2 > 0.94$).

Based on the hypothesis of a MoO_2 surface layer (likely below the XRD detection limit) that can be reduced with H_2[51, 59] all experiments were reproduced using a 4 mol mol^{-1} N_2:H_2 gas mixture (Fig. 6.6). The reducing atmosphere affected the yield of Cr_2N and CrN only slightly but increased the yield of Mo_2N more than six-fold to 21.1 ± 0.7 mol% after 120 min (Fig. 6.6A). MoO_2 was not detected and the formation of the trigonal Cr_2O_3 phase was in average 34 ± 10 % below the yield of Cr_2O_3 when reacting the metal with N_2 only (in the range of 0 to 2.7 mol%).

To support the presence of a hypothesized oxide layer, Figure 6.7 images the tetrahexahedral Mo crystals (Table 6.1) showing a terrace-like pattern on their surface (A) before the exposure to (B) N_2 or (C) N_2/H_2 gas. Upon heating in N_2 the terrace pattern is replaced by a rather even structure without affecting the O_h symmetry of the metal phase. Based on the particle size and XRD analysis at 700 and 750°C this can be rationalized with an approximately 0.2-31.1 nm thick oxide layer (about 3 to 444 times the size of the lattice nitrogen) covering and passivating the metal. Removing the oxide with a reducing gas enables the nitrogen diffusion through the solid (Fig. 6.6A, $R^2 > 0.94$) converting the cubic Mo (Fig. 6.7C) slowly into the tetragonal Mo_2N phase (Table 6.1, Fig. 6.6A).

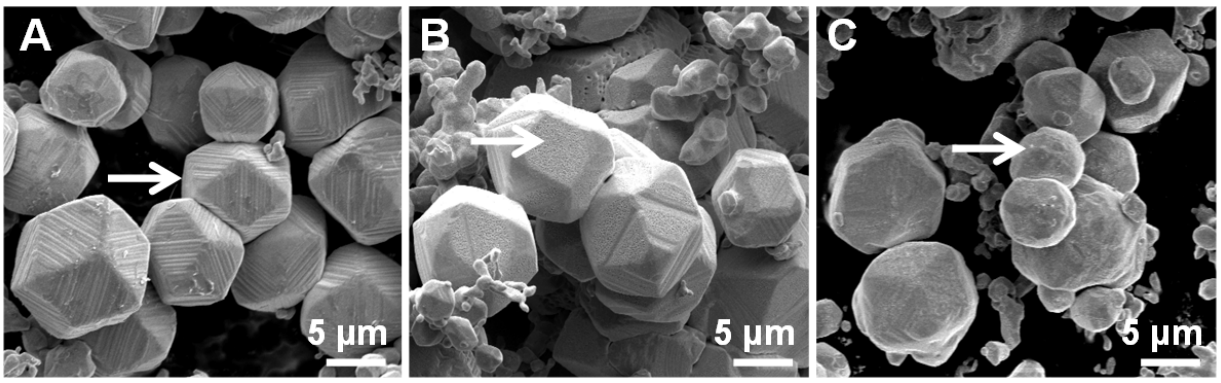

Figure 6.7 Representative scanning electron micrographs of Mo samples (A) as-purchased, (B) after heating for 2 hrs at 750°C in N_2, or (C) in N_2 diluted with H_2 (arrows see text).

6.4.2 Effect of doping Mo with Cr or Fe

To study the effect of doping on the tendency of Mo to fix N_2, Mo was doped with Cr or Fe which form nitrides with a lower or higher free energy of formation (-136.2 kJ mol^{-1} Cr_2N or -34.0 kJ mol^{-1} Fe_2N) than Mo respectively (-95.7 kJ mol^{-1} Mo_2N, all at 25°C)[51, 60].

Figure 6.8 shows the yield of Mo_2N reacting the metal powder mixtures with N_2 or N_2/H_2 gas. The Mo_2N yield differs only slightly from the results obtained with Mo and the N_2/H_2 gas mixture except when reacting Mo/Fe with N_2 (Mo_2N was not detected at any time point tested).

After 120 min 18 ± 2 ($Mo/Cr/N_2$), 23 ± 5 ($Mo/Cr/N_2/H_2$), or 25 ± 2 ($Mo/Fe/N_2/H_2$) mol% are reached. A ternary $CrMoN_x$ ($1 < x < 2$, $P6_3/mmc$)[61] could not be identified in the collected XRD spectra and is more likely formed via ammonolysis reactions[62, 63].

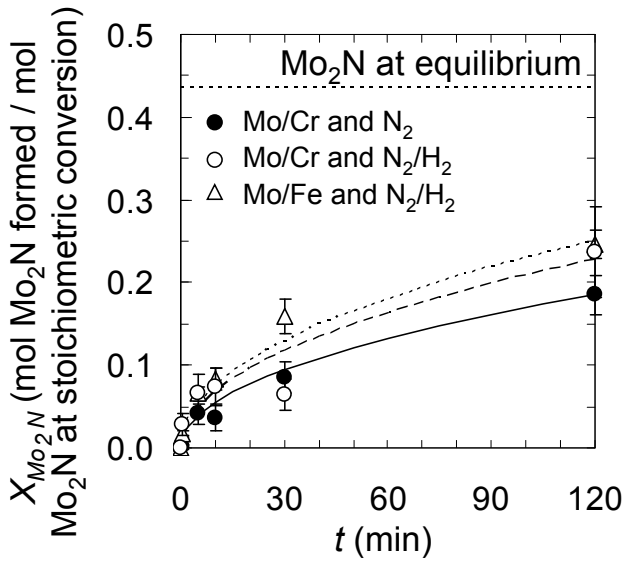

Figure 6.8 Reduction of N_2 by Mo doped with Cr (circles) or Fe (triangles) in presence (empty symbols) or absence (filled symbols) of H_2 (compare Fig. 6.6). Error propagation within a 95% confidence (error bars) yields in average ± 24.34%.

The encouraging formation of Mo_2N in the $Mo/Cr/N_2$ system suggests that H_2 may be replaced with a metallic reducing agent. In practice, this would alleviate the synthesis gas conditioning that is separation of H_2O from hot N_2/H_2 mixtures. Given the probable diffusion-limited formation of Mo_2N (Fig. 6.6A, Fig. 6.8) it can not be concluded whether the Cr-dopant increases the yield of Mo_2N.

However, Figure 6.9 shows that the addition of Cr to Mo decreases the formation of Cr_2N. Similar to Cr_2O_3 the relative yield of CrN increases initially to > 1 at 5 min and decreases after 10 min to < 1 at 120 min. The formation of Cr_2O_3 is transient only in the presence of H_2 and may thus be explained with reduction by H_2 in a system open to mass exchange[51, 64]. To shed

light on the interaction between the Cr-doped Mo-reactant with the N_2 gas the material was analyzed via EDS (Fig. 6.10).

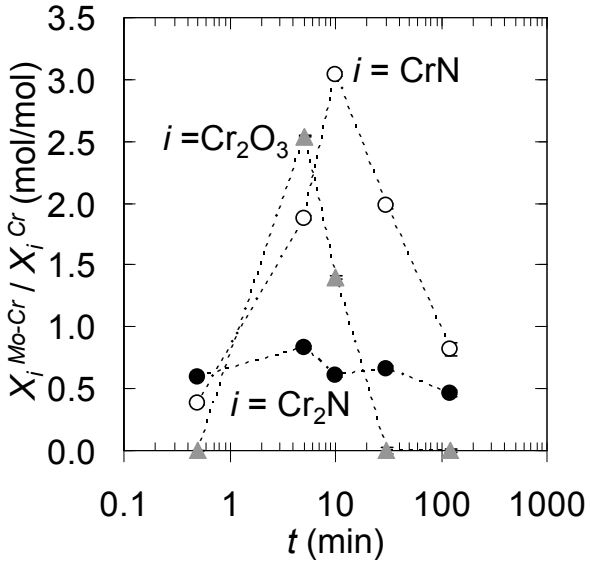

Figure 6.9 The yield of Cr_2N, CrN or Cr_2O_3 when nitridating Mo/Cr powder relative to the yield obtained with pure Cr (both using N_2/H_2 gas, see Section 6.3.1). Dotted lines are to guide the eye. Due to the amount of data used for the computation error propagation within a 95% confidence (error bars omitted for clarity) yields in average ± 45.33%.

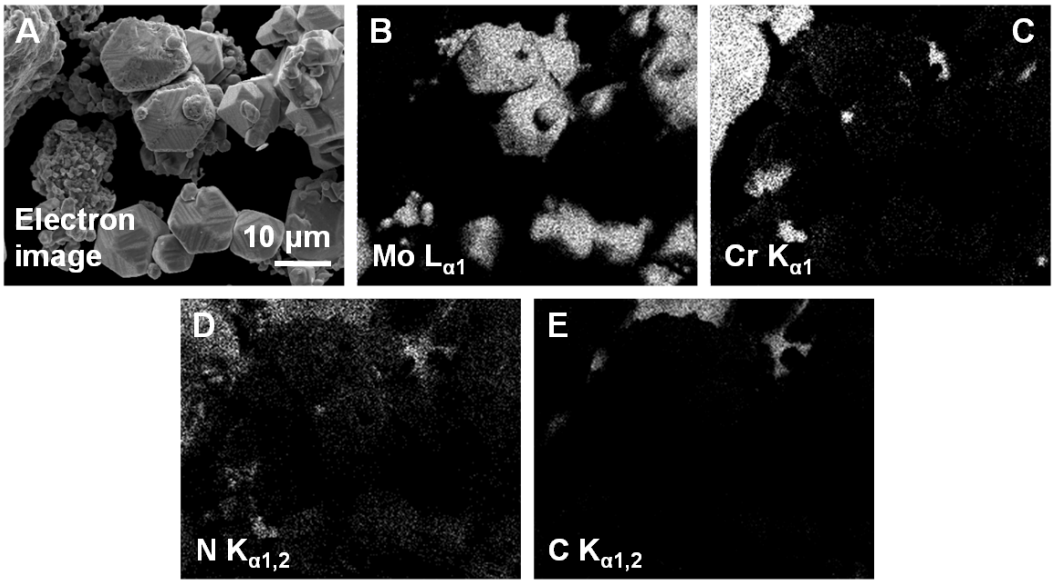

Figure 6.10 EDS of Mo doped with Cr after nitridation for 2 hrs at 750°C in N_2: (A) electron image, (B-E) X-ray emission map for Mo, Cr, N and C (as reference).

A comparison of panel B and C shows weaker X-ray emission (brightness) from Cr atoms located in regions of the electron image (panel A) identified as Mo but not visa versa (Fig. 6.10). This attenuates the possibility that the metals mixed randomly at the nano-scale when handling the materials. Furthermore, panel D confirms significant fixation of nitrogen with Mo and Cr relative to the carbon-specific emission originating potentially from organic contaminations (essentially none on the nitride surface, panel E). One supposable interpretation of these results (Fig. 6.8-6.10) is the migration of Cr atoms given a local gradient of their chemical potential in the macroscopic metal mixture. This results in formation of CrN on the Mo_2N surface without nitrogen diffusion through a CrN layer covering the Cr particle. The relative effect ceases if the Cr particles convert slowly into CrN as well.

The yield of Mo_2N when doping with Fe is ambiguous: Mo_2N formation is below the detection limit in the $Mo/Fe/N_2$ system and up to 25 ± 2 mol% in the $Mo/Fe/N_2/H_2$ system (Fig. 6.8). Oxides or iron nitrides were not found. Whether a weak nitride former such as Fe decreases the formation of lattice nitrogen such as reported for metals that do not form nitrides at atmospheric pressure, e.g., for Pd or Au[65] can not be concluded unerringly at this point.

In summary, doping with Cr has the potential of avoiding the need for separating H_2O traces from the synthesis gas when reducing N_2 with Mo and N_2/H_2 gas mixtures. Assessing the potential of the Cr-dopant to increase the yield of Mo-N bonds will require elimination of the nitrogen diffusion limitation when forming Mo_2N in the future. Whether Fe-doping contributes to the destabilization of the metal-nitrogen bond is addressed in the following.

6.4.3 Reduction of N_2 with Fe-doped Mn

To assess the effect of doping with Fe (see Section 6.4.2, the free energies of formation of Mn_4N or Fe_4N are -172.4 or -57.5 kJ mol^{-1} respectively[60]), Mo was substituted with Mn that is

forming nitrides with increased thermochemical stability at 750°C[60, 66]. Despite the relative small specific surface area of the Mn-starting material (Table 6.1), Mn converts quickly to 85 ± 4 mol% ε-Mn_4N after 30 min (Fig. 6.11A). The Mn_4N phase decreases after approaching the equilibrium yield and is evidently consumed in the formation of 85 ± 8 mol% ζ-$Mn_6N_{2.58}$ after 240 min. In the presence of Fe (Fig. 6.11B) Mn_4N is formed quickly, however, without approaching the equilibrium yield (64 ± 8 mol% after 30 min). This appears to results in a decreased yield of $Mn_6N_{2.58}$ (29 ± 4 mol% after 240 min). Opposing the formation of Mn_4N, diffusion-limited nitridation fits the formation of $Mn_6N_{2.58}$ relatively well (R^2 > 0.80 without Fe or > 0.85 with Fe).

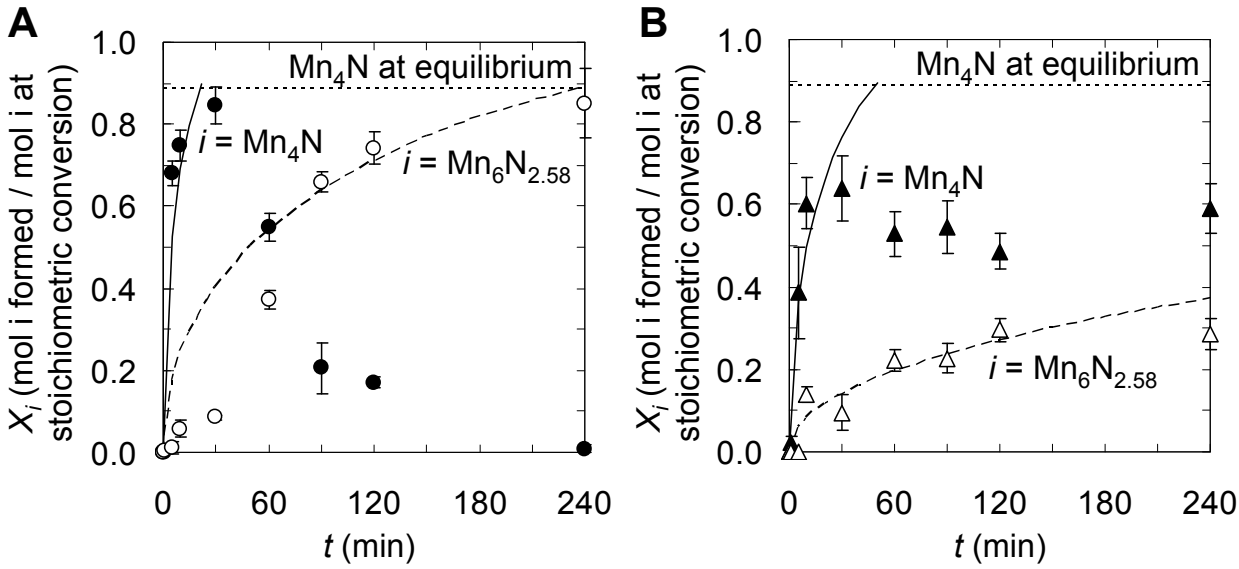

Figure 6.11 Kinetics of the dinitrogen reduction at 750°C with (A) Mn, or (B) Fe-doped Mn forming Mn_4N (filled symbols) and $Mn_6N_{2.58}$ (empty symbols). Error propagation within a 95% confidence (error bars) yields in average ± 17.81%. Equilibrium yield computations were restricted to Mn_4N due to the available data.

In conclusion, Fe appears to catalyses the decomposition of Mn_4N and $Mn_6N_{2.58}$. This may be understood as transient formation of unstable and non-stoichiometric iron nitrides. In fact, the XRD analysis showed (see Appendix E) continuous formation of a $FeN_{0.0324}$ phase (*Fm*-

3*m*) that qualitatively (21 ± 8 or 54 ± 7 mol% after 30 or 240 min respectively) resembled the formation of $Mn_6N_{2.58}$ (Fig. 6.11B). Ternary nitrides containing Fe[63, 67] were not found.

6.4.4 N_2 reduction kinetics dependent on nitrogen diffusion

To better understand the evidenced diffusion limitations Figure 6.3 illustrates two possible nitrogen fixation mechanisms (others, such as grain-boundary diffusion, are conceivable). After adsorption and cleavage of N_2, atomic N may diffuse within the nitride lattice interstices, along the nitrogen activity gradient, towards the metal core[56, 68, 69]. This results in nucleation of a nitride when the crystal lattice is saturated with nitrogen. Alternatively, nitrogen atoms may be reduced near the surface forming N^{3-} ions (with a nominal radius about twice as large as the radius of atomic nitrogen). The related conduction of the N^{3-} anions will then depend on crystal lattice defects and the diffusion of nitrogen vacancies[48-50].

From the experimental data an apparent diffusion constant, *D*, can be estimated with [55].

$$(6.3) \quad D = \frac{\rho_p d_p^2 k_s}{24 b c_g}$$

where ρ_p in mol m^{-3} is the density of the solid reactant, d_p in m is the average particle diameter (Table 6.1), *b* is the molar ratio of reacted solid per reacted N_2, and c_g in mol m^{-3} is the molar concentration of N_2 gas. The computation was limited to data fitting Eq. 6.2 well (R^2 = 0.90-0.98 for CrN or Mo_2N respectively, 0.80-0.85 for $Mn_6N_{2.58}$).

Figure 6.12 plots *D* versus the nitride volume-fraction, f_v, occupied by atoms or ions respectively:

$$(6.4) \quad f_v = \frac{4\pi N_A \rho_n}{3} \sum_{j=all\ constituents} \gamma_j r_j^3$$

where N_A is Avogadro's constant, ρ_n in mol m^{-3} is the molar density of the formed nitride, γ_j is the atomic fraction of metal or nitrogen per nitride, and r_j in m is the radius of the nitrogen or the

metallic constituent of the nitride. Based on the relative low electronegativity of Mn N^{3-} ions were assumed for $Mn_6N_{2.58}$ (Mn in 2+ oxidation state). CrN and Mo_2N[70, 71] were computed as metallic compounds (atomic N in tetrahedral covalent bond and 12-coordinated metal ions). The MoO_2 layer inferred in Section 6.4.1 was included as ideal ionic compound.

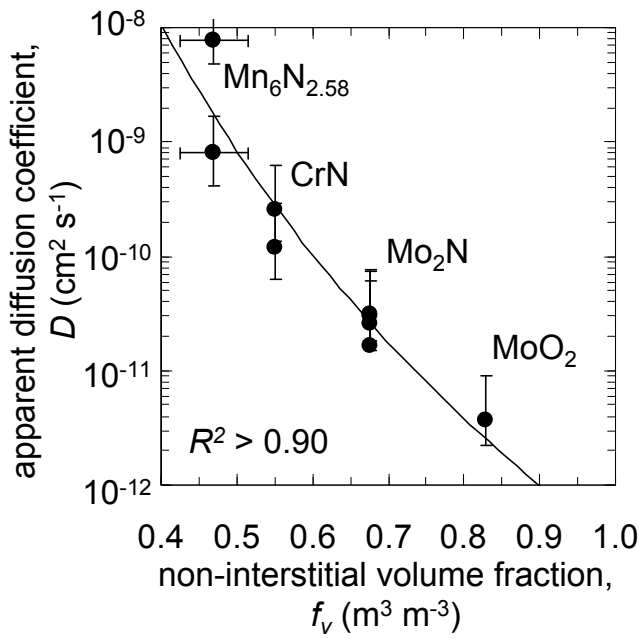

Figure 6.12 Diffusion coefficient for diffusion through the marked solid product at 750°C vs. the volume occupied by metal and nitrogen or oxygen (for assumed bonding and radii see Section 6.4.4). The density of $Mn_6N_{2.58}$ was estimated with 6,131 ± 292 kg m^{-3}. The solid line is to guide the eye. Error propagation within a 95% confidence (error bars) yields in average ± 17.81%.

D correlates nearly quantitatively with f_v ($R^2 > 0.90$, Fig. 6.12). This suggests relative[45, 46, 56 43, 44, 68, 69] slow diffusion of the lattice nitrogen (in agreement with 10^{-9}-10^{-14} cm^2 s^{-1} near 750°C[45, 46]) in Mo_2N likely due to the dense physical structure of the nitride. In contrast, formation of Mn_4N does not appear to be diffusion-limited (Fig. 6.11) and further conversion into $Mn_6N_{2.58}$ proceeds relatively fast (within or close to 10^{-7}-10^{-9} cm^2 s^{-1} near 750°C[45, 46]) likely via interstitial diffusion of a major fraction of atomic nitrogen[72]. Some charge transfer yielding N^{3-} (and ion vacancies) may occur at the Mn/Mn_4N or $Mn_4N/Mn_6N_{2.58}$ interface respectively.

6.5 Conclusions

NH_3 may be synthesized sustainably without fossil fuels from water and air near 100 kPa via a solar thermochemical reaction cycle. This work showed successful (manganese or chromium-doped molybdenum reactants) and fast (with manganese) reductive cleavage of N_2 at below 1200°C with transition metals. Experiments aimed for a relative comparison of the tested materials. The kinetic performance of a prospective reactant may be improved significantly by addressing the physical presentation of the material. Major conclusions are:

- The rapid nitrogen fixation at 750°C forming Mn_4N or Cr_2N respectively is presumably not limited by the diffusion of the lattice nitrogen. Further nitridation yielding $Mn_6N_{2.58}$ ($D = 8 \pm 4 \times 10^{-9}$ cm^2 s^{-1}) or CrN ($D = 3 \pm 2 \times 10^{-10}$ cm^2 s^{-1}) and formation of Mo_2N ($D = 3 \pm 2 \times 10^{-11}$ cm^2 s^{-1}) correlates well with interstitial diffusion of atomic nitrogen species. This may allow altering the diffusion kinetics by controlling the atomic or ionic radii[73, 74], that is, the oxidation state of the reactant[52].
- There is evidence that doping with a weak nitride former (Fe in this work) catalyzes the decomposition of the nitride formed by the reactant. Doping with a strong nitride former (Cr in this work) may shift the equilibrium towards nitrogen fixation. This, however, needs further studies off-setting the diffusion limitations.
- A nano-scale MoO_2 surface layer may be removed without formation of H_2O traces via Cr-doping increasing the apparent diffusion coefficient during Mo_2N formation by an order of magnitude. This may alleviate the conditioning of the synthesis gas in practice.

6.6 Associated content in Appendix E

Supporting Information: Equilibrium yield computations for the thermochemical reduction of MoO_2 or MnO, the mass balance of Mo vs. nitridation temperature and the formation of $FeN_{0.0324}$ nitride when reducing N_2 with Mn/Fe metal powder mixtures.

6.7 References

[1] G. Thomas, G. Parks, Potential roles of ammonia in a hydrogen economy, a study of issues related to the use ammonia for on-board vehicular hydrogen storage, U.S. Department of Energy (2006), Available online at: http://www.hydrogen.energy.gov/-pdfs/nh3_paper.pdf (retrieved December, 2011).

[2] A.J. Churchard, E. Banach, A. Borgschulte, R. Caputo, J.-C. Chen, D.C. Clary, K.J. Fijalkowski, H. Geerlings, R.V. Genova, W. Grochala, T. Jaroń, J.C. Juanes-Marcos, B. Kasemo, G.-J. Kroes, I. Ljubić, N. Naujoks, J.K. Nørskov, R.A. Olsen, F. Pendolino, A. Remhof, L. Románszki, A. Tekin, T. Vegge, M. Zäch, A. Züttel, A multifaceted approach to hydrogen storage, Physical Chemistry Chemical Physics, 13 (2011) 16955-16972.

[3] F. Vitse, M. Cooper, G.G. Botte, On the use of ammonia electrolysis for hydrogen production (vol 142, pg 18, 2005), Journal of Power Sources, 152 (2005) 311-312.

[4] C.H. Christensen, T. Johannessen, R.Z. Sørensen, J.K. Nørskov, Towards an ammonia-mediated hydrogen economy?, Catalysis Today, 111 (2006) 140-144.

[5] A.J. Reiter, S.-C. Kong, Demonstration of compression-ignition engine combustion using ammonia in reducing greenhouse gas emissions, Energy & Fuels, 22 (2008) 2963-2971.

[6] A.J. Reiter, S.C. Kong, Combustion and emissions characteristics of compression-ignition engine using dual ammonia-diesel fuel, Fuel, 90 (2011) 87-97.

[7] V. Smil, Detonator of the population explosion, Nature, 400 (1999) 415-415.

[8] V. Smil, Nitrogen and food production: Proteins for human diets, Ambio, 31 (2002) 126-131.

[9] C.A. Garcia, A. Fuentes, A. Hennecke, E. Riegelhaupt, F. Manzini, O. Masera, Life-cycle greenhouse gas emissions and energy balances of sugarcane ethanol production in Mexico, Applied Energy, 88 (2011) 2088-2097.

[10] M. Bystricky, T. Knödlseder, G. Weber-Blaschke, M. Faulstich, Comparing environmental impacts of electricity, heat and fuel from energy crops: Evaluating biogas utilization pathways by the basket of benefit methodology, Engineering in Life Sciences, 10 (2010) 570-576.

[11] I. Lewandowski, U. Schmidt, Nitrogen, energy and land use efficiencies of miscanthus, reed canary grass and triticale as determined by the boundary line approach, Agriculture Ecosystems & Environment, 112 (2006) 335-346.

[12] A. Hellman, E.J. Baerends, M. Biczysko, T. Bligaard, C.H. Christensen, D.C. Clary, S. Dahl, R. van Harrevelt, K. Honkala, H. Jonsson, G.J. Kroes, M. Luppi, U. Manthe, J.K. Nørskov, R.A. Olsen, J. Rossmeisl, E. Skúlason, C.S. Tautermann, A.J.C. Varandas, J.K. Vincent, Predicting catalysis: Understanding ammonia synthesis from first-principles calculations, Journal of Physical Chemistry B, 110 (2006) 17719-17735.

[13] C.J.H. Jacobsen, S. Dahl, B.S. Clausen, S. Bahn, A. Logadottir, J.K. Nørskov, Catalyst design by interpolation in the periodic table: Bimetallic ammonia synthesis catalysts, Journal of the American Chemical Society, 123 (2001) 8404-8405.

[14] Z. Kirova-Yordanova, Exergy analysis of industrial ammonia synthesis, Energy, 29 (2004) 2373-2384.

[15] I. Rafiqul, C. Weber, B. Lehmann, A. Voss, Energy efficiency improvements in ammonia production - perspectives and uncertainties, Energy, 30 (2005) 2487-2504.

[16] J.J.H. Pijpers, M.T. Winkler, Y. Surendranath, T. Buonassisi, D.G. Nocera, Light-induced water oxidation at silicon electrodes functionalized with a cobalt oxygen-evolving catalyst, Proceedings of the National Academy of Sciences of the United States of America, 108 (2011) 10056-10061.

[17] O. Khaselev, J.A. Turner, A monolithic photovoltaic-photoelectrochemical device for hydrogen production via water splitting, Science, 280 (1998) 425-427.

[18] M. Grätzel, Mesoscopic solar cells for electricity and hydrogen production from sunlight, Chemistry Letters, 34 (2005) 8-13.

[19] J.R. Scheffe, J.H. Li, A.W. Weimer, A spinel ferrite/hercynite water-splitting redox cycle, International Journal of Hydrogen Energy, 35 (2010) 3333-3340.

[20] W.C. Chueh, C. Falter, M. Abbott, D. Scipio, P. Furler, S.M. Haile, A. Steinfeld, High-flux solar-driven thermochemical dissociation of CO_2 and H_2O using nonstoichiometric ceria, Science, 330 (2010) 1797-1801.

[21] J.E. Miller, M.D. Allendorf, R.B. Diver, L.R. Evans, N.P. Siegel, J.N. Stuecker, Metal oxide composites and structures for ultra-high temperature solar thermochemical cycles, Journal of Materials Science, 43 (2008) 4714-4728.

[22] A. Stamatiou, P.G. Loutzenhiser, A. Steinfeld, Solar Syngas Production from H_2O and CO_2 via Two-Step Thermochemical Cycles Based on Zn/ZnO and FeO/Fe_3O_4 Redox Reactions: Kinetic Analysis, Energy & Fuels, 24 (2010) 2716-2722.

[23] M. Roeb, H. Müller-Steinhagen, Concentrating on solar electricity and fuels, Science, 329 (2010) 773-774.

[24] J.W. Warner, R.S. Berry, On the thermodynamics of fuel synthesis, Journal of Physical Chemistry, 91 (1987) 2216-2226.

[25] E. Skúlason, T. Bligaard, S. Gudmundsdóttir, F. Studt, J. Rossmeisl, F. Abild-Pedersen, T. Vegge, H. Jónsson, J.K. Nørskov, A theoretical evaluation of possible transition metal electro-catalysts for N2 reduction, Physical Chemistry Chemical Physics, 14 (2012) 1235-1245.

[26] I.A. Amar, R. Lan, C.T.G. Petit, S. Tao, Solid-state electrochemical synthesis of ammonia: a review, Journal of Solid State Electrochemistry, 15 (2011) 1845-1860.

[27] I. Valov, B. Luerssen, E. Mutoro, L. Gregoratti, R.A. De Souza, T. Bredow, S. Günther, A. Barinov, P. Dudin, M. Martin, J. Janek, Electrochemical activation of molecular nitrogen at the Ir/YSZ interface, Physical Chemistry Chemical Physics, 13 (2011) 3394-3410.

[28] M. Lerch, J. Janek, K.D. Becker, S. Berendts, H. Boysen, T. Bredow, R. Dronskowski, S.G. Ebbinghaus, M. Kilo, M.W. Lumey, M. Martin, C. Reimann, E. Schweda, I. Valov, H.D. Wiemhöfer, Oxide nitrides: From oxides to solids with mobile nitrogen ions, Progress in Solid State Chemistry, 37 (2009) 81-131.

[29] V. Kordali, G. Kyriacou, C. Lambrou, Electrochemical synthesis of ammonia at atmospheric pressure and low temperature in a solid polymer electrolyte cell, Chemical Communications, (2000) 1673-1674.

[30] M.M. Rodriguez, E. Bill, W.W. Brennessel, P.L. Holland, N_2 reduction and hydrogenation to ammonia by a molecular iron-potassium complex, Science, 334 (2011) 780-783.

[31] D.J. Knobloch, E. Lobkovsky, P.J. Chirik, Dinitrogen cleavage and functionalization by carbon monoxide promoted by a hafnium complex, Nature Chemistry, 2 (2010) 30-35.

[32] J.D. Gilbertson, N.K. Szymczak, D.R. Tyler, Reduction of N_2 to ammonia and hydrazine utilizing H_2 as the reductant, Journal of the American Chemical Society, 127 (2005) 10184-10185.

[33] M.D. Fryzuk, Side-on end-on bound dinitrogen: An activated bonding mode that facilitates functionalizing molecular nitrogen, Accounts of Chemical Research, 42 (2009) 127-133.

[34] M.E. Gálvez, M. Halmann, A. Steinfeld, Ammonia production via a two-step Al_2O_3/AlN thermochemical cycle. 1. Thermodynamic, environmental, and economic analyses, Industrial & Engineering Chemistry Research, 46 (2007) 2042-2046.

[35] R. Michalsky, P.H. Pfromm, Thermodynamics of metal reactants for ammonia synthesis from steam, nitrogen and biomass at atmospheric pressure, AIChE Journal, http://onlinelibrary.wiley.com/doi/10.1002/aic.13717/pdf, (in press).

[36] F.J. DiSalvo, New ternary nitrides, Nitrides and Oxynitrides, Proceedings of the Second International Symposium on Nitrides, 325-326 (2000) 3-9.

[37] S. Licht, B. Wang, H. Wu, STEP-A solar chemical process to end anthropogenic global warming. II: Experimental results, Journal of Physical Chemistry C, 115 (2011) 11803-11821.

[38] R. Michalsky, P.H. Pfromm, Chromium as reactant for solar thermochemical synthesis of ammonia from steam, nitrogen, and biomass at atmospheric pressure, Solar Energy, 85 (2011) 2642-2654.

[39] R. Michalsky, B.J. Parman, V. Amanor-Boadu, P.H. Pfromm, Solar thermochemical production of ammonia from water, air and sunlight: thermodynamic and economic analyses, Energy 42 (2012) 251-260.

[40] M.E. Gálvez, A. Frei, M. Halmann, A. Steinfeld, Ammonia production via a two-step Al_2O_3/AlN thermochemical cycle. 2. Kinetic analysis, Industrial & Engineering Chemistry Research, 46 (2007) 2047-2053.

[41] R. Michalsky, P.H. Pfromm, Solar fuel production via decoupled dinitrogen reduction and protonation of mobile nitrogen ions to ammonia, The Journal of Physical Chemistry C, (in preparation).

[42] M.E. Gálvez, I. Hischier, A. Frei, A. Steinfeld, Ammonia production via a two-step Al_2O_3/AlN thermochemical cycle. 3. Influence of the carbon reducing agent and cyclability, Industrial & Engineering Chemistry Research, 47 (2008) 2231-2237.

[43] T. Glück, Mechanisms of nitriding electrolytic manganese metal, Chemical Engineering Journal and the Biochemical Engineering Journal, 54 (1994) 167-173.

[44] J.-Z. Zhang, C.-S. Xu, Y.-P. Zhao, Kinetics of nitrogen diffusion in granular manganese, Journal of Iron and Steel Research International, 15 (2008) 85-88.

[45] I. Jauberteau, J.L. Jauberteau, P. Goudeau, B. Soulestin, M. Marteau, M. Cahoreau, J. Aubreton, Investigations on a nitriding process of molybdenum thin films exposed to (Ar-N_2-H_2) expanding microwave plasma, Surface & Coatings Technology, 203 (2009) 1127-1132.

[46] S. Mändl, D. Manova, J.W. Gerlach, W. Assmann, H. Neumann, B. Rauschenbach, High temperature nitrogen plasma immersion ion implantation into molybdenum, Surface & Coatings Technology, 180 (2004) 362-366.

[47] P. Schaaf, Laser nitriding of metals, Progress in Materials Science, 47 (2002) 1-161.

[48] I. Valov, V. Rührup, R. Klein, T.C. Rödel, A. Stork, S. Berendts, M. Dogan, H.D. Wiemhöfer, M. Lerch, J. Janek, Ionic and electronic conductivity of nitrogen-doped YSZ single crystals, Solid State Ionics, 180 (2009) 1463-1470.

[49] G. Kuri, M. Gupta, R. Schelldorfer, D. Gavillet, Diffusion behaviour of Nb in yttria-stabilized zirconia single crystals: A SIMS, AFM and X-ray reflectometry investigations, Applied Surface Science, 253 (2006) 1071-1080.

[50] M. Kilo, M.A. Taylor, C. Argirusis, G. Borchardt, M. Lerch, O. Kaïtasov, B. Lesage, Nitrogen diffusion in nitrogen-doped yttria stabilised zirconia, Physical Chemistry Chemical Physics, 6 (2004) 3645-3649.

[51] I. Barin, O. Knacke, Thermochemical properties of inorganic substances, Springer-Verlag, Berlin Heidelberg New York, 1973.

[52] P. Hones, R. Sanjinés, F. Lévy, O. Shojaei, Electronic structure and mechanical properties of resistant coatings: The chromium molybdenum nitride system, Journal of Vacuum Science & Technology a-Vacuum Surfaces and Films, 17 (1999) 1024-1030.

[53] D. McKay, J.S.J. Hargreaves, J.L. Rico, J.L. Rivera, X.L. Sun, The influence of phase and morphology of molybdenum nitrides on ammonia synthesis activity and reduction characteristics, Journal of Solid State Chemistry, 181 (2008) 325-333.

[54] A.G. Cairns, J.G. Gallagher, J.S.J. Hargreaves, D. McKay, E. Morrison, J.L. Rico, K. Wilson, The influence of precursor source and thermal parameters upon the formation of beta-phase molybdenum nitride, Journal of Alloys and Compounds, 479 (2009) 851-854.

[55] O. Levenspiel, Chemical reaction engineering, Third Edition, Chapter 25 Fluid-particle reactions: Kinetics, John Wiley & Sons, New York, 1999.

[56] I. Jauberteau, T. Merle-Méjean, S. Touimi, S. Weber, A. Bessaudou, A. Passelergue, J.L. Jauberteau, J. Aubreton, Expanding microwave plasma process for thin molybdenum films nitriding: Nitrogen diffusion and structure investigations, Surface & Coatings Technology, 205 (2011) S271-S274.

[57] P. Ettmayer, System molybdenum - nitrogen, Monatshefte für Chemie, 101 (1970) 127-140.

[58] H. Scott Fogler, Elements of chemical reaction engineering, Prentice Hall PTR, Upper Saddle River, NJ, 2006.

[59] C.A. Ellefson, O. Marin-Flores, S. Ha, M.G. Norton, Synthesis and applications of molybdenum (IV) oxide, Journal of Materials Science, 47 (2012) 2057-2071.

[60] I. Barin, O. Knacke, O. Kubaschewski, Thermochemical properties of inorganic substances, Supplement, Springer-Verlag, Berlin Heidelberg New York, 1977.

[61] H.J. Beattie, F.L. VerSnyder, Microconstituents in high temperature alloys, Transactions of the American Society for Metals, 45 (1953) 397-428.

[62] K.S. Weil, P.N. Kumta, J. Grins, Revisiting a rare intermetallic ternary nitride, Ni_2Mo_3N: Crystal structure and property measurements, Journal of Solid State Chemistry, 146 (1999) 22-35.

[63] D.S. Bem, H.P. Olsen, H.-C. zur Loye, Synthesis and electronic and magnetic characterization of the ternary nitride $(Fe_{0.8}Mo_{0.2})MoN_2$, Chemistry of Materials, 7 (1995) 1824-1828.

[64] L. Pichon, S. Okur, O. Öztürk, J.P. Rivière, M. Drouet, CoCrMo alloy treated by floating potential plasma assisted nitriding and plasma based ion implantation: Influence of the hydrogen content and of the ion energy on the nitrogen incorporation, Surface & Coatings Technology, 204 (2010) 2913-2918.

[65] A.G. Cairns, J.G. Gallagher, J.S.J. Hargreaves, D. McKay, J.L. Rico, K. Wilson, The effect of low levels of dopants upon the formation and properties of beta-phase molybdenum nitride, Journal of Solid State Chemistry, 183 (2010) 613-619.

[66] F. Lihl, P. Ettmayer, A. Kutzelnigg, Beitrag zum System Mangan-Stickstoff, Zeitschrift für Metallkunde, 53 (1962) 715-719.

[67] D.S. Bem, H.-C. zur Loye, Synthesis of the new ternary transition-metal nitride $FeWN_2$ via ammonolysis of a solid-state oxide precursor, Journal of Solid State Chemistry, 104 (1993) 467-469.

[68] J. Lutz, A. Lehmann, S. Mändl, Nitrogen diffusion in medical CoCrNiW alloys after plasma immersion ion implantation, Surface & Coatings Technology, 202 (2008) 3747-3753.

[69] T. Christiansen, M.A.J. Somers, Controlled dissolution of colossal quantities of nitrogen in stainless steel, Metallurgical and Materials Transactions a-Physical Metallurgy and Materials Science, 37A (2006) 675-682.

[70] H. Chen, X.L. Lei, L.R. Liu, Z.F. Liu, H.J. Zhu, Structures and electronic properties of $Mo_{2n}N_n$ (n=1-5): a density functional study, Chinese Physics B, 19 (2010).

[71] J. Qi, L.H. Jiang, Q.A. Jiang, S.L. Wang, G.Q. Sun, Theoretical and experimental studies on the relationship between the structures of molybdenum nitrides and their catalytic activities toward the oxygen reduction reaction, Journal of Physical Chemistry C, 114 (2010) 18159-18166.

[72] H.Q. Yang, H. Al-Brithen, E. Trifan, D.C. Ingram, A.R. Smith, Crystalline phase and orientation control of manganese nitride grown on MgO(001) by molecular beam epitaxy, Journal of Applied Physics, 91 (2002) 1053-1059.

[73] M. Kilo, M.A. Taylor, C. Argirusis, G. Borchardt, B. Lesage, S. Weber, S. Scherrer, H. Scherrer, M. Schroeder, M. Martin, Cation self-diffusion of ^{44}Ca, ^{88}Y, and ^{96}Zr in single-crystalline calcia- and yttria-doped zirconia, Journal of Applied Physics, 94 (2003) 7547-7552.

[74] M. Kilo, R.A. Jackson, G. Borchardt, Computer modelling of ion migration in zirconia, Philosophical Magazine, 83 (2003) 3309-3325.

Chapter 7 - Solar thermochemical production of ammonia from water, air and sunlight: thermodynamic and economic analyses

7.1 Abstract

Ammonia is an important input into agriculture and is used widely as base chemical for the chemical industry. It has recently been proposed as a sustainable transportation fuel and convenient one-way hydrogen carrier. Employing typical meteorological data for Palmdale, CA, solar energy is considered here as an inexpensive and renewable energy alternative in the synthesis of NH_3 at ambient pressure and without natural gas. Thermodynamic process analysis shows that a molybdenum-based solar thermochemical NH_3 production cycle, conducted at or below 1500 K, combined with solar thermochemical H_2 production from water may operate at a net-efficiency ranging from 23-30% (lower heating value of NH_3 relative to the total energy input). Net-present value optimization indicates ecologically and economically sustainable NH_3 synthesis at above about 160 tons NH_3 per day, dependent primarily on heliostat costs (varied between 90 and 164 dollars/m^2), NH_3 yields (ranging from 13.9 mol% to stoichiometric conversion of fixed and reduced nitrogen to NH_3), and the NH_3 sales price. Economically feasible production at an optimum plant capacity near 900 tons NH_3 per day is shown at relative conservative technical assumptions and at a reasonable NH_3 sales price of about 534 ± 28 dollars per ton NH_3.

7.2 Preface

The present analysis is the product of an IGERT collaboration between the Department of Chemical Engineering and the Department of Agricultural Economics at Kansas State University. This material is based upon work supported by National Science Foundation Grant #

0903701: "Integrating the Socioeconomic, Technical, and Agricultural Aspects of Renewable and Sustainable Biorefining Program, awarded to Kansas State University."

This Chapter focuses on the thermochemical and technical aspects of the presented process analysis and provides the major conclusions of the related publication. Appendix F shows the major results of the net-present value analysis that is available elsewhere[1].

7.3 Introduction

The U.S. Census Bureau estimates that between 1900 and 2000, the world's population grew from 1.6 billion to 6.0 billion, and is projected to reach 9.0 billion by 2050[2]. Global human population growth is projected to increase the strain on current natural resources, such as land, fossil hydrocarbons, and fresh water, if technological advances are not made in the production of products and services using these resources.

While technological advances in agriculture in the 20th century - chemical fertilizers, mechanization, breeding, genetic improvement, chemical pest control, processing and storage systems - have contributed to vastly increase the productivity of land globally, the interface between energy and fertilizer production, especially ammonia, promises to challenge the agricultural productivity in the future. At present, over 100 million metric tons of NH_3[3] are produced annually, driven by increasing food demand and the need for higher crop yields[4]. NH_3 is the single-most important synthetic fertilizer, accounting for 58 wt% of all fertilizer consumed for example in the USA in 2007[5]. Its role in the production of bio-energy feedstock and its potential use in solar-derived H_2 storage[6-8] or as a liquid fuel[9, 10] augment its criticality and importance in the global economy.

NH_3 easily reaches the U.S. Department of Energy 2015 hydrogen storage target for H_2-based transportation fuels[9, 11] or it can be blended into diesel for direct combustion in modified

diesel engines releasing mainly H_2O and N_2 as combustion-products[12]. If these competitive uses and the duty of the agricultural industry to feed a growing global population at reasonable prices are to be realized, new and innovative NH_3 synthesis technology will likely be required.

Industrially, the Haber-Bosch process synthesizes NH_3 by shifting the reaction equilibrium of a N_2/H_2 gas mixture at high pressure (about 30 MPa) towards formation of ideally 22.7 mol% NH_3 (relative to stoichiometric conversion) at 673-873 K and in presence of a catalyst[13]. The energy-intensive process[14], including natural gas/steam reforming for H_2 production (accounting for approximately 84% of the total energy required), consumes 28-40 GJ/t NH_3 in form of natural gas[13, 15] (about 1-2% of the world's annual energy production[16]). Approximately 2.3 t of fossil-derived CO_2 are generated per t NH_3 synthesized[15]. Employing steam-reforming of coal increases the energy required for NH_3 production even further (about 47.6-165.9 GJ/t NH_3) and increases the associated generation of fossil CO_2 (16.7 t CO_2 / t NH_3)[7, 15]. Economies of scale have dictated current Haber-Bosch facilities producing above about 1,500 t NH_3 per day, consuming significant quantities of natural gas and influencing that commodity's price trend. This in turn has a direct impact on NH_3 prices and their volatility.

Various alternatives proposed for nitrogen fixation from the atmosphere via synthesis of NH_3 including catalytic formation of NH_3 near ambient temperature and pressure in the liquid phase[17] and electrochemical NH_3 synthesis[18] have not yet reached maturity. Solar thermochemical NH_3 synthesis at ambient pressure is a proposed remedy to some of the difficulties associated with the Haber-Bosch process[6, 19-22]. Reactive NH_3 synthesis via a two-step solar thermochemical cycle of metal oxide nitridation and metal nitride hydrolysis[20, 23] has been demonstrated to form significant quantities of NH_3 from air and water at near 0.1 MPa[20]. The process neither requires a catalyst nor a fossil hydrogen source. The energy required for the

generation of H_2 via H_2O splitting and for the reductive cleavage of N_2 is supplied in form of solar energy[19, 21]. Concentrated solar radiation, absorbed at elevated temperature in an endothermic metal oxide reduction, creates a metal nitride in the presence of N_2. The fixed nitrogen is, thereafter, released from the solid metal nitride as NH_3 in an exothermic steam hydrolysis reaction. Given the abundance of solar radiation in many areas of the world, this approach has the potential of producing NH_3 sustainably and facilitates simultaneously storage of intermittently available solar energy[24, 25].

Solid carbon (biomass or charcoal) has been suggested as reducing agent of the metal oxide in the process discussed above[19, 21]. However, carbon may not be available in the right quantities and proximity to the manufacturing plant, requiring transportation or production, using up arable land, and requiring expensive and energy-intensive processing[26, 27]. On the other hand, reactants forming metal oxides which can be reduced with H_2 unfortunately tend to not fix 0.1 MPa N_2 in form of metal nitrides and show low NH_3 yields when reacting their nitrides with steam[22]. Molybdenum considered here represents a trade-off[22]: The oxide (MoO_2) that is formed during nitride (Mo_2N) hydrolysis at above 800 K can be reduced[28] and nitridated with moderate yields in H_2/N_2 gas mixtures in the range of 800 to 1500 K[29, 30]. Given the relative high ionicity of the nitride[31, 32], significant quantities of NH_3 are liberated during the hydrolysis of Mo_2N at atmospheric pressure.

The work presented here conceptually assesses the technical and economic attractiveness of Mo-based solar thermochemical NH_3 synthesis in the absence of any carbonaceous material or natural gas as feedstock or for energy (Fig. 7.1). Experimentation towards the technical feasibility of the reaction cycle is described elsewhere[21].

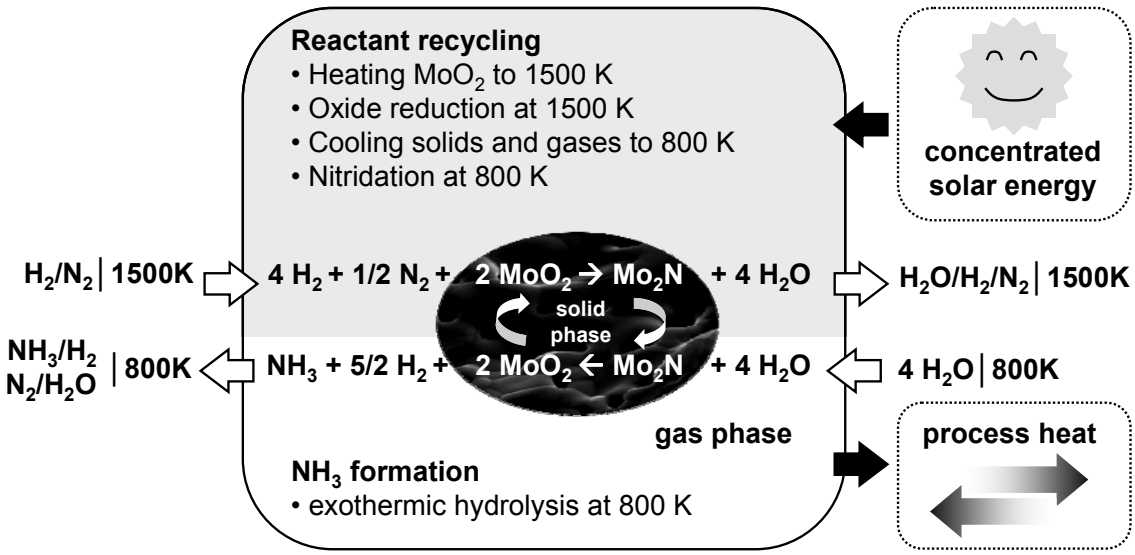

Figure 7.1 Concept for solar thermochemical NH_3 synthesis near atmospheric pressure using a molybdenum reactant.

A thermodynamic analysis for synthesizing NH_3 in a two-step solar thermochemical reaction cycle from H_2 and N_2 with a Mo-based reactant at 0.1 MPa (Fig. 7.1) is presented in Section 7.4.1. Section 7.4.2 determines plant capacity and energy efficiency and CO_2 emissions of the Haber-Bosch process implemented with natural gas as a benchmark for a process analysis of the proposed reaction cycle (Fig. 7.2) in Section 7.4.3. The analysis simulates an implementation of the reaction cycle with H_2 generated via a well-studied solar thermochemical H_2O splitting cycle using zinc[25, 33, 34]. In practice, the proposed NH_3 synthesis may be implemented with other solar-to-hydrogen technologies[34].

Section 7.5 summarizes the generated data input to the economic analysis of the proposed process. An estimation of investment costs for unit operations and chemical commodities and the development of an economical optimization model for scalable solar thermochemical NH_3 synthesis is available elsewhere[1]. The discussion of this net-present value analysis is summarized in Section 7.6 showing that the proposed concept is economically attractive under fairly conservative assumptions.

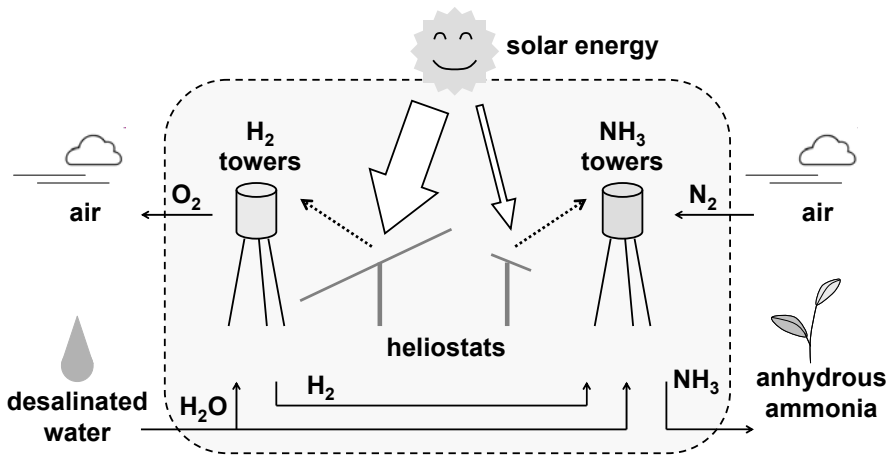

Figure 7.2 Conceptual implementation of solar thermochemical NH_3 synthesis coupled with solar thermochemical H_2 synthesis.

7.4 Molybdenum-based thermochemical NH_3 synthesis

The Gibbs free energy of formation for a metal nitride is relatively small compared to the corresponding oxide. Thus, only a few metals such as Mo allow simultaneously for oxide reduction with H_2 and reductive cleavage of dinitrogen at 0.1 MPa[22, 29, 30]. Mo is shown here to be a promising reactant for solar thermochemical NH_3 synthesis.

To estimate the equilibrium reaction yield achievable in a system closed to mass transfer, the free energy of reaction, $\Delta_{rxn}g$, was computed based on the literature[28]. The absolute error of energy of formation data was estimated previously with ± 3 kJ[35] and was taken as 2% of the value in kJ/mol. The computed formation of Mo_2N was extrapolated at > 800 K using a linear fit (R^2 > 0.999). With the free energy computations in hand, the equilibrium constants, K_T, were determined at atmospheric pressure taking the total number of chemical species in the system for simplicity as the arithmetic mean of the number of reactants and the number of products at complete conversion[36]. This allows solving the elemental mol balances of the given reaction system symbolically ("live" Symbolics, Mathcad 13) as a function of K_T, that is yielding the equilibrium composition of the reaction system as a function of temperature, T, at 0.1 MPa.

7.4.1 Thermodynamic analysis

Conversion of solar energy is accomplished by thermochemical reduction of Mo(IV) oxide with H_2 to Mo metal (Eq. 7.1):

$$(7.1)\quad \begin{aligned} &2MoO_{2\,(s)} + 4H_2 \leftrightarrow 2Mo_{(s)} + 4H_2O \\ &\Delta_{rxn}h_{1500K} \approx 130 \pm 25\ kJ/mol\ N \end{aligned}$$

$\Delta_{rxn}g$ of Eq. 7.1 indicates that the reaction equilibrium is favored thermodynamically at above ca. 1428 K (Fig. 7.3A).

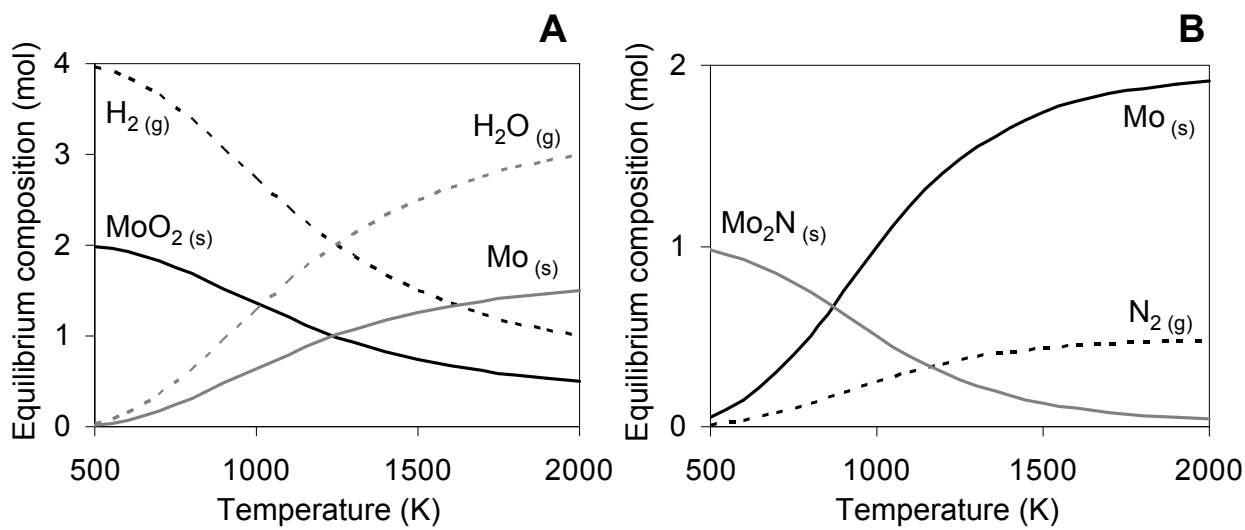

Figure 7.3 To assess the temperatures that are required for thermodynamic feasibility of the reaction cycle proposed: equilibrium composition of (A) MoO_2 reduction (Eq. 7.1) and (B) N_2 fixation via Mo nitridation (Eq. 7.2) as a function of temperature at 0.1 MPa.

The chemical energy stored in the endothermic metal formation (the enthalpy of reaction, $\Delta_{rxn}h$)[28] allows subsequently for slightly exothermic N_2 fixation in form of metal nitridation (Eq. 7.2) favorably at lower temperatures (Fig. 7.3B):

$$(7.2)\quad \begin{aligned} &2Mo_{(s)} + 1/2N_2 \leftrightarrow Mo_2N_{(s)} \\ &\Delta_{rxn}h_{800K} \approx -63.2 \pm 0.8\ kJ/mol\ N \end{aligned}$$

The yield (Y = mol solid reaction product formed / mol solid product at stoichiometric conversion) for reaction 7.1 or 7.2 is below stoichiometric conversion at thermodynamic

equilibrium (Eq. 7.1 at ca. 1428 K, Eq. 7.2 at ca. 1115 K, assuming 0.1 MPa) (Fig. 7.3). However, given the non-equilibrium situation (mass exchange) in an actual flow-through reactor, and assuming a high effective reactant surface, stoichiometric conversion for both reactions is assumed below. The over-stoichiometric supply of H_2 (see Section 7.4.3), may account for excess MoO_2 formed during nitride hydrolysis from Mo that may not have converted to Mo_2N during the nitridation.

The fraction of reactive nitrogen ions yielded in the solid state due to the electron transfer between bonding Mo 4d, Mo 5s and N 2p orbitals allows for exothermic formation of NH_3 when the nitrogen in the solid phase is substituted with more electronegative oxygen (Eq. 7.3):

$$(7.3)\quad \begin{aligned} &Mo_2N_{(s)} + 4H_2O \leftrightarrow 2MoO_{2\,(s)} + NH_3 + 5/2H_2 \\ &\Delta_{rxn}h_{800K} \approx -168 \pm 29\, kJ/mol\, N \end{aligned}$$

Uncharged N^0 in the interstitial space of the metal or metal nitride crystal may form N_2 upon nitride corrosion (Eq. 7.4):

$$(7.4)\quad \begin{aligned} &Mo_2N_{(s)} + 4H_2O \leftrightarrow 2MoO_{2\,(s)} + 1/2N_2 + 4H_2 \\ &\Delta_{rxn}h_{800K} \approx -114 \pm 29\ kJ/mol\ N \end{aligned}$$

The assumptions below (see Section 7.4.3) are based on experimental results (see Chapter 5 and Appendix D) for hydrolysis of 25.5 ± 0.5 wt% Mo_2N powder (balance Mo, 17 ± 8 μm average particle diameter, 429 ± 3 m^2/kg BET surface area) at 773 K with steam supplied for 1 h at a rate of 0.91 ± 0.02 $ml_{(STP)}$/min. The simulation assumes either Y_3 = 100 mol%, Y_4 = 0 (stoichiometric conversion), or Y_3 = 13.9 mol%, Y_4 = 9.1 mol%. Decreasing the hydrolysis temperature (Fig. 7.4) or increasing the availability of effective reactive surface sites may allow increasing the yield of NH_3 in practice. Endothermic decomposition of Mo_2N (Eq. 7.2, when favoring the species on the left side) was neglected at this point due to a positive $\Delta_{rxn}g$ at 800 K. Oxidation of MoO_2 to MoO_3[29] is not favored at equilibrium (105.2 kJ/mol oxide $\Delta_{rxn}g$ at 800

K[28]) but driven when the equilibrium is not established due to MoO_3 vapor formation (MoO_3 boils at about 1428 K). This can be reduced or avoided by low hydrolysis temperatures, low steam flow rates and short reaction times.

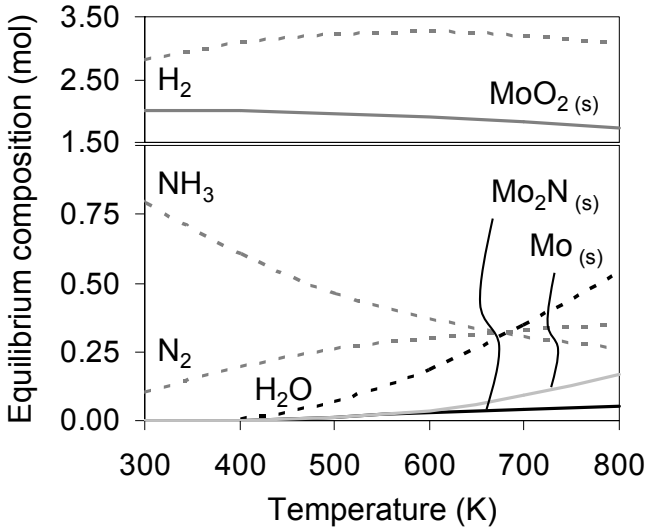

Figure 7.4 To assess the temperatures that are required for thermodynamic feasibility of the reaction cycle proposed: equilibrium composition of Mo_2N hydrolysis forming MoO_2, NH_3 and H_2 (Eq. 7.3), Mo_2N oxidation forming MoO_2, N_2, and H_2 (Eq. 7.4) and thermal dissociation of Mo_2N forming Mo and N_2 as a function of temperature at 0.1 MPa.

The overall reaction represents an alternative for realizing the Haber-Bosch reaction ($1/2N_2 + 3/2H_2 \leftrightarrow NH_3$) near 0.1 MPa. The enthalpy required for breaking the N_2 triple bond is supplied indirectly in form of concentrated solar radiation providing the heat (at 1500 K) for the endothermic reduction of Mo(IV) oxide to Mo metal (Eq. 7.1). The metal is utilized to cleave and thermochemically reduce dinitrogen (Eq. 7.2) increasing the metallic oxidation state formally to $Mo^{+3/2}$ in Mo_2N[31, 32]. Mo_2N is further oxidized to Mo(IV) when reacted with H_2O to liberate NH_3 (Eq. 7.3). The heat released from Eq. 7.2-7.4 is partly integrated[37] (see Section 7.4.3). The significant amount of energy required to form H_2 from H_2O (Fig. 7.2) is supplied as solar radiation at 2000 K employing a two-step solar thermochemical cycle of endothermic ZnO

dissociation (about 679.2 kJ per 3/2 mol H_2 $\Delta_{rxn}h$ at 2000 K), quenching of the Zn/O_2 vapor leaving the reactor, and exothermic oxidation of the condensed Zn with H_2O at 400 K (about -156.6 kJ per 3/2 mol H_2 $\Delta_{rxn}h$ at 400 K) recycling ZnO and producing H_2 (both computed at 0.1 MPa and assumed with stoichiometric conversion). This well-studied cycle has been discussed elsewhere[25, 33].

7.4.2 The scale of industrial NH_3 synthesis

As a benchmark, the Aspen Plus (V7.0) Ammonia Model[38] was used to simulate the industrial NH_3 production using natural gas as a feedstock. The model comprises a reforming unit converting a desulfurized hydrocarbon feed with steam (primary reformer, 3.1-3.3 MPa, 775-1064 K) and air (secondary reformer, 2.9-3.1 MPa, 1251-1530 K) into H_2 and carbon oxides. Subsequently, CO is converted catalytically (2.7-2.9 MPa, 483-721 K) to CO_2 that is removed with NH_3 forming an ammonium hydrogen carbonate byproduct. The synthesis gas obtained is freed from traces of CO and CO_2 employing a nickel catalyst to form CH_4 (methanizer). Thereafter, NH_3 is synthesized at 28.4-29.2 MPa and 686-799 K over a promoted iron catalyst. The major fraction of the 23.9 mol% NH_3 in the synthesis loop (about 33.9 mol% nitrogen-to-NH_3 conversion) is liquefied via refrigeration (27.5 MPa, 288-304 K) and stored at 3 MPa. The model estimates the thermodynamic properties of gases at high temperature and pressure using a modified Redlich-Kwong equation of state (RKS-BM). Liquid and vapor properties in the CO_2 scrubbing unit are modeled with an electrolyte NRTL or a Redlich-Kwong equation of state model respectively. A detailed description of the Haber-Bosch modeling is provided elsewhere[38].

Overall, the process converts approximately 35.9 t/h natural gas (80.0 mol% CH_4, 17.7 mol% C_2H_6, balance hydrocarbons and air, at 3.8 MPa and 303 K) with 308.5 t/h air at 302 K

and 69.0 t/h water at 293 K (both at 0.1 MPa) to 27.5 t/h liquid anhydrous ammonia (99.6 mol% NH_3, 2 MPa, 306 K), 126.9 t/h ammonium bicarbonate salt (98.7 mol% NH_4HCO_3, 0.1 MPa, 293 K), and 259.0 t/h flue gas (7.0 mol% CO_2, 16.1 mol% H_2O, balance N_2, O_2, and Ar, 0.1 MPa, 333 K). To compare this to the discontinuous operation of the solar thermochemical NH_3 synthesis in Section 7.4.3, this equates production of about 1,324 t NH_3 per day (as anhydrous ammonia or ammonium salt, assuming 24 h/d operation).

The enthalpy balance of the process indicates a net heat duty of about 289 MW, mainly due to the heat required in the reforming unit and the CO_2 stripper and the electricity consumed for synthesis gas compression. Taking the lower heating value (LHV) of natural gas at 31.89 GJ/t[39] results in further consumption of about 32.6 t/h natural gas and 549.7 t/h air generating 582.3 t/h flue gas (9.9 mol% CO_2, 18.3 mol% H_2O, balance N_2 and Ar). This yields total CO_2 emissions of the process - flue gas - at about 2.17 t CO_2 per t NH_3. The energy efficiency can be estimated with 46.9% (the LHV of 1,324 t/d NH_3 relative to the LHV of 1,644 t/d natural gas).

7.4.3 Numerical process analysis

Given its conceptual state a conceivable solar thermochemical process that is converting air, desalinated water, and sunlight into liquid ammonia and compressed oxygen (Fig. 7.5) was analyzed similar to other thermochemical processes reported in the literature[24, 37, 40]. To estimate the plant layout mass and energy balances were solved iteratively (Generalized Reduced Gradient nonlinear optimization code, 10^2 iteration steps, 10^{-4} minimum sensitivity, Excel 2003) at steady-state and as a function of a variable NH_3 capacity. Two scenarios were computed: First, assuming Y_3 = 100 mol%, Y_4 = 0 (see Section 7.3.1), and the ratio of gaseous reactant required at minimum to the amount of gaseous reactant supplied to any reaction, r_{gas}, of 90 mol%, "ideal

operation". The second, rather "conservative operation", assumes Y_3 = 13.9 mol%, Y_4 = 9.1 mol%, and r_{gas} = 67 mol%.

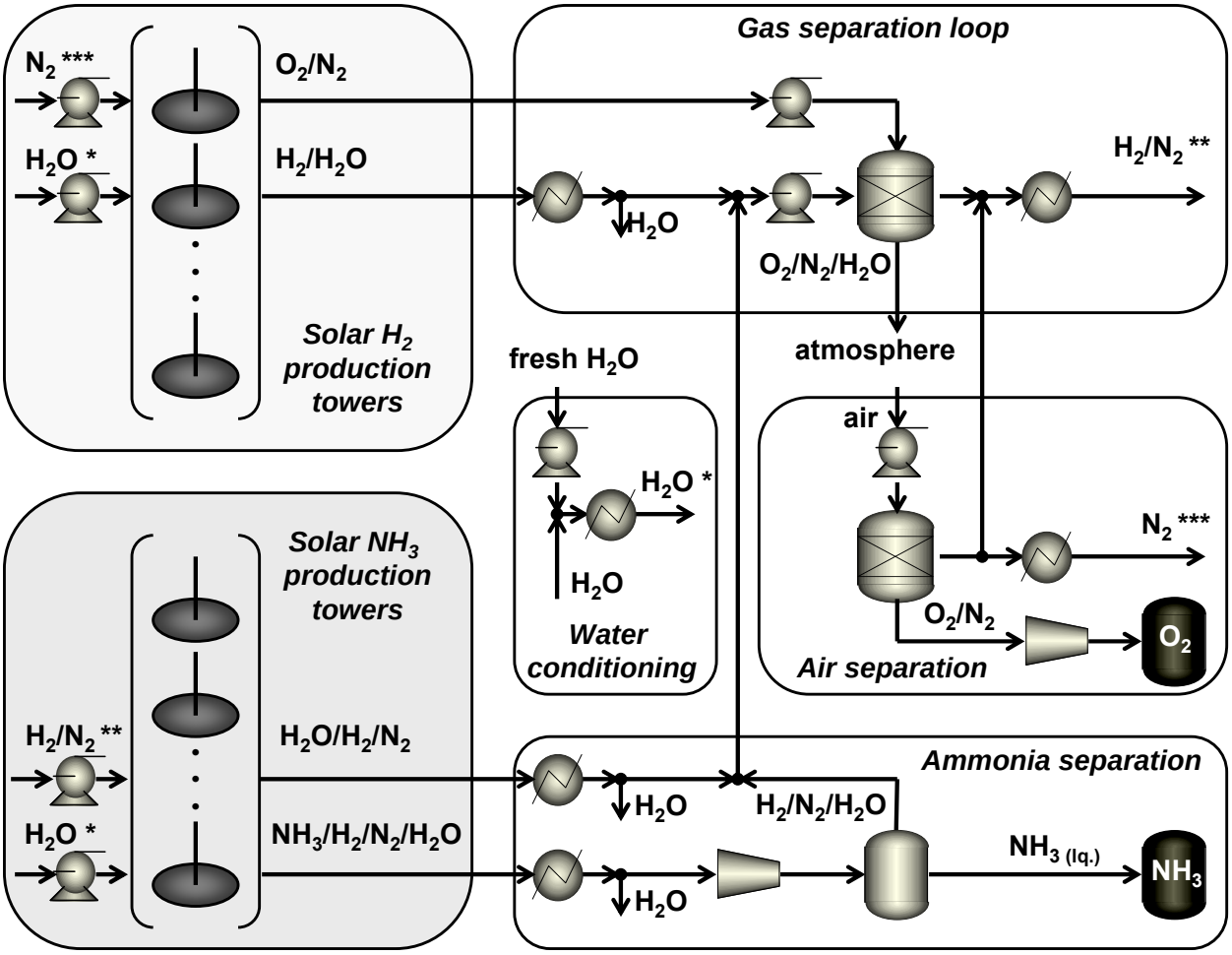

Figure 7.5 Process schematic of solar thermochemical NH_3 synthesis and on-site H_2 production (dry cooling system not shown).

To analyze the performance of the envisioned plant located in a suitable geographic region typical meteorological data from the updated National Solar Radiation Data Base (NSRDB)[41, 42] was used. The hourly direct normal irradiance values provided by the database were averaged over a typical meteorological year to identify several regions in the southwestern U.S. with an averaged normal irradiance in the range of 7.01-7.81 kWh/m^2/d. The analysis presented here assumes a yearly-averaged direct normal irradiance of 7.48 kWh/m^2/d (that is 1

kW/m^2 for annualized 7.48 h/d), based on data for 1997-2005, Palmdale Airport, CA, USA (approximately 80 km linear distance to the Pacific).

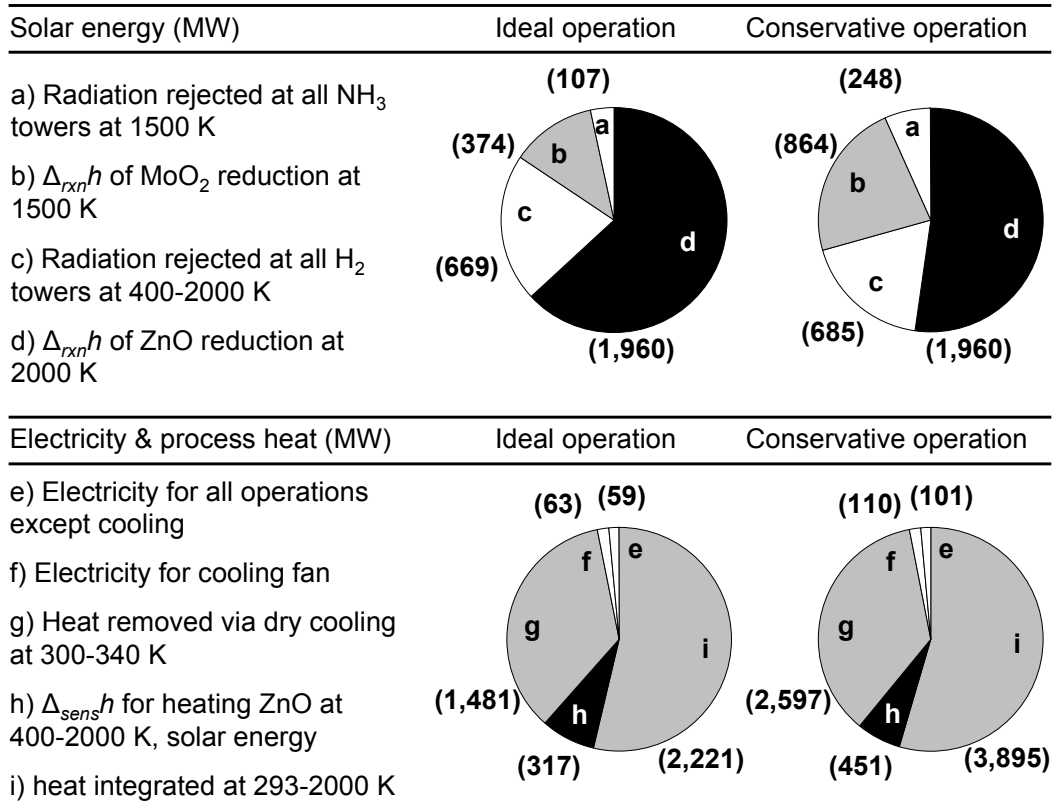

Figure 7.6 Total power requirements at industrial production scale (producing 1,324 t NH_3 per day, within 7.48 h/d operation on average, see Sections 7.4.1-7.4.3). All power values given in brackets are in MW/plant.

Solar radiation is concentrated via heliostats and absorbed at 1500 or 2000 K respectively (Fig. 7.5) with an efficiency of solar radiation converted to chemical reaction heat (dimensionless mean flux concentration ratio at 10^4, for a detailed description see[25]) assumed at 0.78 (Fig. 7.6). The radiation is received by a series of reactors at 100 m above ground (similar in appearance to the Solar Two power tower, Mojave Desert, CA, USA, or the PS10 and PS20 plants near Seville, Spain) splitting H_2O into H_2 and O_2 (2.5 x 2.5 x 5.0 m reactor volume, V_R, Mo-alloy), or converting H_2 and N_2 to NH_3 (15 x 15 x 25 m V_R, ceramic lining). V_R was estimated assuming 1 min residence time of the gaseous species at a given temperature in the

reactor (using a molar ratio of N_2 sweep gas to ZnO of 0.1)[33]. In practice V_R will be determined empirically by reaction kinetics for a reactant with optimized composition and by the heliostat area required per reactor for providing heat at a desired temperature.

Sensible, $\Delta_{sen}h$, and latent, $\Delta_{lat}h$, heat and the $\Delta_{rxn}h$ of exothermic reactions[28] are recovered and integrated at a ratio of 0.6 (that is heat losses at about 40%)[37] estimating heat exchange areas of 1.44 x 10^4 m^2 for temperatures up to 2000 K (lined with molybdenum disilicide) or 8.47 x 10^4 m^2 < 1500 K (Fig. 7.6). This is assuming replication of the production described in Section 7.4.2. The remaining heat is removed via dry (air) cooling (5.71 x 10^5 m^2 heat exchange area, 40 K effective ΔT_{air}, 2 kPa pressure losses[43], efficiency of fans and compressors assumed with 0.86)[44]. Although shown to be by a factor of 4-6 more energy-intensive and by a factor of 4-12 more capital-intensive than wet cooling, dry cooling was employed due to the crucial role of water availability[45].

The N_2 is required only at industrial-grade purity (as sweep gas and feedstock) and is produced via membrane permeation (based on literature values for gas permeability and diffusivity for polysulfone fibers[46]) yielding at 0.2 MPa trans-membrane pressure an effective membrane area of ca. 8.48 x 10^5 m^2. By-product O_2 (Table 7.1) is compressed isentropically and stored. NH_3 is separated from its synthesis vapor and liquefied via cooling and compression to 306 K and 2 MPa (see Section 7.4.2) and stored in steel tanks. H_2 and N_2 gas mixtures recovered from the NH_3 synthesis cycle are enriched with H_2 generated in the H_2 synthesis cycle and desiccated with a silica gel bed (0.4 g H_2O/g SiO_2 adsorption capacity[47], 200 K maximum ΔT_{gas} between H_2O ad- and desorption, 10 kPa pressure drop assumed for all solid beds). Traces of Ar, CO_2, and Zn or MoO_3 vapor have been neglected for simplicity.

Given the net energy content of NH_3 and neglecting the energy stored in the separation of O_2 from air, conversion of solar energy to NH_3 was estimated with an efficiency of about 23-30% at maximum (LHV of NH_3 relative to the total energy requirement, including net electricity as solar heat-equivalent, for conservative or ideal operation respectively) (Table 7.1). This energy is released in form of heat when NH_3 is combusted (e.g., as transportation fuel)[12] or in form of H_2 when NH_3 is used as a single-use hydrogen carrier[7, 8, 10]. The maximum efficiency as estimated is below 46.9% estimated for the NH_3 synthesis with natural gas at this scale (see Section 7.4.2) but within the range estimated for the industrial NH_3 synthesis via steam reforming with natural gas or coal respectively, i.e., 11-66% (Table 7.1).

Overall process mass balance			
Raw materials	m (t/d)	T (K)	p (MPa)
air	1,970	300	0.1
water	2,418	293	0.1
Products	m (t/d)	T (K)	p (MPa)
NH_3 (99 wt% NH_3 in H_2O)	1,344	306	2
O_2 (82 wt% O_2 in N_2)	555	300	15
air (75 wt% O_2, 12 wt% H_2O)	2,489	413	0.1

Comparison of total energy requirements (GJ/t NH_3)	
Solar thermochemical NH_3 [a]	56.4 - 70.6
Natural gas/steam reforming & Haber-Bosch [b]	28 - 40.1
Coal gasification & Haber-Bosch [c]	47.6 - 165.9
Lower heating value (LHV) of NH_3 [d]	18.6
Gibbs free energy of mixing for O_2 separation	0.2

Table 7.1 Total heat and electricity input; a, ideal operation (Y_3 = 100 mol%, Y_4 = 0 mol%, r_{gas} = 90 mol%, see Section 7.4.1) to conservative operation (Y_3 = 13.9 mol%, Y_4 = 9.1 mol%, r_{gas} = 66.7 mol%, see Section 7.4.1); b, taken from[15] and see Section 7.3; c,[7, 15]; d,[50].

The total electricity required for the proposed process (assuming as a worst-case scenario all grid-electricity is generated from coal-fired power plants emitting 0.91 t CO_2/MWh[48]) results in CO_2 emissions in the range of 0.62-1.08 t CO_2 / t NH_3. That is a net reduction of fossil CO_2

emissions by 50-71% relative to the current NH_3 synthesis with natural gas (see Section 7.4.2) or up to 96% relative to the industrial NH_3 synthesis with coal (see Section 7.3).

7.5 Data input to an economic feasibility analysis

The mass and energy balances (see Section 7.4, Fig. 7.6 and Table 7.1) for the described "ideal" or "conservative" operation respectively (see Section 7.4.3) were utilized to estimate operational costs and to generate a generic list of components and equipment required for realizing the proposed process.

For example, if the production described in Section 7.4.2 is to be replicated by this process at "ideal operation", it will require 33.2 t Mo, 17.0 t Zn, 0.48 km^2 lens area for concentration of sunlight, A_{lens}, utilized by the NH_3 synthesis cycle, and 2.95 km^2 A_{lens} utilized by the H_2 synthesis cycle (Fig. 7.5). On the other hand, "conservative operation" would lead to 239.1 t Mo, 17.0 t Zn, 1.11 km^2 A_{lens} to synthesize NH_3, and 3.10 km^2 A_{lens} to produce H_2. The increased amount of Mo does not significantly affect capital costs[1]. However, the increased land requirements (increased totally by 22.7% for provision of sensible and latent heat and $\Delta_{rxn}h$ of Eq. 7.1) under the "conservative operation" lead to a significantly increased amount of capital that needs to be raised for reactors and solar concentrators.

The economic feasibility of the plant was determined by its ability to generate a positive net present value with NH_3 output as the only choice variable in the optimization model. Appendix F shows the major results of this analysis that is available in the literature[1].

7.6 Conclusions

The solar thermochemical synthesis of ammonia using a molybdenum-based reactant was presented and analyzed from a technical and an economic perspective.

7.6.1 Technical perspective

Major conclusions of the analysis presented above are:

- It appears technically feasible to form NH_3 with a reaction cycle conducted at near 0.1 MPa and at ≤ 1500 K and without natural gas or solid reducing agents. This may allow synthesis of artificial nitrogen fertilizer without sophisticated machinery and less depended on the volatility of the natural gas price. As outlined for the U.S., geographical regions with high annual insolation and a relative close supply of coastal or fresh water appear suited for this technology.
- Maximum energy efficiencies of converting solar radiation to the lower heating value of NH_3 were estimated (23-30%) between the efficiency of the industrial NH_3 synthesis employing coal (about 11%) or natural gas (up to 66%). As an aside, this approaches the DOE performance target for solar thermochemical H_2 (i.e., 30% by 2017 or > 35% by 2020 respectively)[34] and includes convenient storage of H_2 in form of NH_3. In the future, research addressing yield and kinetics of the NH_3 formation via materials design[22], heat integration[49], and solar-to-hydrogen technology[34] will be critical for approaching efficiencies realized with the Haber-Bosch process.
- Indirect fossil CO_2 emissions (from coal-derived grid-electricity) are in the range of 4-50% of the CO_2 emitted by the current industrial NH_3 synthesis employing a coal or natural gas feedstock. Yet, no special monetary benefits for technologies utilizing renewable resources via regulations, e.g., for CO_2 emissions are regarded.

7.6.2 Economic perspective

The conducted net-present value analysis computed four scenarios: (1) "ideal operation" (see Section 7.4.3) and conservative cost estimates[1], (2) "ideal operation" and optimistic cost

estimates, (3) “conservative operation” and conservative costs, and (4) “conservative operation” and optimistic costs. Compare Appendix F. Major conclusions[1] of the analysis are:

- The cost of heliostats is a major factor determining the economic feasibility of the proposed technology. About 74-86% of the heliostat capital investment is absorbed for H_2 production. Thus, low-cost heliostats (i.e., 90 dollars/m^2) or reduced H_2 reactor costs (< 16 million dollars, as estimated here), or replacing H_2 with another gaseous reducing agent, may result in a positive net-present value (Scenario 4) or augment the return of investment (Scenario 1 or 2 at > 450 t NH_3 per day).
- The sales price increase of NH_3 required for Scenario 4 to break even (2.19%) is below the standard deviation of the Monte Carlo price simulation (5.19%) indicating that an only slightly increased NH_3 market price will further the development of the proposed technology. The present simulation suggests economic feasibility even under conservative assumptions at 534 ± 28 dollars per ton NH_3. If natural gas prices rise break even will be possible at production levels below 900 t NH_3 per day.
- Production at small scale (144-178 t NH_3 per day when employing only a single H_2 tower) would reduce initial capital requirements (e.g., 770 million dollars at 902 t NH_3 per day, Scenario 1) and facilitate market entry. Fertilizer production in regions with relatively undeveloped infrastructure, e.g., in developing countries with significant population growth might then be conceivable.

7.7 Associated content in Appendix F

Supporting Information taken from the literature[1]: Net-present value and total initial plant costs as a function of NH_3 output for two selected scenarios and a sensitivity analysis of these two scenarios with respect to variations in the NH_3 sales price.

7.8 References

[1] R. Michalsky, B.J. Parman, V. Amanor-Boadu, P.H. Pfromm, Solar thermochemical production of ammonia from water, air and sunlight: thermodynamic and economic analyses, Energy 42 (2012) 251-260.

[2] V. Smil, Nitrogen and food production: Proteins for human diets, Ambio, 31 (2002) 126-131.

[3] D.A. Kramer, Nitrogen (fixed) - Ammonia, U.S. Geological Survey, Mineral Commodity Summaries, (2003) 118-119.

[4] B.J. Parman, V. Amanor-Boadu, P.H. Pfromm, R. Michalsky, Third generation biofuels and the food versus fuel debate: a systems perspective, The International Journal of Environmental, Cultural, Economic and Social Sustainability 2(2011) 287-300.

[5] http://www.ers.usda.gov/Data/FertilizerUse/ (retrieved March, 2011).

[6] M.E. Gálvez, M. Halmann, A. Steinfeld, Ammonia production via a two-step Al_2O_3/AlN thermochemical cycle. 1. Thermodynamic, environmental, and economic analyses, Industrial & Engineering Chemistry Research, 46 (2007) 2042-2046.

[7] G. Thomas, G. Parks, Potential roles of ammonia in a hydrogen economy, a study of issues related to the use ammonia for on-board vehicular hydrogen storage, U.S. Department of Energy (2006), Available online at: http://www.hydrogen.energy.gov/-pdfs/nh3_paper.pdf (retrieved December, 2011).

[8] S.S. Penner, Steps toward the hydrogen economy, Energy, 31 (2006) 33-43.

[9] T. Lipman, N. Shah, Ammonia as an alternative energy storage medium for hydrogen fuel cells: Scientific and technical review for near-term stationary power demonstration projects (Final Research Report, UCB-ITS-TSRC-RR-2007-5), Institute of Transportation Studies UC Berkeley Transportation Sustainability Research Center (University of California, Berkeley), (2007).

[10] C.H. Christensen, T. Johannessen, R.Z. Sørensen, J.K. Nørskov, Towards an ammonia-mediated hydrogen economy?, Catalysis Today, 111 (2006) 140-144.

[11] P. Wang, X.D. Kang, Hydrogen-rich boron-containing materials for hydrogen storage, Dalton Transactions, (2008) 5400-5413.

[12] A.J. Reiter, S.C. Kong, Combustion and emissions characteristics of compression-ignition engine using dual ammonia-diesel fuel, Fuel, 90 (2011) 87-97.

[13] Z. Kirova-Yordanova, Exergy analysis of industrial ammonia synthesis, Energy, 29 (2004) 2373-2384.

[14] M.H. Panjeshahi, E.G. Langeroudi, N. Tahouni, Retrofit of ammonia plant for improving energy efficiency, Energy, 33 (2008) 46-64.

[15] I. Rafiqul, C. Weber, B. Lehmann, A. Voss, Energy efficiency improvements in ammonia production - perspectives and uncertainties, Energy, 30 (2005) 2487-2504.

[16] S.K. Ritter, The Haber-Bosch reaction: An early chemical impact on sustainability, Chemical & Engineering News, 86 (2008) 53.

[17] D.V. Yandulov, R.R. Schrock, Catalytic reduction of dinitrogen to ammonia at a single molybdenum center, Science, 301 (2003) 76-78.

[18] M. Lerch, J. Janek, K.D. Becker, S. Berendts, H. Boysen, T. Bredow, R. Dronskowski, S.G. Ebbinghaus, M. Kilo, M.W. Lumey, M. Martin, C. Reimann, E. Schweda, I. Valov, H.D. Wiemhöfer, Oxide nitrides: From oxides to solids with mobile nitrogen ions, Progress in Solid State Chemistry, 37 (2009) 81-131.

[19] M.E. Gálvez, I. Hischier, A. Frei, A. Steinfeld, Ammonia production via a two-step Al_2O_3/AlN thermochemical cycle. 3. Influence of the carbon reducing agent and cyclability, Industrial & Engineering Chemistry Research, 47 (2008) 2231-2237.

[20] M.E. Gálvez, A. Frei, M. Halmann, A. Steinfeld, Ammonia production via a two-step Al_2O_3/AlN thermochemical cycle. 2. Kinetic analysis, Industrial & Engineering Chemistry Research, 46 (2007) 2047-2053.

[21] R. Michalsky, P.H. Pfromm, Chromium as reactant for solar thermochemical synthesis of ammonia from steam, nitrogen, and biomass at atmospheric pressure, Solar Energy, 85 (2011) 2642-2654.

[22] R. Michalsky, P.H. Pfromm, Thermodynamics of metal reactants for ammonia synthesis from steam, nitrogen and biomass at atmospheric pressure, AIChE Journal, http://onlinelibrary.wiley.com/doi/10.1002/aic.13717/pdf, (in press).

[23] N. Auner, S. Holl, Silicon as energy carrier - Facts and perspectives, Energy, 31 (2006) 1395-1402.

[24] A. Steinfeld, C. Larson, R. Palumbo, M. Foley, Thermodynamic analysis of the co-production of zinc and synthesis gas using solar process heat, Energy, 21 (1996) 205-222.

[25] A. Steinfeld, A.W. Weimer, Thermochemical production of fuels with concentrated solar energy, Optics Express, 18 (2010) A100-A111.

[26] J.P. Murray, E.A. Fletcher, Reaction of steam with cellulose in a fluidized-bed using concentrated sunlight, Energy, 19 (1994) 1083-1098.

[27] J. Lédé, Reaction temperature of solid particles undergoing an endothermal volatilization - Application to the fast pyrolysis of biomass, Biomass & Bioenergy, 7 (1994) 49-60.

[28] I. Barin, O. Knacke, Thermochemical properties of inorganic substances, Springer-Verlag, Berlin Heidelberg New York, 1973.

[29] R.S. Wise, E.J. Markel, Synthesis of high-surface-area molybdenum nitride in mixtures of nitrogen and hydrogen, Journal of Catalysis, 145 (1994) 344-355.

[30] A.G. Cairns, J.G. Gallagher, J.S.J. Hargreaves, D. McKay, E. Morrison, J.L. Rico, K. Wilson, The influence of precursor source and thermal parameters upon the formation of beta-phase molybdenum nitride, Journal of Alloys and Compounds, 479 (2009) 851-854.

[31] H. Chen, X.L. Lei, L.R. Liu, Z.F. Liu, H.J. Zhu, Structures and electronic properties of $Mo_{2n}N_n$ (n=1-5): a density functional study, Chinese Physics B, 19 (2010).

[32] J. Qi, L.H. Jiang, Q.A. Jiang, S.L. Wang, G.Q. Sun, Theoretical and experimental studies on the relationship between the structures of molybdenum nitrides and their catalytic activities toward the oxygen reduction reaction, Journal of Physical Chemistry C, 114 (2010) 18159-18166.

[33] R. Palumbo, J. Lédé, O. Boutin, E.E. Ricart, A. Steinfeld, S. Möller, A. Weidenkaff, E.A. Fletcher, J. Bielicki, The production of Zn from ZnO in a high-temperature solar decomposition quench process - I. The scientific framework for the process, Chemical Engineering Science, 53 (1998) 2503-2517.

[34] R. Perret, Solar thermochemical hydrogen production research (STCH), Thermochemical cycle selection and investment priority, Sandia report SAND2011-3622, Sandia National Laboratories, (2011).

[35] M. Lundberg, Model-calculations on some feasible 2-step water splitting processes, International Journal of Hydrogen Energy, 18 (1993) 369-376.

[36] H. Scott Fogler, Elements of chemical reaction engineering, Prentice Hall PTR, Upper Saddle River, NJ, 2006.

[37] M.T. Balta, I. Dincer, A. Hepbasli, Energy and exergy analyses of a new four-step copper-chlorine cycle for geothermal-based hydrogen production, Energy, 35 (2010) 3263-3272.

[38] Aspen Plus Ammonia Model, Aspen Technology, Inc., Version Number V7.0, 2008.

[39] http://www.eia.doe.gov/cneaf/electricity/forms/eia920.doc (retrieved January 28, 2012).

[40] M. Sturzenegger, P. Nüesch, Efficiency analysis for a manganese-oxide-based thermochemical cycle, Energy, 24 (1999) 959-970.

[41] National Solar Radiation Database, 1991-2005 Update: Typical Meteorological Year 3, http://rredc.nrel.gov/solar/old_data/nsrdb/1991-2005/tmy3/by_state_and_city.html#C (retrieved January 6, 2012).

[42] National Solar Radiation Database 1991+2005 Update: User's Manual, Technical Report NREL/TP-581-41364, National Renewable Energy Laboratory, 2007, Available online at: http://www.nrel.gov/docs/fy07osti/41364.pdf (retrieved January 6, 2012).

[43] R.H. Perry, D.W. Green, J.O. Maloney, Perry's Chemical Engineers' Handbook, McGraw-Hill, New York, 1984.

[44] J. Logan, E., R. Ramendra, Handbook of Turbomachinery, Marcel Dekker, Inc., New York, 2003.

[45] J.S. Maulbetsch, Comparison of alternate cooling technologies for California power plants, California Energy Commission and Electrical Power Research Institute (EPRI), Final Report, February 2002. Available online at: http://www.energy.ca.gov/reports-/2002-07-09_500-02-079F.PDF (retrieved October 15, 2007).

[46] S. Ernst, Advances in Nanoporous Materials, Elsevier, Amsterdam, 2009.

[47] http://www.sorbentsystems.com/about.html (retrieved July 21, 2011).

[48] M. Ramezan, T.J. Skone, N. Nsakala, G.N. Liljedahl, Carbon dioxide capture from existing coal-fired power plants, National Energy Technology Laboratory, Final Report (Original Issue Date, December 2006), DOE/NETL-401/110907 (2007).

[49] J. Lapp, J.H. Davidson, W. Lipiński, Efficiency of two-step solar thermochemical non-stoichiometric redox cycles with heat recovery, Energy, 37 (2012) 591-600.

[50] V. Hacker, K. Kordesch, Ammonia crackers, in: W. Vielstich, A. Lamm, H.A. Gasteiger (Eds.) Handbook of Fuel Cells – Fundamentals, Technology and Applications, John Wiley & Sons, Ltd, Chichester, 2003, pp. 121-127.

Chapter 8 - Ammonia formation at ambient pressure via solar thermochemical reaction cycles of metal nitrides and hydrides

8.1 Abstract

For achieving food security, ammonia is an irreplaceable fertilizer supplying a growing global demand for food and biofuel. It has attracted current attention due to alternative uses for hydrogen storage and combustion fuel blends. Motivated by a prospective solar thermochemical synthesis of NH_3 at ambient pressure and without biomass or a fossil fuel, this study characterizes the heterogeneous reactions of manganese, calcium, or strontium nitrides with H_2. $Mn_6N_{2.58}$ and Mn_4N reacted at 700°C for 60 min with 0.5 $L_{(STP)}$ H_2 min^{-1} yielded about 9 ± 8 mol% of the lattice nitrogen with 85 mol% liberated as NH_3 at a rate of 9 ± 1 μmol NH_3 mol^{-1} Mn s^{-1} (98 ± 7 kJ mol^{-1} activation energy). Regardless of the metallic constituent of the reactant, slow formation of NH_3 is likely not a surface reaction (e.g., progressing approximately 40-507 nm below the $Mn_6N_{2.58}$ particle surface) and is presumably limited by the diffusion of H_2 in the gas phase boundary layer or the adsorptive cleavage of H_2. Based on Gibbs free energy of mixing, aiming for NH_3 gas phase concentrations near 2.8-6.8 mol% in the future will require the development of a novel high-specific surface area perhaps Mn-based reactive material.

8.2 Introduction

The impacts of the global capacity for ammonia synthesis, currently (2001/2) at approximately 162 million metric tons (t)[1], on the world's energy economy have been described previously. In a nutshell, NH_3-based fertilizer is an irreplaceable fertilizer[2] supplying a growing global demand for food (projected to increase by 70% by 2050[3]) and bio-energy. In the U.S., for instance, the expanded renewable fuel standard, RFS2, requires to increase use of corn- and

cellulose-based biofuel approximately 4-fold in volume between 2008 and 2022[4]. Additionally, NH_3 (or ammonia-based compounds[5-7]) is a promising one-way hydrogen carrier[7-11] and NH_3 blended into diesel is currently studied as transportation fuel substitute[12, 13]. On the other hand, the primary feedstock of the global NH_3 synthesis are finite fossil resources, i.e., natural gas (e.g., Europe and North America), coal (mainly China), or Naphtha (e.g., India)[14].

The industrial synthesis of NH_3 via heterogeneous catalysis[15-17] converts a highly inert N_2 feedstock with H_2 (generated by steam reforming with a fossil fuel such as natural gas) near 30 MPa and 400-600°C into NH_3. Currently, the process consumes between 28-166 GJ t^{-1} NH_3 in form of natural gas or coal[1, 18] (about 1-2% of the world's annual energy production[19]). The production of H_2 from fossil fuel alone accounts for about 84% of the total energy requirement of the industrial NH_3 synthesis. Per ton NH_3 synthesized about 2.3-16.7 t of fossil-derived CO_2 are generated, dependent on the utilized fossil resource[1].

The reliance of this process on natural gas makes the production of food and biofuels vulnerable to natural gas price fluctuations[20, 21]. The required high-pressure and temperature operations are technologically sophisticated and dictate the need for large facilities producing between 1,000-3,000 t NH_3 per day[1] complicating the production of NH_3 in regions with relatively undeveloped infrastructure such as developing countries[19].

At present several alternatives utilizing renewable resources for the production of H_2 are being developed, including, e.g., photovoltaic/electrolytic and photocatalytic[22-24] or high-temperature solar thermochemical[25-28] H_2O cleavage. Employing a renewable H_2 feedstock for the NH_3 production via heterogeneous catalysis would alleviate the fossil-fuel decency of the industrial NH_3 synthesis. However, the technical requirements for a production near 30 MPa and 400-600°C would remain.

The synthesis of NH_3 from non-fossil resources and at ambient pressure is a long standing goal of chemistry[15, 29]. Promising alternatives include electrochemical/electrocatalytic[30-35], solar thermochemical[36-39], or bio-mimetic[29, 40-43] approaches. Focusing on the solar thermochemical synthesis of NH_3, substantial formation of NH_3 from the lattice nitrogen of a metal nitride[37, 39] when reacted at 0.1 MPa with steam yields a metal oxide that can be recycled to the nitride to allow for continued NH_3 synthesis. The endothermic reduction[44-46] and nitridation of the oxide is usually accomplished at 1200-2000°C with concentrated solar radiation and a chemical reducing agent (e.g., coal, biomass, syngas, or methane)[37, 38, 47, 48]. However, temperatures above 1500°C may be difficult to contain physically in an industrial-scale solar furnace. Handling a solid reducing agent may be technically cumbersome and reliance on a carbonaceous reducing agent leads inherently to the production of a byproduct (such as methanol) with different economics cycles and markets.

Preceding the development of the catalytic NH_3 formation at high pressure Fritz Haber and collaborators had studied the formation of NH_3 by the action of H_2 on calcium or manganese nitride[49]. The work incentivized the development of the high-pressure NH_3 synthesis due to the unfavorable equilibrium of NH_3, N_2 and H_2 at 0.1 MPa and above 530°C (manganese nitride) to 600°C (calcium nitride) required to liberate NH_3 from these nitrides.

Building on this work, NH_3 may be produced alternatively without establishing the equilibrium. Illustrated in Figure 8.1, this study attempts assessing the utility of a reaction cycle based on the formation of NH_3 from lattice nitrogen and H_2 gas near ambient pressure (e.g., strontium nitride, see Section 8.3.6[50], compare Mars and Van Krevelen catalysis[51]):

(8.1) $$1/2Sr_3N_{2(s)} + 3H_2 \leftrightarrow 3/2SrH_{2(s)} + NH_3$$

Dependent on the kinetics, the exothermic NH_3 formation (reaction enthalpy, Δh_r, at 300°C of about -134 ± 5 kJ mol^{-1} NH_3[52, 53]) at above about 313°C might be driven by the continuous removal of NH_3. Opposed to highly stable metal oxides (see above), metal hydrides may be reformed with concentrated solar radiation (e.g., 92 ± 4 kJ mol^{-1} NH_3 Δh_r for Sr_3N_2 at 700°C[52, 53]) and N_2 to the nitride at relative low temperatures and without a chemical reducing agent:

$$(8.2) \quad 3/2SrH_{2(s)} + 1/2N_2 \leftrightarrow 1/2Sr_3N_{2(s)} + 3/2H_2$$

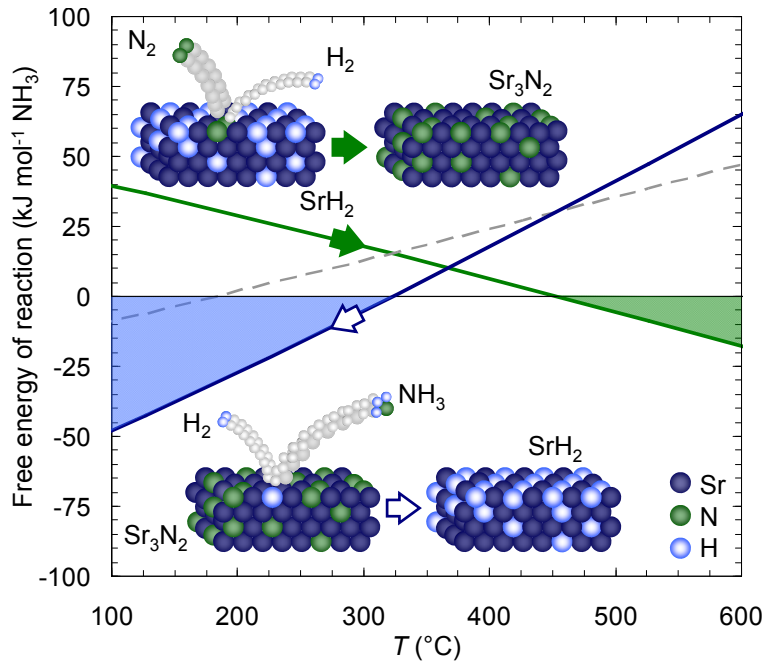

Figure 8.1 Reactive ammonia synthesis at 0.1 MPa via separate cleavage and hydrogenation of N_2. Reactions are thermodynamically favorable (shaded regions) if their free energy is negative (i.e., higher temperatures for the endothermic N_2 cleavage and lower temperatures for the exothermic NH_3 formation). The equilibrium of $2NH_3$ with $3H_2$ and N_2 favoring NH_3 at below about 180°C is shown as reference at 0.1 MPa (dashed line).

To assess the feasibility of a metal nitride/hydride-based solar thermochemical synthesis of NH_3 near ambient pressure the reaction of the lattice nitrogen of manganese nitride with H_2[49] is discussed in Sections 8.4.2-8.4.4. The discussion attempts to characterize the reaction mechanism and assesses the possibility of destabilizing the nitride by doping with Fe[54-56].

Sections 8.4.5-8.4.7 focus on the reaction of calcium or strontium nitride with H_2 respectively[49, 50]. The presented experimentation is intended as a relative comparison of the NH_3 formation from metal nitrides with different bonding character. To guide future materials design, Section 8.4.8 provides a simplified estimation of the separation work that is required for the NH_3 formation with continuous removal of the gaseous product, e.g., using ceramic membranes[57].

8.3 Experimental

8.3.1 Reacting manganese nitride with 0.1 MPa H_2

To describe the reaction kinetics of manganese nitride with H_2, 651 ± 2 mg Mn_4N powder containing about 3.01 ± 0.01 mmol total lattice nitrogen (see Section 8.3.6) in a quartz boat was heated inside a tube furnace (60 mm ID, 1 m length, quartz, model HTF55347C, temperature controller model CC58434C, Lindberg/Blue, before each experiment purged for about 10 min with 0.5-0.9 $L_{(STP)}$ N_2 min^{-1} to remove residual O_2 and H_2O) from 100 or 400°C to 300 or 550, 700, or 1000°C respectively (Fig. 8.2). The heating rate, r_H, was approximately (R^2 = 0.69-0.99) $r_H = At + B$, where t is the heating time in min and A or B range, dependent on the final temperature, from -41.5 to -5.09 °C min^{-2} or 76.2 to 126 °C min^{-1} respectively. H_2 was supplied at 0.5 ± 0.1 $L_{(STP)}$ H_2 min^{-1} and final temperatures were held for 60 min.

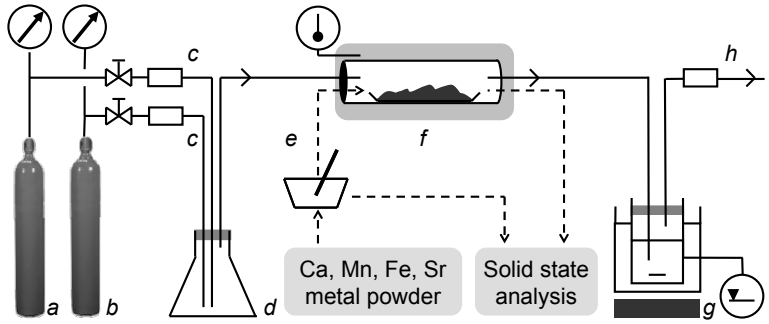

Figure 8.2 Experimental setup (*a*, N_2 gas; *b*, H_2 gas; *c*, flow meter; *d*, gas mixing; *e*, metal powder mixing; *f*, tubular flow-through furnace; *g*, 10 mM HCl absorbent chilled with ice-cold H_2O, magnetic stirrer and liquid level control; *h*, NH_3 gas detection tube).

The gas leaving the furnace was routed through a liquid absorbent (50 ± 5 $mL_{(STP)}$ hydrochloric acid, 10 mM HCl, chilled with ice-cold H_2O). To estimate the yield of absorbed ammonium in the liquid phase, 5 mL samples were taken at 0 (this includes the heating phase), 5, 10, 30 and 60 ± 0.5 min after the reaction temperature was reached. After 60 min the furnace was opened and cooled (at about -520 to -49.5 °C min^{-1} within the first minute, -88.3 to -8.81 °C min^{-1} at below 10 min, and -15.5 to -1.17 °C min^{-1} at above 10 min) to below 100°C. Solids were stored under air at 4°C. All liquids were stored at room temperature.

8.3.2 Reacting Fe-doped manganese nitride with 0.1 MPa H_2

To possibly catalyze the decomposition of manganese nitride[54] 1.69 g of an Fe/Mn_4N powder mixture with about 3.8 mmol lattice nitrogen (see Section 8.3.6) was heated consecutively in H_2 (to liberated NH_3) or N_2 (to regenerated the nitride). Using the setup described in Section 8.3.1, reactants were heated in 0.5 ± 0.1 $L_{(STP)}$ H_2 min^{-1} at in average 40 ± 11 °C min^{-1} from 100 to 700°C. Temperatures were held for 10 min. To estimate the kinetics of the NH_3 formation, 5 mL samples from the absorbent were taken at 0, 5, and 10 min after the reaction temperature was reached and after cooling the furnace. After analyzing the solid the powder was reintroduced into the furnace and heated at in average 42 ± 4 °C min^{-1} from 100 to 750°C in 0.5 ± 0.1 $L_{(STP)}$ H_2 min^{-1}. At 750 ± 5 °C the gas flow was switched to 1.9 ± 0.1 $L_{(STP)}$ N_2 min^{-1}. The furnace was held for 10 min at 750°C and thereafter cooled (see Section 8.3.1) to below 100°C. The experiment was repeated in triplicate.

8.3.3 Reacting calcium or strontium nitride with 0.1 MPa H_2

The optimum temperature for reacting Ca_3N_2 with 0.5 ± 0.1 $L_{(STP)}$ H_2 min^{-1} was determined using the experimental setup described in Section 8.3.1, without the absorption vessel. The powder (476 ± 170 mg, i.e., 6 ± 2 mmol lattice nitrogen) was hold for 60 min at 300,

500, 700, or 1000°C and analyzed thereafter for the loss of lattice nitrogen. All Ca-containing solids were stored under Ar at 4°C.

Similarly, the effect of the H_2 gas flow rate on the yield of NH_3 was analyzed by heating 491 ± 42 mg Ca_3N_2 (6.6 ± 0.5 mmol lattice nitrogen) for 120 min at 700°C (40 ± 2 °C min^{-1} average heating rate) in 0.19, 0.47, 0.93, or 1.86 ± 0.09 $L_{(STP)}$ H_2 min^{-1}. At 0, 1, 5, 10, 30, 60, and 120 min after reaching 700 ± 5 °C 5 mL samples were taken from the liquid absorbent.

To compare the NH_3 formation from transition metal or alkaline earth metal nitrides 519 ± 18 mg $Mn_6N_{2.58}$, Ca_3N_2, or Sr_2N (2.8-7.0 mmol lattice nitrogen, see Section 8.3.6) or 1.2 ± 0.3 g $Mn_6N_{2.58}$ mixed with Ca_3N_2 or Sr_2N (8.0-9.4 mmol total lattice nitrogen, atomic ratios of about 1.11 Ca/Mn or 1.17 Sr/Mn) were heated in 0.5 ± 0.1 $L_{(STP)}$ H_2 min^{-1} from 250 to 850 ± 5 °C (A = -5.21 °C min^{-2}, B = 85.4 °C min^{-1}, R^2 > 0.80). After holding temperatures for 2 min the furnace was cooled (see Section 8.3.1) to 250 °C. Without removing the solids the cycle was repeated in triplicate. Samples from the absorbent were taken at near 250, 550, or 850°C for each cycle. After analyzing the solids the samples were reintroduced into the furnace and heated for 120 min at 750°C in 1.9 ± 0.1 $L_{(STP)}$ N_2 min^{-1} (see Section 8.3.1).

8.3.4 Solid state analysis

Solids were analyzed gravimetrically (AE260 DeltaRange balance, ± 0.1 mg, Mettler). Powder X-ray diffraction (XRD) patterns were taken with a Miniflex II diffractometer (Cu-target X-ray tube, 30 kV / 15 mA output, diffracted beam monochromator, Rigaku) with a 5-80 °2θ range, 1 or 10 °2θ/min scan speed, and 0.02 data points/°2θ, continuous mode for quantitative solid phase identification (PDXL Software Version 1.6.0.0). To confirm N_2 reduction energy-dispersive X-ray spectroscopy (EDS) was employed using the S-3500N scanning electron microscope (SEM, 20 keV, Hitachi; Link Pentafet 7021 X-ray detector and Inca Energy X-ray

analysis software, both Oxford Instruments). The specific BET surface area was analyzed by NanoScale Inc., Manhattan, KS.

8.3.5 Liquid and gas phase analysis

NH_3 was quantified with an NH_3 Ion Selective Electrode and a pH/ISE Controller (model 270) (both Denver Instrument), combined with the liquid level in the absorption vessel (error ± 5 mL). The concentration of dissolved NH_3 was estimated with zeroing for the signal from pure water (the uncertainty of NH_3 concentrations was taken as the average of one standard deviation of about 65 liquid samples analyzed in triplicate). The outlet of the absorption vessel was equipped with an NH_3 gas detection tube (0.25-3 or 5-70 ppm NH_3 detection range, Dräger).

8.3.6 Nitrogen reduction

Manganese nitride was produced[58, 59 60] by heating 2.1 ± 0.2 g Mn metal for 120 min at 700°C (denoted here as "Mn_4N", 59-67 wt% ε-Mn_4N, 25-34 wt% ζ-$Mn_6N_{2.58}$) or 240 min at 750°C ("$Mn_6N_{2.58}$", 91-94 wt% ζ-$Mn_6N_{2.58}$) in a flow of N_2. Similarly, Fe-doped manganese nitride denoted as Fe/Mn_4N was prepared[54] by heating 2 g of an equimolar mixture Mn and Fe powder for 120 min in N_2 yielding 26 ± 1 wt% ε-Mn_4N and 16 ± 1 wt% ζ-$Mn_6N_{2.58}$. All Mn-containing powders were pre-treated at 60°C for 10 min to remove water. Ca_3N_2 or Sr_2N powders respectively[50, 61] were prepared by heating 4.4 ± 0.7 g metal pieces for 240 min (Ca) or 420 min (Sr) in N_2 and milling for about 5 min with pestle and mortar. The fraction of hydroxides formed during the XRD analysis (under air) of Ca_3N_2 or Sr_2N samples were disregarded in the NH_3 yield calculations (assuming 100 wt% nitride) since these materials were otherwise handled under Ar. All N_2 flows were 1.9 ± 0.1 $L_{(STP)}$ N_2 min^{-1}. Figure 8.3 gives a representative characterization of the prepared nitrides.

nitride	α-Ca_3N_2 (Ca_2N)	ε-Mn_4N (ζ-$Mn_6N_{2.58}$)	Sr_2N
space group	$Ia\bar{3}$ ($R\bar{3}m$)	$Pm\bar{3}m$ ($P6_322$)	$R\bar{3}m$
d_p [a] (μm)	105 ± 25	46 ± 19	125 ± 46
A_{BET} [b] (m^2 kg^{-1})	1253 ± 6	270 ± 3	1048 ± 4
Φ [c] (m^3 m^{-3})	0.55 ± 0.03	0.62 ± 0.01	0.53 ± 0.01

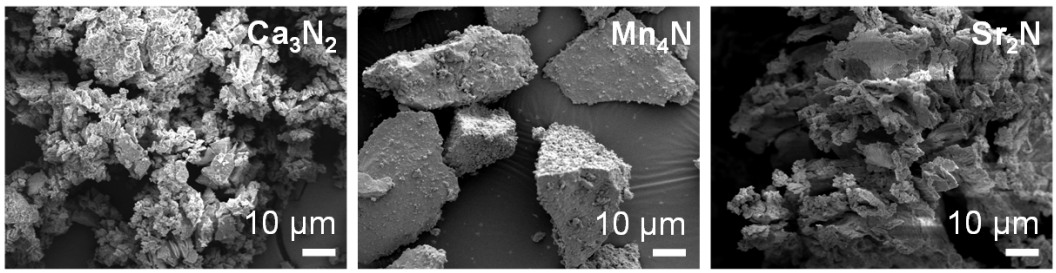

Figure 8.3 Characterization of binary metal nitride reactants: *a*) average particle diameter, *b*) BET surface area, *c*) void space fraction $\Phi = 1 - \rho_{bulk}/\rho_{particle}$, where ρ_i is the density in kg m^{-3}. Generally, powder bed surface = 33 ± 2 cm^2 and powder bed thickness < 1 mm.

8.3.7 Chemicals

Solid chemicals were Mn (99.9% pure, -325 mesh) and Fe metal (99.9% pure, -325 mesh) both from Noah Technologies; Ca metal (99% pure, granular) and NH_4Cl (99.5%, extra pure) both from Acros; Sr metal (99% pure, pieces) from MP Biomedicals; and NaOH (99.6%, certified ACS pellets) from Fisher Scientific. HCl acid (12.1 N, certified ACS Plus) was from Fisher Scientific. H_2O was deionized (Direct-Q 3 UV, Millipore) and degassed with Ar. H_2, N_2, or Ar gas were UHP Zero grade (Linweld).

8.4 Results and Discussion

8.4.1 Data processing

To determine the kinetics of the reaction between the binary nitrides of Mn, Ca, or Sr and 0.1 MPa H_2 the yield of NH_3, $X_{ammonia}$, is reported as molar ratio of NH_3 captured by the acidic absorbent (n in mol) at a given time, t, relative to the lattice nitrogen of the reactant:

$$(8.3) \quad X_{ammonia} = \frac{n_{absorbed\ NH_3,t}}{n_N} = \frac{\sum_{t=0-60\,\mathrm{min}} \left(c_{NH_3,t} - c^*_{NH_3}\right) V_t}{m_r \sum_{i=all\ nitrides} b_i x_i M_i^{-1}}$$

where c_{NH3} in mol L^{-1} is the concentration of NH_3 detected in the absorbent, the asterisk marks pure water used as a reference, V in L is the sample volume, m_r in g is the mass of metal nitride powder reacted, b is the molar ratio of lattice nitrogen per nitride, x in g g^{-1} is the nitride weight fraction (see Section 8.3.6), and M in g mol^{-1} is the molar mass.

The reaction kinetics are represented[28, 37, 39] with a shrinking-core model for nitride particles with constant size limited by the chemical reaction[62]:

$$(8.4) \quad k_r t = 1 - (1 - X_{ammonia})^{1/3}$$

or by the diffusion of reaction participants through the gas film covering the particles[62]:

$$(8.5) \quad k_g t = X_{ammonia}$$

where k_r and k_g are specific rate constants.

8.4.2 NH_3 from manganese nitride and H_2

The reaction of "Mn_4N" (see Section 8.3.6) with H_2 yielded up to 8 ± 3 mol% NH_3 (after 60 min at 700°C) relative to the total lattice nitrogen of the reactant initially (Fig. 8.4). The decreasing NH_3 yields found for the lowest values of $X_{ammonia}$, e.g., at 300 or 1000°C respectively, are likely due to unwanted stripping of the absorbent by the gas routed through the liquid phase.

The absolute NH_3 yields may change significantly if the physical presentation of the reactant is altered. More important than the absolute values reported, relative comparison of the data shows that NH_3 formation limited by the making and breaking of bonds (Eq. 8.4) or by gas phase diffusion (Eq. 8.5) describe that data equally well (i.e., R^2 > 0.98 or 0.99 at 550 or 700°C

respectively). The activation energy of the NH_3 formation can be determined from Arrhenius plots[28] of the specific rate constants, k_r or k_g, in a temperature range where increasing temperatures result in increased NH_3 yields (300-700°C, $R^2 > 0.99$, lower yields at 1000°C are presumably due to increased thermal decomposition of the formed NH_3). The estimated value of 98 ± 7 kJ mol^{-1} is approximately 55% higher than the activation energy of the steam hydrolysis of Mn_4N[39], i.e., about 63 kJ mol^{-1}, which was described as solid-state diffusion limited process.

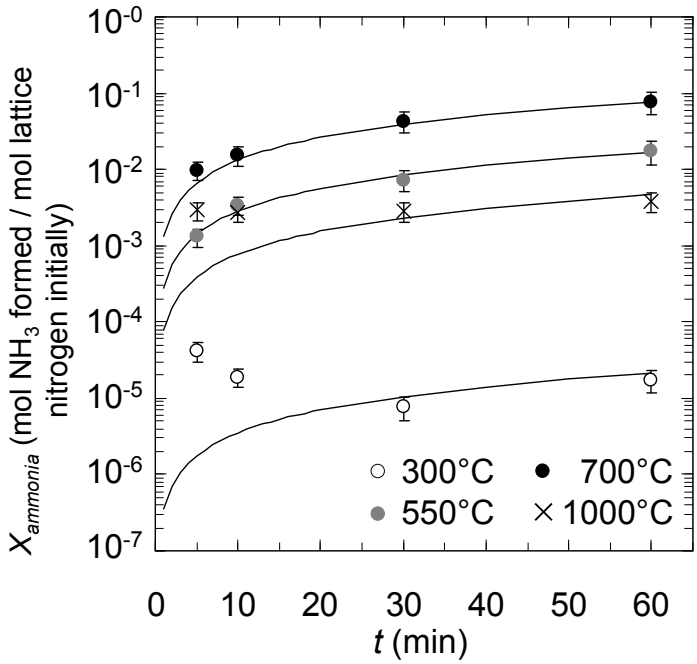

Figure 8.4 NH_3 from manganese nitride reacted with H_2 near 0.1 MPa (see Section 8.3.1). Error propagation within a 95% confidence interval (error bars) yields in average about ± 29.36%. Shrinking-core models[62] controlled by the chemical reaction or gas phase diffusion yield matching fits (solid lines) and describe the data well at the intermediate temperatures ($R^2 > 0.98$ at 550°C or $R^2 > 0.99$ at 700°C respectively).

In agreement with the relative high activation energy of the NH_3 formation with H_2, the fraction of lattice nitrogen liberated from the solid was below 6 mol% at below 700°C, about 9 ± 8 mol% at 700°C, and 79 ± 2 mol% at 1000°C. This compares to about 86 ± 1 mol% liberated

nitrogen when employing steam at 500°C as hydrogen source[39]. However, at 700°C about 85% of the liberated lattice nitrogen is recovered as NH_3.

In summary, it can not be inferred from the presented data whether the NH_3 formation is limited by the chemical reaction or the diffusion of reaction participants through the gas phase boundary layer. This will be revisited in Section 8.4.6. The following section provides evidence for a reaction that is not limited to the materials surface. To increase the liberation of N from the nitride Section 8.4.4 attempts to destabilize manganese nitride by doping with Fe[54-56].

8.4.3 Liberation of lattice nitrogen from the bulk nitride

The XRD data suggest that the liberation of lattice nitrogen at below 1000°C is presumably due to conversion of ζ-$Mn_6N_{2.58}$ (decreased concentration after the reaction) to ε-Mn_4N (increased concentration after the reaction, see Appendix G). At 1000°C the nitride likely decomposes thermally[52, 53]. Stoichiometrically, the conversion of 4 mol $Mn_6N_{2.58}$ to 6 mol Mn_4N liberates 4.32 mol N, i.e., at maximum X_N^r = 41.86 mol% of the total lattice nitrogen. Experimentally, after heating manganese nitride for 60 min at 700°C in H_2 the solid retained about X_N^s = 91 ± 8 mol% of the initially contained lattice nitrogen (see Section 8.3.2).

The depth of this reaction (l_r) can be estimated from a nitrogen mass balance with:

$$(8.6) \quad l_r = N_{SL} z = z \frac{n_N^0}{n_N^U U} \frac{(100 - X_N^s)}{X_N^r}$$

where N_{SL} is the number of reacted surface layers with the thickness, z, of one unit cell ζ-$Mn_6N_{2.58}$ with hexagonal basal face ($a = b$ = 489.16 pm, c = 455.45 pm)[63]. Dependent on the projection of the (001), (010), or (100) facet, z = 0.455-0.847 nm. The amount of lattice nitrogen contained in the nitride, n_N^0, covering an approximately spherical particle (Fig. 8.3) is about 7.054 mmol N g^{-1} $Mn_6N_{2.58}$. The amount of N per unit cell, n_N^U, is about 3.979 x 10^{-23} mol[63] and

the number of unit cells, U, in a single surface layer (in first approximation planar) is about 3.422-6.366 x 10^{16} unit cells g^{-1} $Mn_6N_{2.58}$, dependent on the unit cell projection and assuming a nitride density of 6.131 ± 0.292 g cm^{-3} [54].

Independent on the orientation of the projected unit cell the calculation estimates the thickness of the reacted nitride layer with 507 ± 217 nm (> 1,100 nitride unit cells with about 24 N each). Based on the specific BET surface area (Fig. 8.3, i.e., without assuming a spherical particle) Eq. 8.6 yields 40 ± 5 nm (i.e., 88 unit cells). Assuming N is liberated from the cubic Mn_4N phase[64] results in l_r = 50-631 nm. This is evidence for a bulk reaction yielding continuously NH_3 (see Section 8.3.2 and, e.g., Eq. 8.5).

8.4.4 Fe-doping to destabilize the metal-nitrogen bond

Iron-doped manganese nitride, Fe/Mn_4N, was prepared, analogously to the nitride employed in Section 8.3.1, from an equimolar Mn/Fe metal mixture. Figure 8.5 shows that the reaction of Fe/Mn_4N with H_2 at 700°C yielded after 10 min 3.3 ± 0.4, 2.1 ± 0.2, or 2.0 ± 0.2 mol% NH_3 after the first, second or third reaction cycle respectively. This compares to 2.7 ± 0.3 mol% after 10 min at 700°C in absence of Fe (Fig. 8.4). Thus, the addition of Fe had no lasting beneficial effect on the yield of NH_3. In fact, only approximately 38, 42, or 46 % of the liberated lattice nitrogen were recovered as NH_3 suggesting that Fe catalyzes the undesired thermal decomposition of the formed NH_3.

Furthermore, the addition of Fe may inhibit the formation of manganese nitride[54]. This would explain that heating the reactive material after the reaction with H_2 in N_2 did not increase the concentration of lattice nitrogen above the analytical uncertainty (Fig. 8.5). As an aside, the addition of Ni displayed a comparable effect (see Appendix G).

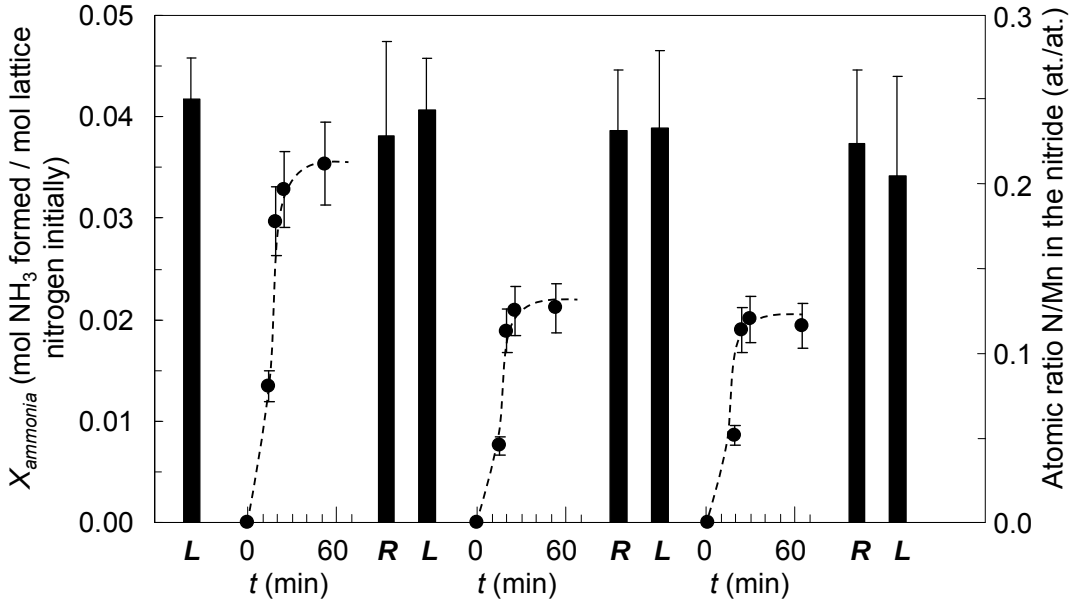

Figure 8.5 The yield of NH_3 (circles, about ± 11.43% via error propagation) when exposing Fe-doped Mn_4N repeatedly to H_2 at 700°C (data points: before heating, when reaching 700 ± 5 °C, 5 or 10 min after reaching 700°C, after cooling, see Section 8.3.2). The lattice nitrogen (bars, about ± 26.75% via error propagation) was analyzed after the reaction with H_2 (*R*) or after subsequent exposure for 10 min to N_2 at 750°C (*L*). Dashed lines are a guide.

8.4.5 Comparing the NH_3 formation from manganese and calcium nitride

Reacting α-Ca_3N_2 with H_2 at 300-1000°C resulted in increased formation of calcium imide (Ca_2NH)[65] with increasing temperature (Fig. 8.6). A major CaH_2 phase was not found[49]. Given the rapid decomposition of Ca_3N_2 with traces of moist yielding NH_3 and calcium oxide/hydroxide[66, 67] the activation energy of the NH_3 formation (see Section 8.4.2) from Ca_3N_2 and H_2 was estimated with 42 ± 7 kJ mol^{-1} based on the yield of Ca_2NH relative to stoichiometric conversion. However, a comparison of this value to the 2.35-fold higher activation energy obtained for manganese nitride (see Section 8.4.2) is complicated by the 4.64-fold higher specific surface area of Ca_3N_2 (Fig. 8.3).

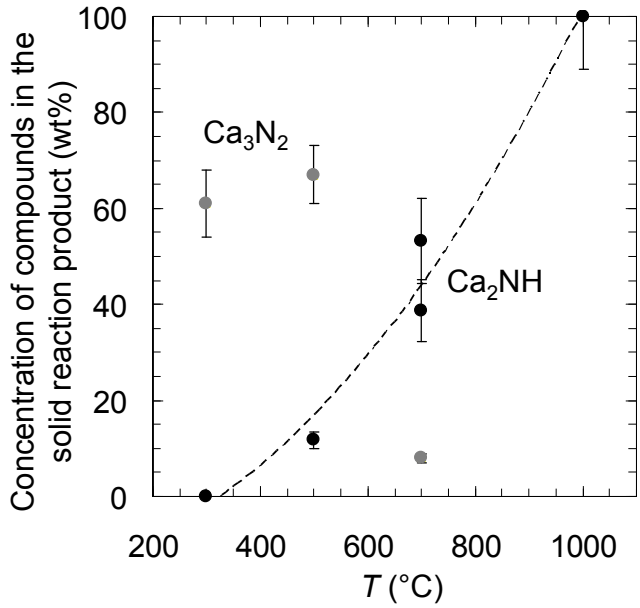

Figure 8.6 Consumption of Ca_3N_2 and production of Ca_2NH versus temperature. Error bars are taken as estimated by XRD analysis. The dashed line is to guide to the eye.

To estimate the most probable resistance to the NH_3 formation the enthalpy required to liberate the lattice nitrogen of Ca_3N_2, i.e., 692 kJ mol^{-1} N at 25°C (yielding Ca, disregarding Ca_2NH for comparison purposes at this point) is higher than 575 or 600 kJ mol^{-1} N (yielding the metal) for Mn_5N_2 or Mn_4N respectively[52, 53]. This may indicate that the activation energy of the NH_3 formation is not primarily required for breaking the metal-nitrogen bond. Furthermore, the actual enthalpy absorbed to break one Ca-N bond will be significantly below the stated value due the coordination[61, 65] of one N^{3-} ion by six Ca^{2+} ions or one Ca^{2+} by four N^{3-} ions respectively. Formally, this yields 115-173 kJ mol^{-1} N, which is significantly below the enthalpy required to cleave H_2 (about 436 kJ mol^{-1} H_2, without catalytic substances). This suggests adsorptive cleavage of H_2 may be the rate limiting NH_3 formation step.

8.4.6 Limiting gas phase diffusion can not be excluded

The attempt to exclude possible mass transport limitations due to diffusion of H_2 or NH_3 in the gas phase boundary layer covering the nitride particle (i.e., reacting Ca_3N_2 powder at

700°C with 0.19-1.86 $L_{(STP)}$ H_2 min^{-1}, see Section 8.3.3) is inconclusive (Fig. 8.7). The highest and lowest gas flow rates resulted in maximum NH_3 yields at 30 min and above, that is, no evident correlation between the gas flow rate and the yield of NH_3. However, the data support the assumed absence of diffusion limitations in the solid phase. An inconsistent physical presentation of the reactive powder (e.g., uneven material distribution in the quartz boat, varying actual specific surface areas due to preparation conditions, etc.) is a likely reason for the unexpected change in the yield of NH_3 with varying gas flow rates.

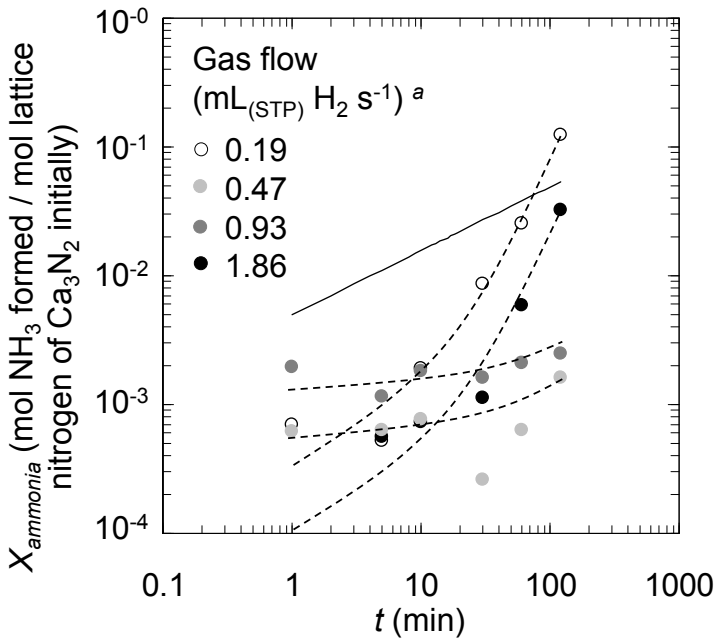

Figure 8.7 NH_3 from Ca_3N_2 and H_2 at 700°C for various reaction times and gas flow rates (*a*, ± 0.09 L min^{-1}). Error propagation (error bars omitted for clarity) yields in average about ± 26.58%. Dashed lines are a guide only. Solid-state diffusion limited shrinking-core models[62] do not represent the data well as demonstrated (solid line) for 0.19 $L_{(STP)}$ H_2 min^{-1}.

8.4.7 NH_3 from the nitrides of Mn, Ca or Sr

$Mn_6N_{2.58}$, Ca_3N_2 or Sr_2N were reacted with H_2 in a comparable setup (heating in triplicate from 250-850°C with holding for 2 min at 850°C, see Section 8.3.3) to determine if the more reactive alkaline earth metal nitrides may yield more NH_3 than $Mn_6N_{2.58}$. Figure 8.8A shows an

initially nearly instantaneous formation of NH_3 at 550°C from reactants containing Ca_3N_2 (not observed in Section 8.4.6, Fig. 8.7) or Sr_2N respectively, followed by a slower evolution of NH_3.

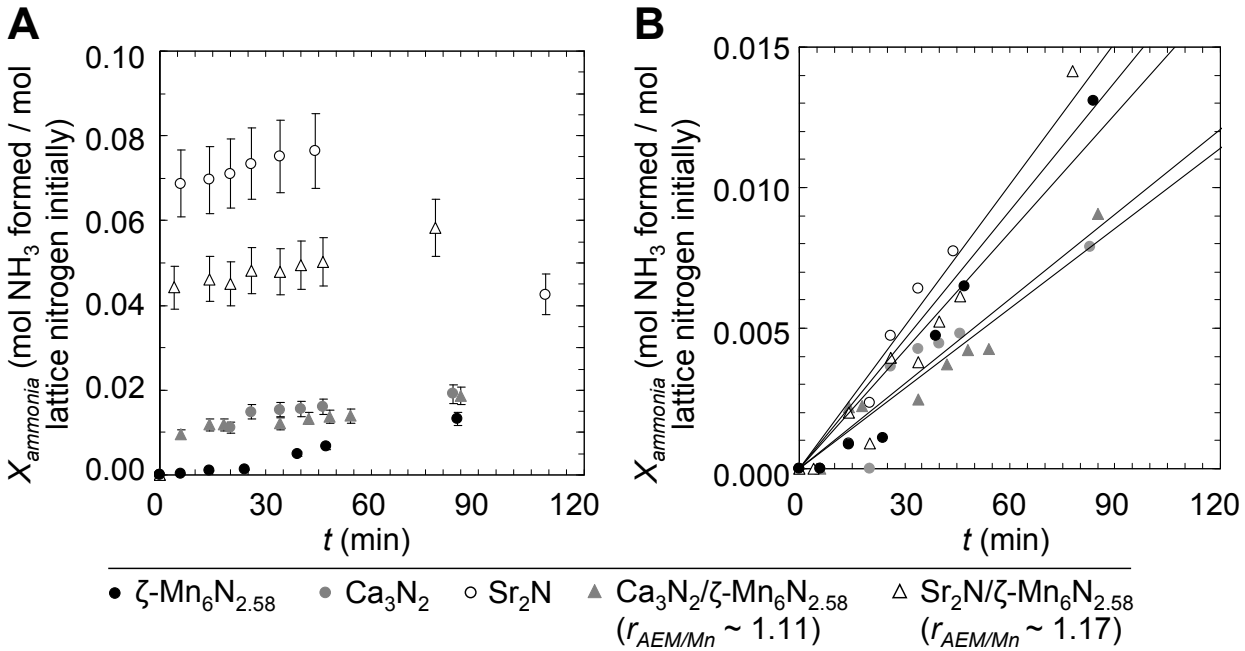

Figure 8.8 NH_3 from the nitrides of Ca, Mn, or Sr or their mixtures and H_2 near 0.1 MPa (see Section 8.3.3): A) computed as described in Section 8.4.1 (error bars are via error propagation in average ± 12.22%), B) such as A and subtracting the initial NH_3 yield (error bars omitted for clarity, solid lines are linear regressions with R^2 ranging from 0.89-0.94).

Analogous to Section 8.4.3, an exceptionally fast surface reaction of these nitrides with H_2 yielding NH_3 can be excluded (a nitride layer with a thickness > 10 unit cells would be required). Alternatively, an initial hydrolysis reaction forming NH_3 from traces adsorbed moist followed by the slower formation of NH_3 from H_2 appears more likely. Focusing on the reaction with H_2, Figure 8.8B shows the yield of NH_3 (Fig. 8.8A) with zeroing for the initial NH_3 yield near 550°C. The slopes of related linear regressions (R^2 = 0.89-0.94, Fig.8.8B) indicate relatively similar reaction rates of, e.g., 1.1 ± 0.1, 1.2 ± 0.2, or 2.1 ± 0.2 μmol NH_3 mol^{-1} metal s^{-1} for $Mn_6N_{2.58}$, Ca_3N_2 or Sr_2N respectively. The detection of NH_3 in the gas phase exiting the absorption vessel (0.49-2.2 ppm NH_3 mol^{-1} metal s^{-1}) supports the conclusion of comparable NH_3

formation kinetics (see Appendix G). Mixing the nitrides does not show a beneficial effect on the formation of NH_3. Thus, Figure 8.8 supports the idea (see Section 8.4.5) that the metal-nitrogen bond is not the major resistance to the NH_3 formation with the tested experimental conditions.

With regard on the materials choice for a prospective reactant, Figure 8.9 shows that Sr_2N (yielding SrH_2 hydride instead of the SrNH[65] imide) liberates a larger fraction lattice nitrogen than Ca_3N_2 (yielding Ca_2NH imide instead of the CaH_2 hydride) when reacted with H_2. Likely due to the undesirable formation of hydroxides, the nitrogen liberation is not reversible within the uncertainty of the detection assay.

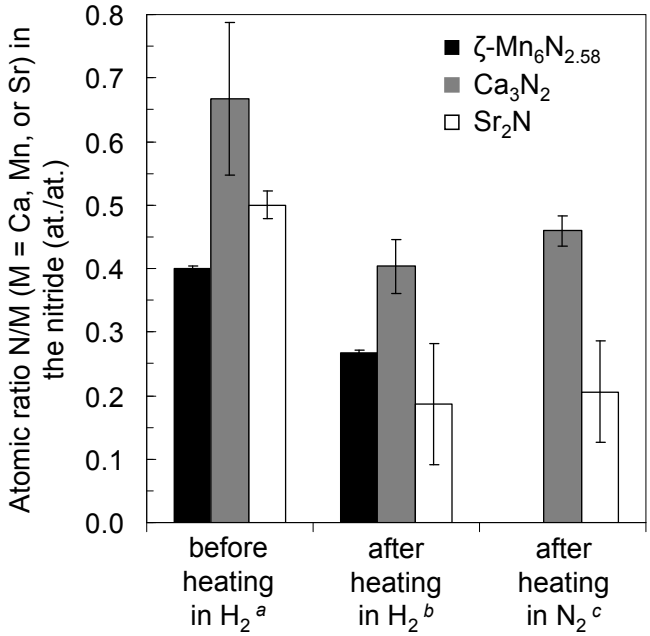

Figure 8.9 Nitrogen-content of metal nitrides (*a*) as-prepared (see Section 8.3.6), (*b*) after heating for about 90 min at 50-850°C in H_2 (compare Fig. 8.5 for manganese nitride), or (*c*) Ca_3N_2 or Sr_2N respectively after subsequent heating for 120 min at 750°C in N_2. Error propagation within a 95% confidence interval (error bars) yields in average ± 16.30%.

In summary, due to comparable NH_3 yields and the relative resistance of manganese nitride to oxidation, a high-specific surface area $Mn_6N_{2.58}$-based material may be a good choice for designing a prospective reactant for a solar thermochemical NH_3 synthesis from N_2 and H_2.

8.4.8 Gibbs free energy of mixing as a guide for future reactant development

To compare the energy required for separating NH_3 from an (ideal) $NH_3/N_2/H_2$ gas mixture, E_{sep} in GJ (lower heating value) t^{-1} NH_3, to the compression energy required for the conventional NH_3 synthesis (Fig. 8.10), E_{sep} can be estimated from the molar Gibbs free energy of mixing[68], $\Delta_{mix}g$ in J mol^{-1}:

$$(8.7) \qquad E_{sep} = \frac{1}{n_{NH_3} M_{NH_3}} \frac{\Delta_{mix} g}{\eta_C \eta_{sep}} \sum_i n_i = \frac{RT}{n_{NH_3} M_{NH_3} \eta_C \eta_{sep}} \sum_i n_i \sum_i x_i \ln x_i$$

where x_i is the mol fraction of i = NH_3, H_2, or N_2, R is the gas constant in kJ mol^{-1} K^{-1}, T is the gas temperature in K, and η_C or η_{sep} are the efficiency of generating mechanical energy with a coal-fired power plant (assumed at 35%) or the efficiency of the employed separation device (assumed at 50%) respectively. In practice, heat integration of the absorbed solar energy may provide the driving force for the required gas separation.

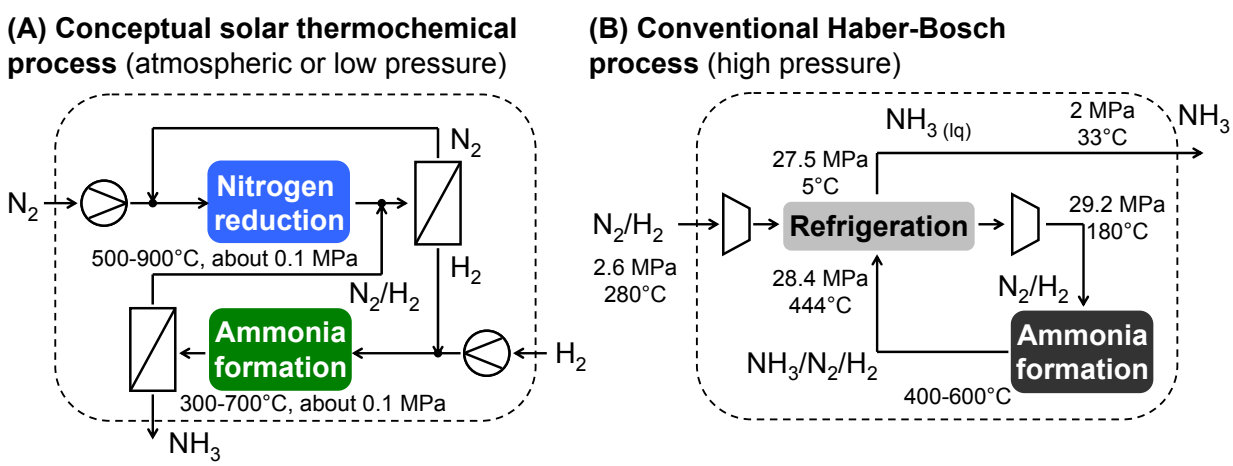

Figure 8.10 Simplified process schematics of (A) a conceptual solar thermochemical NH_3 synthesis (both reaction chambers are cycled between nitrogen fixation and NH_3 formation) and (B) the conventional NH_3 synthesis via heterogeneous catalysis.

From the reported experimental data (gas mixtures at 700°C, 0.19-0.47 $L_{(STP)}$ H_2 min^{-1} gas compositions from Sections 8.4.2, 8.4.4, or 8.4.6 respectively) E_{sep} can be estimated with 48-

76 GJ t^{-1} NH_3. This is prohibitively above the compression energy consumed by the Haber-Bosch process, i.e., about 5.5 GJ (lower heating value) t^{-1} NH_3[1].

As a guide for the development of a perhaps manganese-based high-specific surface area reactant, the separation of the N_2/H_2 gas mixture generated when regenerating the nitride reactant may be significantly easier since this step does not require product removal (i.e., small gas volumes that may require separation) and the fraction of H_2 may be negligible if no hydride is formed (e.g., during a conceivable $Mn_6N_{2.58}/Mn_4N$ reaction cycle). Thus, assuming an acceptable NH_3 separation energy of 4-5 GJ t^{-1} NH_3 and separation of an NH_3/H_2 gas mixture at 120°C estimates the required NH_3 gas concentration with 2.8-6.8 mol%. This is, as intended, below the NH_3 gas phase concentration of the conventional technology (e.g., 23.9 mol%, Aspen Plus Ammonia Model) and about five orders of magnitude above the values reported in this work. Paths to perhaps achieve this in the future include rational materials design, optimized physical presentation of the reactant, and use of reactors that ensure a sufficient supply of H_2 and removal of NH_3.

8.5 Conclusions

To produce ammonia at atmospheric pressure with a solar thermochemical reaction cycle that does not require a chemical reducing agent (such as solid coal or solid or gasified biomass), the reactions of some binary metal nitrides formed by manganese, calcium, or strontium respectively with H_2 were studied in this work.

The presented experimentation intended a relative comparison of the NH_3 formation from metal nitrides with different bonding character to outline reaction conditions that may facilitate the proposed concept. Absolute NH_3 yields may change significantly if the physical presentation of the reactant is altered.

$Mn_6N_{2.58}$ powder reacted at 700°C for 60 min with 0.5 ± 0.1 $L_{(STP)}$ H_2 min^{-1} yielded approximately 9 ± 8 mol% of the lattice nitrogen with 85% NH_3 liberated at a rate of 9 ± 1 μmol NH_3 mol^{-1} Mn s^{-1}. The slow bulk reaction yielded Mn_4N with a high activation energy (relative to hydrolysis reactions) of about 98 ± 7 kJ mol^{-1} and progressed after 60 min approximately 40-507 nm below the $Mn_6N_{2.58}$ particle surface. Presumably, the diffusion of H_2 in the gas phase boundary layer covering the reacting particle or the adsorptive cleavage of H_2 limit the NH_3 formation kinetics. The reactions of Ca_3N_2 or Sr_2N with H_2 resulted in formation of Ca_2NH or SrH_2 respectively and yielded NH_3 with formation rates comparable to those found for $Mn_6N_{2.58}$ (1.1-2.1 μmol NH_3 mol^{-1} metal s^{-1} when heating from 250-850°C with holding for 2 min at 850°C). Given the experimental setup, the metal-nitrogen bond does not appear to be the major resistance to the NH_3 formation.

Based on Gibbs free energy of mixing computations, aiming for NH_3 gas phase concentrations near 2.8-6.8 mol% will require the development of an exceptionally high-specific surface area reactant and perhaps the use of high local gas velocities to yield the lattice nitrogen of the nitride as NH_3. $Mn_6N_{2.58}$ may be a good material choice for future reactant development.

8.6 Associated content in Appendix G

Supporting Information: XRD analysis of manganese nitride ("Mn_4N", see Section 8.3.6) reacted at different temperatures with H_2, NH_3 yield from manganese nitride ("Mn_4N", see Section 8.3.6) with or without Fe- or Ni-doping and H_2, and detection of NH_3 in the gas phase leaving the absorption vessel for reaction cycles with $Mn_6N_{2.58}$, Ca_3N_2 or Sr_2N respectively (see Section 8.3.3).

8.7 References

[1] I. Rafiqul, C. Weber, B. Lehmann, A. Voss, Energy efficiency improvements in ammonia production - perspectives and uncertainties, Energy, 30 (2005) 2487-2504.

[2] V. Smil, Detonator of the population explosion, Nature, 400 (1999) 415-415.

[3] How to Feed the World in 2050, Report of the Food and Agriculture Organization of the United Nations (FAO), Available online at: http://www.fao.org/fileadmin/templates/wsfs-/docs/expert_paper/How_to_Feed_the_World_in_2050.pdf (retrieved April 2, 2012).

[4] R. Schnepf, B.D. Yacobucci, Renewable Fuel Standard (RFS): Overview and issues, Congressional Research Service, (2010).

[5] F.H. Stephens, V. Pons, R.T. Baker, Ammonia - borane: the hydrogen source par excellence?, Dalton Transactions, (2007) 2613-2626.

[6] C.W. Hamilton, R.T. Baker, A. Staubitz, I. Manners, B-N compounds for chemical hydrogen storage, Chemical Society Reviews, 38 (2009) 279-293.

[7] A.J. Churchard, E. Banach, A. Borgschulte, R. Caputo, J.-C. Chen, D.C. Clary, K.J. Fijalkowski, H. Geerlings, R.V. Genova, W. Grochala, T. Jaroń, J.C. Juanes-Marcos, B. Kasemo, G.-J. Kroes, I. Ljubić, N. Naujoks, J.K. Nørskov, R.A. Olsen, F. Pendolino, A. Remhof, L. Románszki, A. Tekin, T. Vegge, M. Zäch, A. Züttel, A multifaceted approach to hydrogen storage, Physical Chemistry Chemical Physics, 13 (2011) 16955-16972.

[8] C.H. Christensen, T. Johannessen, R.Z. Sørensen, J.K. Nørskov, Towards an ammonia-mediated hydrogen economy?, Catalysis Today, 111 (2006) 140-144.

[9] G. Thomas, G. Parks, Potential roles of ammonia in a hydrogen economy, a study of issues related to the use ammonia for on-board vehicular hydrogen storage, U.S. Department of Energy (2006), Available online at: http://www.hydrogen.energy.gov-/pdfs/nh3_paper.pdf (retrieved December, 2011).

[10] J. Brandhorst, Henry, M. Baltazar-Lopez, B. Tatarchuk, D.R. Cahela, T. Barron, Ammonia – It's transformation and effective utilization, 6th International Energy Conversion Engineering Conference (IECEC), 28 - 30 July 2008, Cleveland, Ohio, (2008) AIAA 2008-5610.

[11] F. Vitse, M. Cooper, G.G. Botte, On the use of ammonia electrolysis for hydrogen production (vol 142, pg 18, 2005), Journal of Power Sources, 152 (2005) 311-312.

[12] A.J. Reiter, S.-C. Kong, Demonstration of compression-ignition engine combustion using ammonia in reducing greenhouse gas emissions, Energy & Fuels, 22 (2008) 2963-2971.

[13] A.J. Reiter, S.C. Kong, Combustion and emissions characteristics of compression-ignition engine using dual ammonia-diesel fuel, Fuel, 90 (2011) 87-97.

[14] P.L. Louis, Feedstock and energy sources for ammonia production, International Fertilizer Industry Association, with some assistance from CEDIGAZ, France, Available online at: www.fertilizer.org/ifacontent/download/5571/88112/.../1/.../76.pdf (retrieved April 2, 2012).

[15] A. Hellman, E.J. Baerends, M. Biczysko, T. Bligaard, C.H. Christensen, D.C. Clary, S. Dahl, R. van Harrevelt, K. Honkala, H. Jonsson, G.J. Kroes, M. Luppi, U. Manthe, J.K. Nørskov, R.A. Olsen, J. Rossmeisl, E. Skúlason, C.S. Tautermann, A.J.C. Varandas, J.K. Vincent, Predicting catalysis: Understanding ammonia synthesis from first-principles calculations, Journal of Physical Chemistry B, 110 (2006) 17719-17735.

[16] G. Ertl, Reactions at surfaces: From atoms to complexity (Nobel lecture), Angewandte Chemie-International Edition, 47 (2008) 3524-3535.

[17] G. Ertl, Heterogeneous catalysis on the atomic scale, Chemical Record, 1 (2001) 33-45.

[18] Z. Kirova-Yordanova, Exergy analysis of industrial ammonia synthesis, Energy, 29 (2004) 2373-2384.

[19] S.K. Ritter, The Haber-Bosch reaction: An early chemical impact on sustainability, Chemical & Engineering News, 86 (2008) 53.

[20] W.-Y. Huang, Impact of rising natural gas prices on U.S. ammonia supply / WRS-0702 / A report from the Economic Research Service, in, 2007.

[21] L.C. Skinner, H.R. Batchelder, S. Katell, Comparative cost study of ammonia plants - using either natural gas or coal gasification as a source of synthesis gas, Industrial and Engineering Chemistry, 44 (1952) 2381-2385.

[22] J.J.H. Pijpers, M.T. Winkler, Y. Surendranath, T. Buonassisi, D.G. Nocera, Light-induced water oxidation at silicon electrodes functionalized with a cobalt oxygen-evolving catalyst, Proceedings of the National Academy of Sciences of the United States of America, 108 (2011) 10056-10061.

[23] O. Khaselev, J.A. Turner, A monolithic photovoltaic-photoelectrochemical device for hydrogen production via water splitting, Science, 280 (1998) 425-427.

[24] M. Grätzel, Mesoscopic solar cells for electricity and hydrogen production from sunlight, Chemistry Letters, 34 (2005) 8-13.

[25] J.R. Scheffe, J.H. Li, A.W. Weimer, A spinel ferrite/hercynite water-splitting redox cycle, International Journal of Hydrogen Energy, 35 (2010) 3333-3340.

[26] W.C. Chueh, C. Falter, M. Abbott, D. Scipio, P. Furler, S.M. Haile, A. Steinfeld, High-flux solar-driven thermochemical dissociation of CO_2 and H_2O using nonstoichiometric ceria, Science, 330 (2010) 1797-1801.

[27] J.E. Miller, M.D. Allendorf, R.B. Diver, L.R. Evans, N.P. Siegel, J.N. Stuecker, Metal oxide composites and structures for ultra-high temperature solar thermochemical cycles, Journal of Materials Science, 43 (2008) 4714-4728.

[28] A. Stamatiou, P.G. Loutzenhiser, A. Steinfeld, Solar Syngas Production from H_2O and CO_2 via Two-Step Thermochemical Cycles Based on Zn/ZnO and FeO/Fe_3O_4 Redox Reactions: Kinetic Analysis, Energy & Fuels, 24 (2010) 2716-2722.

[29] M.D. Fryzuk, Side-on end-on bound dinitrogen: An activated bonding mode that facilitates functionalizing molecular nitrogen, Accounts of Chemical Research, 42 (2009) 127-133.

[30] E. Skúlason, T. Bligaard, S. Gudmundsdóttir, F. Studt, J. Rossmeisl, F. Abild-Pedersen, T. Vegge, H. Jónsson, J.K. Nørskov, A theoretical evaluation of possible transition metal electro-catalysts for N_2 reduction, Physical Chemistry Chemical Physics, 14 (2012) 1235-1245.

[31] I. Valov, B. Luerssen, E. Mutoro, L. Gregoratti, R.A. De Souza, T. Bredow, S. Günther, A. Barinov, P. Dudin, M. Martin, J. Janek, Electrochemical activation of molecular nitrogen at the Ir/YSZ interface, Physical Chemistry Chemical Physics, 13 (2011) 3394-3410.

[32] D.-K. Lee, C.C. Fischer, I. Valov, J. Reinacher, A. Stork, M. Lerch, J. Janek, An EMF cell with a nitrogen solid electrolyte-on the transference of nitrogen ions in yttria-stabilized zirconia, Physical Chemistry Chemical Physics, 13 (2011) 1239-1242.

[33] M. Lerch, J. Janek, K.D. Becker, S. Berendts, H. Boysen, T. Bredow, R. Dronskowski, S.G. Ebbinghaus, M. Kilo, M.W. Lumey, M. Martin, C. Reimann, E. Schweda, I. Valov, H.D. Wiemhöfer, Oxide nitrides: From oxides to solids with mobile nitrogen ions, Progress in Solid State Chemistry, 37 (2009) 81-131.

[34] V. Kordali, G. Kyriacou, C. Lambrou, Electrochemical synthesis of ammonia at atmospheric pressure and low temperature in a solid polymer electrolyte cell, Chemical Communications, (2000) 1673-1674.

[35] I.A. Amar, R. Lan, C.T.G. Petit, S. Tao, Solid-state electrochemical synthesis of ammonia: a review, Journal of Solid State Electrochemistry, 15 (2011) 1845-1860.

[36] M.E. Gálvez, M. Halmann, A. Steinfeld, Ammonia production via a two-step Al_2O_3/AlN thermochemical cycle. 1. Thermodynamic, environmental, and economic analyses, Industrial & Engineering Chemistry Research, 46 (2007) 2042-2046.

[37] M.E. Gálvez, A. Frei, M. Halmann, A. Steinfeld, Ammonia production via a two-step Al_2O_3/AlN thermochemical cycle. 2. Kinetic analysis, Industrial & Engineering Chemistry Research, 46 (2007) 2047-2053.

[38] R. Michalsky, P.H. Pfromm, Thermodynamics of metal reactants for ammonia synthesis from steam, nitrogen and biomass at atmospheric pressure, AIChE Journal, http://onlinelibrary.wiley.com/doi/10.1002/aic.13717/pdf, (in press).

[39] R. Michalsky, P.H. Pfromm, Solar fuel production via decoupled dinitrogen reduction and protonation of mobile nitrogen ions to ammonia, The Journal of Physical Chemistry C, (in preparation).

[40] M.M. Rodriguez, E. Bill, W.W. Brennessel, P.L. Holland, N_2 reduction and hydrogenation to ammonia by a molecular iron-potassium complex, Science, 334 (2011) 780-783.

[41] D.J. Knobloch, E. Lobkovsky, P.J. Chirik, Dinitrogen cleavage and functionalization by carbon monoxide promoted by a hafnium complex, Nature Chemistry, 2 (2010) 30-35.

[42] J.D. Gilbertson, N.K. Szymczak, D.R. Tyler, Reduction of N2 to ammonia and hydrazine utilizing H2 as the reductant, Journal of the American Chemical Society, 127 (2005) 10184-10185.

[43] R.B. Yelle, J.L. Crossland, N.K. Szymczak, D.R. Tyler, Theoretical studies of N_2 reduction to ammonia in $Fe(dmpe)_2N_2$, Inorganic Chemistry, 48 (2009) 861-871.

[44] A. Steinfeld, A.W. Weimer, Thermochemical production of fuels with concentrated solar energy, Optics Express, 18 (2010) A100-A111.

[45] T. Kodama, High-temperature solar chemistry for converting solar heat to chemical fuels, Progress in Energy and Combustion Science, 29 (2003) 567-597.

[46] R. Perret, Solar thermochemical hydrogen production research (STCH), Thermochemical cycle selection and investment priority, Sandia report SAND2011-3622, Sandia National Laboratories, (2011).

[47] M.E. Gálvez, I. Hischier, A. Frei, A. Steinfeld, Ammonia production via a two-step Al_2O_3/AlN thermochemical cycle. 3. Influence of the carbon reducing agent and cyclability, Industrial & Engineering Chemistry Research, 47 (2008) 2231-2237.

[48] R. Michalsky, P.H. Pfromm, Chromium as reactant for solar thermochemical synthesis of ammonia from steam, nitrogen, and biomass at atmospheric pressure, Solar Energy, 85 (2011) 2642-2654.

[49] F. Haber, G. van Oordt, Über die Bildung von Ammoniak aus den Elementen, Zeitschrift für anorganische Chemie, 44 (1905) 341-378.

[50] R. Chemnitzer, G. Auffermann, D.M. Többens, R. Kniep, $(Sr_2N)H$: On the redox-intercalation of hydrogen into Sr_2N, Zeitschrift Fur Anorganische Und Allgemeine Chemie, 631 (2005) 1813-1817.

[51] P. Mars, D.W. van Krevelen, Oxidations carried out by means of vanadium oxide catalysts, Special Supplement to Chemical Engineering Science, 3 (1954) 41-59.

[52] I. Barin, O. Knacke, Thermochemical properties of inorganic substances, Springer-Verlag, Berlin Heidelberg New York, 1973.

[53] I. Barin, O. Knacke, O. Kubaschewski, Thermochemical properties of inorganic substances, Supplement, Springer-Verlag, Berlin Heidelberg New York, 1977.

[54] R. Michalsky, P.H. Pfromm, Dinitrogen reduction near ambient pressure using solar energy and molybdenum or manganese nitride-based redox reactions, Journal of Solid State Chemistry, (in preparation).

[55] D. McKay, J.S.J. Hargreaves, J.L. Rico, J.L. Rivera, X.L. Sun, The influence of phase and morphology of molybdenum nitrides on ammonia synthesis activity and reduction characteristics, Journal of Solid State Chemistry, 181 (2008) 325-333.

[56] A.G. Cairns, J.G. Gallagher, J.S.J. Hargreaves, D. McKay, E. Morrison, J.L. Rico, K. Wilson, The influence of precursor source and thermal parameters upon the formation of beta-phase molybdenum nitride, Journal of Alloys and Compounds, 479 (2009) 851-854.

[57] R.M. de Vos, H. Verweij, High-selectivity, high-flux silica membranes for gas separation, Science, 279 (1998) 1710-1711.

[58] T. Glück, Mechanisms of nitriding electrolytic manganese metal, Chemical Engineering Journal and the Biochemical Engineering Journal, 54 (1994) 167-173.

[59] A. Leineweber, R. Niewa, H. Jacobs, W. Kockelmann, The manganese nitrides eta-Mn_3N_2 and theta-Mn_6N_{5+x}: nuclear and magnetic structures, Journal of Materials Chemistry, 10 (2000) 2827-2834.

[60] C. Qiu, A.F. Guillermet, Predicative approach to the entropy of manganese nitrides and calculation of the Mn-N phase-diagram, Zeitschrift für Metallkunde, 84 (1993) 11-22.

[61] P. Höhn, S. Hoffmann, J. Hunger, S. Leoni, F. Nitsche, W. Schnelle, R. Kniep, beta-Ca_3N_2, a metastable nitride in the system Ca-N, Chemistry-a European Journal, 15 (2009) 3419-3425.

[62] O. Levenspiel, Chemical reaction engineering, Third Edition, Chapter 25 Fluid-particle reactions: Kinetics, John Wiley & Sons, New York, 1999.

[63] M. Nasr Eddine, E.F. Bertaut, Structure cristallographique de $Mn2N_{0,86}$, Acta Cryst., B33 (1977) 2696-2698.

[64] R. Juza, K. Deneke, H. Puff, Ferrimagnetismus der Mischkristalle von Mn_4N mit Chrom, Eisen und Nickel, Zeitschrift Fur Elektrochemie, 63 (1959) 551-557.

[65] D.H. Gregory, Nitride chemistry of the s-block elements, Coordination Chemistry Reviews, 215 (2001) 301-345.

[66] I. Valov, V. Rührup, R. Klein, T.C. Rödel, A. Stork, S. Berendts, M. Dogan, H.D. Wiemhöfer, M. Lerch, J. Janek, Ionic and electronic conductivity of nitrogen-doped YSZ single crystals, Solid State Ionics, 180 (2009) 1463-1470.

[67] D.R. Glasson, S.A.A. Jayaweera, Formation and reactivity of nitrides .2. Calcium and magnesium nitrides and calcium cyanamide, Journal of Applied Chemistry of the USSR, 18 (1968) 77-83.

[68] J.M. Prausnitz, R.N. Lichtenthaler, E. Gomes de Azevedo, Molecular thermodynamics of fluid-phase equilibria, Prentice Hall PTR, Upper Saddle River, NJ, 1999.

Chapter 9 - Conclusions and Outlook

9.1 Conclusions

9.1.1 Confirming the hypothesized utility of transition metal nitride reactants

Determining the feasibility of a solar thermochemical ammonia synthesis near ambient pressure, below 1500°C, without a solid carbonaceous reducing agent, and without a fossil hydrogen source (see Sections 1.3.1 and 1.3.2), the present work confirms the transition metal nitride-based synthesis hypothesized in Section 1.3.2.

Generally, the proposed process is technically feasible with a molybdenum or manganese reactant. Prospective materials design needs to ensure elimination of significant mass transport limitations found here for molybdenum-based reactants. Optimization of manganese-based reactants will require addressing the relative low conversion of the nitrogen liberated from the nitride to ammonia. The provided process analyses demonstrated economic competitiveness of the solar thermochemical ammonia synthesis with transition metals. The conditions for molybdenum- (employing CO or H_2, that is, e.g., gasified biomass as reducing agent) or manganese-based (using methane as reducing agent, but not as hydrogen source) ammonia synthesis have been outlined. Sections 9.1.2 to 9.1.5 summarize the major conclusions of this work.

9.1.2 Feasibility studies for proposed transition metal reactants

Free energy computations were utilized to screen for metals that may enable an accord of conflicting thermochemical properties. Theoretical ratios of the heating value of the generated solar fuel (NH_3 and syngas) to the supplied solar and chemical energy in the range of 52-85% were estimated. Guided by this analysis the presented effort focused on d^3 to d^5 metal reactants

and assessed experimentally chromium, manganese, molybdenum and magnesium chromite or ferrite respectively for their utility to conduct the contemplated reaction cycle.

Feasibility studies with chromium confirmed the expectedly simplified transition metal oxide (TMO) reduction. Cr_2O_3 was converted to the metal employing simulated gasified biomass and solar radiation concentrated with a Fresnel lens to above 1200°C. After 40 min heating at 1600°C a maximum reduction yield near the surface of the particles of approximately 82.85 mol% was obtained at a rate of 2.7 x 10^{-3} mol Cr mol^{-1} Cr_2O_3 min^{-1}. The feasibility to reduce other TMO's of interest (such as MnO or MoO_2) was supported with thermochemical equilibrium computations.

Similarly, N_2 reduction with Cr, Mn, and Mo approached equilibrium conversions with most promising results for Cr and Mn reactants (e.g., 85 ± 4 mol% of Cr_2N after 5.6 min and 75-85 mol% Mn_4N after 10-30 min). The formation of transition metal nitrides (TMN) with a favorably high lattice nitrogen concentrations, however, revealed partly (see, e.g., Mo_2N in Section 9.1.3) crucial mass transport limitations.

Most importantly, these preliminary studies identified the Achilles' heel of the hypothesized transition metal reactants: Many TMN's are either highly resistant to corrosion, i.e., they do not liberate the lattice nitrogen readily, or the liberated nitrogen does not form ammonia efficiently. This central aspect will be revisited in Section 9.1.4.

Many fields have demonstrated[1-4] and partly rationalized[5, 6] the possibility of developing a mixed reactive material that exhibits the desirable properties of its single metallic constituents. The speculated concert of efficient NH_3 formation and mild TMO reduction conductions with double oxide reactants (i.e., MgM_2O_4 spinel with M = Cr, Fe) could not be supported experimentally. Although the presence of the transition metal apparently alleviated the reduction

of Mg^{2+} - leading to the removal of in average 43 ± 26 at% Mg from the solid presumably in form of a Mg^0 vapor, relative to 0.5 ± 1.6 at% Mg in absence of the transition metal when heating in the presence of graphite and a N_2 gas flow for 240 min at 1200°C - reduction of N_2 with Mg could not be confirmed.

Therefore, the here documented work focused primarily on characterizing the N_2 reduction and NH_3 formation with binary TMN's.

9.1.3 Reaction cycle kinetics limited by mass transport

Shrinking-core models were utilized throughout this work to describe collected kinetic data and to identify reaction limitations. With regard on the d^3 to d^5 TMN/TMO's of interest, diffusion limitations in the solid state were evidenced for all three major reaction steps.

The implications are twofold:

First, prospective design and testing of an optimized reactant for the solar thermochemical NH_3 synthesis needs to provide and maintain sufficient specific surface area for the single reactions to be conducted over many cycles (see Section 9.2.2.1). However, experimentation with H_2 as hydrogen source - with the potential of avoiding the difficulties of an oxide reduction step - indicate that solely increased surface area may not assure the desired reaction yields and kinetics in any case. Assuming an NH_3 yield from manganese nitride and H_2 proportional to the surface area over volume ratio of a spherical nitride particle correlates the desired 2.8-6.8 mol% NH_3 in the gas phase to nitride particles in the impractical order of 1 nm in diameter.

Thus, secondly, the choice of the reactant may be similarly important as a thorough physical presentation of the reactive material. This could be demonstrated by N_2 reduction studies with Mn or Mo metal respectively (the apparent nitrogen diffusion constant at 750°C for

the desirably nitrogen-rich $Mn_6N_{2.58}$ was estimated with $8 \pm 4 \times 10^{-9}$ cm^2 s^{-1} versus undesirably low $3 \pm 2 \times 10^{-11}$ cm^2 s^{-1} for Mo_2N).

9.1.4 Average lattice nitrogen charge controlling ammonia formation

With regard on the 60 min steam hydrolysis at 500°C, 2 ± 5 (Cr_2N/CrN), 23 ± 3 (Mo_2N), or 89 ± 1 (Mn_4N/$Mn_6N_{2.58}$) mol% lattice nitrogen was liberated from the targeted TMN's. From the liberated nitrogen 1 ± 3 (Cr_2N/CrN), 60 ± 8 (Mo_2N), or 2.9 ± 0.2 (Mn_4N/$Mn_6N_{2.58}$) mol% could be recovered as NH_3. These yields are, on one hand, significantly below the yields obtained from the undesirably exothermic hydrolysis of ionic metal nitrides. On the other hand, these experiments outline significant differences: the nitrides of Cr (and to some extend Mo) are relatively resistant to corrosion and yield NH_3 only if the lattice nitrogen carries a relative high electric charge (Mo). The nitrides of the relative electropositive Mn are expected to be less corrosion resistant, as observed, but do not yield NH_3 effectively. That is, NH_3 is either not formed from the liberated lattice nitrogen or it is formed but not removed efficiently from the oxide surface. Economic conversion of the liberated lattice nitrogen to ammonia requires further studies.

The hydrolysis of the less ionic nitrides tested appears to be limited by diffusion of reaction participants through the oxide layer covering the nitride. The apparent diffusion constants estimated from the hydrolysis experiments with AlN, Cr_2N/CrN, Mn_4N/Mn_2N, Zn_3N_2, or Mo_2N powders were correlated with the nitride ionicity - a measure of the average charge of the lattice nitrogen. This suggests an NH_3 formation mechanism governed by the volumetric concentration of active nitrogen ions or their vacancies respectively. Employing the nitride ionicity for the development of an atomic scale understanding of the reaction mechanism in the future may be useful when designing an optimized prospective reactant and reactant surface.

The evidenced correlation of the apparent nitrogen diffusion constant with the interstitial volume of the nitride lattice support the central role of the nitrogen charge (affecting atomic radii and crystal configuration) of the proposed NH_3 synthesis and sustain the potential utility of a manganese-based reactant given its relative fast diffusion characteristics (see Section 9.1.3).

9.1.5 Process economics

From these studies, Mo_2N appeared as the most promising TMN for the pursued purpose. Therefore Mo was employed for a mass and energy balance-based process analysis[7-9] intended to identify process and market conditions that may allow for economic competitiveness of the proposed process and the current high-pressure NH_3 synthesis from fossil resources.

Maximum energy efficiencies of converting solar radiation to the lower heating value of NH_3 estimated with 23-30% locate the solar thermochemical NH_3 production between the industrial NH_3 synthesis with coal at the lower end and natural gas at the high end. Indirect fossil CO_2 generation (from coal-derived grid-electricity) was in the range of 4-50% of the CO_2 emitted by the current industrial NH_3 synthesis. The collaboratively conducted net-present value analysis suggests economic feasibility of the proposed process even under fairly conservative assumptions at 534 ± 28 dollars t^{-1} NH_3. That is relative close to the current market price of anhydrous ammonia, dependent on the natural gas price and the demand of NH_3. The proposed technology may contribute to a prospectively increased global ammonia production capacity with particular regard on countries with less developed infrastructure and a limited availability of fossil resources[10].

The necessity to generate the H_2 reducing agent from H_2O (in the presented process analyses via an adjunct solar thermochemical H_2O splitting process that itself has not yet entered the market) absorbed approximately 74-86% of the heliostat capital investment. Due to the

related uncertainty of the model, future process simulation efforts may augment the clarity and certainty of the simulation predictions from treating both processes (in geographical vicinity) separately. See also Section 9.2.2.2.

Furthermore, the analysis suggests optimum NH_3 production economics near 900 t NH_3 day^{-1} plant capacity, i.e., when the difference of H_2 production and consumption at the given plant configuration is minimized. This reinforces the need to treat both processes separately and demonstrates the insensitivity of the model to account yet for non-linear economies of scale.

9.2 Outlook

9.2.1 Prospective transition metal nitride reactants

Fortified by the conclusions of this work, prospective materials and process design may enable the development of a transition metal-based solar thermochemical NH_3 synthesis at relative moderate process conditions - as a viable alterative to the current industrial implementation of the Haber-Bosch process. Manganese and molybdenum were identified here as promising reactants. Therefore, future efforts should focus on two questions:

First, what are the actual reaction rates and yields that can be achieved with Mn- or Mo-based reactants when presenting them to the gaseous reactants in a reaction environment that minimizes mass transfer limitations? This addresses the physical presentation of the reactive material as well as the layout of the reaction chamber.

Second, is it feasible to alleviate the specific reaction limitations for Mn (limited conversion of the liberated nitrogen to ammonia) or Mo (limited fixation of nitrogen) via materials design? Optimized ternary transition metal nitrides reactants could be based on Mn and a secondary metal that helps increasing the yield of NH_3 from the liberated lattice nitrogen. The secondary metal choice would have to be based on the origin of the low NH_3 yield (NH_3 is either

not formed effectively or NH_3 is formed but not removed quickly enough from the materials surface, see Section 5.5.4). Alternatively, metals that fix nitrogen readily (e.g., Cr) may be employed to develop a ternary Mo-based nitride reactant (see Section 6.4.2) with optimized nitrogen fixation properties.

The following outlines a few major steps that should further the transition metal-based reactive synthesis of ammonia (Fig. 9.1).

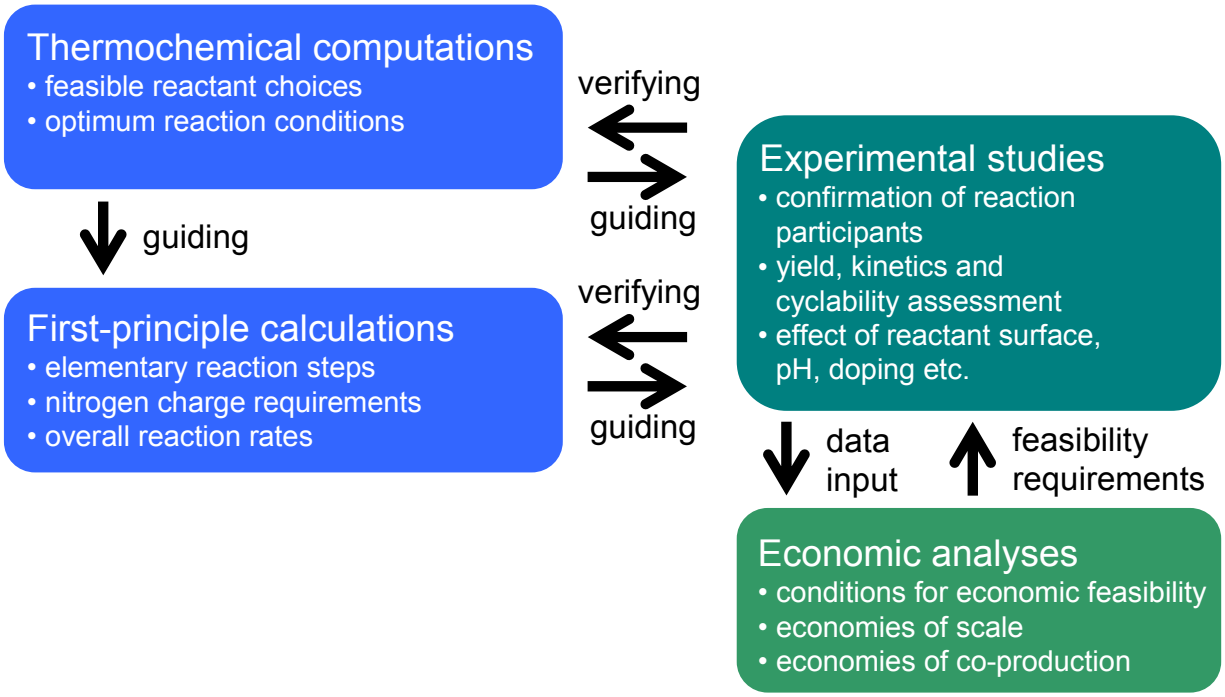

Figure 9.1 Conceptual sections of future work towards solar thermochemical ammonia.

9.2.2 Ammonia from lattice nitrogen and water

9.2.2.1 Rational reactant design

Given the promising performance of the suboptimal prepared and presented molybdenum nitride reactant and given the relative rapid diffusion and liberation of lattice nitrogen from manganese nitride, these two transition metals should be focused in prospective efforts towards a

TMN/TMO-based solar thermochemical NH_3 synthesis. Given its electronic similarities, tungsten may be included in future work.

The intriguing effect of the nitrogen charge on the reaction kinetics and reaction equilibria suggest the utility of first-principle computations for a better understanding of the relevant elementary reaction steps and as a tool for the search for optimized reactive materials. Future tasks could be:

Theoretical studies

- Use of density function theory (DFT) to determine the lowest-energy pathway identified as the process sequence with the lowest free energy change between any two reaction steps[11, 12]. Possibly, the grid-based projector-augmented wave method (GPAW) electronic structure code[13] may be a good starting point due to the elimination of core electrons. This allows for efficient calculations of the transition metals and 2nd row elements such as oxygen and nitrogen without the need to normalize the wave functions of the remaining valence electrons. The python-based electronic structure code is open-source[14] and may be utilized most easily with the Atomic Simulation Environment (ASE) which is available online as well[15].
- The nitride ionicity may guide these DFT calculations to account for the statistic nature of the electron transfer from metal atoms to the lattice nitrogen. This may allow for predicting the existence of intermediate nitrogen oxidation states or nitrogen containing species other than N^{3-} and N^0 (dependent on their potential energies) and may outline charge transfer requirements for the ammonia formation from lattice nitrogen and some hydrogen-containing chemical species.

- Overall reaction rates may then be estimated when coupling the required transport equations (concentration, temperature and electric potential gradients to account for reaction barriers) with the DFT computations[12, 16].

Experimental studies

Experimental studies to confirm such simulations and to provide optimized kinetic data for a detailed process analysis (see Section 9.2.2.2) may include the assessment of:

- The diffusing nitrogen species, e.g., via nitrogen-isotope marking (to trace the origin of depleted nitrogen in the solid using ^{15}N and sensitive high-resolution ion microprobe or secondary-ion mass spectroscopic analysis or ^{13}N and quantification of the γ-decay) and X-ray photoelectron spectroscopy (to determine the oxidation state of nitrogen).
- Yield, kinetics, and cyclability of the N_2 reduction and hydrogenation reactions with optimized Mn, Mo, and/or W-based reactive materials. The metals may be deposited on an inert, temperature shock-resistant and high specific surface area substrate (e.g., SiO_2, Al_2O_3, ZrO_2, or yttria-stabilized zirconia) via chemical vapor or atomic layer deposition (Mo and W potentially as oxides or halides with subsequent H_2 treatment)[17]. These studies should address a conceivably decreased performance of the reactant due to formation of spinel-like material at elevated temperatures[1].
- Furthermore, TMO vapor formation (perhaps including the effect of temperature and gas flow rates on the vapor pressure of the oxides of Mo or W respectively and the formation of Mn metal vapor) and the pH at the reactant surface (with expected effects on the corrosion potential of the hydrolysis reaction and the adsorption of reaction products from the oxide) should be assessed.

- Finally, elimination of the transport limitations reported in this work may allow for studying the possible control of bonding properties by reactant doping[18].

9.2.2.2 Economic analyses

Based on the conclusions from studies similar to those outlined in Section 9.2.2.1, next-level economic analyses of a promising reactant may benefit from:

- Use of actual kinetic data, rational reactor design and consideration of actual heliostat array configurations (perhaps in collaboration with mechanical engineers) to ensure simulation results are feasible and realistic.
- Incorporation of non-linear effects of scale: An ammonia producing facility of any production capacity will require, besides the reactor(s) producing NH_3, auxiliary machinery (e.g., a solar tracking system, ammonia compression and storage, etc.). The relative capital investment required for these unit operation usually decreases with increasing plant capacity. Accounting for these effects may facilitate a fair comparison to the current industrial NH_3 synthesis that is economically attractive at capacities ranging from 1000-3000 t NH_3 per day[19].
- Simulating the NH_3 synthesis cycle separately from the process providing the required reducing agent. This may allow for increased clarity when comparing the simulation results to the currently employed heterogeneous catalysis. Furthermore, such a process model could account more flexibly for various market situations of the reducing agent, available production technologies[10], and delivery distances. Generally, the gaseous reducing agent (e.g., CO/H_2 to reduce the oxides of Mo or W respectively and CH_4 for the reduction of MnO yielding a syngas or methanol byproduct) may be purchased or generated on site. Potential processes producing the reducing agent sustainably include

biomass gasification or CO_2/H_2O reduction technology utilizing renewable energy sources and including a catalytic methanation process if needed.

- Use of a single code to interface and simultaneously execute the process simulation and its economic evaluation. Thereby, the assessment of the impact of specific process variables, process adaptation, and sensitivity analyses may be simplified significantly.

9.2.3 Ammonia from lattice nitrogen and hydrogen-sources other than water

If H_2 is employed as hydrogen source for the NH_3 synthesis from the lattice nitrogen of a TMN the formation of a TMO could be avoided (see Chapter 8). This would circumvent the energy-intensive TMO reduction step that is required when employing water directly as hydrogen source.

In absence of a H_2O cleavage process, the overall reaction accomplished is the exergonic conversion of N_2 and $3H_2$ to $2NH_3$. This indicates the need keep track of the total energy requirements to conduct such a reaction cycle (see Section 8.4.8) that would compete with the highly energy efficient catalytic NH_3 formation irrespective of the process employed in practice for the H_2 generation[12, 19].

Manganese nitride may be good material for theoretical and experimental studies (comparable to those outlined in Section 9.2.2.1) of such a reaction cycle. With regard on reactor design and experimental setups, experiments can be most likely conducted throughout below 1000°C. On the other hand, a sufficient supply of H_2 to the materials surface needs to be ensured to avoid mass transport limitations in the gas phase layer covering the reactant.

Attempting to chemically activate the hydrogen source and thereby perhaps increase ammonia yields and formation kinetics, hydrogen may be bonded covalently to elements with electronegativities between those of hydrogen and oxygen. This could be achieved by use of

gaseous hydrogen halides as hydrogen source. Such endeavors need to demonstrate the required reduction of the metal halide. Aiming for thermochemical reduction of a transition metal halide reactant, the high volatility of the metal halide will lead to steeply increased entropy values of the oxidized material at increased temperatures. This will constrain the range of feasible metallic reactants. Free energy computations would be a helpful guide, e.g., as outlined in Sections 2.4 and 2.5 or utilizing thermochemical simulation software such as Outokumpu HSC chemistry for Windows proving a database with more than 25,000 chemical compounds[20], FactSage software[21, 22] or the open source NASA SP-273 code[23].

Use of such software when developing novel solar thermochemical reaction cycles in the future will ensure realistic simulations (given the increased reaction network complexity) with minimized time expenditure, will avoid expensive trial-and-error experimentation, and will help with determining optimum reaction conditions.

9.3 References

1 J.R. Scheffe, J.H. Li, A.W. Weimer, A spinel ferrite/hercynite water-splitting redox cycle, International Journal of Hydrogen Energy, 35 (2010) 3333-3340.

2 M. Roeb, H. Müller-Steinhagen, Concentrating on solar electricity and fuels, Science, 329 (2010) 773-774.

3 C.J.H. Jacobsen, Novel class of ammonia synthesis catalysts, Chemical Communications, (2000) 1057-1058.

4 M. Jacoby, Rechargeable metal-air batteries, Chemical and Engineering News, 88 (2010) 29-31.

5 J.E. Miller, M.D. Allendorf, R.B. Diver, L.R. Evans, N.P. Siegel, J.N. Stuecker, Metal oxide composites and structures for ultra-high temperature solar thermochemical cycles, Journal of Materials Science, 43 (2008) 4714-4728.

6 C.J.H. Jacobsen, S. Dahl, B.S. Clausen, S. Bahn, A. Logadottir, J.K. Nørskov, Catalyst design by interpolation in the periodic table: Bimetallic ammonia synthesis catalysts, Journal of the American Chemical Society, 123 (2001) 8404-8405.

[7] A. Steinfeld, C. Larson, R. Palumbo, M. Foley, Thermodynamic analysis of the co-production of zinc and synthesis gas using solar process heat, Energy, 21 (1996) 205-222.

[8] M.T. Balta, I. Dincer, A. Hepbasli, Energy and exergy analyses of a new four-step copper-chlorine cycle for geothermal-based hydrogen production, Energy, 35 (2010) 3263-3272.

[9] M. Sturzenegger, P. Nüesch, Efficiency analysis for a manganese-oxide-based thermochemical cycle, Energy, 24 (1999) 959-970.

[10] S.K. Ritter, The Haber-Bosch reaction: An early chemical impact on sustainability, Chemical & Engineering News, 86 (2008) 53.

[11] W.J. Durand, A.A. Peterson, F. Studt, F. Abild-Pedersen, J.K. Nørskov, Structure effects on the energetics of the electrochemical reduction of CO_2 by copper surfaces, Surface Science, 605 (2011) 1354-1359.

[12] A. Hellman, E.J. Baerends, M. Biczysko, T. Bligaard, C.H. Christensen, D.C. Clary, S. Dahl, R. van Harrevelt, K. Honkala, H. Jonsson, G.J. Kroes, M. Luppi, U. Manthe, J.K. Nørskov, R.A. Olsen, J. Rossmeisl, E. Skúlason, C.S. Tautermann, A.J.C. Varandas, J.K. Vincent, Predicting catalysis: Understanding ammonia synthesis from first-principles calculations, Journal of Physical Chemistry B, 110 (2006) 17719-17735.

[13] J.J. Mortensen, L.B. Hansen, K.W. Jacobsen, Real-space grid implementation of the projector augmented wave method, Physical Review B, 71 (2005) 035109-1 to 035109-11.

[14] https://wiki.fysik.dtu.dk/gpaw/ (retrieved April 14, 2012).

[15] https://wiki.fysik.dtu.dk/ase/ (retrieved April 14, 2012).

[16] G. Ertl, Reactions at surfaces: From atoms to complexity (Nobel lecture), Angewandte Chemie-International Edition, 47 (2008) 3524-3535.

[17] J.R. Scheffe, M.D. Allendorf, E.N. Coker, B.W. Jacobs, A.H. McDaniel, A.W. Weimer, Hydrogen Production via Chemical Looping Redox Cycles Using Atomic Layer Deposition-Synthesized Iron Oxide and Cobalt Ferrites, Chemistry of Materials, 23 (2011) 2030-2038.

[18] P. Hones, R. Sanjinés, F. Lévy, O. Shojaei, Electronic structure and mechanical properties of resistant coatings: The chromium molybdenum nitride system, Journal of Vacuum Science & Technology a-Vacuum Surfaces and Films, 17 (1999) 1024-1030.

[19] I. Rafiqul, C. Weber, B. Lehmann, A. Voss, Energy efficiency improvements in ammonia production - perspectives and uncertainties, Energy, 30 (2005) 2487-2504.

[20] http://www.hsc-chemistry.net/ (retrieved April 14, 2012).

[21] http://132.207.164.4/fact/factsage/FactSage.pdf (retrieved April 14, 2012).

[22] http://www.crct.polymtl.ca/factsage/fs_family.php (retrieved April 14, 2012).

[23] http://www.engr.colostate.edu/~marchese/combustion08/cec.html (retrieved April 14, 2012).

Appendix A - Content associated with Chapter 2

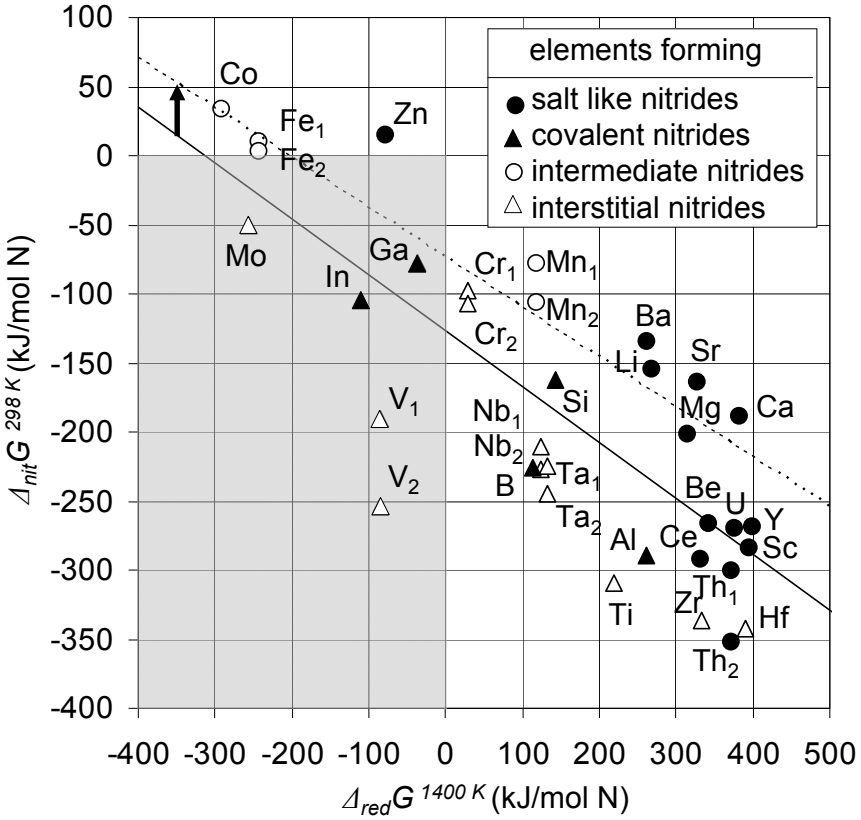

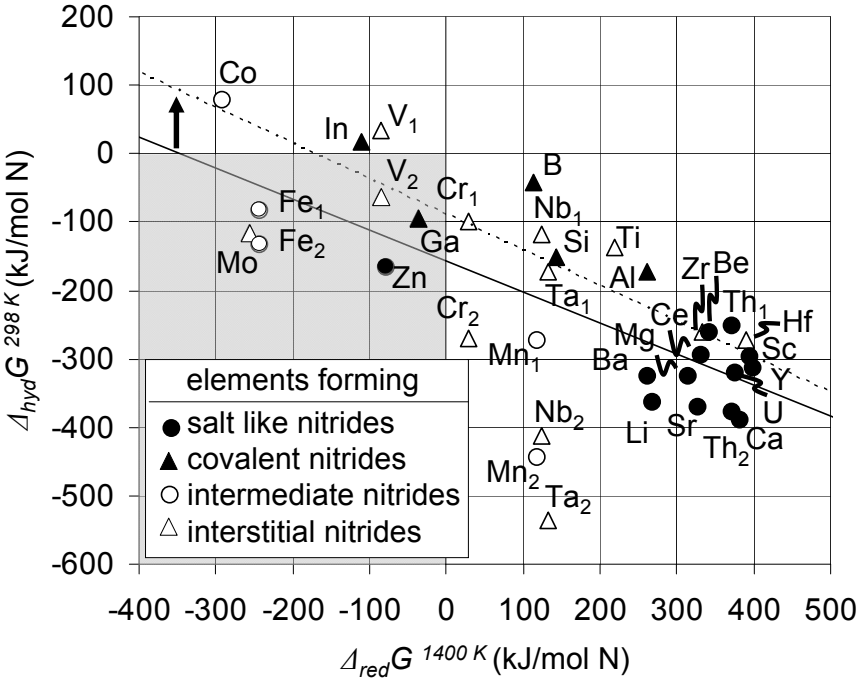

M	M_aN_b/M_cO_d
Li	Li_3N/Li_2O
Be	Be_3N_2/BeO
B	BN/B_2O_3
Mg	Mg_3N_2/MgO
Al	AlN/Al_2O_3
Si	Si_3N_4/SiO_2
Ca	Ca_3N_2/CaO
Sc	ScN/Sc_2O_3
Ti	TiN/TiO_2
V_1	VN/V_2O_5
V_2	$VN_{0.465}/V_2O_5$
Cr_1	CrN/Cr_2O_3
Cr_2	Cr_2N/Cr_2O_3
Mn_1	Mn_5N_2/MnO
Mn_2	Mn_4N/MnO
Fe_1	Fe_2N/Fe_2O_3
Fe_2	Fe_4N/Fe_2O_3
Co	Co_3N/Co_3O_4
Zn	Zn_3N_2/ZnO
Ga	GaN/Ga_2O_3
Sr	Sr_3N_2/SrO
Y	YN/Y_2O_3
Zr	ZrN/ZrO_2
Nb_1	NbN/Nb_2O_5
Nb_2	Nb_2N/Nb_2O_5
Mo	Mo_2N/MoO_2
In	InN/In_2O_3
Ba	Ba_3N_2/BaO
Ce	CeN/CeO_2
Hf	HfN/HfO_2
Ta_1	TaN/Ta_2O_5
Ta_2	Ta_2N/Ta_2O_5
Th_1	Th_3N_4/ThO_2
Th_2	ThN/ThO_2
U	UN/UO_2

Figure A.1 (previous page) Utility of various elements for reactive NH_3 synthesis at atmospheric pressure: $\Delta_{rxn}G$ of metal nitridation vs. $\Delta_{rxn}G$ of carbothermal metal oxide reduction (top), and $\Delta_{rxn}G$ of metal nitride hydrolysis vs. $\Delta_{rxn}G$ of carbothermal metal oxide reduction (bottom). The desired region of negative $\Delta_{rxn}G$ for nitride formation *or* of nitride hydrolysis *and* oxide reduction is the gray rectangular area. A linear fit is marked with a solid line. Computation are repeated for nitridation at 1000 K and hydrolysis at 800 K (or lower, limited by available data), represented by a linear fit (dashed line, no individual data points shown).

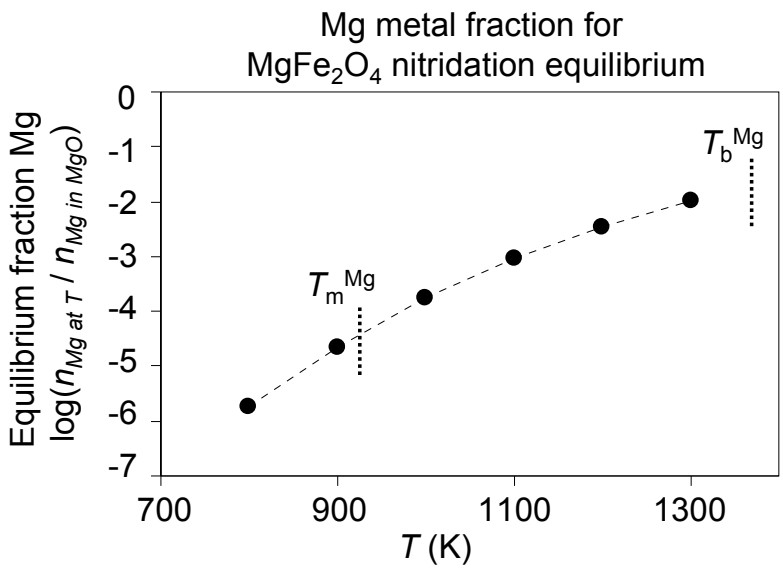

Figure A.2 Magnesium vapor formation during carbothermal nitridation of $MgFe_2O_4$.

Appendix B - Content associated with Chapter 3

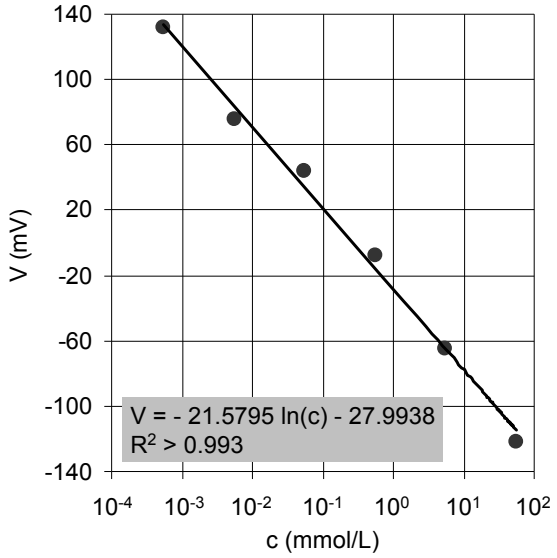

Figure B.1 Representative calibration curve of the NH_3 analysis in the liquid phase using an NH_3 ion selective electrode (see Section 1.4.4.2).

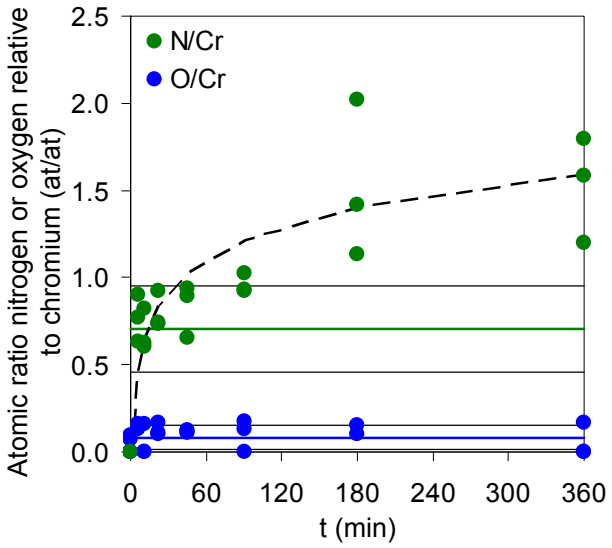

Figure B.2 N_2 fixation using Cr metal and concentrated sunlight: EDS of the solid reactant over the course of the reaction. Dashed lines are a guide only. The solid green line is the average (one standard deviation indicated with the flanking solid lines) of three analyses of purchased chromium nitride. The solid blue line is the average (one standard deviation indicated with the flanking solid lines) of the presented O/Cr data.

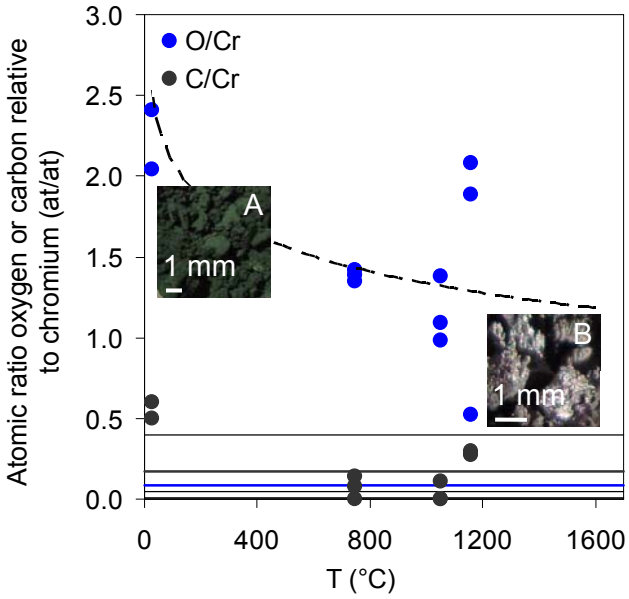

Figure B.3 Cr_2O_3 reduction with simulated gasified biomass: Energy-dispersive X-ray spectroscopy data of the solid reactant at various temperatures adjusted with the solar furnace. Dashed lines are a guide only. The solid blue and gray lines are the average (one standard deviation indicated with the flanking solid lines) of three analyses of purchased chromium metal. The inlets are photographs of the Cr2O3 reactant surface (A) before the reaction, or (B) after heating for 60 min at 1600°C in the reducing atmosphere.

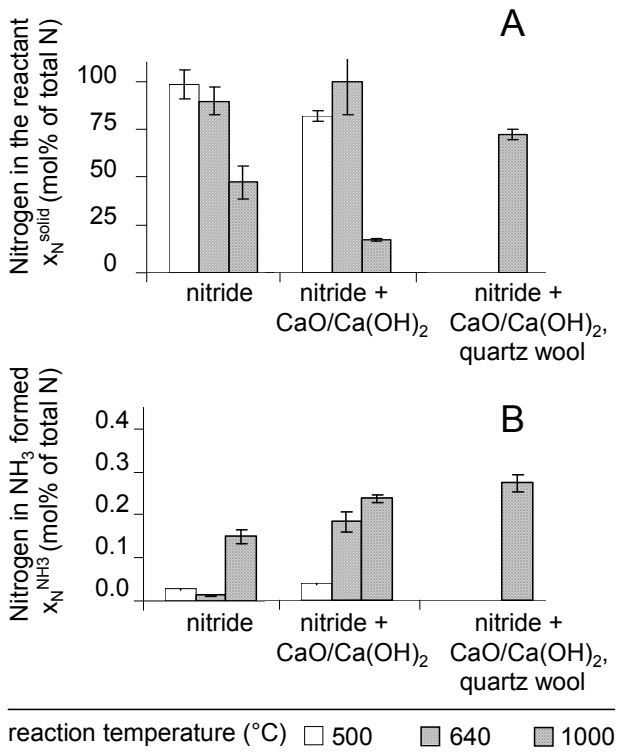

Figure B.4 Liberation of NH_3 due to hydrolysis of Cr nitride in presence or absence of calcium oxide/hydroxide: solid phase composition (A), NH_3 absorbed into a liquid absorbent (B). Error bars are via error propagation.

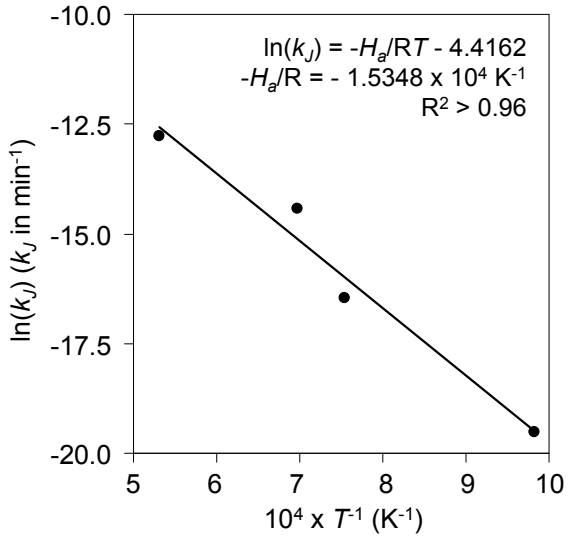

Figure B.5 Arrhenius plot estimating the activation energy (H_a) of the solar thermochemical reduction of Cr_2O_3 with simulated gasified biomass (R is the gas constant, see Section 2.4.2; R^2 is the coefficient of determination, see Section 1.4.2).

Appendix C - Content associated with Chapter 4

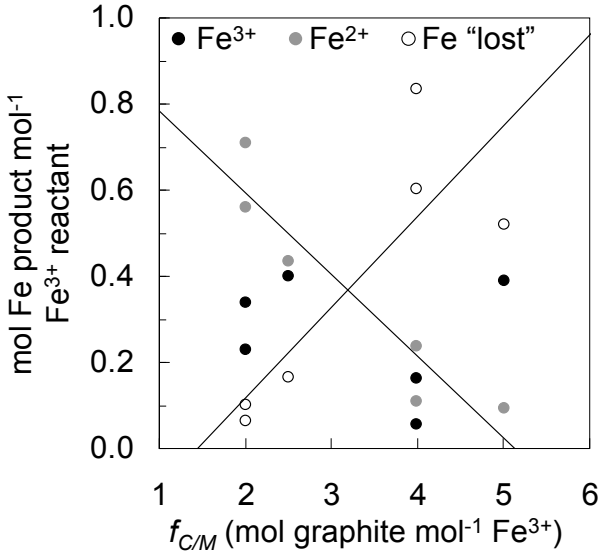

Figure C.1 Iron products formed after solar heating experiments: Fe^{3+} accounts for iron as Fe_2O_3, $MgFe_2O_4$, and Fe_3O_4, Fe^{2+} accounts for FeO and Fe_3O_4, "lost" marks the (unbalanced) remainder of an iron mass balance. Lines are guide to eye. The analytical uncertainty of the XRD analysis is indicated with the repeated analysis of selected samples.

Opposed to the formation of carbide and nitride in the $MgO/Cr_2O_3/C$ system (see Fig. 4.2), heating $MgO/Fe_2O_3/C$ powder mixtures for 30 min under N_2 flow at 1200°C with concentrated solar radiation yielded reduced iron species (FeO and Fe_3O_4). An iron mass balance indicates increasing disappearance of iron with increasing graphite concentrations. This may be explained by increased reduction of Fe^{2+} intermediates at increased graphite concentration yielding Fe^0 that is removed from the open system (N_2 gas flow) due to evaporation.

Appendix D - Content associated with Chapter 5

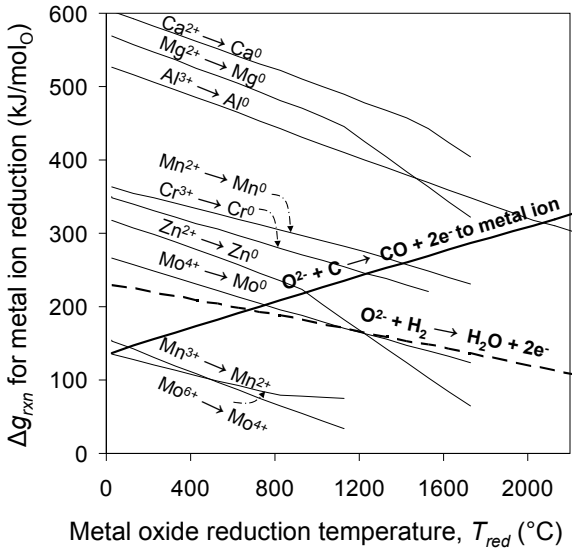

Figure D.1 Ellingham diagram to determine required temperatures and necessary reducing agents (solid graphite or gaseous H_2 if the metal ion reduction intersects their oxidation or none if $\Delta g_{rxn} = 0$) of the solar thermochemical metal oxide reduction step.

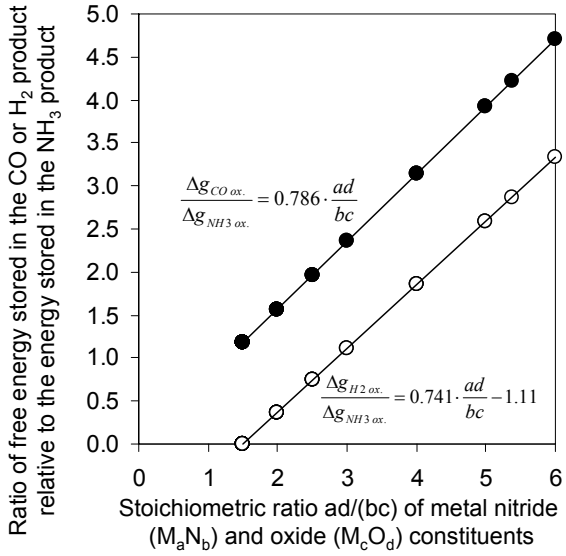

Figure D.2 N_2 Correlation of the free energy (at 25°C and 0.1 MPa) released by oxidation (ox.) of the cycle products (NH_3,CO or H_2 with O_2 to N_2, H_2O, or CO_2) and the stoichimetric composition of the nitride/oxide reactant. *a*, *b*, *c*, and *d*, stoichiometric constants in Eq. 5.1-5.3 (see Section 5.2).

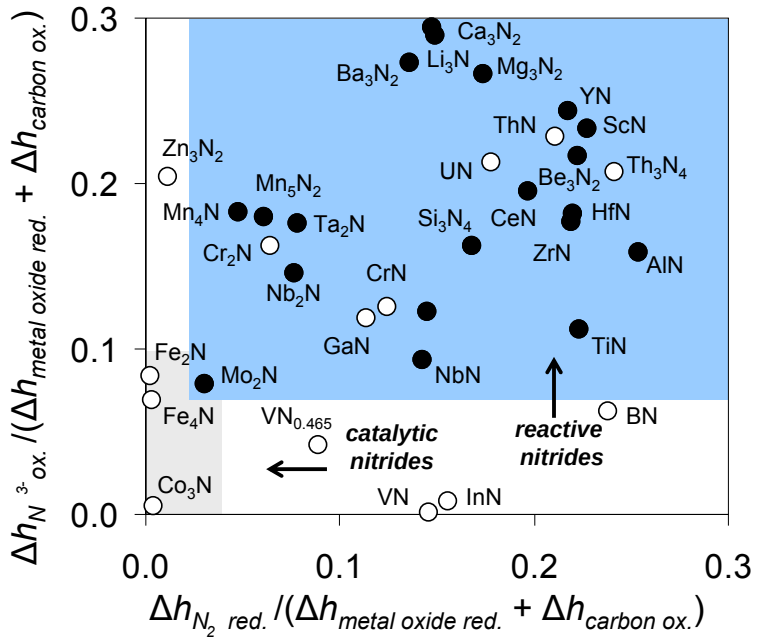

Figure D.3 Heat liberated during the N^{3-} oxidation (ox.) vs. N_2 reduction (red.), both relative to the energy supplied during the carbothermal metal oxide reduction step (all at 25°C and 0.1 MPa). Empty circles mark materials that do not fix 0.1 MPa N_2, do not liberate NH_3 effectively, or are radioactive.

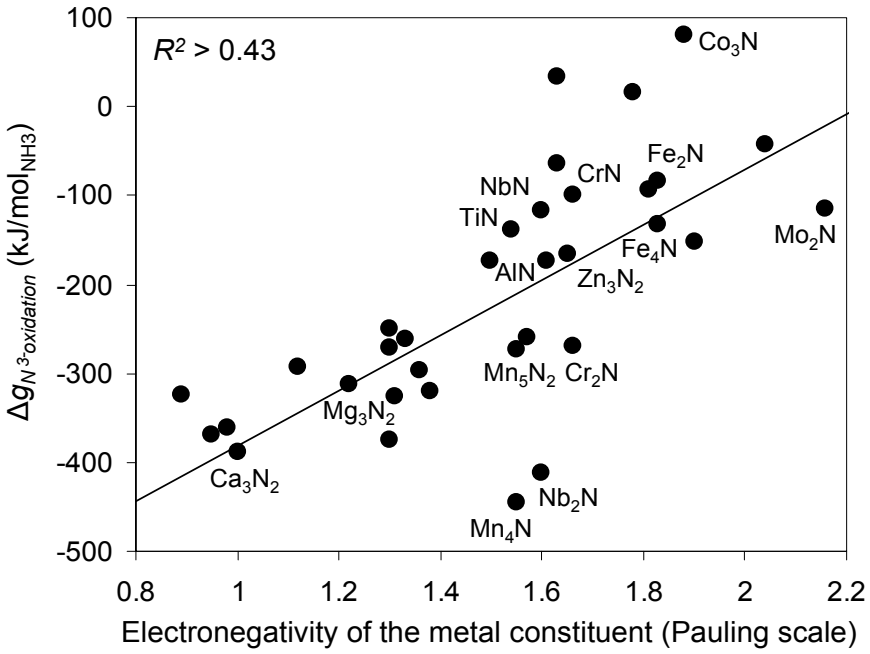

Figure D.4 Free energy (at 25°C and 0.1 MPa) of NH_3 formation via H_2O cleavage with metal nitrides versus the electronegativity of the metal constituent of the nitride.

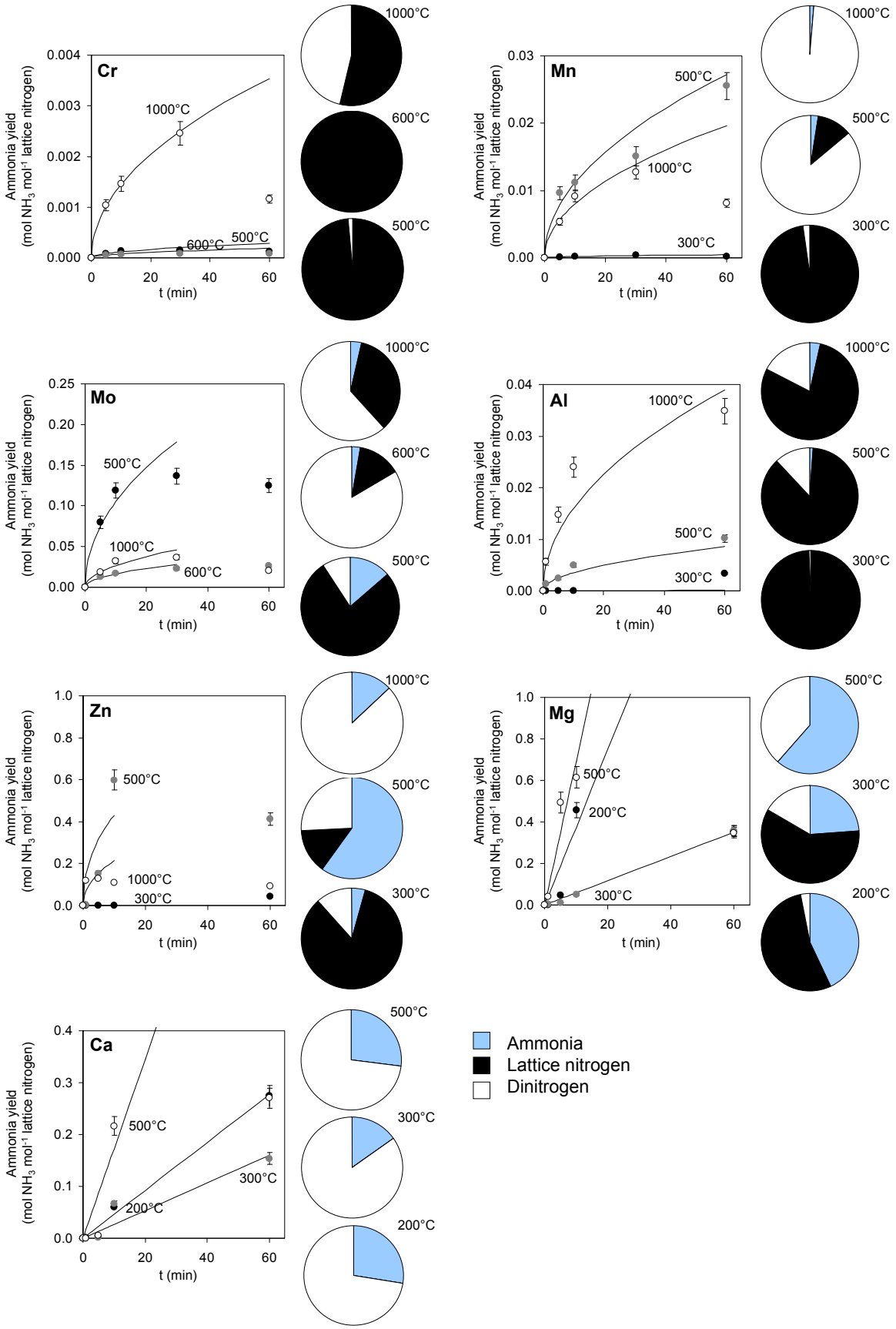
Cr
Mn
Mo
Al
Zn
Mg
Ca
Ammonia yield
(mol NH3 mol-1 lattice nitrogen)
t (min)
1000°C
600°C
500°C
300°C
200°C
Ammonia
Lattice nitrogen
Dinitrogen

Figure D.5 (previous page) Steam hydrolysis of binary metal nitrides (metallic constituent indicated). Lines are shrinking core models limited by diffusion in the solid state (Al, Cr, Mn, Zn, Mo) or in the gas phase (Mg, Ca). Error bars indicated are via error propagation.

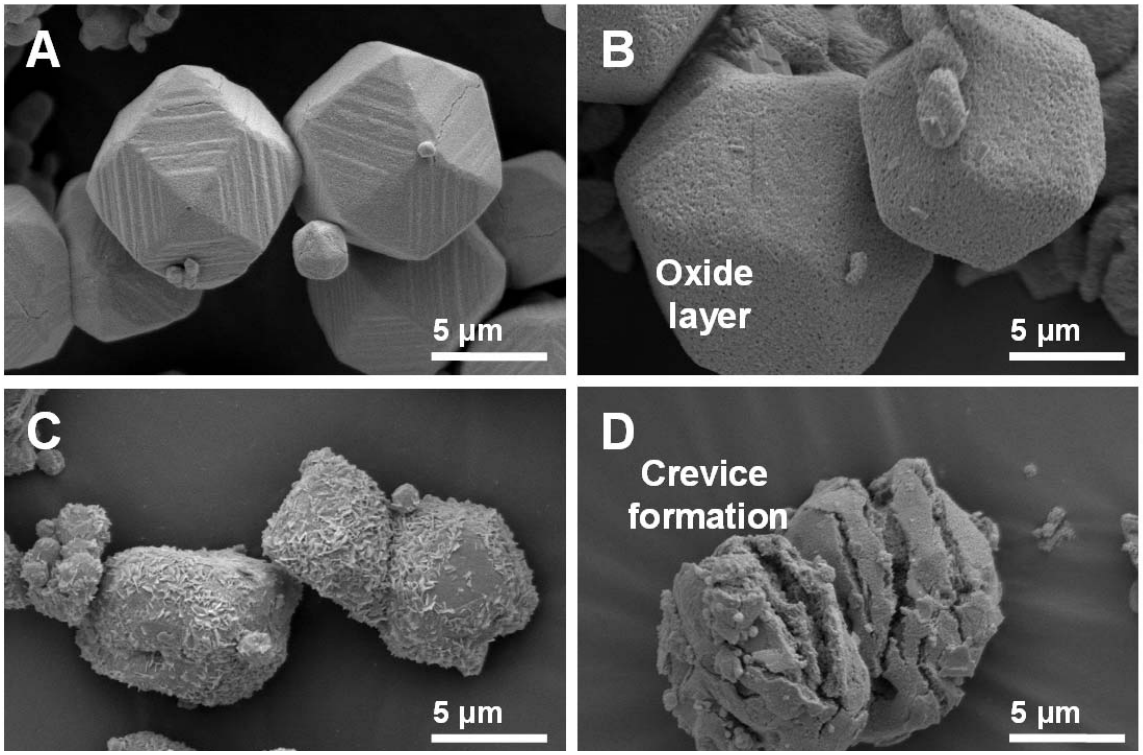

Figure D.6 SEM micrographs of Mo_2N (A, B) or Zn_3N_2 (C, D) before (A, C) or after (B, D) hydrolysis for 60 min at 500°C

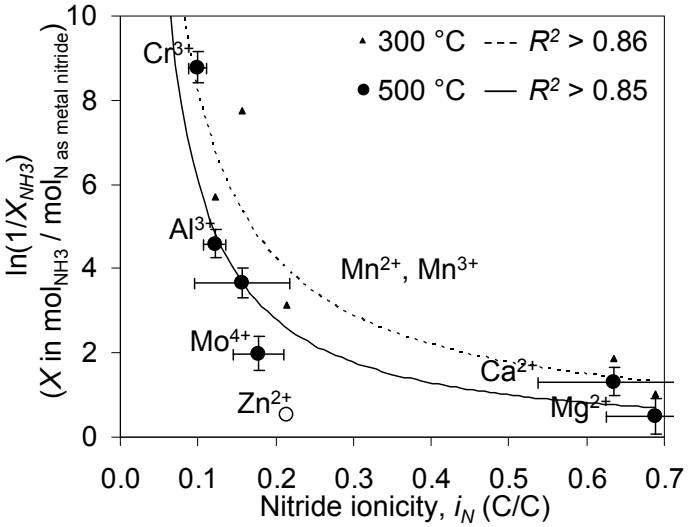

Figure D.7 Maximum ammonia yields vs. the nitride ionicity.

Appendix E - Content associated with Chapter 6

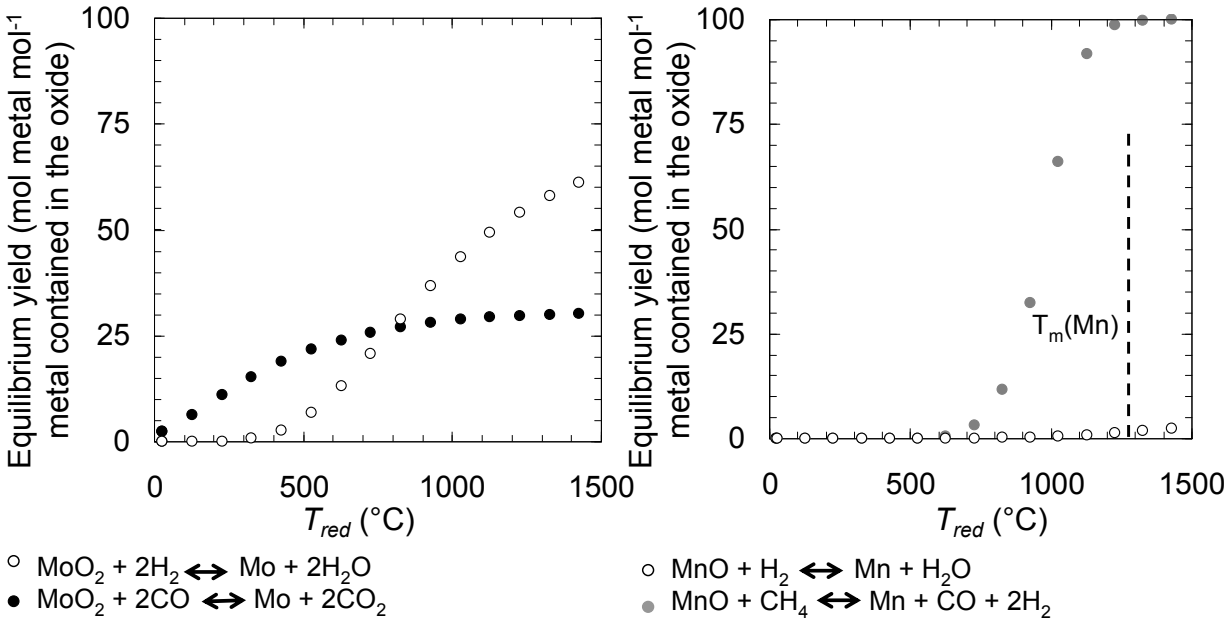

Figure E.1 Equilibrium yield computations for the thermochemical reduction of MoO_2 or MnO with various chemical reducing agents and concentrated solar radiation at elevated temperatures (the superscript of the molar amount, *n*, of metal marks the assumed reducing agent, K_T is the reaction equilibrium constant, see Section 1.4.1 for computation details, the dashed line marks the melting point of Mn).

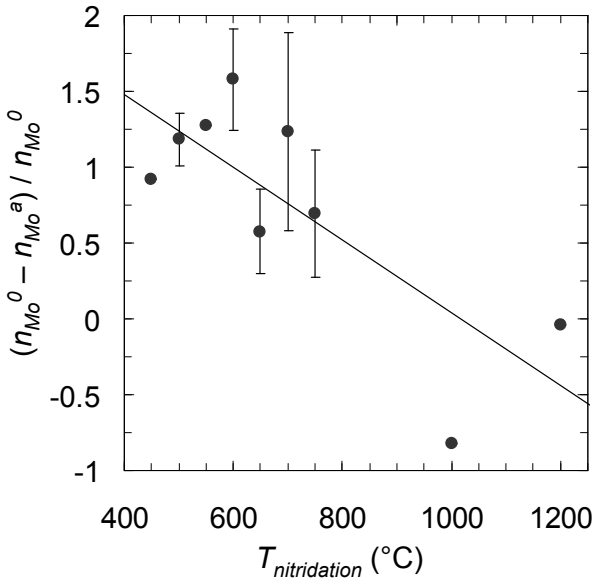

Figure E.2 Mo mass balance for 100 kPa N_2 reduction experiments with Mo metal (0, before the experiment; a, after the experiment). The analytical uncertainty of the data (error bars) is in average ± 36.48 %. The line is to guide the eye.

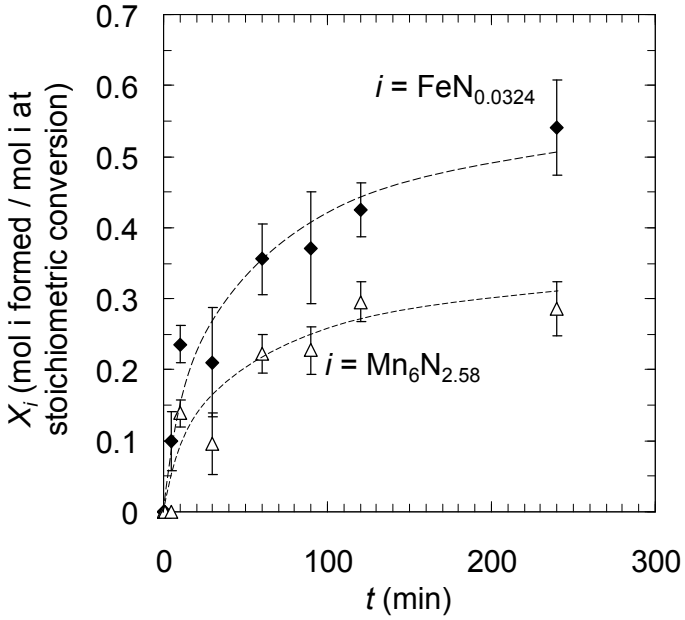

Figure E.3 Formation of iron nitride with low nitrogen content (filled symbols) during the dinitrogen reduction at 750°C with Fe-doped Mn (formation of $Mn_6N_{2.58}$ is shown with empty symbols as reference). Lines are a guide only. Error propagation within a 95% confidence (error bars) yields in average ± 20.83% for the $FeN_{0.0324}$ data set.

Appendix F - Content associated with Chapter 7

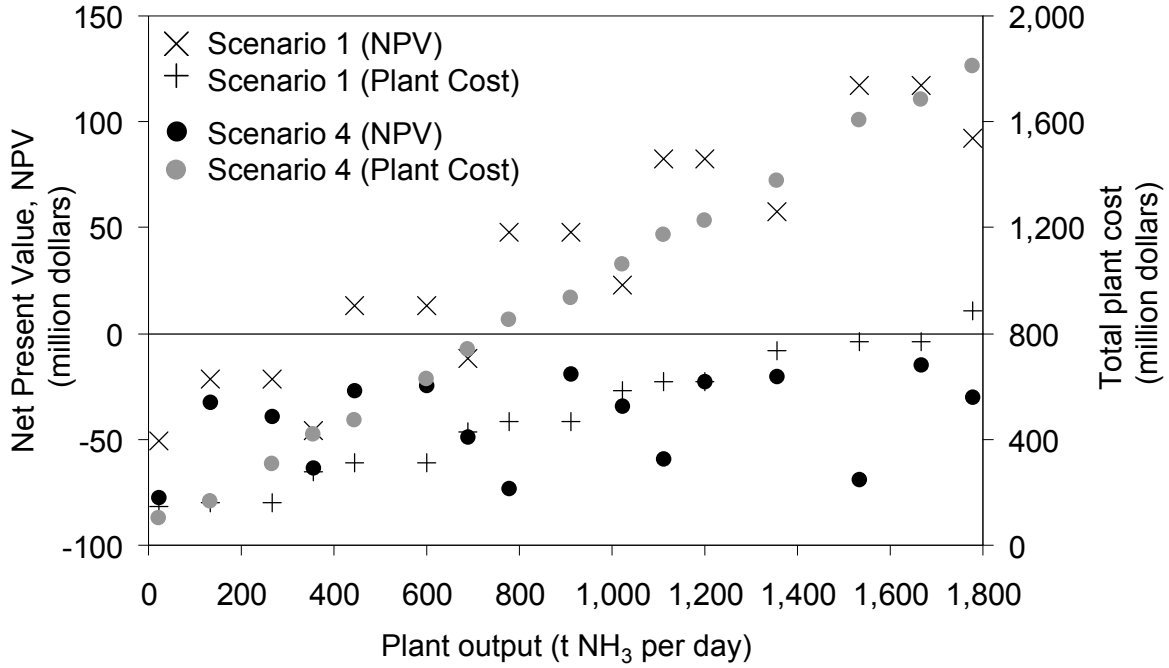

Figure F.1 Net-present value (NPV) and total initial plant costs as a function of NH_3 output. Scenario 1) "ideal operation" (see Section 7.4.3) and conservative cost estimates (see Section 7.6.2); Scenario 4) "conservative operation" and optimistic costs.

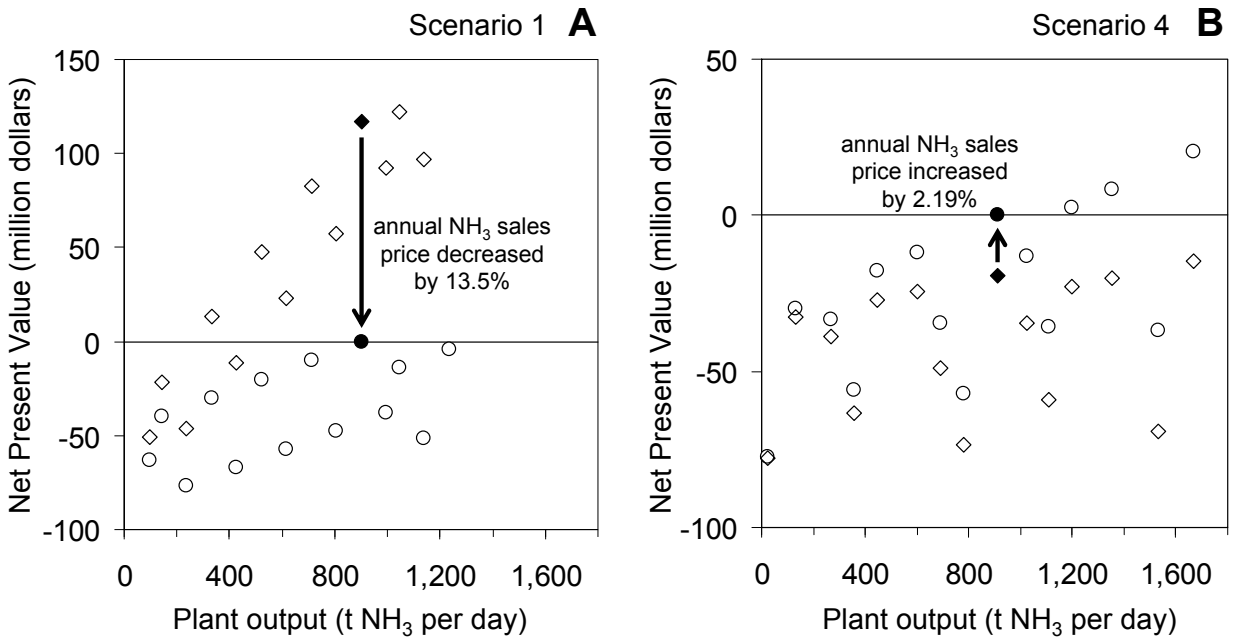

Figure F.2 Sensitivity of (A) Scenario 1 or (B) Scenario 4 to variations in the NH_3 sales price Monte Carlo-simulated over a 20 year plant lifespan (diamonds mark simulations with baseline-NH_3 sales prices, circles mark simulations with in- or decreased NH_3 sales prices, as indicated, to break even at "optimum plant size" shown with filled symbols). For descriptions of Scenarios 1 or 4 respectively see Figure F.1.

Appendix G - Content associated with Chapter 8

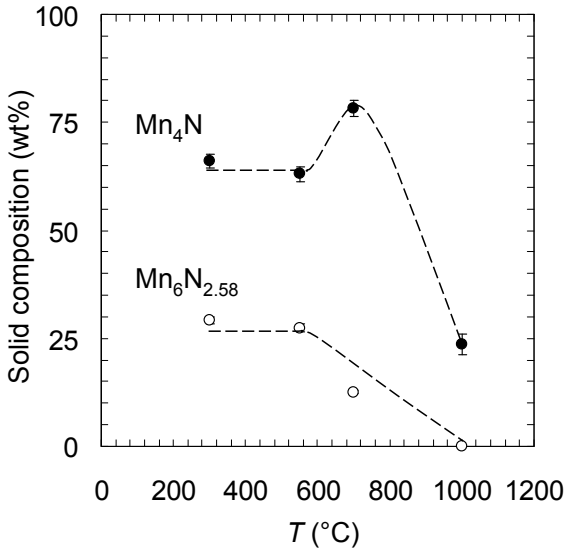

Figure G.1 Manganese nitrides formed after reacting a powder containing initially 59-67 wt% ε-Mn_4N, 25-34 wt% ζ-$Mn_6N_{2.58}$ for 60 min with 0.5 ± 0.1 $L_{(STP)}$ H_2 min^{-1}. Error bars are the analytical uncertainty of the XRD analysis. Lines are to guide to the eye.

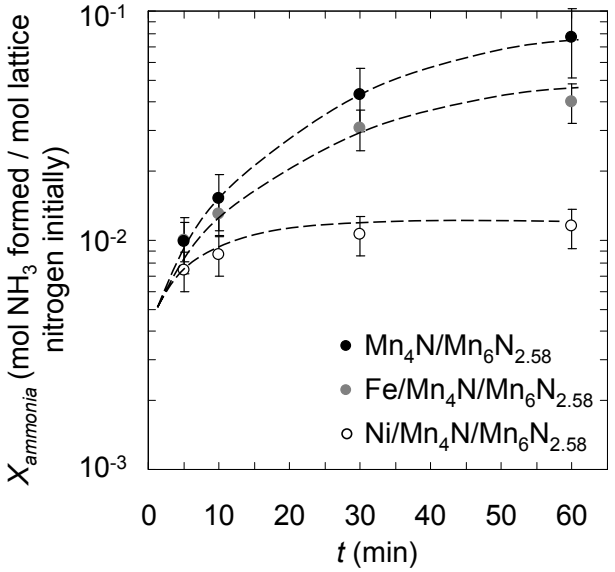

Figure G.2 NH_3 from manganese nitride powder (59-67 wt% ε-Mn_4N , 25-34 wt% ζ-$Mn_6N_{2.58}$) with or without equimolar Fe or Ni doping and 0.5 ± 0.1 $L_{(STP)}$ H_2 min^{-1}. Error bars are via error propagation within a 95% confidence interval. Lines are to guide to the eye.

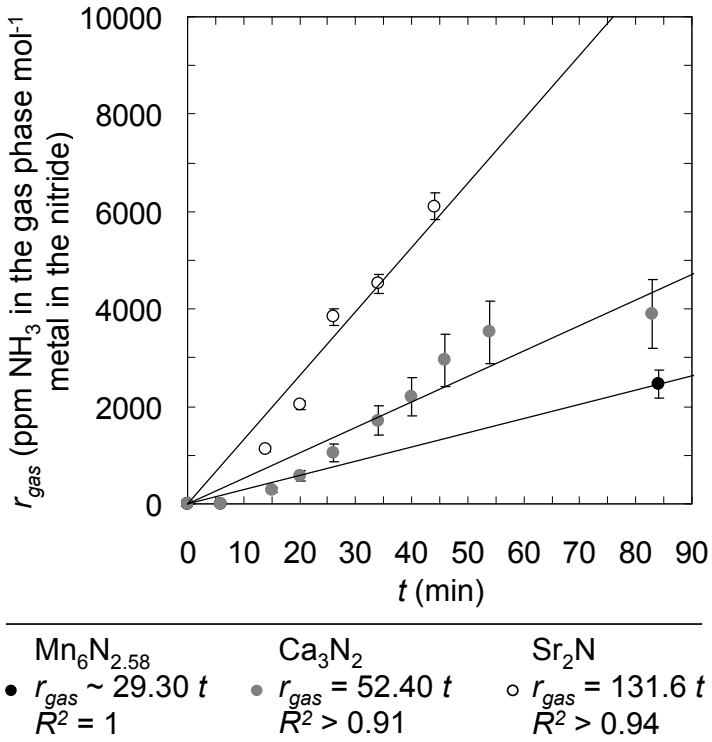

Figure G.3 NH_3 in the gas phase leaving the absorption vessel for reaction cycles with $Mn_6N_{2.58}$, Ca_3N_2 or Sr_2N respectively (see Section 8.3.3) with zeroing for the initial NH_3 reading (compare Section 8.4.7, Fig. 8.8). Error bars are via error propagation accounting for the XRD analysis of the nitride within a 95% confidence interval. Lines are linear regressions.